



Polarised Fluorescence and Stimulated Emission Depletion Studies of Excited State Dynamics

Elinor J. Bailey

A thesis submitted in partial fulfilment
of the requirements for the degree of
Doctor of Philosophy

Department of Physics & Astronomy
University College London

July 2013

Abstract

This thesis presents the research undertaken in time-resolved fluorescence intensity and anisotropy techniques and their application. New information is revealed concerning the emission behaviour of a synthetic multipolar branched chromophore (AF257). Investigation of the relative radiative rates of fluorescing components in fluorescent proteins EGFP and mCherry was carried out using stimulated emission depletion (STED). Previous assumptions in the modelling of both continuous wave (CW) and pulsed STED are shown to be insufficient, and refinements are proposed and tested.

The fluorescence techniques employed in this thesis utilise photoselection of an ordered excited state through polarised single and two-photon laser excitation, in addition to polarised, time-resolved measurement of sample fluorescence. Chapter one introduces the fluorescence process, the time-evolution of the alignment in the excited state, and the core measurement processes used. Chapter two examines in detail the absorption-emission mechanism of AF257 using both two-photon and single-photon excitation. By combining fluorescence intensity and anisotropy measurements, it was possible to resolve the emission into that from two distinct excited state geometries. Such a thorough analysis has not been previously published for a molecule of this type; this synthesis of information enables the proposition of a new model for the absorption-emission process.

The second half of the thesis concerns the use of STED, which incorporates the orientationally sensitive de-excitation of the excited state distribution. Chapter 3 employs CW STED to probe the fluorescence lifetimes and radiative rates of the commonly used fluorescent probes EGFP and mCherry. It is shown that each of these molecules consist of two fluorescing components with individual radiative rates and varying amplitudes (with STED power). A single ‘average’ lifetime and radiative rate is often used for these molecules in biological applications, and the differences observed here could have major implications for the accuracy of results obtained in their application in the biosciences. The chapter goes on to assess the assumption of an average STED rate in CW STED. Using fluorescence anisotropy measurements and numerical simulation, the importance of orientational dependence of fluorescence lifetimes in the analysis of STED measurements is shown.

Chapter 4 investigates the effects of pulse stretching and solvent viscosity in pulsed STED. Analysis of this data shows the breakdown of the previously used model with the use of very long (of the order of 2-10 times the rotational correlation time) STED pulses. Revisions to the model are developed and tested. From the results of

these revised models it is concluded that the rotation of the higher order spherical harmonic moments in the excited state distribution has a highly significant effect on the observed depolarisation of the excited state alignment, and that further improvements to the model are needed to incorporate this effect.

Acknowledgments

Thanks to my supervisor Angus Bain for his help and support throughout this PhD and to all the other people who have been responsible for me having such great times. In places. Here they are:

Firstly, thanks to all the (special) people from my lab who not only gave me so much help but also managed to make being stuck in an underground bunker with no natural light for four years seem like a good idea. My post-docs who looked after me so well and who were always there to Sporcle or to make me attend ridiculous sports classes (Nick), help me pick out the best stationary (Daven) or to remind me how bad buses are (Rich). You taught me so much; some of it even about Physics. Also thanks to Sian for the baking and dead plants, Tom B for your google search abilities and Tom W for introducing me to Turkish food. And to all of you for generally making the lab a better place (not hard).

Thanks also to the rest of the UCL Physics gang for fun times and especially to Arne for the Mathematica help, and of course for all the photos. Also to James for the tea, to Alexandros for helping with inter-lab equipment-lending networks (taking our stuff), and to Duncan for nitrogen-evaporation support. I would also like to acknowledge the generosity of all the UCL Physics technical support and admin staff who have helped me over the years.

Many thanks to my housemates throughout this PhD who have put up with me and been so nice about this whole thing, particularly: Rich, Dan, Emma, Welbirg, Katy and Lucy. I owe you all a few years of being a better housemate. Good luck claiming that back.

Thanks to my mum for being so invariably supportive. I suppose I should start paying you back now?

And finally, thanks to Michael. You didn't write anything but you did the whole thing with me. Panda says Smash.

Contents

1	Fluorescence Spectroscopy Measurements	1
1.1	Introduction	1
1.2	Absorption and Emission in a Chromophore	3
1.2.1	The Born-Oppenheimer approximation	4
1.2.2	Fluorescence Measurements	11
1.3	Fluorescence Anisotropy	15
1.4	Rotational Diffusion	18
1.4.1	Debye Small Step Diffusion	19
1.4.2	Ellipsoidal Rotational Diffusion Approximation	21
1.5	Anisotropy Decay	22
1.6	Time Correlated Single Photon Counting	23
1.7	Summary	24
	References	25
2	Two-Photon Excited State Dynamics in a Branched Nonlinear Fluorophore	29
2.1	Introduction	29
2.2	Optimisation of 2PA in molecules	33
2.3	Excitation distribution in Branched Molecules	35
2.4	2PA cross-section	38
2.5	Dependence of 2PA on excitation pulse profile	41
2.6	Reference Samples: p-Bis (o-methylstyryl)-benzene (bis-MSB) and Rhodamine-B	42
2.7	2PA Polarisation Dependence	42
2.8	Experimental Methods	47
2.8.1	Excitation System	47
2.8.2	Detection System	49
2.8.3	Instrument Response and Reconvolution	52
2.8.4	Data Analysis	53
2.8.5	Experimental procedure	56
2.9	Results	63
2.9.1	$\sigma^{(2)}$ Measurement	63
2.9.2	Two Photon Fluorescence Lifetime Measurement	65
2.9.3	Calculation of Ω	66
2.9.4	Fluorescence Anisotropy Measurements	70

2.9.5	Transition Tensor Analysis	74
2.9.6	Discussion	85
2.10	1PA Measurements	92
2.10.1	Discussion	98
2.11	Conclusions	100
	References	102
3	Radiative Decay Dynamics in Fluorescent Proteins Probed by Continuous Wave Stimulated Emission Depletion	110
3.1	Introduction	110
3.2	Green Fluorescent Protein (GFP) and Derivatives	113
3.2.1	Photophysics of EGFP	114
3.3	mCherry (Fluorescent Protein)	115
3.4	Stimulated Emission Depletion	116
3.5	Experimental Set-Up	119
3.6	Fluorescence Intensity of EGFP following 1PA	122
3.7	EGFP and mCherry Fluorescence Intensity Decays in the presence of CW STED	128
3.8	Fluorescence Anisotropy induced by STED	142
3.9	Orientationally Dependent Lifetimes	145
3.10	Simulated data	148
3.11	Conclusions	158
	References	160
4	Pulsed Stimulated Emission Depletion Dynamics	165
4.1	Introduction	165
4.2	Two-Level Model of STED Dynamics	168
4.3	Experimental Set-up	171
4.4	Rotation of Excited State Population During DUMP	177
4.4.1	Dump Pulse Length	177
4.4.2	Solvent Viscosity	179
4.4.3	Discussion	183
4.5	Further Investigation of the Model	184
4.5.1	Alteration of Alignment Moment Amplitudes	191
4.5.2	Addition of a Constant to the Excited State Distribution	193
4.5.3	Model in which Amplitude of Higher Order Moments is Reset to Zero Part-way Through the DUMP Pulse	195
4.6	Conclusions	200
	References	202
	Summary	204

Chapter 1

Fluorescence Spectroscopy

Measurements

1.1 Introduction

Time-resolved fluorescence spectroscopy is used as a research tool in many areas of science including chemical physics, biochemistry and biophysics and has been responsible for significant advances in the understanding of the dynamics and structure of biological macromolecules [1-3]. Advances in laser engineering and the development of fluorescent probes have enabled the widespread use of this technique beyond the academic environment; for example in biotechnology, gene sequencing, and pharmaceuticals etc. [4-6]. This thesis covers time-resolved single and two-photon excited fluorescence of molecules in solution, assessed using fluorescence intensity and anisotropy measurements, as well as examining the technique of Stimulated Emission Depletion (STED) in particular detail.

Fluorescence anisotropy occurs when a weak (in that it excites a small sub-set of sample molecules), polarised, excitation source is used to create a specific orientational distribution of excited fluorophores from a ground state distribution that can be isotropic, or itself ordered. The probability of excitation is related to the

angle between the polarisation of the excitation light source and the direction of the electric dipole absorption moment of the fluorescent chromophore. Emission then occurs at a fixed angle to the absorption moment (often approximately zero), resulting in an angular dependence to the measured fluorescence intensity. Measurement of this fluorescence anisotropy in turn enables observation of the time evolution of the excited state distribution of emission dipole directions; the fluorescence becomes depolarised as the molecules rotationally diffuse. Often a fluorescent molecule is attached to a non-fluorescent molecule, performing the function of a fluorescent probe; behaviour of the non-fluorescent molecule is then inferred from that of the fluorescent probe. The depolarization of the fluorescence is dependent on the size and shape of the fluorescent molecule, or in the case of fluorescent probes, additionally to the non-fluorescent molecule to which the probe is attached. Other factors affecting depolarisation in the case of fluorescent molecules/probes in solution include the viscosity, temperature and other properties of the solution (such as solute-solvent interactions, intrinsic ordering and dynamic solvation effects). Fluorescence anisotropy measurements using a fluorescent probe can yield information about the overall rotation of the molecule to which the fluorescent probe is attached, in addition to information about internal rotational modes which can include localised motion of the probe. Early work in this field was carried out by Perrin [7, 8], who developed basic equations to predict the amount of fluorescence depolarisation by Brownian motion depending on a range of factors, such as those cited above. The use of extrinsic fluorescent probe labelling to study proteins was subsequently introduced by Weber [9]. Jablonski simplified the mathematical evaluation by introducing ‘fluorescence anisotropy’ as a linear parameter [10, 11], and Albrecht examined further the theory of polarised electronic transitions [12]. The main concepts of fluorescence anisotropy along with its applications are discussed in ‘Principles of Fluorescence Spectroscopy’ by Lakowicz [13], for example. Recent applications of fluorescence anisotropy measurements include determination of molecular parameters such as size, conformation, orientation and folding states, in addition to revealing information about the local environment such as temperature and viscosity of solvent, and

information about solvent-solute interactions [14].

This thesis summarises the research undertaken under the supervision of Dr Angus Bain in the Ultrafast Spectroscopy laboratory: part of the UCL Atomic, Molecular and Positron Physics group. The Ultrafast Spectroscopy research group studies single and two-photon induced fluorescence in biological molecules and in ordered systems as a method of investigating molecular probe dynamics, in addition to studies of molecules designed for high two-photon absorption (2PA). Work includes development and application of time-resolved polarised laser techniques such as STED (stimulated emission depletion), FCS (fluorescence correlation spectroscopy), FRET (fluorescence/Förster resonance energy transfer), and fluorescence polarisation measurement. The group's most recent work includes preparation of an ordered initial excited state through use of STED, which enables investigation of local protein structures and dynamics. It also includes development of STED as a tool to enhance resolution in confocal microscopes. Investigation of branched chromophores with three-fold symmetry is ongoing, as well as analysis techniques for the methods outlined above. The following work involves a number of these technologies, enabling familiarity with a range of research areas within the group and with different experimental techniques. It consists of three main sections detailing the application of fluorescence anisotropy techniques; anisotropy measurements of a 2PA optimised branched chromophore; CW STED measurements of fluorescent proteins; and a further investigation of pulsed STED as a technique and its limitations including computational modelling of polarised photoselection.

1.2 Absorption and Emission in a Chromophore

Electronic transitions in atoms and molecules are caused by perturbations to the electron wavefunction caused by an oscillating dipolar electric field i.e. that of the incident light (electric dipole approximation) resulting in an induced polarisation at the driving frequency. This polarisation feeds back on the driving electric

field exchanging energy between the field and the electron. The energy exchange is maximised when the resonance condition is met i.e. the frequency of the incident radiation matches the natural frequency of the electronic transition (in the case of single-photon absorption) as given by the equation

$$\Delta E = h\nu \quad (1.2.1)$$

where ΔE is the change in energy and ν is the resonant frequency of the transition. In fluorescent molecules the region that is polarisable in this way is governed by the extent of the electronic wavefunctions involved and is known as the chromophore (in the case of small fluorescent molecules this may be the entire molecule). The transition rates can be calculated using the time dependent Schrödinger equation, if all the particle interactions with each other and the electric field can be solved. This is not generally the case for all but the very simplest systems. In fluorescence studies the perturbing electric field is extremely weak compared with the internal electric fields binding the electrons in the atom or molecule and thus perturbation theory can be used. Solutions to perturbation theory treatments are still not possible for all systems without further simplifying approximations. Two of the most commonly used, the Born-Oppenheimer approximation and the Franck-Condon principle, are described below.

1.2.1 The Born-Oppenheimer approximation

The Born-Oppenheimer (BO) approximation was proposed in 1927 [15] and is used to simplify the computation of energy levels and wavefunctions of molecules. It allows the separation of the wavefunction Φ into electronic and nuclear (vibrational, rotational and spin) components since it considers the inertia of the electron to be negligible compared to the nucleus to which it is bound.

$$\Phi_{Total} = \phi_{electronic} * \phi_{nuclear} \quad (1.2.2)$$

The BO approximation is an important tool in quantum chemistry as without it only H_2^+ could be handled theoretically in full. A consequence of the BO approximation

is that the electron energies depend only on the nuclear configuration and not on the kinetic energy of the nuclei; the electronic energy levels can thus be calculated first by assuming the nuclear energy levels to be static on the timescale of electronic absorption or emission. The energy levels of the nuclear states can then be calculated from this. For diatomic molecules, the electronic states can be represented by plots of potential energy as a function of internuclear distance. Larger polyatomic molecules can be described in a similar way to the diatomic case, but would have more complex rotational and vibrational levels and a greater number of degrees of freedom: $3N-3$, where N is the number of nuclei [16]. The lowest energy level (ground state) of a molecule with zero net charge and an even number of electrons is in general a singlet state in which all electrons are spin-paired in accordance with the Pauli exclusion principle, and is labelled S_0 . Higher energy electronic singlet states labelled S_1, S_2, \dots, S_n ('excited' states) can be reached through absorption of the appropriate amount of energy, for example via single-photon absorption (1PA) or via two-photon absorption (2PA) as described in Chapter 2. However, occupation of excited electronic states at thermal equilibrium is negligible due to the energetically unfavourable Boltzmann factor; $\exp\left(\frac{-E_i}{k_B T}\right)$.

The Franck-Condon principle

The Franck-Condon principle explains the relative intensities of vibrational transitions within a molecule. Electronic excitation transitions often involve simultaneous electronic and vibrational transitions, and the principle states that the likelihood of such a transition depends on the overlap of the vibrational part of the initial and resulting wavefunctions. Specifically, the probability of a transition between two vibrational states with wave functions $|v\rangle$ to $|v'\rangle$ depends on the squared modulus of their overlap [17] :

$$P_{v \rightarrow v'} = |\langle v' | v \rangle|^2 \quad (1.2.3)$$

This calculates the probability that a molecule in the final vibrational state would have the same nuclear positions and momenta as one in the initial state as these

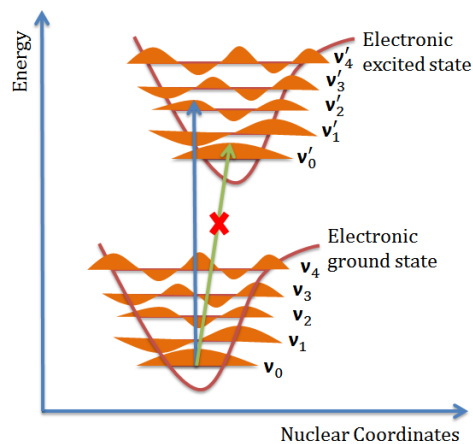


Figure 1.1: Illustration of the Franck-Condon principle for a vibronic transition from the ground electronic state S_0 to excited state S_1 . The transition probability is maximised from ground vibrational state to higher lying vibrations states of S_1 ; this incurs the maximum overlap between initial and final vibrational wave functions. Figure modified from ucdavis.edu.

are effectively frozen during the electronic transition. For the $S_0 \rightarrow S_1$ transition in general the greatest overlap from the lowest vibrational level of the ground state will occur to one of the higher-lying vibrational states in the S_1 excited state. This is due to the often larger inter-nuclear separation in the excited state as generally the electron configuration is less tightly bound. This is illustrated in Figure 1.1

Excited state relaxation

Due to the Franck-Condon principle and the reasons state above, the $S_0 \rightarrow S_1$ transition will have a high likelihood of reaching a vibrationally excited level in S_1 . The molecule will then be vibrationally hot and the state unstable as the molecule is not in thermal equilibrium with the solvent. Thus follows a rapid sub-picosecond ($10^{-13} - 10^{-11}s$) vibrational relaxation to the ground vibrational state of S_1 via collisions with solvent molecules. Spontaneous emission can follow the absorption; due to the relative timescales involved (ns vs ps), the emission process usually takes place following full vibrational relaxation in the excited state.

The emission transition is also governed by the Franck-Condon principle and therefore the probability of transition $S_1 \rightarrow S_0$ is greatest to the higher vibrational levels of the ground state S_0 as reflected in the emission spectrum with transitions to the lowest vibrational levels (blue edge emission) and highest vibrational levels (red edge emission) of relatively low probability. Again, the molecule undergoes vibrational relaxation to reach the lowest vibrational states reaching thermal equilibrium with the solvent. The fluorescence emission spectrum is therefore red-shifted from the absorption spectrum due to the energy lost in vibrational relaxation; this phenomenon is observed in polar molecules where electronic excitation causes a change in its permanent electric dipole moment. The solvent molecules will rearrange around the excited solute in order to minimise the free energy of the system. This gives rise to a time-dependent red shift in the $S_1 \rightarrow S_0$ fluorescence. The magnitude of the red shift is governed by the dipole moment change and solvent polarity. The rate of solvent relaxation is governed by the time taken for the solvent to reorganise around the solute, which is dependent upon solvent viscosity and temperature. This is known as Stoke's shift [18]. A further red shift can be caused by solvent relaxation; if a large change in permanent electric dipole moment occurs on transition to the excited state, the solvent molecules may rearrange to minimise the energy of the system. This is called the 'solvation effect' and increases with solvent polarity [19]. It is normally fast compared with the fluorescence lifetime but can be seen with high time resolution and/or viscous solvent.

Non-fluorescence decay pathways

Emission of a photon is not the only pathway for the $S_1 \rightarrow S_0$ transition; other non-radiative decay routes exist. These pathways are summarised in the Jablonski diagram in Figure 1.2. Non-radiative mechanisms include energy transfer (if a suitable acceptor is within the range of the transfer mechanism), collisional quenching, and internal conversion to another state of the same spin multiplicity (on a timescale of $10^{-11} - 10^{-9}$ s [13]). Alternatively, the non-radiative mechanism of intersystem

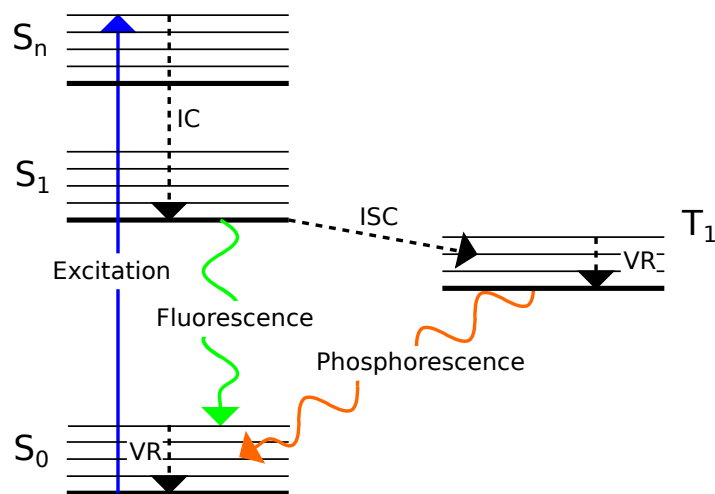


Figure 1.2: A simplified Jablonski diagram showing possible decay routes in a fluorescent molecule. Blue, absorption; green, fluorescence; orange, phosphorescence; IC, Internal conversion; VR, vibrational relaxation; ISC, Intersystem crossing; S_0 , ground electronic state; S_1 , first electronic excited state; S_n , n th excited electronic state; T_1 , first excited triplet state.

crossing to the lowest molecular triplet state T_1 (assuming a singlet ground state) can occur (on a timescale of $10^{-10} - 10^{-8}s$ [13]) which results in a transition to a state of different spin multiplicity. Intersystem crossing involves a change in spin direction of an electron upon emission, resulting in two unpaired electrons of the same spin orientation and a spin multiplicity of 3 (vice versa for a triplet ground state). The spin must flip again to make the transition $T_1 \rightarrow S_0$ via emission of a photon; this is known as phosphorescence [19]. Since a change of electron spin direction is very unlikely without a suitable external perturbation (e.g. triplet quenchers), these transitions are termed ‘forbidden’ and any molecules reaching the triplet state remain there for longer than the singlet state fluorescence lifetime. A build up of molecules in the triplet state can be a problem in fluorescence measurements as this removes the fluorescing population, reducing the fluorescence signal unless limited by some process such as diffusion of new fluorescent molecules into the excitation region [20]. A further non-radiative decay mechanism known as internal conversion involves electronic relaxation without emission of a photon.

The intensity of fluorescence and fluorescence lifetime τ_f following excitation depends on the relative amounts of the radiative and non-radiative processes shown in Figure 1.2. The population of the excited state S_1 , labelled $[S_1(t)]$, is given by the rate equation

$$-\frac{d[S_1(t)]}{dt} = (k_r + k_{nr})[S_1(t)] \quad (1.2.4)$$

where k_r is the radiative decay rate and k_{nr} is the total non-radiative decay rate equal to the sum of the internal conversion rate k_{IC} and the inter-system crossing rate k_{ISC} . Solving this rate equation gives

$$[S_1(t)] = [S_1(0)]\exp\left(-\frac{t}{\tau_f}\right) \quad \text{where} \quad \tau_f = \frac{1}{k_r + k_{nr}} \quad (1.2.5)$$

The total emission intensity at time t following excitation, $I_f(t)$, is directly proportional to the excited state population S_1

$$I_f(t) \propto k_r[S_1(0)]\exp\left(-\frac{t}{\tau_f}\right) \quad (1.2.6)$$

This shows that the intensity of the fluorescence follows an exponential decay that depends not only on the rate of radiative decay k_r , but also on the rate of non-radiative decay, k_{nr} . Therefore the measured fluorescence intensity can give information about the local environment parameters of the probe that affect either the radiative or non-radiative pathways, or the relative rates of each such as polarity, acidity and viscosity .

The relative rates of radiative and non-radiative decay can be summarised using the the probability of an excited molecule emitting a fluorescence photon, known as the fluorescence quantum yield Φ . This is given by

$$\Phi = \frac{k_r}{k_r + k_{nr}} \quad (1.2.7)$$

It is usually necessary to choose a fluorescent probe with a high ‘brightness’ where brightness is equal to the product of molar extinction coefficient (absorption probability for a particular wavelength) and the quantum yield. A high fluorophore brightness gives the highest signal to noise ratio, especially for instances when low concentration is desirable.

Fluorescent probes

A fluorophore is a fluorescent chemical compound that has desirable absorption and emission characteristics such as high absorption cross-section, a practical fluorescence lifetime, high quantum yield, and absorption and emission spectra compatible with the equipment available. Those that emit in the visible spectrum typically contain conjugated π bonds in aromatic or planar constituent parts. As mentioned in Section 1.1, fluorophores can be used independently as a probe or indicator of a factor affecting the fluorescence, as a dye or as a tracer in fluids, but fluorophores are commonly covalently bonded to a macromolecule that is under investigation. In this case, it serves as a marker enabling imaging and spectroscopy measurements to take place. Due to the sensitivity of the fluorescent molecules to the immediate environment, it is possible to use their fluorescence characteristics to obtain information about the surrounding structure and physical environment [19] including relevant order parameters, polarity, viscosity, intermolecular distances and intramolecular and solvent-solute bonds [21, 22]. Information about the chemical composition of the surroundings [23] such as pH value or ion concentration can also be inferred [24].

The choice of a fluorescent probe is dependent on the spectral properties of the probe and the required information. For polarised photoselection and anisotropy experiments it is necessary for the chosen probe to have an absorption and emission spectrum compatible with available excitation sources and detection devices, a fluorescence lifetime that is compatible with the excited state relaxation time, and a well-defined transition dipole moment direction. Sensitivity of the emission spectrum to physical environment or presence of certain chemicals is an important factor in many biological applications [13]. Shifts in emission or changes in fluorescence lifetimes of fluorophores can be signs of energy transfer which in turn can be used to examine conformational changes or folding of proteins [25].

Several fluorescent molecules are found occurring naturally, the most important for research purposes being Green Fluorescent Protein (GFP) which is produced by the jellyfish *Aequorea victoria* [26]. However, to meet the specific needs of research,

many fluorescent probes have been synthesised [27]. Chapter 2 describes the characterisation of a fluorescent probe designed for a high 2PA cross-section, AF257, and an investigation into its photophysical behaviour. Other fluorescent probes used in this work include Enhanced Green Fluorescent Protein (EGFP), mCherry, and Fluorescein.

1.2.2 Fluorescence Measurements

For single-photon absorption by a linearly polarised excitation source, in this case light from a laser, within the limit of weak excitation (i.e. no significant depletion of the ground state) it can be shown that the orientationally dependent excitation probability is given by $W(\theta, \phi)$ [28]:

$$\begin{aligned} W(\theta, \phi) &= B |\langle f | \underline{E} \cdot \underline{\mu} | i \rangle|^2 \\ &= B |E|^2 |\mu_{fi}|^2 \cos^2 \theta \end{aligned} \tag{1.2.8}$$

where B is a constant of proportionality, i and f denote initial and final electronic wavefunctions, \underline{E} is the electric field of the excitation source, $\underline{\mu}$ is the dipole moment operator and μ_{fi} are its matrix elements. The angle θ is defined as the angle between the electric dipole absorption moment and the polarisation direction of the excitation source as shown in Figure 1.3.

Preferential excitation of the molecules with transition dipole moments in the direction of \underline{E} will cause a non-isotropic distribution of excited state orientations. The resulting difference in fluorescence intensities between different polarisation directions with respect to the lab frame is encapsulated in the ‘fluorescence anisotropy’ parameter, and gives information about the excited state orientational distribution that has been created.

The orientation of a group of molecules can be described by the orientational distribution function, $P(\theta, \phi)$ with θ and ϕ defined as in Figure 1.3. This gives the probability of finding a molecule oriented between an angle θ and $\theta + d\theta$ with respect to the z axis and between an angle ϕ and $\phi + d\phi$ to the x axis. The distribution

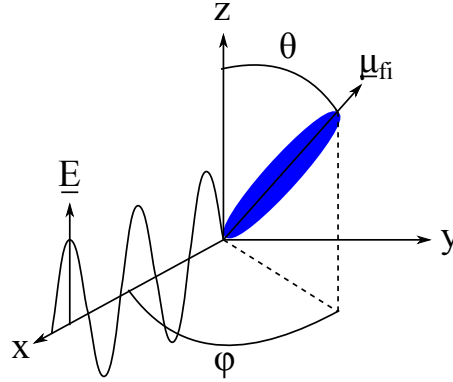


Figure 1.3: Position of molecular dipole moment μ_{fi} with respect to the excitation polarisation in the lab frame, defined using spherical coordinates.

can be expressed as the sum of a number of spherical harmonics $Y_{KQ}(\theta, \phi)$, of rank K and projection Q [29]. Graphical representations of relevant spherical harmonics functions are shown in Figure 1.4. Expressing the distribution function in this way gives

$$P(\theta, \phi) = \sum_{KQ} \langle C_{KQ} \rangle Y_{KQ}(\theta, \phi) \quad (1.2.9)$$

where $\langle C_{KQ} \rangle$ are the expansion coefficients of the respective spherical harmonics.

It is convenient if all intensity and anisotropy measurements are performed in the weak excitation regime i.e. $N_{gs} \gg N_{ex}$ where N_{gs} and N_{ex} are the number of molecules in the ground and excited states. This ensures that the ground state distribution function can be treated as constant over the excitation timescale allowing a much more simple prediction of the excited state alignment. Significant depletion of the ground state would lead to a reduction in the excited state alignment.

The typical transitions involved in a fluorescence cycle (absorption and emission) are summarised in Figure 1.5. For the limiting case of rapid transfer from level 1 to 2 and 4 to 3 (as defined in Figure 1.5), reabsorption from level 4 to 3 can be neglected and the rate equation to describe the emission from level 3 (neglecting ground state depletion i.e. $\frac{dN_1}{dt} = 0$) can be given by

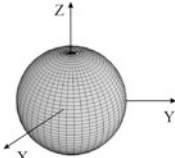
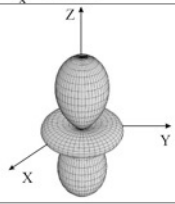
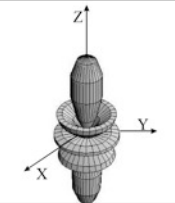
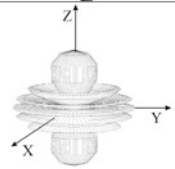
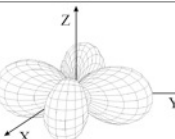
$Y_{00} = \left(\frac{1}{4\pi} \right)^{\frac{1}{2}}$	
$Y_{20} = \left(\frac{5}{4\pi} \right)^{\frac{1}{2}} \frac{1}{2} (3 \cos^2 \theta - 1)$	
$Y_{40} = \left(\frac{1}{4\pi} \right)^{\frac{1}{2}} \frac{3}{8} (35 \cos^4 \theta - 30 \cos^2 \theta + 3)$	
$Y_{60} = \left(\frac{13}{4\pi} \right)^{\frac{1}{2}} \frac{1}{16} \left(231 \cos^6 \theta - 315 \cos^4 \theta + 105 \cos^2 \theta - 5 \right)$	
$Y_{2\pm 2} = \left(\frac{15}{32\pi} \right)^{\frac{1}{2}} \sin^2 \theta e^{\pm 2i\phi}$	

Figure 1.4: Graphical representations of relevant spherical harmonics plotted using Mathematica, those with Projection $Q = 0$ being cylindrically symmetric. Ground or excited state distributions of molecular orientations can be described as a linear combination of spherical harmonics.

$$\frac{dN_3}{dt} = \frac{I(t)\sigma^{(1)}}{h\nu} N_1 - N_3 k_{rad} \quad (1.2.10)$$

where $\sigma^{(1)}$ is the single photon absorption cross section, and k_{rad} is the rate of spontaneous emission from level 3 to 4. Considering the case of pulsed excitation where the pulse duration can be considered fast in comparison to the fluorescence rate, the first term on the right side of 1.2.10 can be considered a constant. This gives rise to an initial population of level 3, the second term on the right hand side leading to an exponential decay in this population. The proportion of the total molecules in the initial excited state population in the limit of weak excitation is

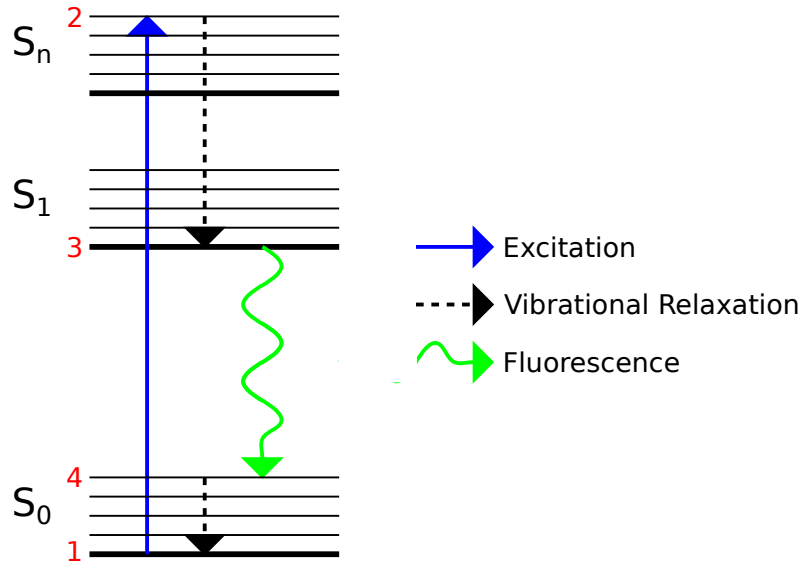


Figure 1.5: Initial excitation from ground state (level 1) to a higher energy excited state S_n (level 2) by the pump laser is immediately followed by internal conversion to the lowest vibrational levels of the first excited electronic state S_1 (level 3). From here the molecule can relax to the upper vibrational levels of the ground state (level 4) through a number of different pathways. Most likely is a radiative transition to any of the vibration levels of the ground electronic state (levels 3-4 diagram). From here the (high compared with thermal) vibrational energy is rapidly lost to the local solvent environment until thermal equilibrium is reached (level 4). The individual transitions shown in the diagram are described in the text.

approximately equal to ‘saturation parameter’ for the absorption transition S_{abs} :

$$\frac{N_3(t=0)}{N_1} \approx \frac{\sigma^{(1)} E_P}{h\nu A} = S_{abs} \ll 1 \quad (1.2.11)$$

where A is the area of the excitation laser at the focus, and E_P is the energy of the excitation pulse. In the weak limit, and therefore for all experiments in this thesis, $S_{abs} \ll 1$ and observed fluorescence is as described in Section 1.3.

1.3 Fluorescence Anisotropy

As described in Section 1.2.2 the order created in the excited state can be described by the summation of a number of spherical harmonic functions and their respective coefficients as given in Equation 1.2.9. As explained later in this section information on the magnitude of the ($K=2$, $Q=2,0,-2$) coefficients can be obtained through measurement of the fluorescence anisotropy: the difference between fluorescence intensity in the polarisation directions parallel and perpendicular to the excitation polarisation.

The fluorescence polarisation is conventionally defined in the lab frame with reference to a system of coordinates based on the directions of excitation polarisation and observation directions. In this frame (i.e. 90° excitation detection geometry) the fluorescent sample is placed at the origin, O , and the x and y axes are along the directions of excitation and observation respectively as in Figure 1.3. For a laser pulse polarised in the z direction, it is common to label the measured fluorescence intensities from the direction of observation as I_V or I_{\parallel} for fluorescence polarised in the lab z direction, and I_H or I_{\perp} for fluorescence polarised in the lab x direction. For the case of an isotropic sample and an excitation beam polarised in the z direction there is cylindrical symmetry about the z axis such that $I_x = I_y$, the total fluorescence intensity I_{tot} can then be stated as:

$$I_{tot} = I_V + 2I_H \quad (1.3.1)$$

The anisotropy, R , is then the difference in vertical and horizontal polarisation intensities normalised by the total intensity:

$$R = \frac{I_V - I_H}{I_V + 2I_H} \quad (1.3.2)$$

It is possible to find expressions for the respective fluorescence intensities in terms of the excited state distribution and the initial and final states $|i\rangle$ and $|f\rangle$ of the emitting transition for each polarisation \hat{e}_i :

$$I_i(t) = B \int_0^{2\pi} \int_0^{\pi} |\langle f | \mu \cdot \hat{e}_i | i \rangle|^2 N_{ex}(\theta, \phi, t) \sin\theta d\theta d\phi \quad (1.3.3)$$

Where B is a constant of proportionality. The components of \hat{e}_i in the vertical and horizontal directions are given by

$$\hat{e}_v = \cos \theta, \quad \hat{e}_h = \sin \theta \cos \phi \quad (1.3.4)$$

The excited state population $N_{ex}(\theta, \phi, t)$ can be factorised into the excited state orientational probability distribution $P_{ex}(\theta, \phi, t)$ and time-dependent population $N_{ex}(t)$:

$$N_{ex}(\theta, \phi, t) = N_{ex}(t)P_{ex}(\theta, \phi, t) \quad (1.3.5)$$

Substituting Equations 1.3.4 and 1.3.5 into Equation 1.3.3 yields expressions for the vertical and horizontal components of the fluorescence intensity of:

$$\begin{aligned} I_V(t) &= BN_{ex}(t)|\mu_{fi}|^2 \int_0^{2\pi} \int_0^{\pi} \cos^2 \theta P_{ex}(\theta, \phi, t) \sin \theta d\theta d\phi \\ I_H(t) &= BN_{ex}(t)|\mu_{fi}|^2 \int_0^{2\pi} \int_0^{\pi} \sin^2 \theta \sin^2 \phi P_{ex}(\theta, \phi, t) \sin \theta d\theta d\phi \end{aligned} \quad (1.3.6)$$

The angular parts can then be expressed in terms of spherical harmonics utilising Equation 1.2.9:

$$\begin{aligned} I_V(t) &= BN_{ex}(t)|\mu_{fi}|^2 \frac{\sqrt{4\pi}}{3} \sum_{KQ} \langle C_{KQ}^{ex}(t) \rangle \int_0^{2\pi} \int_0^{\pi} Y_{KQ}(\theta, \phi) \\ &\quad \left[Y_{00}(\theta, \phi) + \frac{2}{\sqrt{5}} Y_{20}(\theta, \phi) \right] \sin \theta d\theta d\phi \end{aligned} \quad (1.3.7)$$

$$\begin{aligned} I_H(t) &= BN_{ex}(t)|\mu_{fi}|^2 \frac{\sqrt{4\pi}}{3} \sum_{KQ} \langle C_{KQ}^{ex}(t) \rangle \int_0^{2\pi} \int_0^{\pi} Y_{KQ}(\theta, \phi) \\ &\quad \left[Y_{00}(\theta, \phi) - \frac{1}{\sqrt{5}} Y_{20} + \sqrt{\frac{3}{10}} Y_{22}(\theta, \phi) + Y_{2-2}(\theta, \phi) \right] \sin \theta d\theta d\phi \end{aligned} \quad (1.3.8)$$

Solving these integrals gives [30]

$$\begin{aligned}
I_V &= BN_{ex}(t)|\mu_{fi}|^2 \frac{\sqrt{4\pi}}{3} \left[\langle C_{00}^{ex} \rangle + \frac{2}{\sqrt{5}} \langle C_{20}^{ex}(t) \rangle \right] \\
I_H &= BN_{ex}(t)|\mu_{fi}|^2 \frac{\sqrt{4\pi}}{3} \left[\langle C_{00}^{ex} \rangle - \frac{1}{\sqrt{5}} \langle C_{20}^{ex}(t) \rangle + \sqrt{\frac{3}{10}} (\langle C_{22}^{ex} \rangle + \langle C_{2-2}^{ex} \rangle) \right]
\end{aligned} \tag{1.3.9}$$

It can be seen that the intensity components depend solely on the $\langle C_{00} \rangle$, $\langle C_{20} \rangle$ and $(\langle C_{22}^{ex} \rangle + \langle C_{2-2}^{ex} \rangle)$ coefficients. These coefficients can be normalised to $\langle C_{00} \rangle$ using $\langle \alpha_{KQ}^{ex} \rangle = \frac{\langle C_{KQ}^{ex} \rangle}{\langle C_{00}^{ex} \rangle}$ and substituted into Equation 1.3.2, the general anisotropy definition. Provided the fluorescence lifetime is independent of molecular orientation all intensity components vanish from the anisotropy leaving

$$R = \frac{\frac{1}{\sqrt{5}} \langle \alpha_{20}^{ex}(t) \rangle - \frac{1}{\sqrt{30}} [\langle \alpha_{22}^{ex}(t) \rangle + \langle \alpha_{2-2}^{ex}(t) \rangle]}{1 + \frac{2}{\sqrt{30}} [\langle \alpha_{22}^{ex}(t) \rangle + \langle \alpha_{2-2}^{ex}(t) \rangle]} \tag{1.3.10}$$

In this way the fluorescence anisotropy can be described in terms of the orientational distribution that has been created in the excited state. It can be seen that the anisotropy created by a single photon excitation from an isotropic ground state is dependent only on the cylindrically symmetric ($K = 2, Q = 0$) moment, and the cylindrically asymmetric ($K = 2, Q = \pm 2$) moments. However, for systems that exhibit cylindrical symmetry the detection geometry is no longer sensitive to ($K = 2, Q = \pm 2$) moments, and Equation 1.3.10 reduces to

$$R = \frac{1}{\sqrt{5}} \langle \alpha_{20}^{ex}(t) \rangle \tag{1.3.11}$$

such that the time-dependent anisotropy depends solely on the $K = 2, Q = 0$ moment. This moment can therefore be evaluated directly through measurement of fluorescence anisotropy.

However, certain processes can contribute to a reduction in the initial anisotropy observed. Non-parallel absorption and emission dipole moments is one pathway for such depolarisation. The conversion from high to low vibronic level in the excited state typically happens on a timescale much shorter than that of the fluorescent lifetime (which is typically of the order of nanoseconds), so this process is usually

completed before fluorescence occurs. As this results in emission transition between different vibronic levels compared to absorption it can lead to non-equivalence of absorption and emission dipole moments[13]. In this case, and with vertically polarised excitation, the initial (or time-independent) anisotropy R_0 depends on the angle between absorption and emission dipole moments, γ , and can be represented as

$$R_0 = (3 \cos^2 \gamma - 1)/5 \quad (1.3.12)$$

where γ is the angle between absorption and emission dipole moments [13]. The effect of non-parallel absorption and emission dipole moments is more thoroughly explored in Section 1.5. Further depolarisation could be caused by rotation of the molecular orientations during the finite duration of the excitation pulse. In conventional condensed phase fluorescence experiments the excitation laser pulse is short compared with the characteristic rotational time of the chromophores as detailed in the next section.

1.4 Rotational Diffusion

The evolution of fluorescence anisotropy with time is affected by rotational diffusion of the fluorophores within the solution. Shortly after excitation, the measured anisotropy will reflect the initial excited state order. However, with time the orientation of the excited molecules becomes randomised, tending towards a ‘steady state’ distribution which will have an anisotropy value of zero, which will be isotropic unless the environment possesses intrinsic order that prevents the probes from obtaining a globally isotropic distribution. The timescale of this randomisation process is a useful probe of the interaction of the fluorescent molecule with its host environment. These interactions are commonly the subject of fluorescence anisotropy investigations in the physical and more lately the life sciences. The latter often involves a fluorescent probe attached to a biomolecule of interest, and uses fluorescence from the probe to infer information about the behaviour of the adjoined molecule.

1.4.1 Debye Small Step Diffusion

Unlike in the gas phase where molecules can freely rotate and individual rotational states are observed, the rotational motion of probe molecules in solution is continually interrupted by frequent collisions with solvent molecules. A typical timescale for these collisions is ca. 10^{-14} s [31] which is orders of magnitude faster than typical molecular orientation times (ps to ns). The Debye small step diffusion model describes reorientation of a molecule in these circumstances as a random walk trajectory resulting from a large number of very small angular displacements in random directions caused by the myriad of solvent collisions [32]. In this model, the evolution of an initial orientational distribution of molecules in an isotropic liquid is described by an equation analogous to Fick's second law for translational diffusion [33]:

$$\frac{\delta P_{ex}(\theta, \phi, t)}{\delta t} = D \nabla^2 P_{ex}(\theta, \phi, t) \quad (1.4.1)$$

Where $P_{ex}(\theta, \phi, t)$ is the orientational distribution function of the group of molecules, ∇ is the Laplacian operator, D is the rotary diffusion coefficient, and where

$$D \nabla^2 = \sum_i D_i L_i^2 \quad (1.4.2)$$

Here, L_i^2 is the orbital angular momentum operator in the molecular frame [34].

Expressing Equation 1.4.1 in terms of spherical harmonics gives:

$$\frac{\delta}{\delta t} \sum_{KQ} \langle C_{KQ}(t) \rangle Y_{KQ}(\theta, \phi) = D \sum_{K'Q'} \nabla^2 \langle C_{K'Q'}(t) \rangle Y_{K'Q'}(\theta, \phi) \quad (1.4.3)$$

The spherical harmonics $Y_{KQ}(\theta, \phi)$ are the angular part of the eigenfunctions of the Laplacian operator in spherical coordinates and have the eigenvalues $-K(K+1)$ such that Equation 1.4.3 becomes

$$\frac{\delta}{\delta t} \sum_{KQ} \langle C_{KQ}(t) \rangle Y_{KQ}(\theta, \phi) = D \sum_{K'Q'} K'(K'+1) \langle C_{K'Q'}(t) \rangle Y_{K'Q'}(\theta, \phi) \quad (1.4.4)$$

When multiplied by the complex conjugate $Y_{KQ}^*(\theta, \phi)$ and integrated over θ and ϕ this gives

$$\begin{aligned} \frac{\delta}{\delta t} \sum_{KQ} \langle C_{KQ}(t) \rangle Y_{KQ}(\theta, \phi) &= -D \sum_{K'Q'} K'(K'+1) \langle C_{K'Q'}(t) \rangle \int_0^{2\pi} \int_0^{\pi} Y_{KQ}^*(\theta, \phi) Y_{K'Q'}(\theta, \phi) \\ &= -D \sum_{K'Q'} K'(K'+1) \langle C_{K'Q'}(t) \rangle \delta_{KK'} \delta_{QQ'} \\ &= -DK(K+1) \langle C_{K'Q'}(t) \rangle \end{aligned} \quad (1.4.5)$$

The solution to this first order differential equation [34] is

$$\langle C_{KQ}(t) \rangle = \langle C_{KQ}(0) \rangle \exp[-DK(K+1)t] \quad (1.4.6)$$

Each moment in the excited state distribution will therefore have an individual rotational relaxation rate given by

$$\zeta_{KQ} = \frac{1}{DK(K+1)} \quad (1.4.7)$$

This demonstrates that all moments of equal rank $K = 2$ will have the same rotational relaxation rate, and therefore the same re-orientational time $\tau_{or} = \frac{1}{\zeta}$. The rotational relaxation rate does not depend on the projection Q ; this holds as rotational diffusion must be independent of choice of axes with respect to the lab frame in an isotropic environment. This result is dependent on the assumptions about the molecular motion described above. In situations where the molecular motion cannot be described by random small step diffusion Equation 1.4.6 does not hold [35].

Estimates for the diffusion coefficient can be made from knowledge of the hydrodynamic volume of the molecule and the solvent viscosity [32, 36–38] and is related to the friction felt between the molecule and solvent as the molecule rotates. This frictional force can be characterised as falling between two limiting cases. Firstly, ‘stick’ conditions describe the case where the closest solvent molecules are effectively bound to the fluorescent molecule (and therefore contribute to the hydrodynamic volume) and must pass other solvent molecules as they rotate, the frictional force therefore primarily arising from solvent viscosity [39]. Secondly, ‘slip’ conditions describe the case where little friction from the solvent is experienced by the molecule,

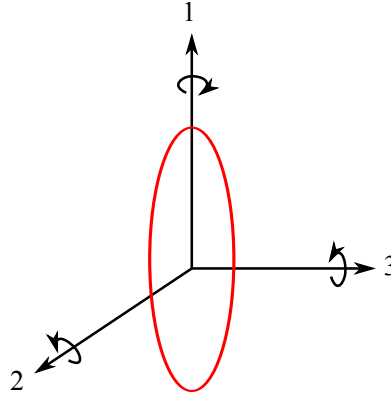


Figure 1.6: The three axes of diffusion in a prolate ellipsoid which have corresponding diffusion coefficients D_1 , D_2 , and D_3 . In this case, $D_2 = D_3$

and the only impediment to rotation is displacing solvent molecules from its path. Under such conditions, the diffusion constants are given by

$$D_{rot}^1 = \frac{k_B T}{8\pi\eta R^3} \quad (1.4.8)$$

$$D_{rot}^2 = \frac{k_B T}{C\pi\eta R^3} \quad (1.4.9)$$

where k is the Boltzmann constant, T the temperature of the solvent, η the solvent viscosity, C is a molecular shape factor which varies between 0 and 1, and R^3 is the hydrodynamic volume for an idealised spherical molecule of radius R [38].

1.4.2 Ellipsoidal Rotational Diffusion Approximation

The diffusional behaviour of the majority of fluorescence chromophores cannot be approximated by a rigid spherical shape. Many have one axis that is significantly different from the other two (including all of those used in this work), and these can be approximated in a similar way as that described above but using a rigid ellipsoid to describe the molecular shape.

The rotation of an ellipsoid can occur about each of its three axes with respective diffusion coefficients D_1 , D_2 and D_3 (see Figure 1.6). For the case of axis 1 being the principle symmetry axis, D_1 represents ϕ diffusion, and rotation about axes 2 and 3 is equal such that $D_2 = D_3$; D_2 and D_3 represent θ diffusion where here θ

and ϕ represent molecular frame axis. These diffusion coefficients can be related to D_0 of the equivalent sphere (where D_0 is the diffusion coefficient given by either Equation 1.4.8 or 1.4.9 as appropriate, and to the the ratio of the semi-major to the semi-minor axis of the ellipsoid, P [40]:

$$\frac{D_2}{D_0} = \frac{3}{2}P \frac{[(2P^2 - 1)\beta - P]}{(P^4 - 1)} \quad (1.4.10)$$

$$\frac{D_1}{D_0} = \frac{3}{2} \frac{P(P - \beta)}{(P^2 - 1)} \quad (1.4.11)$$

Where $\beta = (P^2 - 1)^{-\frac{1}{2}} \ln \left[P + (P^2 - 1)^{\frac{1}{2}} \right]$.

1.5 Anisotropy Decay

Consideration of the evolution of molecular orientations is not sufficient in itself to describe the observed fluorescence anisotropy. The evolution of the fluorescence anisotropy with time depends not only on the evolution of the molecular distribution but where the absorption and emission transition dipoles point in the molecular frame. An emission dipole that is not directed along one molecular axis may describe a complex path if diffusion about each molecular axis is not equal.

The most general form of the anisotropy decay for an ellipsoidal chromophore has been derived by Belford *et al* [41]:

$$R(t) = \frac{6}{5} \sum_{i=1}^3 c_i e^{(-\frac{t}{\tau'_i})} + \left[\frac{(F + G)}{4} \right] e^{[-(6D - 2\Delta)t]} + [(F - G)/4] e^{[-(6D + 2\Delta)t]} \quad (1.5.1)$$

Here $D = \frac{D_1 + D_2 + D_3}{3}$, $\Delta = (D_1^2 + D_2^2 + D_3^2 - D_1 D_2 - D_1 D_3 - D_2 D_3)^{\frac{1}{2}}$ and $c_i = \alpha_j \alpha_k \epsilon_j \epsilon_k$ ($ijk = 123, 231$ or 312) where α_1, α_2 and α_3 are the cosines of the angles that the absorption dipole moment forms with each axis, and ϵ_1, ϵ_2 and ϵ_3 are the cosines of the angles that the emission dipole moment forms with each axis. The other parameters used are defined:

$$\tau'_i = \frac{1}{3D + 3D_i} \quad (1.5.2)$$

$$F = \sum_{i=1}^3 3\alpha_i^2 \epsilon_i^2 - \frac{1}{3} \quad (1.5.3)$$

$$G\Delta = \sum_{i=1}^3 D_i(\alpha_i^2\epsilon_i^2 + \alpha_j^2\epsilon_j^2 + \alpha_k^2\epsilon_k^2) - D \quad (i \neq j \neq k) \quad (1.5.4)$$

For many common fluorescent probes however this expression can be greatly simplified. For the case of spherical diffusers this reduces to

$$R(t) = R(0)e^{-t/\tau_0} \quad (1.5.5)$$

where $\tau_0 = \frac{1}{6D_0}$. For an ellipsoidal diffuser, described in the previous section, the anisotropy reduces from 5 to 3 components. However, for many common fluorescent probes the absorption and emission dipole moments are both normally assumed to lie close to the symmetry axis of the molecule. This substantially reduces the complexity of the observed anisotropy decay in that only a single decay component remains, which is dependent only on the perpendicular diffusion coefficient, D_2 .

$$R(t) = \frac{2}{5} \exp(-6D_2t) \quad (1.5.6)$$

Under these circumstances the fluorescence anisotropy represents a direct measurement of the degree of second order alignment (ie. the amplitude of orientational components of rank 2).

$$R(t) = \sqrt{5} \frac{C_{20}(t)}{C_{00}(t)} \quad (1.5.7)$$

1.6 Time Correlated Single Photon Counting

Time dependent anisotropy measurements can be conducted using Time Correlated Single Photon Counting (TCSPC), which is a well-established technique that can be used to measure fluorescence intensity and anisotropy decays. TCSPC is a coincidence method whereby many consecutive measurements of the time delay between the polarised excitation pulse and the first detected fluorescence photon for polarisations parallel and perpendicular to the excitation polarisation are recorded. The frequency of these intervals are plotted on separate histograms that after many events will show the correlation between the polarised fluorescence emission and the

excitation laser pulse for all delays. All practical detection systems have a finite instrument response that will be convoluted with the fluorescence decay. If the excitation pulse is sufficiently short, it may be treated effectively as a delta function. Therefore on correlation with the fluorescence signal it simply returns the fluorescence itself. The anisotropy decay can then be constructed using Equation 1.3.2. This can be used to find the rotational diffusion coefficient τ_{20} in addition to the initial anisotropy. The value τ_{20} is discussed in previous sections and gives information about the environment of the probe molecule. The initial excited state distribution, of which $R(0)$ is a measure, is the product of the ground state distribution function with the excitation operator. $R(0)$ therefore gives information about the ground state which cannot be directly measured with fluorescence techniques (complex fluorescence anisotropy is discussed in Chapter 2). Measurements can also be taken at the ‘magic angle’ of 54.7° when the excited state distribution has cylindrical symmetry in the plane perpendicular to the z axis. At this angle the probability of detecting fluorescence photons polarised in the direction perpendicular to excitation polarisation is twice that of the parallel direction (assuming $I_x = I_y$). Therefore an artificial measure of total intensity is generated [42]. Alternatively, when the excited state orientational distribution is cylindrically symmetric, the total fluorescence intensity can be constructed using $I_V + 2I_H$. The intensity decay can be deconvoluted if necessary and fitted to find the fluorescence lifetime, τ_f . More detail on data analysis following TCSPC is given in Chapter 2.

1.7 Summary

Use of an ultrashort (fast compared with fluorescence) linearly polarised laser pulse allows orientational photoselection of a fluorescent population and the creation of an ordered distribution in the excited state. The probability of excitation of a fluorescence molecule with a finite transition dipole moment has an angular dependence upon the excitation pulse polarisation, giving rise to an excited state distribution that is dependent on the distribution in the ground state. Measurement of orien-

tational distribution and its time-evolution as described by rotational diffusion is possible using fluorescence anisotropy measurements, which can give information on the degree of freedom to rotate that the molecule experiences in its immediate environment. The following chapter uses fluorescence intensity measurements to investigate the two-photon excitation processes in a tri-branched molecule, showing the existence of two independent fluorescence components. Fluorescence anisotropy experiments are also used to gain information on complex depolarisation effects in the excited state. This data is reinforced by further single-photon fluorescence experiments.

References

- [1] D. Jameson, T. Hazlett, and T. Dewey, "Biophysical and biochemical aspects of fluorescence spectroscopy," *Biophysical and Biochemical Aspects of Fluorescence Spectroscopy*, 1991.
- [2] J. R. Lakowicz, "Time-resolved laser spectroscopy in biochemistry," tech. rep., Bellingham, WA; SPIE Society of Photo-Optical Instrumentation Engineers, 1988.
- [3] D. M. Jameson and G. D. Reinhart, *Fluorescent biomolecules: methodologies and applications*. Plenum Pub Corp, 1989.
- [4] L. Brand and J. R. Gohlke, "Fluorescence probes for structure," *Annual review of biochemistry*, vol. 41, no. 1, pp. 843–868, 1972.
- [5] M. Schena, D. Shalon, R. Heller, A. Chai, P. O. Brown, and R. W. Davis, "Parallel human genome analysis: microarray-based expression monitoring of 1000 genes," *Proceedings of the National Academy of Sciences*, vol. 93, no. 20, pp. 10614–10619, 1996.
- [6] X. Zhu, A. Gong, and S. Yu, "Fluorescence probe enhanced spectrofluorimetric method for the determination of gatifloxacin in pharmaceutical formulations and biological fluids," *Spectrochimica Acta Part A: Molecular and Biomolecular Spectroscopy*, vol. 69, no. 2, pp. 478–482, 2008.
- [7] F. Perrin, "Polarisation de la lumière de fluorescence. vie moyenne des molécules dans l'état excité," *J. phys. radium*, vol. 7, no. 12, pp. 390–401, 1926.

-
- [8] R. Delorme, F. Perrin, *et al.*, “Durées de fluorescence des sels d’uranyle solides et de leurs solutions,” *J. phys. radium*, vol. 10, no. 5, pp. 177–186, 1929.
- [9] G. Weber, “Polarization of the fluorescence of macromolecules. 1. theory and experimental method,” *Biochemical Journal*, vol. 51, no. 2, p. 145, 1952.
- [10] A. Jablonski, “On the notion of emission anisotropy,” *Bulletin de l’Academie Polonaise des Sciences, Serie sci. math. astr. phys.*, vol. 8, pp. 259–264, 1960.
- [11] A. Jablonski, “Depolarization of fluorescence of liquid solutions,” *Bulletin de l’Academie Polonaise des Sciences, Serie sci. math. astr. phys.*, vol. 8, pp. 655–660, 1960.
- [12] A. Albrecht, “Polarizations and assignments of transitions: The method of photoselection,” *Journal of Molecular Spectroscopy*, vol. 6, pp. 84–108, 1961.
- [13] J. R. Lakowicz, *Principles of fluorescence spectroscopy*. Springer, 2009.
- [14] C. C. Gradinaru, D. O. Marushchak, M. Samim, and U. J. Krull, “Fluorescence anisotropy: from single molecules to live cells.,” *The Analyst*, vol. 135, pp. 452–9, Mar. 2010.
- [15] M. Born and R. Oppenheimer, “Zur quantentheorie der molekülen,” *Annalen der Physik*, vol. 389, no. 20, pp. 457–484, 1927.
- [16] P. W. Atkins and R. S. Friedman, *Molecular Quantum Mechanics*, vol. 3. Oxford University Press Oxford, 1997.
- [17] C. Cohen-Tannoudji, B. Diu, and F. Laloë, “Quantum mechanics, 2 volume set,” 2006.
- [18] T. Pawson and P. Nash, “Protein–protein interactions define specificity in signal transduction,” *Genes & Development*, vol. 14, no. 9, pp. 1027–1047, 2000.
- [19] B. Valeur *et al.*, *Molecular fluorescence: principles and applications*. Wiley-Vch, 2012.
- [20] R. J. Marsh, M. A. Osborne, and A. J. Bain, “Control of single-molecule fluorescence dynamics by stimulated emission depletion,” in *Optical Science and Technology, SPIE’s 48th Annual Meeting*, pp. 78–86, International Society for Optics and Photonics, 2003.
- [21] D. L. Sackett and J. Wolff, “Nile red as a polarity-sensitive fluorescent probe of hydrophobic protein surfaces,” *Analytical biochemistry*, vol. 167, no. 2, pp. 228–234, 1987.
- [22] M. A. Haidekker and E. A. Theodorakis, “Molecular rotors—fluorescent biosensors for viscosity and flow,” *Organic & biomolecular chemistry*, vol. 5, no. 11, pp. 1669–1678, 2007.

-
- [23] R. Y. Tsien, "Fluorescent probes of cell signaling," *Annual Review of Neuroscience*, vol. 12, no. 1, pp. 227–253, 1989.
- [24] G. Miesenböck, D. A. De Angelis, and J. E. Rothman, "Visualizing secretion and synaptic transmission with pH-sensitive green fluorescent proteins," *Nature*, vol. 394, no. 6689, pp. 192–195, 1998.
- [25] X. Michalet, S. Weiss, and M. Jäger, "Single-molecule fluorescence studies of protein folding and conformational dynamics," *Chemical Reviews*, vol. 106, no. 5, p. 1785, 2006.
- [26] M. Chalfie, Y. Tu, G. Euskirchen, W. W. Ward, and D. C. Prasher, "Green fluorescent protein as a marker for gene expression," *Science*, vol. 263, no. 5148, pp. 802–805, 1994.
- [27] J. R. Lakowicz, *Topics in Fluorescence Spectroscopy: Volume 4: Probe Design and Chemical Sensing*. Plenum Publishing Corporation, 1994.
- [28] A. Bain and A. McCaffery, "On the measurement of molecular anisotropies using laser techniques. iii. detection of the higher multipoles," *The Journal of chemical physics*, vol. 83, p. 2641, 1985.
- [29] R. P. Boas, *Entire functions*, vol. 5. Academic Press, 1954.
- [30] A. Bain, P. Chandna, and J. Bryant, "Picosecond polarized fluorescence studies of anisotropic fluid media. i. theory," *The Journal of Chemical Physics*, vol. 112, p. 10418, 2000.
- [31] G. R. Fleming, "Subpicosecond spectroscopy," *Annual Review of Physical Chemistry*, vol. 37, no. 1, pp. 81–104, 1986.
- [32] P. J. W. Debye, *Polar molecules*, vol. 172. Dover New York, 1929.
- [33] J. Philibert, "One and a half century of diffusion: Fick, Einstein, before and beyond," *Diffusion Fundamentals*, vol. 2, no. 1, pp. 1–10, 2005.
- [34] A. Yariv, *An introduction to theory and applications of quantum mechanics*. Wiley, 1982.
- [35] D. Cook, J. Chen, E. Morlino, and R. Hochstrasser, "Terahertz-field-induced second-harmonic generation measurements of liquid dynamics," *Chemical physics letters*, vol. 309, no. 3, pp. 221–228, 1999.
- [36] A. Einstein, "Investigations on the theory of brownian motion, reprint of the 1st english edition (1926)," 1956.

-
- [37] R. Moog, D. Bankert, and M. Maroncelli, "Rotational diffusion of coumarin 102 in trifluoroethanol: the case for solvent attachment," *The Journal of Physical Chemistry*, vol. 97, no. 8, pp. 1496–1501, 1993.
- [38] C.-M. Hu and R. Zwanzig, "Rotational friction coefficients for spheroids with the slipping boundary condition," *The Journal of Chemical Physics*, vol. 60, p. 4354, 1974.
- [39] K. Mali, G. Dutt, and T. Mukherjee, "Rotational diffusion of a nonpolar and a dipolar solute in 1-butyl-3-methylimidazolium hexafluorophosphate and glycerol: Interplay of size effects and specific interactions," *The Journal of chemical physics*, vol. 128, p. 054504, 2008.
- [40] R. F. Steiner, "Fluorescence and anisotropy: Theory and applications," in *Topics in Fluorescence Spectroscopy: Volume 2: Principles* (J. R. Lakowicz, ed.), Plenum Publishing Corporation, 1991.
- [41] G. Belford, R. Belford, and G. Weber, "Dynamics of fluorescence polarization in macromolecules," *Proceedings of the National Academy of Sciences*, vol. 69, no. 6, pp. 1392–1393, 1972.
- [42] M. Bydder, A. Rahal, G. Fullerton, and G. Bydder, "The magic angle effect: a source of artifact, determinant of image contrast, and technique for imaging," *Journal of Magnetic Resonance Imaging*, vol. 25, no. 2, pp. 290–300, 2007.

Chapter 2

Two-Photon Excited State Dynamics in a Branched Nonlinear Fluorophore

2.1 Introduction

Two-photon absorption (2PA) is the process by which excitation occurs through simultaneous absorption of two photons which can be of the same or different energies [1]. The possibility of non-resonant absorption of two photons in the same quantum event was predicted in 1931 by Maria Göppert-Meyer [2], and was first demonstrated in a $CaF_2 : Eu^{2+}$ crystal by Kaiser and Garrett in 1961 [3]. This was made possible in the 1960's with the development of millijoule range Q-switched nanosecond pulsed lasers which were capable of providing the photon fluxes necessary for the simultaneous interaction of two photons at the atomic or molecular interaction site. The development of broadly tunable near infra-red Titanium:Sapphire lasers with pulse widths in the femtosecond range (typically 100-200 fs) enabled 2PA excitation to be achieved at significantly lower (ca. 100 pJ to nJ) energies and at higher (100 MHz) repetition rates [4], and as a result the use and applications of 2PA became much more widespread. 2PA is a third-order perturbation process several

orders of magnitude weaker than linear absorption. Unlike linear 1PA the strength of absorption depends on the square of the excitation intensity: it is a nonlinear optical process. 2PA spectroscopy can be used to probe the two-photon excited states of a molecule and to infer information about the relevant transitions within the molecule. The excitation selection rules are different for one and two-photon excited states, which means that 2PA spectroscopy can give complementary information to that obtainable from 1PA. The mechanism of 2PA is shown in figure 2.1. This can be thought of as occurring via a ‘virtual’ state reached as the first photon interacts with the molecule which exists for a time of the order of $10^{-15} - 10^{-16}$ s for visible photons, which can be estimated from the uncertainty principle. 2PA can happen if the second photon coincides with the molecule within that time duration [5]. Symmetry selection rules must also be satisfied in order for the 2PA process to occur. Since 2PA can be described as reaching the final state $|f\rangle$ from the initial state $|i\rangle$ through an intermediate ‘virtual’ state $|v\rangle$, it can be described as a two-step process; the transition probability $P_{i \rightarrow f}$ is given by third order perturbation theory from the product of the two single photon transition probabilities $|i\rangle \rightarrow |v\rangle$ and $|v\rangle \rightarrow |f\rangle$ [6]. All real molecular energy levels $|k_n\rangle$ that can be reached from $|i\rangle$ with allowed single photon transitions are therefore represented in $|v\rangle$ and the probability of the transition $|i\rangle \rightarrow |v\rangle$ is the sum of the transition probabilities to all real states $|i\rangle \rightarrow |k\rangle$. The same applies for the transition $|v\rangle \rightarrow |f\rangle$. The symmetry of the two-photon excited state will therefore differ from that reached by single-photon excitation. The excitation to one of the higher vibronic states of the S_1 energy level is however then followed by rapid vibrational relaxation and/or internal conversion to the lower vibrational levels of the excited state (see figure 2.1), with the result that both single and two-photon excitation can result in emission from the same excited state even though the states initially accessed were different. For visible two-photon excited fluorescence the light absorbed is usually in the red or infra-red regions of the spectrum, a region in which there are ideally no single-photon transitions; 1PA absorption should be minimised in order to maximise 2PA.

There is much interest in the development of new fluorescent chromophores opti-

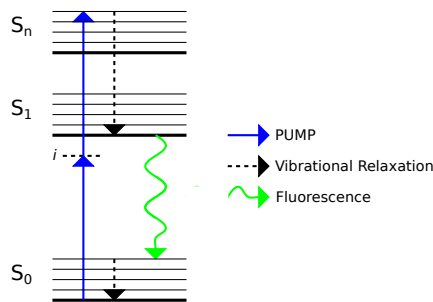


Figure 2.1: Schematic energy level diagram showing absorption of two photons of the same energy (degenerate), as is the case in the following experiments. After excitation the system rapidly relaxes to state S_1 via vibrational decay. From there it returns to the ground state by radiative or non-radiative decay.

mised for two-photon absorption, due to recent advances in technologies designed to exploit this phenomenon [7], including current applications in optical limiting [8, 9], bioimaging [10, 11], 3D optical data storage [12] and up-converted lasing [13, 14]. Two-photon excitation has a number of advantages over single-photon excitation [15, 16] including highly spatially confined excitation [17], increased penetration depth in tissues [18], three-dimensional resolution, and reduced photodamage in organic molecules due to the longer wavelengths used (typically 700-1200 nm) [19]. The experiments outlined in this chapter build upon experiments carried out previously within the group [20] on the linear quadrupole molecule BH101 and the corresponding branched molecule OM77, the structure of which are shown in figure 2.2. This work measured the differences in 2PA cross-sections in a selection of new fluorescent chromophores for linearly and circularly polarised excitation as a function of wavelength, and the degree of initial anisotropy created with each process. Unlike single photon transitions that can be characterised by a single transition dipole moment, two-photon excitation is a third order nonlinear optical process; the polarisation dependence of the excitation probability is thus governed by a third-rank tensor [7]. Polarisation resolved two-photon excitation and emission measurements can be used to provide information about the structure of the two-photon transition tensor. A common 2PA model assumes a planar transition tensor [21] i.e.. that the

third rank tensor can be fully described using solely the elements in the molecular plane. In its simplest form the emission dipole moment μ_{EM} is taken to lie parallel to or at a small angle, γ , to the molecular symmetry axis. Measurements of BH101 [20] gave results suggesting that the angle γ has a wavelength dependence. It was also found that the structure of the two-photon transition tensor for OM77 showed significant variation across the excitation wavelength region of highest absorption. It was concluded that in OM77 the combination of three quadrupolar chromophores gives rise to a two-photon transition of significantly different symmetry to that of the single chromophore. The investigation into AF257 conducted here include polarisation resolved measurements of the 2PA cross-section, the 2PA excited fluorescence, and the 2PA excited fluorescence anisotropy decay dynamics. Initial anisotropy values $R_L(0)$ and $R_C(0)$ were measured following linearly and circularly polarised two-photon excitation and were used in conjunction with the 2PA polarisation parameter Ω to analyse the two-photon tensor governing the absorption transition. No previous examination of anisotropy decay correlation times as a method of investigation into the photophysical properties of such branched chromophores has been found in the literature. Through comparison of the wavelength-dependent results from the range of measurements conducted, a thorough and in-depth investigation into the inherent photophysical properties of branched two-photon absorbing chromophores is performed. The behaviour of such molecules is of major interest as it must be fully understood to enable optimum design of further 2PA enhanced molecules, especially so due to the large effort of synthesis of such large and complex molecules.

In this work we establish that the fluorescence decay of AF257 is characterised by two main lifetime components. Anisotropy measurements demonstrate that these components correspond to different 2PA states and an overall model for the photo-physics leading to emission in AF257 is proposed.

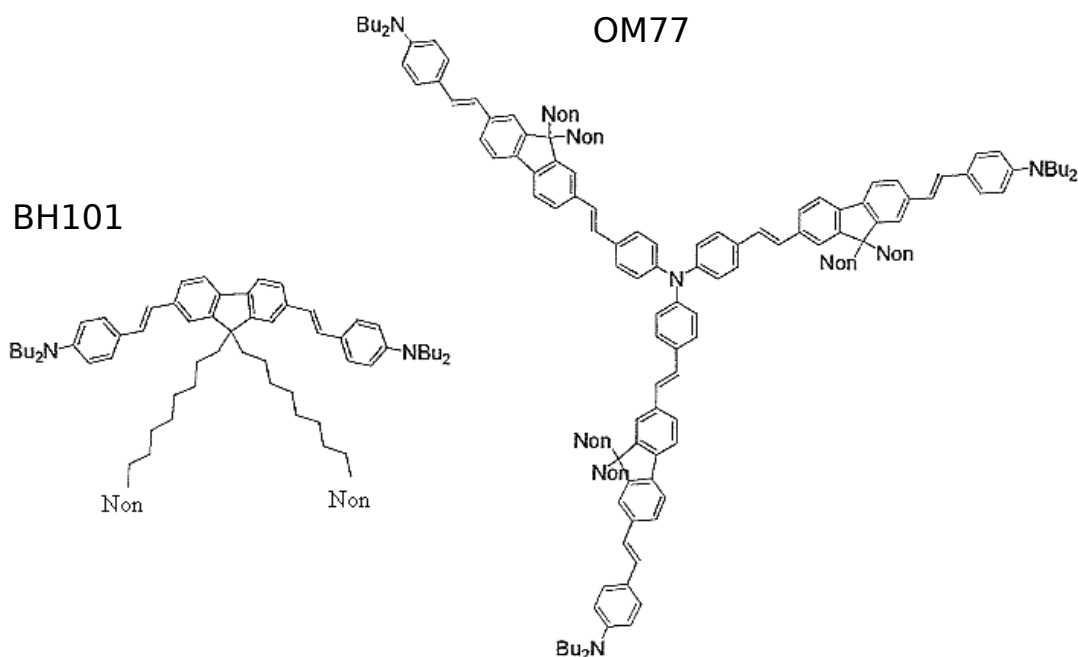


Figure 2.2: a) Structure of linear quadrupolar molecule BH101 and the corresponding branched molecule OM77 [22]

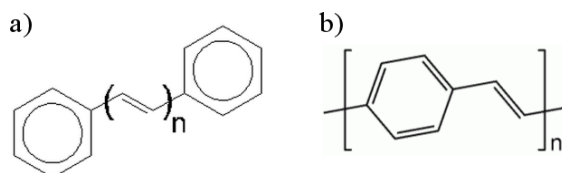


Figure 2.3: a) Phenylpolyene and b) Phenylene-vinylene type bridges used in 2PA optimised molecules.

2.2 Optimisation of 2PA in molecules

The 2PA cross section in naturally occurring fluorophores is often of the order of $1 \times 10^{-50} - 1 \times 10^{-48} \text{ cm}^4 \text{ s/photon}$ [23]. However, with optimum design it is possible to create molecules where this value is increased to $4 \times 10^{-48} - 1 \times 10^{-47} \text{ cm}^4 \text{ s/photon}$.

A number of molecules have been successfully developed for high 2PA cross section [24–26]. These include molecules with a large hyperpolarisability such as donor-acceptor-donor, donor- π -donor and donor- π -acceptor type molecules, where - π - is a

π conjugated bridge or linker. Other molecules with this property include polymers, dendrimers and multi-branched molecules [27, 28]. Studies have revealed that extending the conjugation length for charge transfer within the molecule or including electron withdrawing (EW) or electron donating (ED) end groups to create molecular dipoles or quadrupoles in the molecule increase 2PA cross section significantly [29, 30]. It was found that increases in chain length result mainly in an increase in the ground to excited state transition dipole moment $\mu_{g \rightarrow e}$, whereas the addition of donor end groups or going from diphenylpolyene- (Figure 2.3 a) to phenylene-vinylene-type bridges (Figure 2.3 b)) leads primarily to an increase in excited state absorption transition dipole moment $\mu_{e \rightarrow e'}$ [31]. These molecules are also found to remain transparent over a large wavelength range; a property that is important for optical limiting applications [32]. Optical limiting materials are designed to protect delicate optical sensors (or human eyes) from laser damage; this is achieved in materials that exhibit an increase in absorption coefficient with increasing optical intensity. At low incident intensities transmission through the material is high, allowing the normal function of the sensor whilst affording protection at high intensities. In case of near infra-red and infra-red light, two-photon absorption followed by subsequent excited state (single photon) absorption provides such a mechanism [32].

A number of photophysical effects have been noted in branched molecules such as cooperative enhancement [28, 33, 34], additive behaviour [35, 36], or in some cases a reduction in 2PA [36] depending on the particular molecular structure and the nature of the branches. Coherent coupling between branches may result in a localisation or delocalisation of charge in the ground or excited state, depending on the nature of the coupling[37]. It is this feature that is responsible for the 2PA amplification in branched molecules over their linear analogues [38].

AF257 is based around a triazine core with three triphenylamine based branches as shown in Figure 2.4. The molecule was first synthesised by the Prasad group at SUNY Buffalo as part of a US AirForce program in molecular nonlinear optics. The

compounds produced in this program are identified by the prefix AF (Air Force) and a number. AF257 was produced by Dr K. McEwan (DSTL, Porton Down) with the synthesis undertaken by N. Davis in the group of Prof. H. Anderson (Oxford University). Multi-branched triazines with triarylamine end groups very similar to this have been found to exhibit a large 2PA cross-section [39]. Triphenylamine (see Figure 2.4) has been used extensively as a building block in optically active molecules due to its high EW capability and its propeller-like structure. Addition of EW or ED end groups to enrich the π -electron density can further enhance the optoelectronic properties. This can increase the electron density delocalisation in the π -bond, increasing the electron-donating abilities and significantly decreasing the energy of the lowest unoccupied molecular orbital. This results in a red-shift in the absorption of the molecule, and an increase in π -electron accepting abilities of the material. Molecules oriented around a strongly EW 1,3,5-triazine base, particularly when combined with a strong ED end group, have been shown to have excellent optical properties due to their high electron affinities and symmetrical propeller structure [40–44].

2.3 Excitation distribution in Branched Molecules

Planar molecules with three-fold symmetry exhibit ultrafast dynamics following electronic excitation involving intramolecular redistribution of the excitation such that the initial localisation of the emission transition dipole moment is averaged over the three branches on a sub picosecond to picosecond timescale [46]. This effective reorientation of the emission transition dipole moment can be measured using subpicosecond fluorescence anisotropy [47] and four-wave mixing techniques. It has then been shown through experiment [47, 48] and theory [49, 50] that the delocalised excitation becomes localised such that individual emission events come from a single branch. Electronic detection methods of fluorescence such as TCSPC are not sufficiently fast to record these events and the initial single-photon excited fluorescence anisotropy reflects this averaging with a value of 0.1 [46?]. This is the same

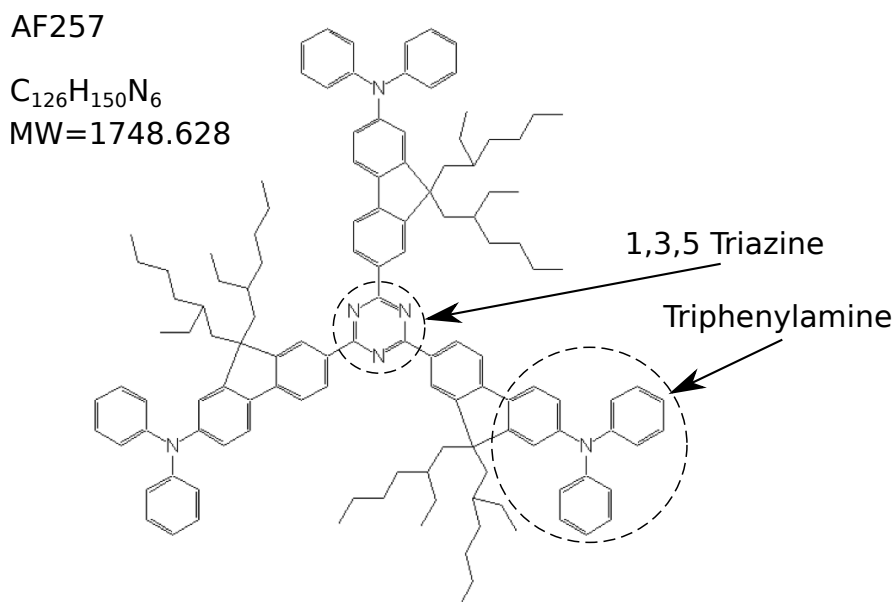


Figure 2.4: a) Structure of compound AF257, a 1,3,5-triazine based structure [45]. Both the triphenylamine branch end groups and the triazine core exhibit electron-withdrawing activity, such that quadrupolar intramolecular transfer occurs upon 2PA.

value that is recorded by continuous wave excitation and detection methods where there is negligible rotational diffusion and the intramolecular redistribution is fast compared to the fluorescence lifetime [52]. A reduction in single-photon anisotropy from 0.4 to 0.1 is based on transition moment orientation and reorganisation within the plane of the molecule perpendicular to the axis of symmetry [46, 51]. Out of plane transition dipole moment reorientation decreases this value whilst inhibition of the intramolecular energy transfer process has the opposite effect [53].

The optical spectra and excitation behaviour of C_3 branched chromophores are often described using the exciton model [54]. In this model the three branches are fully independent and the branch aligned with the excitation polarisation will be preferentially photoselected. The excitation will then stay on this branch if there is weak interbranch coupling and become delocalised over the three branches if strong coupling exists.

Fluorescence anisotropy measurements in branched molecules have shown a wavelength dependence in the vicinity of the red edge of the absorption spectrum [55, 56].

It has been found that in this region the anisotropy surpasses the limit of 0.1, indicating that excitation transfer between the three branches becomes less efficient [? ?]. The exciton model can also be used to explain this phenomena. If the three-fold symmetry of the excited state is broken, for example due to solvent-solute interaction [?], then exergonic hopping is allowed to branches of lower energy[59]. With red edge excitation, the lower energy branches will be populated and inter-branch transfer is thus restricted. Fluorescence will then take place from the same branch that was excited, and the initial anisotropy values will approach the limiting value of 0.4 [46, 51]. Leroy and Lami suggest that such symmetry lowering is due to a ‘matrix-induced’ dipole (or inhomogeneous broadening) rendering excitation on one of the branches more favourable than the others, and their paper shows the lowering of symmetry in benzene (in a glass matrix) in the first excited singlet state following 0-0 band excitation [?]. An increased initial anisotropy further requires that the transfer of the energy to other branches be energetically unfavourable, resulting in a decreased transfer rate. Leroy and Lami suggest that the matrix must ‘lock’ the branches in this symmetry-reduced state upon entering the excited state, and that it should be possible to select these ‘matrix-locked’ molecules from the whole by excitation at the red edge of the absorption spectrum. They report this increase in initial anisotropy as genuine after ruling out the existence of a Raman band of the solvent in this region and the possibility that it is caused by ground state aggregates with a red-shifted absorption spectrum. However, the exciton model cannot be fully applied to molecules such as AF257 that are mutually conjugated about a common core; these show a delocalised electron system in two dimensions [38].

A further model (‘essential state’) is proposed by Terenziani to explain the observed anisotropy behaviour [59]. This stems from the Jahn-Teller distortion that can occur in the relaxed excited state of symmetric molecules [60]. The model asserts that the first excited state is multistable with three energy minima corresponding to distortion along each molecular branch, with the electronic distribution of each mainly localised on the corresponding branch. This excited state multistability may or may not result in symmetry breaking in the excited state; if electronic excitation

proceeds from one minimum to another on a timescale shorter than that of molecular vibrations then the molecular symmetry is preserved. However, if residence in a particular minimum is longer than a vibrational period then the molecular symmetry is broken and the excitation becomes localised on one branch [61]. This model further states that polar solvation favours symmetry breaking by stabilising the excited localised electronic distribution, fully breaking the symmetry in the excited state. However, this cannot explain the anisotropy results in such branched systems. If symmetry is preserved in the ground state then vertical excitation cannot break it, as excitation results in a symmetric excited state involving all three branches. After this, the excitation can localise on any arm with equal probability such that the initial anisotropy $R(0)=0.1$ (see Chapter 1). Symmetry breaking in the excited state has no influence on $R(0)$ value. In order to explain the observed anisotropy values it is necessary to introduce some symmetry breaking before excitation. The degeneracy in the first two excited states is therefore removed, such that excitation will preferentially excite to one or the other depending on wavelength. This lowered symmetry in the ground state previous to excitation would be expected in highly symmetric molecules dissolved in polar solvents at finite temperature due to the different possible solvent configurations[61]. Such symmetry lowering in the ground state has been shown by Stahl in the lowering of the D_3 symmetry of tris(4-carbazolyl-2,6-dimethylphenyl)-borane [51].

2.4 2PA cross-section

The absorption cross-section is the effective area that governs the probability of an absorption event, and it depends upon the wavelength of excitation and the permittivity, shape and size of the absorber. The 1PA cross-section $\sigma^{(1)}$ and the 2PA cross-section $\sigma^{(2)}$ at a particular excitation energy do not always correspond because of fundamental differences in the selection rules and the effects of vibronic coupling [17].

2PA cross-sections can be measured directly by measuring attenuation of the excitation beam, or indirectly by measurement of secondary processes such as induced fluorescence; as is the case here. Direct absorption measurements suffer from a number of experimental restrictions, mainly due to the high incidence powers needed to measure a significant proportion of beam attenuation. This can lead to saturation, photobleaching and stimulated emission, and cause photo-damage to the sample [62]. Indirect measurements such as collection of induced fluorescence can give measurable signal with a low excitation power (of the order of pico-Joules as shown in this chapter) with just a small percentage of molecules undergoing absorption. Measurement of induced fluorescence differs between single-photon and two-photon excitation. Two-photon excitation only takes place in the region of highest intensity - within the Rayleigh range of the beam waist, which therefore restricts the excitation area. However, the measurement of 2PA cross-sections using this method still poses a number of experimental complications. These include; lack of exact knowledge of the proportion of fluorescence measured, the absolute efficiency of the detector, the focusing characteristics of the excitation pulse, and the excitation pulse shape (see Section 2.5). For this reason a reference sample of known 2PA cross-section is often used. There can be significant variation in the experimental values measured depending on the methodology used [17, 63, 64]. Further knowledge of 2PA processes would be useful to further this area of research and to enable effective use of 2PA measurements in physical applications.

Two photon absorption is one example of a third order nonlinear optimised process which as mentioned previously, is defined by the third order nonlinear susceptibility $\chi^{(3)}$ of the material. $\chi^{(3)}$ is dependent on the two signal fields and their polarisations. Two photon absorption is the third order nonlinear process which gives rise to a third order polarisation $P_i^{(3)}(\omega)$ that oscillates at the same frequency as the (degenerate) signal fields.

$$P_i^{(3)}(\omega) = \chi_{ijkl}^{(3)}(\omega, \omega, -\omega, \omega) E_j(\omega) E_k(\omega) E_l(\omega) \quad (2.4.1)$$

$$P_i^{(1)}(\omega) = \chi_{ij}^{(1)} E_j(\omega) \quad (2.4.2)$$

This is analogous to the linear optical susceptibility $P_i^{(1)}(\omega)$, however the intensity dependence of $P_i^{(3)}(\omega)$ is indicated by the product $E_k^*(\omega)E_l(\omega)$. The real component of $\chi_{ijkl}^{(3)}(\omega, \omega, -\omega, \omega)$ gives rise to the nonlinear index of refraction $n_2(\omega)$ [65]. The corresponding imaginary component is proportional to the 2PA cross-section [15]. Neglecting excited state relaxation processes the population of two-photon excited molecules can be determined from the following rate equation

$$\frac{dN_{ex}(t)}{dt} = \frac{\sigma^{(2)} I^2(t) G^{(2)}}{(h\nu)^2} [N_{gs}(t) - N_{ex}(t)] \quad (2.4.3)$$

where $N_{gs}(t)$ and $N_{ex}(t)$ are the populations of ground and excited states at time t ; $I(t)$ is the excitation intensity and $G^{(2)}$ is the degree of second order coherence of the laser pulse [5]. Given weak excitation, in a system in thermal equilibrium with its surroundings $N_{gs} \gg N_{ex}$ at all times. Integration of Equation 2.4.3 gives

$$N_{ex} = \frac{N_{gs} \sigma^{(2)}}{(h\nu)^2} \left(\frac{E_P}{A} \right)^2 \left(\frac{0.664}{\tau} \right) \quad (2.4.4)$$

where E_P and A are energy and coincident area of the laser pulse. Typical $\sigma^{(2)}$ values range from 10^{-51} to 10^{-48} $\text{cm}^4 \text{ s photon}^{-1}$. It can be seen from this equation that 2PA is inversely proportional to excitation pulse length; to achieve significant 2PA there is therefore a requirement for short pulse lengths, typically sub-picosecond with energies of $10^{-11} - 10^{-9}$ Joules. 2PA cross-section values are often quoted in units of *Göppert – Meyer* (GM) to honour Maria Göppert-Meyer’s contribution to this area of Physics [2], where $1 \text{ GM} = 10^{-50} \text{ cm}^4 \text{ s photon}^{-1}$.

The experimental measurement of $\sigma^{(2)}$ must take account of the indirect measurement technique used. The number of fluorescence photons measured, $F(t)$, will depend on the fluorescence quantum yield of the particular fluorophore η_2 , the collection efficiency of the combination of all equipment used C_e , and will include a factor of 1/2 to account for the fact that one fluorescence photon is given out for each 2PA. This is given in Equation 2.4.5.

$$F(t) = \frac{1}{2}C_e\eta_2N_{ex}(t) \quad (2.4.5)$$

2.5 Dependence of 2PA on excitation pulse profile

Due to dependence of 2PA on excitation intensity, the pulse shape can exert a significant effect on absorption, as opposed to 1PA which has no dependence on pulse shape. 2PA thus depends on the temporal pulse profile, and calculation of 2PA cross-section requires prior knowledge of the pulse shape, or use of a reference sample. A Gaussian pulse is assumed in equation 2.4.4, and any deviation of pulse shape from this can result in systematic error.

Due to the difficulty in measuring and maintaining pulse shape and to the factors discussed in Section 2.4, 2PA cross-section measurements are often given in relative terms, as shown in Equation 2.5.1, where R and U subscripts stand for Reference fluorophore signal and Unknown fluorophore signal, $\langle P_R(t) \rangle$ and $\langle P_U(t) \rangle$ are the incident laser powers, and n_R and n_U are the respective refractive indices. Values of $G^{(2)}$ at a given wavelength will be the same for both fluorophores, so as long as laser wavelength is not adjusted in between the measurements it will not need to be determined to obtain the relative fluorescence.

$$\frac{\langle F_R(t) \rangle}{\langle F_S(t) \rangle} = \frac{\phi_R\eta_R^{(2)}\sigma_R^{(2)}C_Rn_R\langle P_R(t) \rangle^2}{\phi_U\eta_U^{(2)}\sigma_U^{(2)}C_Un_U\langle P_U(t) \rangle^2} \quad (2.5.1)$$

Equation 2.5.1 can be rearranged to obtain the 2PA cross-section of the unknown fluorophore:

$$\sigma_U^{(2)}(\lambda)\eta_U^{(2)} = \frac{\phi_R\eta_R^{(2)}\sigma_R^{(2)}(\lambda)C_Rn_R\langle P_R(t) \rangle^2\langle F_U(t) \rangle}{\phi_U C_U \eta_U \langle P_U(t) \rangle^2 \langle F_R(t) \rangle} \quad (2.5.2)$$

Using this method the typical uncertainties expected are $\sim 15\%$ when the same reference material is used [66]. Generally, $G^{(2)}$ is given by $(\tau f)^{-1}$ so as can be seen from Equation 2.4.3 2PA scales with τ^{-1} , as has been demonstrated [67]. The 2PA cross-section however has been shown to have no pulse duration dependence (at least up to pulse durations of the ns timescale)[31]. Effects of pulse profile change over

the timescale of the pulse can be minimised by keeping the proportion of photons absorbed from the excitation pulse low.

2.6 Reference Samples: p-Bis (o-methylstyryl)-benzene (bis-MSB) and Rhodamine-B

The 2PA cross-section measurements in this chapter were all performed using the reference samples p-Bis (o-methylstyryl)-benzene (bis-MSB) in the solvent cyclohexane, and Rhodamine B in methanol, for calibration of the experimental set-up as both have a well-characterised 2PA cross-sections [38, 68, 69]. Additional properties necessary for reference samples include a significant 2PA over the region to be tested, as the wavelength cannot be changed between the reference and sample measurements for a spectrum. This necessitates the use of two reference samples to cover the full 2PA range to be tested in the following experiments; bis-MSB has a significant 2PA cross-section from 470 to 720 nm, and Rhodamine B has from 690 to 880 nm as shown in Figures 2.5 and 2.6 respectively.

2.7 2PA Polarisation Dependence

A fundamental property of single photon absorption in an anisotropic medium is that it is independent of the excitation polarisation [71]. In an ordered system in which an already aligned population of transition dipoles is present with the laboratory frame of reference this condition does not hold [72].

Two-photon absorption can be expressed as the summation of products of single photon transitions that connect the ground (initial) and excited (final) states. In simplistic terms the first photon prepares a polarised (aligned) virtual state which then interacts with the ‘second’ photon to reach the final state. This is analogous (in symmetry terms) to single photon absorption from an ordered ground state and so a polarisation dependence of the two photon cross section can be expected.

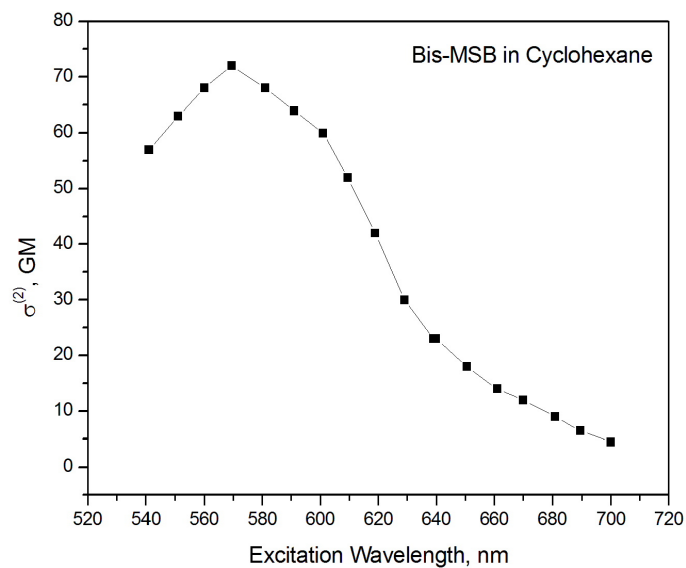


Figure 2.5: Variation in the 2PA cross-section of bis-MSB in cyclohexane with excitation wavelengths spanning 540-700 nm [38]

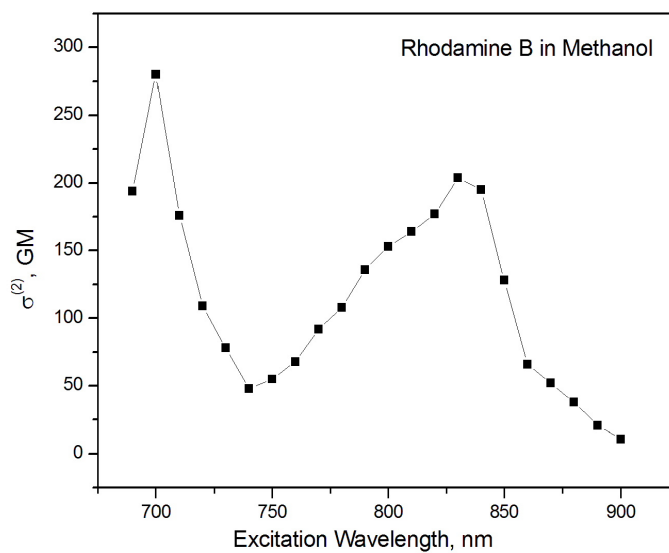


Figure 2.6: Variation in the 2PA cross-section of Rhodamine B in methanol in the excitation wavelength range 690-1050 nm [70]

Degenerate 2PA photoselection can be described in terms of a second rank tensor S :

$$S_{\alpha,\beta}^{(f,i)} = \sum_n \left(\frac{(\alpha \cdot \langle i|\mathbf{r}|n\rangle \langle n|\mathbf{r}|f\rangle \cdot \beta)}{\nu_n - \nu_\alpha + i\Gamma_n} \right) \quad (2.7.1)$$

where α and β are the polarisations of the two excitation photons, ν_n is the transition frequency, and Γ_n is the homogeneous linewidth of state n [21].

The two-photon absorption cross section $\sigma^{(2)}$ is proportional to $|S_{\alpha,\beta}^{(f,i)}|^2$ [21]. The polarisation dependence of 2PA is expressed in the ratio Ω given by

$$\Omega = \frac{\sigma_C^{(2)}}{\sigma_L^{(2)}} \quad (2.7.2)$$

where C and L denote linearly and circularly polarised photons respectively [73]. The determination of Ω does not require the use of a reference sample and the ratio can be determined from the integrated linear and circularly polarised fluorescence intensity decays $I_F^C(t)$ and $I_F^L(t)$ (assuming equal excitation intensities)

$$\Omega = \frac{\int I_F^C(t) dt}{\int I_F^L(t) dt} \quad (2.7.3)$$

Single and two photon excitation both lead to the creation of ordered excited state populations. In single photon absorption the initial fluorescence anisotropy is dependent solely upon the angle between absorption and emission transition dipole moment directions in the molecular frame θ

$$R_L(t) = \frac{1}{5}(3 \cos^2 \theta - 1) = \frac{I_V(t) - I_H(t)}{I_V(t) + 2I_H(t)} \quad (2.7.4)$$

$$R_C(t) = \frac{1}{10}(3 \cos^2 \theta - 1) = \frac{I_V(t) - I_H(t)}{I_H(t) + 2I_V(t)} \quad (2.7.5)$$

For $\theta = 0$ then $R_L(0) = 0.4$ and $R_C(0) = 0.2$. In 2PA the fluorescence anisotropy depends on the structure of the two photon transition tensor and the direction of the emission transition dipole moment in the molecular frame. Two photon linear and circularly polarised fluorescence anisotropies are defined in a similar way to those for single-photon excited fluorescence in Equations 2.7.4 and 2.9.5. The experimental geometries for their detection together with those for Ω are shown in Figure 2.7

For planar aromatic molecules the 2PA is dominated by excitation in the plane of the molecule such that the out-of-plane components of this to the transition tensor

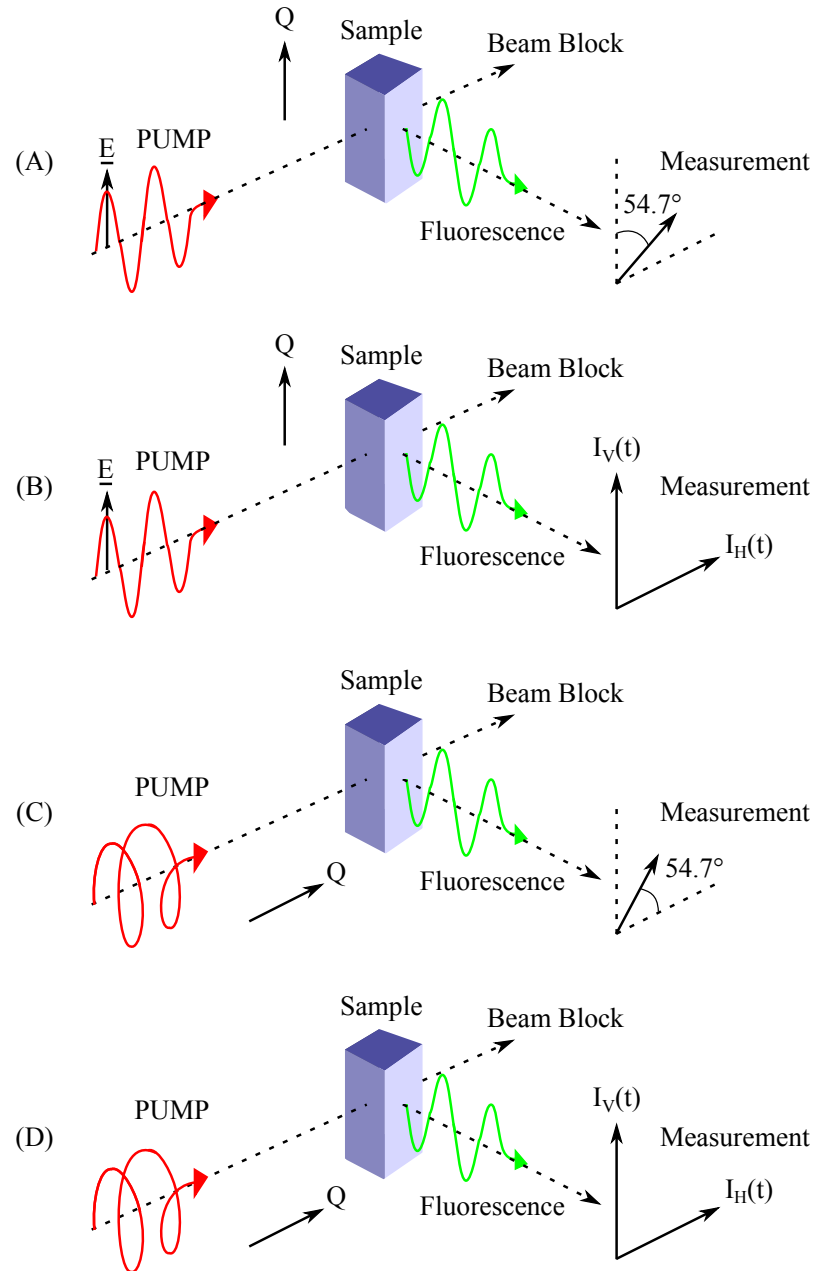


Figure 2.7: Polarisation directions of excitation and detection used with respect to the laboratory frame for 2PA, with the left-most arrows giving the direction of excitation polarisation, and the right most the polarisations of detection. (A) and (C) show total fluorescence intensity measurement for (A), linearly, and (C), circularly polarised light. (B) and (D) show detection polarisations used to measure fluorescence anisotropy for (B) linear, and (D) circularly polarised excitation. The Quantization axis Q denotes the direction of cylindrical symmetry in the excited state population [74]. This affects the measurement of both total intensity and magic angle intensity.

may be ignored [75–77]. The tensor thus reduces to the two dimensions, with the axis system chosen such that the molecular plane is in the X and Y directions. As previously stated, degeneracy of the two photons absorbed is assumed, giving $S_{XY} = S_{YX}$. Assuming the emission dipole moment is aligned along the X axis, the initial values of parameters $R_L(0)$, $R_C(0)$ and Ω can then be given (assuming fluorescence in the direction X and transition dipole aligned along X) as [76]

$$R_L(0) = \left(\frac{1}{7}\right) \frac{2(S_{XX} + S_{YY})^2 + (S_{XX} - S_{YY})^2 + 4S_{XY}^2 + 9(S_{XX}^2 - S_{YY}^2)}{2(S_{XX} + S_{YY})^2 + (S_{XX} - S_{YY})^2 + 4S_{XY}^2} \quad (2.7.6)$$

$$R_C(0) = \left(\frac{1}{7}\right) \frac{3(S_{XX} - S_{YY})^2 - (S_{XX} + S_{YY})^2 + 12S_{XY}^2 + 6(S_{XX}^2 - S_{YY}^2)}{(S_{XX} + S_{YY})^2 + 3(S_{XX} - S_{YY})^2 + 12S_{XY}^2} \quad (2.7.7)$$

$$\Omega = \frac{1}{2} \frac{(S_{XX} + S_{YY})^2 + 3(S_{XX} - S_{YY})^2 + 12S_{XY}^2}{2(S_{XX} + S_{YY})^2 + (S_{XX} - S_{YY})^2 + 3S_{XY}^2} \quad (2.7.8)$$

The initial anisotropies $R_L(0)$ and $R_C(0)$ are only sensitive to the relative magnitudes of the tensor elements. For the general case the full equations are [21].

$$R_L(0) = \left(\frac{1}{7}\right) \left[1 + \frac{9(1 - S^2)(\cos^2 \theta - \sin^2 \theta) + 4D(1 + S) \sin \theta \cos \theta}{2(1 + S)^2 + (1 - S)^2 + 4D^2} \right] \quad (2.7.9)$$

$$R_C(0) = \left(\frac{1}{7}\right) \left[1 + \frac{[6(1 - S^2)(\cos^2 \theta - \sin^2 \theta) + 4D(1 + S) \sin \theta \cos \theta] - 2(1 + S)^2}{(1 + S)^2 + 3(1 - S)^2 + 12D^2} \right] \quad (2.7.10)$$

$$\Omega = \frac{1}{2} \frac{(1 + S)^2 + 3(1 - S)^2 + 12D^2}{2(1 + S)^2 + (1 - S)^2 + 4D^2} \quad (2.7.11)$$

where the equations have been normalised by S_{XX} and the parameters $S = S_{YY}/S_{XX}$ and $D = S_{XY}/S_{XX}$ have been substituted.

Reducing the two-photon transition tensor to its simplest one-dimensional form, S_{XX} becomes the single non-zero element (i.e.. S and D are zero) and equations 2.7.11, 2.7.9 and 2.7.10 reduce to

$$\Omega = \frac{2}{3} \quad (2.7.12)$$

$$R_L(0) = \left(\frac{4}{7}\right) \left[\frac{3 \cos^2 \theta - 1}{2} \right] \quad (2.7.13)$$

$$R_C(0) = \left(\frac{2}{7}\right) \left[\frac{3 \cos^2 \theta - 1}{2} \right] \quad (2.7.14)$$

These are also the expressions obtained through sequential 1PA by transitions from an initial to ‘real’ state, followed by a transition from this ‘real’ state to the final state as discussed above. A simple linear molecule could be represented in this way, but a molecule with significant two-dimensional charge displacement between the initial and final states would have non-zero S and D that must be incorporated when calculating Ω and the expected initial anisotropies. Alternatively, for the case of excitation distributed over the three branches of a tri-branched planar molecule with inter-branch angles of 120° , equations 2.7.9 and 2.7.10 reduce to

$$R_L(0) = \left(\frac{1}{7}\right) \quad (2.7.15)$$

$$\begin{aligned} R_C(0) &= \left(\frac{1}{7}\right) \left[1 - \frac{2(1+S)^2}{(1+S)^2 + 3(1-S)^2 + 12D^2} \right] \\ &= \left(\frac{1}{7}\right) \left[\frac{3(1-S)^2 + 12D^2 - (1+S)^2}{(1+S)^2 + 3(1-S)^2 + 12D^2} \right] \end{aligned} \quad (2.7.16)$$

If $S=1$ (ie. $S_{YY} = S_{XX}$)

$$R_C(0) = \left(\frac{1}{7}\right) \left[\frac{12D^2 - 4}{4 + 12D^2} \right] \quad (2.7.17)$$

$$\Omega = \frac{4 + 12D^2}{16 + 8D^2} \quad (2.7.18)$$

2.8 Experimental Methods

2.8.1 Excitation System

Excitation pulses were generated using the partial output of a regeneratively amplified Titanium sapphire laser (Coherent Mira 900-F) with all pulse generation components shown as part of Figure 2.8. Titanium sapphire lasers have found widespread use in fluorescence spectroscopy (and anisotropy measurements) due to the ability to produce ultrashort pulses that are continuously tunable over a broad spectral

region (680-1100 nm). The laser is tuned using a birefringent filter and is typically set to 800 nm as this is near the gain maximum. A solid-state frequency-doubled Neodymium Vanadate ($Nd : YVO_4$) laser is used as a pump source (Coherent Verdi V-18), which provides 18 W of continuous wave (CW) radiation at 532 nm, of which 6 W is used as the pump source for the Titanium sapphire laser. The Titanium sapphire laser is mode-locked to create pulses of high energy rather than lower power continuous radiation in CW operation. The many possible longitudinal modes in the laser cavity due to the broadband emission spectrum of the Titanium sapphire are aligned using the nonlinear optical technique of Kerr Lens Modelocking [78]. This technique utilises the nonlinear focussing effect that occurs in certain materials such that the refractive index, n , experienced by light passing through is proportional to the intensity $I(t)$

$$n = n_0 + n_2 I(t) \quad (2.8.1)$$

where n_0 is the linear refractive index and n_2 is the intensity dependent refractive index. For a TEM_{00} Gaussian mode the refractive index depends on the radial position r

$$n(r) = n_0 I_0(t) e^{-\frac{a^2}{r^2}} \quad (2.8.2)$$

where $I_0(t)$ is the centre of beam intensity, and a is a unit of length depending on the fundamental mode of the laser cavity. High intensity mode-locked pulses will experience a higher refractive index and will be more strongly focused; use of a slit at an appropriate position within the laser cavity can selectively reduce the CW modes. Self phase modulation and group velocity dispersion occur within the laser cavity, but are compensated for by a pair of prisms placed prior to the exit of the laser cavity. This produces 140 fs long pulses at 76 MHz with pulse energies of around 10 nJ. This output was then amplified using a regenerative amplifier (Coherent RegA 9000) which has a Titanium sapphire laser cavity, and is pumped by the remaining 12 W from the Verdi V-18. A seed pulse from the Mira laser is injected into the amplifier through a Faraday Isolator by a Tellurium oxide (TeO_2) cavity dumper. The injected pulse is first stretched to avoid damage to the amplifier optics by passing through a (TeO_2) Q-switch which prevents the occurrence of lasing

before the seed has entered the cavity. The seed pulse is amplified to several μJ over 20-30 cavity round-trips, and also becomes temporally wider due to group velocity dispersion. The amplified pulse is then ejected by the cavity dumper and the pulse width compressed through use of a diffraction grating. The amplifier output is typically a pulse of 4 J and width of 200 fs, with pulse frequency controllable from 100-250 kHz and wavelength tunable from 780-840 nm.

The final stage of excitation pulse generation involved use of an Optical Parametric Amplifier (OPA) as a wavelength conversion tool. The OPA splits the incoming RegA output into two portions: one part is used to generate a white light continuum seed for the OPA, while the other part is converted to the second harmonic at 400 nm, which is then used to amplify a wavelength selected from the white light continuum. This produces 200-250 fs pulses at a repetition rate of 250 KHz, with a wavelength tunable between 440 and 710 nm and an average power of 70mW. It also produces and idler signal at 0.94 to 2.4 μm , a remnant pump beam at 400 nm, and white light.

Data for excitation wavelengths 710-900 nm was previously obtained within the group by Dr N Nicolau also using a Titanium Sapphire laser (Coherent Mira 900-F) but in this case pumped using a Verdi V-10 (Coherent) 10 W CW laser and with the Titanium Sapphire output not regeneratively amplified. Additionally, in this case the OPA was not used but the output was pulse picked using Pulse Select (APE). This data had not been previously analysed.

2.8.2 Detection System

The technique of Time Correlated Single Photon Counting (TCSPC) was used to measure induced fluorescence in anisotropy experiments following 1PA and 2PA in AF257 in the wavelength ranges 470 to 500 nm (1PA) and 530 to 710 nm (2PA). Induced fluorescence was measured using a microchannel plate photomultiplier (MCP) (Hamamatsu R3809U). A small amount of light split from the excitation source (4-6%) was detected by a fast photodiode (Hamamatsu S2381). The time interval

between the two signals was measured using a time to amplitude converter (TAC) (EG&G Ortec 475). This uses a linear voltage ramp with the fluorescence signal acting as a ‘start’ signal and the photodiode signal acting as a ‘stop’ to measure the time interval; the final voltage is proportional to the elapsed time. The ‘start’ and ‘stop’ signals of each event can vary in intensity: for this reason the signals were first sent through constant fraction discriminators (CFD) (Tennelec Model TC454 quad CFD). These produced a triggered signal, with the triggering dependent on a constant fraction of the peak height rendering the time of the trigger independent of signal amplitude; this has an advantage over simple threshold triggering which does have a dependence on the signal peak height. The trigger signals are therefore regular and have very little associated time jitter. It is possible to adjust the threshold fraction of the CFDs to ensure a level above the inherent noise in the system is used. This final voltage value is digitised and stored in the appropriate channel in the multi-channel buffer (MCB) (EG&G Ortec ADCAM & MCB Model 918A). Using the two signal this way round is known as ‘reverse mode’ [79].

From the MCB the signal for each event was sent to a PC (Viglen 486 DX) which increased the appropriate histogram channel for the measured time interval by a value of one. Many fluorescence events were recorded in this way such that the histogram built up to give an accurate representation of the time between excitation and fluorescence. The excitation intensity was kept low so that less than 1% of excitation pulses resulted in a measured fluorescence event. This minimises the possibility of a second fluorescence event occurring from a particular excitation pulse; this would create a systematic error in the histogram plotted as this measurement technique would only record the earlier of the two events.

The optical layout that was used is illustrated in Figure 2.8. The laser output intensity was first controlled using neutral density filters, and any remaining infra-red light removed from the pulse using a short pass LS700 filter. The split to the photodetector was achieved using a 1% beamsplitter. The remaining beam was directed through two neutral density wheels (optical density 0-3.5) which were used to keep

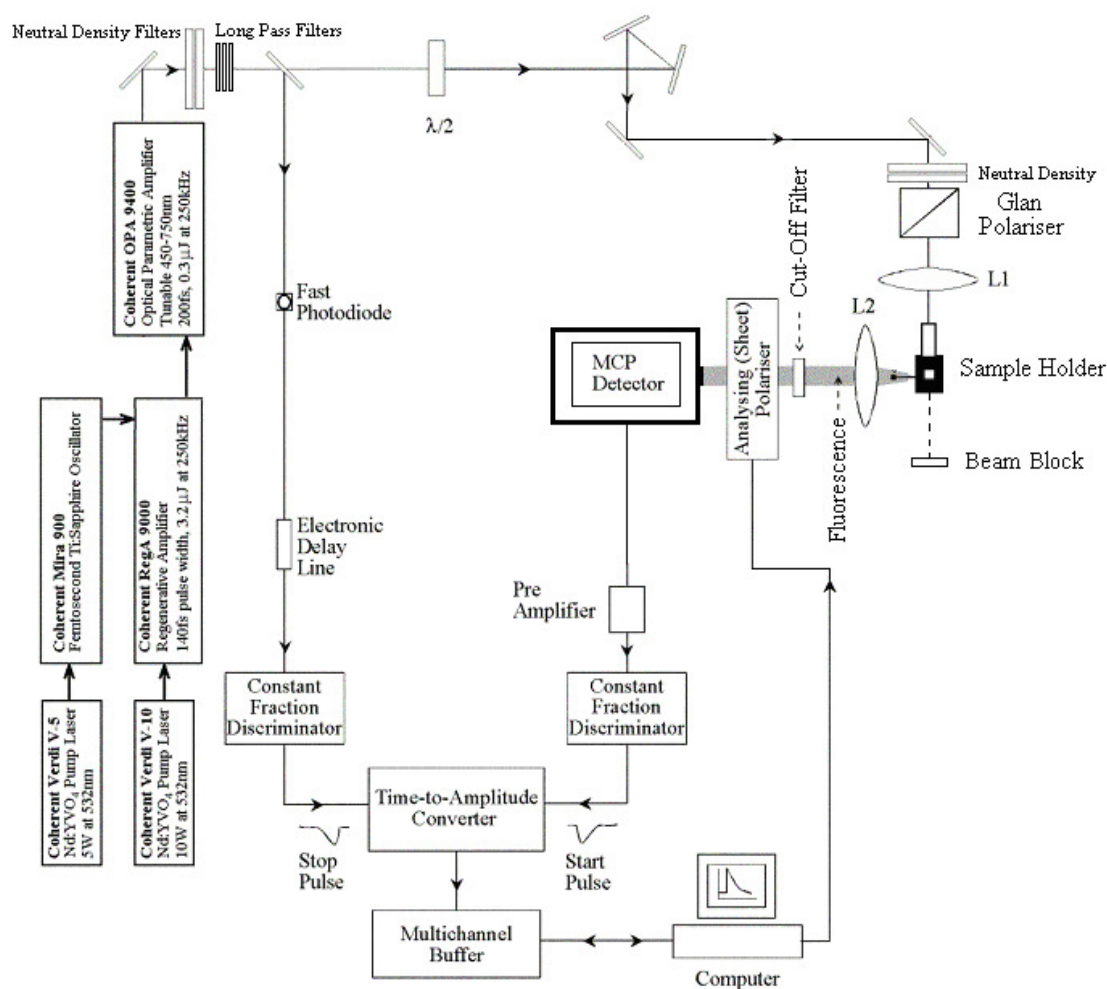


Figure 2.8: Experimental set-up for the excitation and detection of single and two-photon excited fluorescence using TCSPC.

the count rate below 1% of the pulse repetition rate, and then through a high quality Glan Taylor cube polariser (extinction ratio $10^6:1$) which was mounted on a rotation stage (Photon Control RM100). The excitation beam was then focused into the sample using a 25 mm focal length achromatic doublet lens (Melles Griot). A perpendicular detection geometry allowed the remaining excitation light to be blocked easily with a beam block, while fluorescence was collected at 90° and collimated using quartz lenses of 6.3 cm and 25 cm focal length respectively. Filters were situated in front of the MCP detector to block any remaining laser light. Finally, the fluorescence passed through a sheet linear polariser attached to a stepper motor to allow selection of polarisation angle; this was controllable via the PC. To start and stop the experiment a program by Dr Gary Holtom of Pacific North Western Research Laboratory was used, in conjunction with a polarisation dependent data collection program written by W J. Noad, formally of the Rutherton Appleton Laboratory.

2.8.3 Instrument Response and Reconvolution

For purposes of simplicity it was assumed in Chapter 1 that the excitation pulse could be approximated to a δ -function. This holds true as long as the pulse width τ_{PT} is small compared to the relaxation processes under investigation. In the measurement of fluorescence lifetimes which typically span the range of $10^{-10} - 10^{-8}$ seconds a picosecond range laser pulse will not generally result in the fluorescence decay that a δ function pulse would be expected to produce. An additional distortion arises from the finite time response of the detection system. The effects of this and a finite laser pulse are encapsulated in what is termed the instrument response function $P(t)$. The detected fluorescence signal $F(t)$ is given by the convolution of $P(t)$ with the response of the population to a δ function pulse,

$$F(t) = \int_{-\text{inf}}^t P(t')i(t-t')dt' \quad (2.8.3)$$

For a homogeneous population of excited states the simplest form of $i(t-t')$ is a single exponential decay with lifetime τ_f

$$\begin{aligned} i(t-t') &= \exp[-(t-t')/\tau_f] & t' \leq t \\ &= 0 & t' > t \end{aligned} \quad (2.8.4)$$

$P(t')$ can be determined by assessing the response of the system to scattered laser light, $i(t-t') = \delta t', 0$. Knowing $P(t')$, $F(t)$ can be compared to the experimental data and a best fit found by varying τ . More complicated exponential decays of the form

$$i(t-t') = \sum_{i=1}^n \alpha_i \exp[-(t-t')/\tau_i] + \alpha_0 \quad (2.8.5)$$

may be necessary where α_i is the weight (photon counts) of component i and α_0 is the background fluorescence signal. Determination of the best α_0 , α_i and τ_i is accomplished using nonlinear least squares method discussed in Section 2.8.4. The shortest fluorescence decay lifetime that can be obtained through reconvolution analysis can not be deduced from the theory, but lifetimes of $\frac{1}{5} - \frac{1}{10}$ of the IRF width have been found in practice [80, 81]. A thorough review of the IRF analysis process is discussed by Leissman et. al [82]. The IRF test was carried out using low intensity light from a scattering sample of dilute milk in water; to avoid damage to the sensitive MCP the laser intensity was slowly increased from zero using the neutral density wheels until the photon count rate became sufficient. Although the measurement of an instrument response profile $P(t)$ is an imperfect measure of the response of the detector, the use of instrument response profiles when performing decay curve analysis often brings significant improvements in time resolution and the ability to fit decay profiles in a meaningful way. The IRF should be measured for each experiment to minimise error due to instrumental response drift.

2.8.4 Data Analysis

The data obtained from TCSPC is in the form of an intensity decay curve, synthesised from many repeated measurements of the delay times between absorption and

emission events. The decay parameters can then be obtained through statistical methods of data analysis using decay analysis software. The statistical method employed for this task in the following work is the reconvolution least squares method [83]. The data analysis should aim to minimise any error inherent in the system, both systematic including non-linear detection response, finite width of pulse and finite response speed, and random error, for example noise.

Including a background noise factor, the final reconvolution calculation for comparison with the measured fluorescence decay is [84]

$$F_Y(i) = B + A \cdot F(i + \Delta) \quad (2.8.6)$$

Where B is the background noise, A is a scaling parameter, Δ is the time shift parameter, and i is the measurement channel number for the case when τ_f is measured in channels.

Least Squares Fitting Method

The least squares fitting method uses the quantity χ_R^2 as a measure of the goodness of fit of the calculated function in Equation 2.8.6 to the collected data. It iteratively determines the best fit parameters A', B', τ' and Δ' using the example given by Equation 2.8.6. The reduced chi-squared value χ_R^2 represents the weighted squared deviation of the model from the data per degree of freedom [85]

$$\chi_R^2 = \frac{1}{n-p} \sum_{i=1}^n \frac{1}{\sigma_i^2} [Y(t_i) - F_Y(t_i)]^2 = \frac{1}{n-p} \sum_{i=1}^n [W(i)]^2 \quad (2.8.7)$$

where n is the number of channels, p is the degrees of freedom, $Y(t_i)$ is the measured fluorescence decay value at time t_i (the time label of the ith channel), and σ_i^2 is the variance or 'weighting factor'. The weighting factor represents the statistical uncertainty and depends on the statistical model used. Since the probability of a photon arriving in a particular channel can be classed as low, a Poisson distribution is used and $\sigma_i^2 \approx i$. For intensity decays taken at the magic angle the weighting factor the variance used is simply

$$\sigma_m^2 = I_m \quad (2.8.8)$$

where m is used to denote the magic angle. However for the anisotropy, since it is a construction of I_V and I_H the weighting factor must be calculated using error propagation methods. This results in a weighting factors for linearly and circularly excited anisotropy decays

$$\sigma_{R(L)}^2 = \frac{2 + 3R(t) - 3R(t)^2 - 2R(t)^3}{3I_{tot}} \quad (2.8.9)$$

$$\sigma_{R(C)}^2 = \frac{2 - R(t) - 3R(t)^2 + 2R(t)^3}{3I_{tot}} \quad (2.8.10)$$

Since the weighting factor represents the expected statistical uncertainty on the model used, Equation 2.8.7 can be expressed simply as

$$\chi^2 = \frac{1}{n - p} \sum_{Data} \left[\frac{\text{actual deviation}}{\text{expected deviation}} \right]^2 \quad (2.8.11)$$

The minimum error that can be measured would match the statistically expected error for each data point i.e.. $\chi_R^2 = 1$ (after normalisation to the number of degrees of freedom) if the model shows a perfect fit to the data. A typical reconvolution analysis with minimised $\chi_R^2 = 1$ value is shown in Figure 2.9. Here the decay model with best-fit parameters $F_U(i)$ is shown superimposed on the collected data points $Y(i)$, in addition to the IRF $P(i)$. The quantity shown within the brackets in Equation 2.8.7 is called the ‘weighted residual’ and can be used to assess the goodness of fit as it represents the standard deviations of the data noise. They can be useful to assess whether the appropriate number of exponentials have been used in the model (a residual with a definite shape implies further decay correlation times are present) and to note the times t at which there is deviation from the model. These assessments can be made by eye; methods of analysing the data given in the weighted residual mathematically exist such as the autocorrelation function and the Durbin-Watson parameter [86], however assessment by eye is usually sufficient for practical purposes [84].

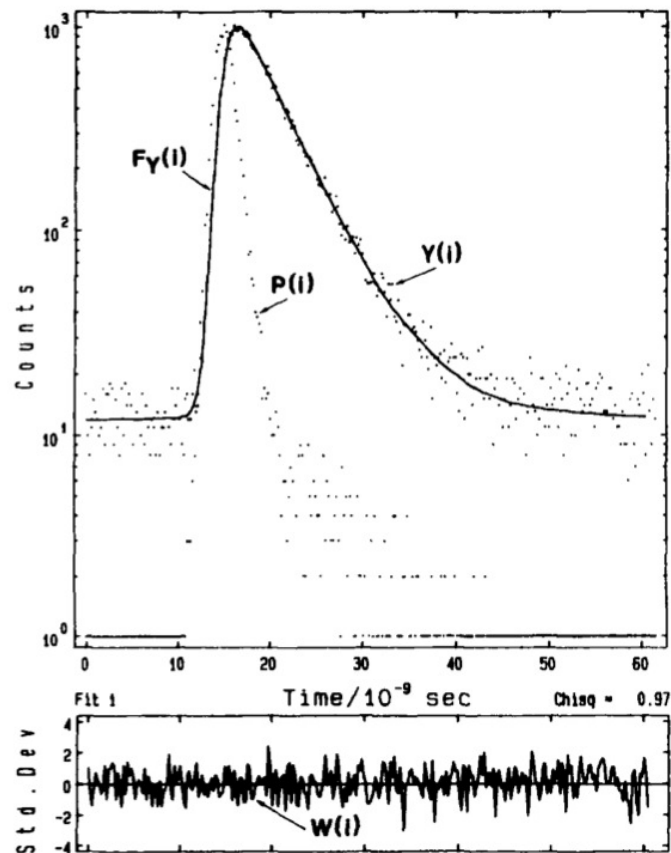


Figure 2.9: A logarithmic plot of a typical fluorescence decay dataset $Y(i)$ with instrument response function $P(i)$ and least squared reconvolution fit $F_Y(i)$. Below is shown the weighted residual $W(i)$. Figure reproduced from [84]

2.8.5 Experimental procedure

Optical alignment

Prior to beginning an experiment some preparatory steps were carried out. The laser systems used were optimised for power and stability using the standard procedure as outlined in the equipment handbooks. All optical components were carefully aligned such that the excitation beam arrives at the correct position in the sample whilst the beam quality and collimation is preserved. After aligning the excitation beam into the sample such that any back reflections were directed back down the laser pathway, the intermediate optics were inserted (see Figure 2.8. The cube polariser was inserted and adjusted such that there was maximum beam extinction when its

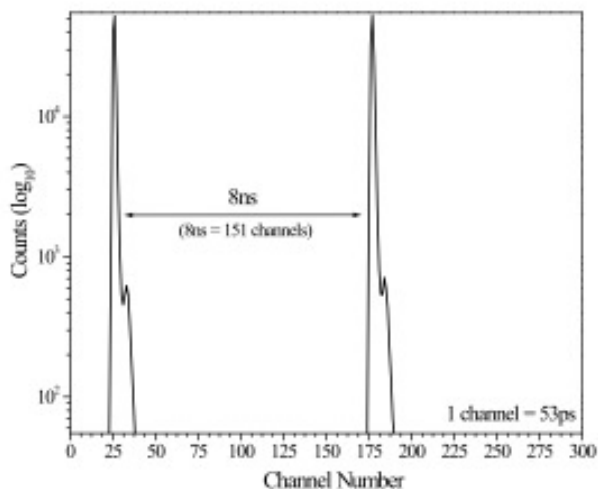


Figure 2.10: A logarithmic plot of an instrument response function calibration for TCSPC measurement. The separation of the two response functions for a known delay gives a calibration of 53 ps per channel.

polarisation direction was perpendicular to that of the sheet polariser. The lenses and beam block were then placed in position and aligned.

An instrument response function (IRF) was then recorded to check the response of the MCP and to check that there were no excitation beam reflections directed into the detector. An IRF of less than 100 ps was considered acceptable for the experiments carried out in this thesis. If the measured IRF was greater, or if laser reflections were present (indicated by multiple spikes in the IRF) then the alignment procedure and IRF were repeated. Surfaces causing reflections of laser into the detector could be moved or blocked. The system was then calibrated through measurement of the time between two pulses separated by a known delay. A typical IRF calibration is shown in Figure 2.12.

G-factor

The G-factor refers to experimental differences in the instrumental sensitivity to the vertically and horizontally polarised fluorescence signals that are selected by the

analysing polariser (see Figures 2.7 and 2.8). A G-factor measurement was made before each experiment to check for polarisation bias in the detection geometry. During analysis slight differences in detection efficiencies in the vertical and horizontal polarisations can be corrected for using the technique of ‘tail-fitting’ [87]: when the anisotropy has decayed to zero the intensity of fluorescence in both polarisation directions should be equal, so any differences can be corrected for by offsetting one of the readings. However, this correction is not exact as the instrument response may not be exactly linear, so if a significant G-factor could be seen then the alignment process was repeated until the measured polarisation bias was negligible (i.e. $G \approx 1$). Measurement bias could also occur during the experiment due to factors such as heating effects or laser drift. To minimise the relative effect of this measurements were taken at vertical and horizontal polarisations for 10 seconds each consecutively until the end of the measurement. This was accomplished using the motorised rotatable polaroid sheet in front of the photodetector (Figure 2.8).

Data collection

Two-photon excited fluorescence of AF257 was measured following excitation of 530-710 nm. The sample used was of concentration 2.84×10^{-4} M in the solvent toluene. The detection filter used was an S500 \pm 20 in addition to the LS700 short pass filter used to block remaining infra-red from the excitation pulse. The reference sample used was Bis-MSB of concentration 1.18×10^{-4} M in Cyclohexane. The sample was contained in a 200 μ L optical cuvette (Hellma). As well as measuring fluorescence in vertical and horizontal directions, isotropic intensity decays used to find fluorescence lifetimes were recorded by measuring fluorescence at the ‘magic angle’ of $\theta_m \approx 54.74^\circ$ to the vertical at which $\langle C_{20} \rangle$ moments vanish and the intensity decay is independent of rotation [76] (see Chapter 1 Section 1.6). Data was analysed using FluoFit (PicoQuant) as this allows the use of a global fit i.e.. data sets over a range of wavelengths could be fit to the same three correlation times.

Following 2PA the fluorescence induced by circularly polarised excitation was mea-

sured in addition to that induced by linearly polarised excitation. Circularly polarised excitation was generated by a $\lambda/4$ wave plate with the molecular axis set at 45° to the vertical. Measurements were again taken of emission in the vertical, horizontal and magic angle polarisations, but following circularly polarised excitation the magic angle is at 35.3° to the vertical. In the case of the 2PA experiments all lifetime and anisotropy decay time fitting was done using Origin.

Additional data that is plotted in conjunction with the experiments detailed in this chapter was taken previously within the group [20]. Data following 1PA of 360-520 nm was excited using the direct output of the Mira which produces pulse-picked (PulseSelect APE) 3.8 MHz pulses with a power of 25 nJ and a pulse width of 100 fs. Data taken following 2PA of 710-900 nm was excited using the frequency doubled output of the Mira. Frequency doubling was achieved using an LBO crystal.

The collection count rate was maintained at less than 2500 counts per second ($< 1\%$ of the laser pulse repetition rate). The quadratic dependence of the two-photon fluorescence signal with excitation intensity was checked at each wavelength by measuring the count rate at an incident laser power P and at $P/2$. Deviations from a purely quadratic power dependence were observed as the excitation wavelengths were shortened to 520 nm indicating significant 1PA. Data from excitation wavelengths below 530 nm were omitted from the overall 2-photon analysis.

Anisotropy decays were analysed by simultaneous deconvolution of the vertically and horizontally polarised measurements using the software Fluofit (PicoQuant). Intensity decays taken at the magic angle were analysed using the software Origin (OriginLab). Both of these measurements were fit to single or multiple exponential decays, depending on the number needed to get an accurate fit to the data. The quality of fit was judged using the reduced chi squared parameter, χ^2 [88]. Although IRF measurements were taken for each experiment, initial analysis showed that for this experimental set-up reconvolution using the IRF made negligible difference to the best fit parameters. An example is included in Figure 2.12 in which the data (measured fluorescence decay in AF257 following linearly polarised 2PA) is fit to

Method	Correlation times (ns)	Amplitude	χ^2
FluoFit +IRF	1.605 (+0.014 -0.013)	392000 (+15000 -17000)	3.004
	0.917 (± 0.036)	217000 (+17000 - 15000)	
FluoFit no IRF	1.607 (+0.015 -0.013)	301000 (+12000 -14000)	3.134
	0.932 (± 0.037)	141000 (+13000 -12000)	
Origin	1.623 (± 0.005)	384695 (± 5867)	2.684
	0.914 (± 0.015)	207162 (± 5060)	

Table 2.1: Results of best fit parameters using different analysis methods: A reconvolution analysis using software FluoFit (PicoQuant); a standard fit with no reconvolution using FluoFit; and a standard fit with no reconvolution in Origin (OriginLab). The sample data used was the intensity decay of AF257 following linearly polarised 2PA at 700 nm.

a double exponential using FluoFit both with and without reconvolution analysis. The same data was additionally analysed using Origin. The resulting fluorescence lifetime correlation times for all three analysis methods are tabulated in Table 2.1. It should be noted that in FluoFit the weighting factor used for the least squares fit is derived from a Poisson distribution by default; this means that the weighting factor for total intensity derived from a magic angle measurement is correct, but that the weighting factor for total intensity derived from a summation of $I_{tot} = I_V + 2I_H$ is not. In Origin the weighting factor can be specified such that the exact weighting factor was used at all times. This is a reason for use of Origin over FluoFit for data analysis if a global fit (as described earlier in this section) is not needed (global fitting is not possible in Origin). However, the difference in the use of the correct weighting factor ($\sigma_{I_{tot}} = \sqrt{I_V + 4I_H}$ vs $\sigma_{I_{tot}} = \sqrt{I_V + 2I_H}$) makes for generation of fit parameters is typically very small, as can be seen by the similarity of fit parameters using Origin and FluoFit in table 2.1.

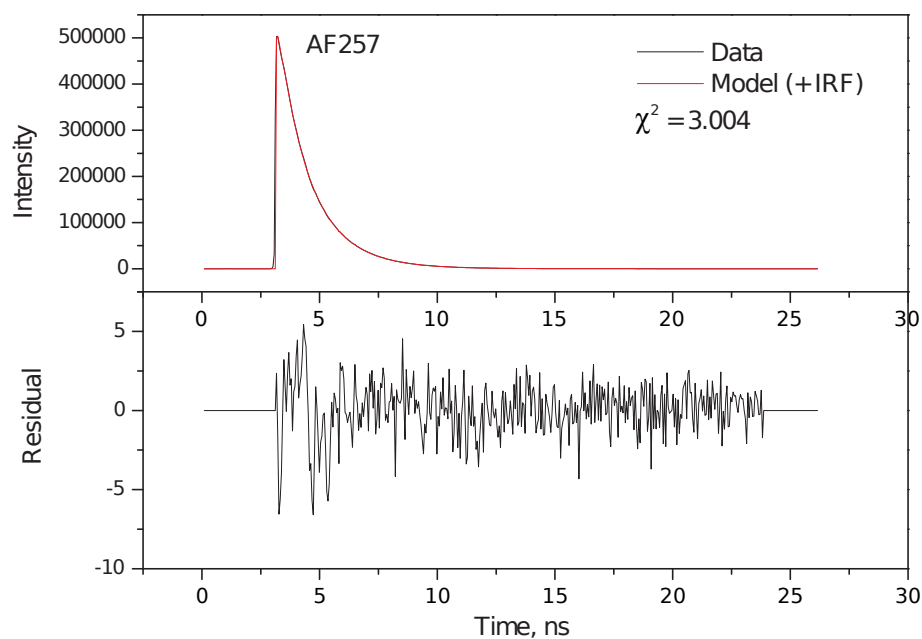


Figure 2.11: Double exponential least-squares fit to AF257 intensity decay using software FluoFit with no reconvolution analysis.

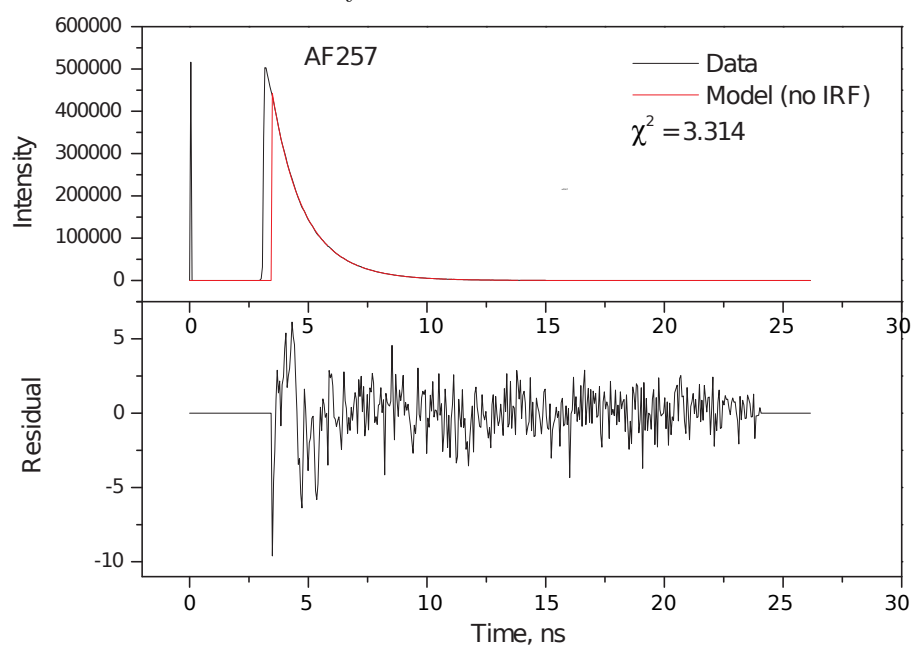


Figure 2.12: Double exponential least-squares fit to AF257 intensity decay using software FluoFit with reconvolution analysis using IRF. The two cases (using IRF and not using IRF) are virtually indistinguishable.

$\sigma^{(2)}$ and Ω Measurements

Two-photon excited fluorescence in AF257 was detected for excitation wavelengths spanning 530 nm to 900 nm. Excitation wavelengths below 530 nm were investigated as previous work on the branched chromophore OM77 [64] had showed the existence of a giant two-photon resonance ($\sigma^{(2)}$ 1.2×10^4 GM) at wavelengths approaching the red edge of the single photon absorption. From 510-520 nm the fluorescence intensity exhibited an excitation power dependence mid way between that of 2PA (quadratic) and 1PA (linear). In order to determine $\sigma^{(2)}$ at a particular excitation wavelength (given a quadratic intensity dependence) the mean values for five measurements of the fluorescence intensity were made for both linear and circularly polarised excitation (Ω determination) together with a measurement of the linearly polarised 2PA fluorescence for the relevant 2PA reference materials Bis-MSB and Rhodamine B.

Correction factors k_S and k_R (S and R denoting the sample and reference sample respectively) were employed to account for the effects of differences in emission spectra on the signal yield. $k_{S/R}$ is given by

$$k_{S/R} = \sum_{\lambda} QE_{\lambda} FT_{\lambda} E_{S/R,\lambda} \quad (2.8.12)$$

where QE is the quantum efficiency of the detector, FT is the filter transmission, and $E_{S/R}$ is the emission of the the sample/reference sample.

The cross-section of the sample is then calculated from the relative measured signals (counts (N)/Power (P)²), quantum yields (QY), refractive indices (n), concentrations (c), and k values

$$\sigma_S = \frac{(\frac{N}{P^2})_S \cdot \sigma_R \cdot QY_R \cdot k_R \cdot n_S \cdot C_R}{(\frac{N}{P^2})_R \cdot QY_S \cdot k_S \cdot n_R \cdot C_S} \quad (2.8.13)$$

The single photon absorption spectrum was obtained from a home-built absorption spectrometer consisting of a focused white light flash lamp and a USB4000 spectrometer (Ocean Optics), sample holder and collection optics. The absorption of the white light was measured relative to a blank reference sample. The two-photon

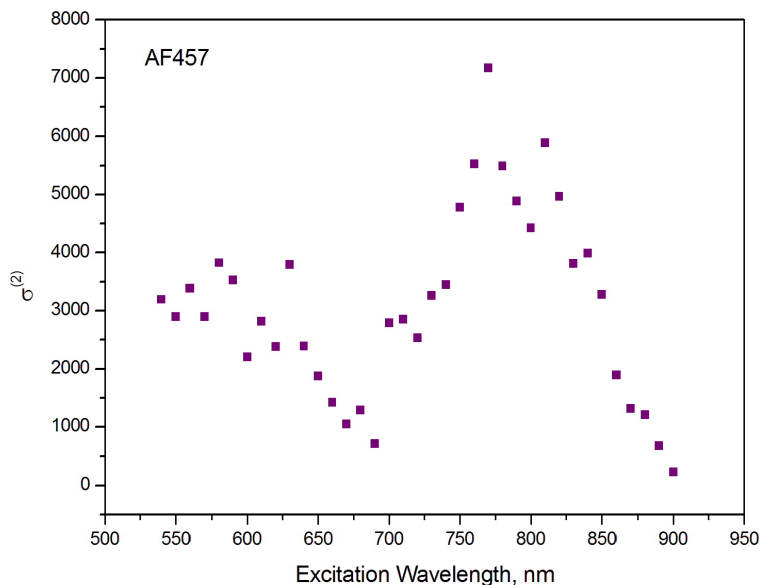


Figure 2.13: Measured 2PA cross section (in GM) of AF257 following excitation of 530-900 nm. Data taken in the region 710-900 nm was taken previously by N Nicolau, but has been re-analysed.

excited emission spectrum was obtained using the 800 nm output of the regenerative amplifier system described previously. The emitted fluorescence was collected using the USB4000 spectrometer.

2.9 Results

2.9.1 $\sigma^{(2)}$ Measurement

2PA cross-sections for AF257 between 540-900 nm are shown in Figure 2.13. A strong near infra-red 2PA cross section is observed with a peak value of $\sigma^{(2)} = 7.2 \times 10^3$ GM between 710 and 900 nm. A second broad maximum ($\sigma^{(2)} = 3.8 \times 10^3$ GM) is observed between 550 and 700 nm.

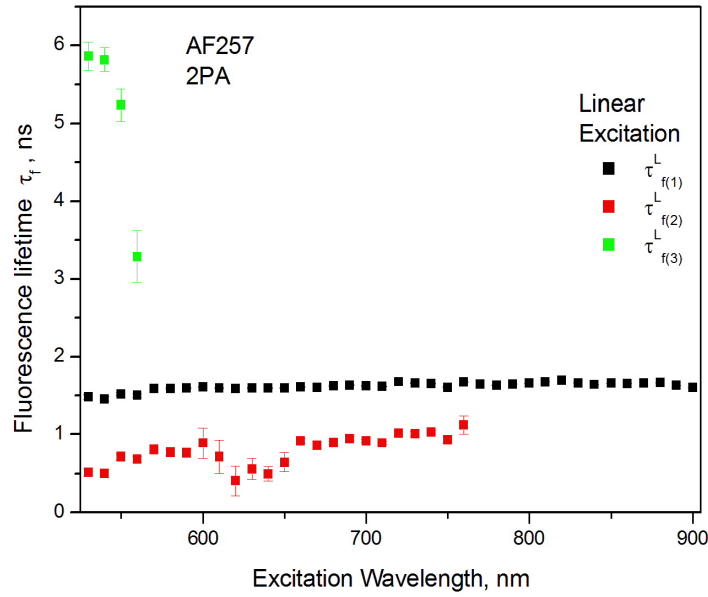


Figure 2.14: Measured fluorescence decay times for AF257 as a function of excitation wavelength.

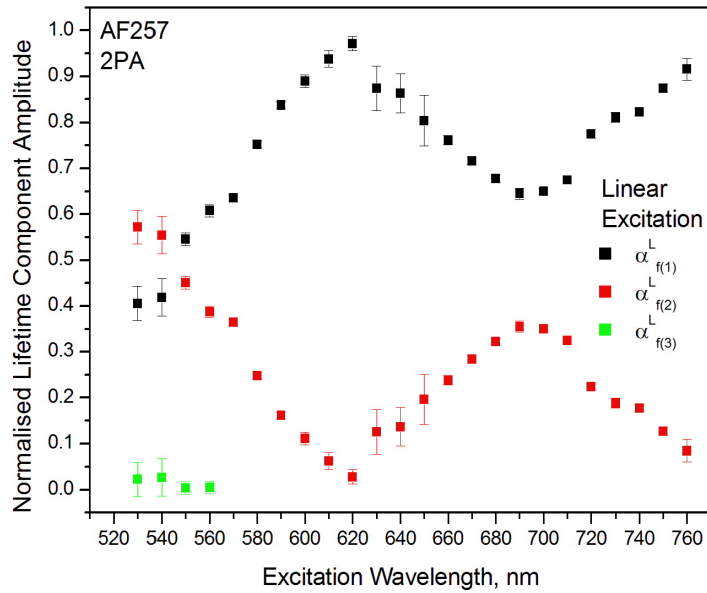


Figure 2.15: Fractional contributions of the three lifetime components to the measured fluorescence decay for two-photon excitation wavelengths spanning 530-760 nm (error bars are smaller than data points in most cases). Between 570 and 760 nm a bi-exponential decay is observed ($\alpha_{f(3)} = 0$). The contribution to the decay between 530 and 560 nm is small with ($\alpha_{f(1)} \cong \alpha_{f(2)} \gg \alpha_{f(3)}$) Above 760 nm a mono-exponential decay is observed ($\alpha_{f(2)} = \alpha_{f(3)} = 0$).

2.9.2 Two Photon Fluorescence Lifetime Measurement

Fluorescence intensity decays for two-photon excited AF257 were analysed for excitation wavelengths between 530 and 900 nm. The results are shown in Figures 2.14 and 2.15 with the fits typically generating a χ_R^2 of 1.6-2.7; χ_R^2 was below 2.5 in all cases. With the exception of a narrow wavelength range close to the onset of 1PA (530-560 nm) the fluorescence decay is characterised by up to two lifetimes. A common lifetime of 1.5 ns is observed for all excitation wavelengths. This is the sole decay component in the region of the near infra red 2PA resonance. With increasing two-photon excitation energy a second shorter decay component with a lifetime between 0.5 and 1 ns is observed. These two components fully characterise the decay dynamics for two-photon absorption wavelengths above 570 nm. For 560-530 nm a small (ca. 1-2.5% contribution to the total decay amplitude) longer lived additional decay component is observed. The spectral footprint of this contribution is small and with this narrow wavelength range its contribution to the total signal is low (2-5 % of total amplitude) and the analysis of the fluorescence decay dynamics below will be restricted to the two dominant components.

Multi-exponential fluorescence decays clearly indicate the presence of multiple emitting states; the origin of these can be varied. Ground state heterogeneity has been assumed as the cause of the bi-exponential decay in EGFP [89] (see Chapter 4). Variations in the environment of fluorescent probes attached to proteins can give rise to multi-exponential relaxation dynamics [90]. The existence of two (or more) molecular conformations such as in the case of the open and closed forms of NaDH and NADPH gives rise to bi-exponential decay dynamics [91]. Correlations between absorption strength, fluorescence intensity, and fluorescence anisotropy observables can help in this respect [91]. For fluorescent molecules in a homogeneous environment a bi-exponential decay could, in the absence of ground state heterogeneity (i.e.. two different molecular configurations), arise from excitation leading to the population of two distinct emitting states.

If the lifetime amplitudes $\alpha_{f(1)}$ and $\alpha_{f(2)}$ showed a strong correlation with the two-

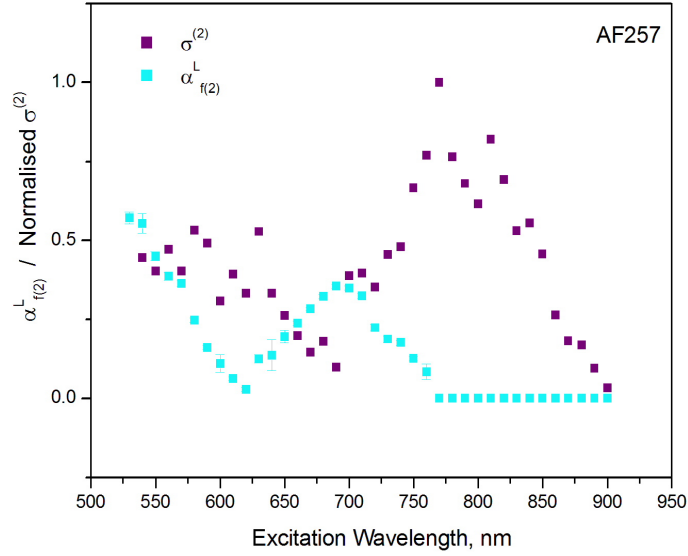


Figure 2.16: The two-photon absorption spectra for AF257 for the wavelength range 540nm-900nm along with the the amplitude of component 2, $\alpha_{f(2)}$.

photon action cross section, it would be a convincing indication that two distinct ground state configurations and/or transitions were responsible for $\tau_{f(1)}$ and $\tau_{f(2)}$. From Figure 2.16 it can be seen that no such clear cut correlation exists.

2.9.3 Calculation of Ω

A clearer indication of individual excitation pathways in two-photon absorption should be provided by the polarisation dependence of the two-photon cross section; the Ω ratio discussed in Section 2.7. Fluorescence lifetime and intensity decay amplitudes for circularly polarised excitation are shown in Figure 2.18. These follow the same pattern as those following linearly polarised excitation. The variation in Ω calculated from the integrated fluorescence intensity with excitation wavelength is shown in Figure 2.17 together with the variation in $\alpha_{f(2)}$. The excitation wavelength dependence of Ω and $\alpha_{f(2)}$ appear uncorrelated.

In the 700-550 nm region where the interchange between $\alpha_{f(1)}$ and $\alpha_{f(2)}$ is most marked Ω shows a slight increase from ca. 0.6 to 0.7. As discussed previously, Ω is independent of the transition dipole moment direction, it is also independent

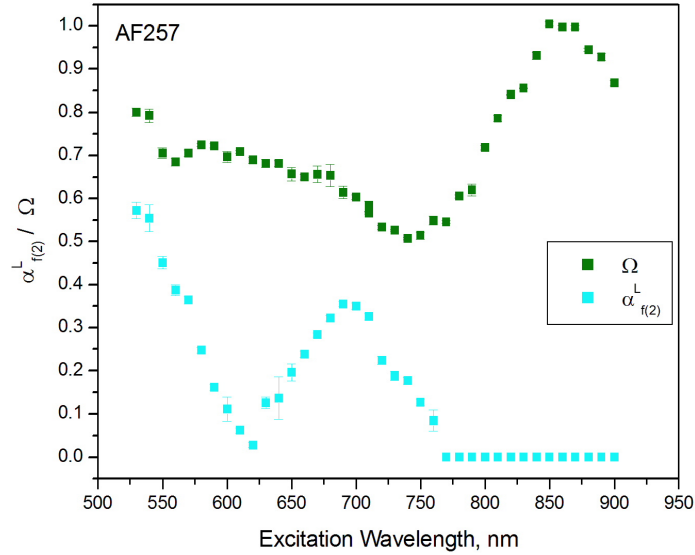


Figure 2.17: Calculated Ω following 2PA at different excitation wavelengths plotted with the amplitude of component 2. No correlation between the two data sets is seen.

of quantum yield variations provided these are similar for the states accessed by linearly and circularly polarised 2PA. The similarity in the lifetime decay dynamics (see Figure 2.18) is indicative of equivalent fluorescence dynamics.

The results so far are consistent with the model of two-photon excitation leading to two distinct emitting components rather than two separate excitation (single) emission routes. To test this hypothesis further it is necessary to calculate the polarisation dependence of the two decay components, that is to define Ω_1 and Ω_2 . The action cross section for each decay component is proportional to the products $\alpha_f \tau_f$

$$\Omega = \frac{\alpha_{f(1)}^C \tau_{f(1)}^C + \alpha_{f(2)}^C \tau_{f(2)}^C}{\alpha_{f(1)}^L \tau_{f(1)}^L + \alpha_{f(2)}^L \tau_{f(2)}^L} \quad (2.9.1)$$

where the suffixes C and L denote circularly and linearly polarised excitation respectively.

It is possible to calculate separate Ω values for each fluorescence lifetime component through introduction of a constant k to account for the possible differences in total

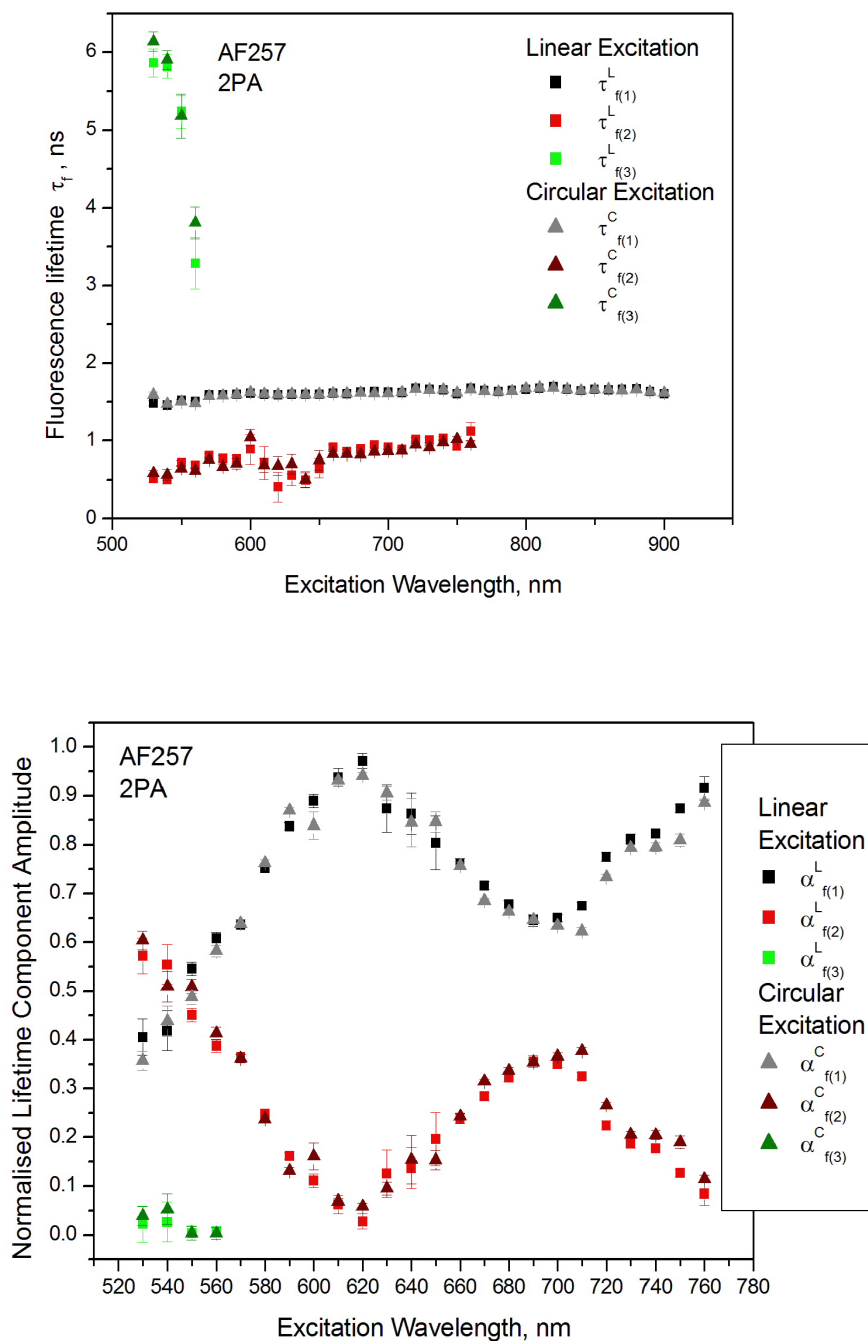


Figure 2.18: Fluorescence lifetimes and relative proportions of lifetime components following linear and circular excitation in the wavelength range 530-900 nm.

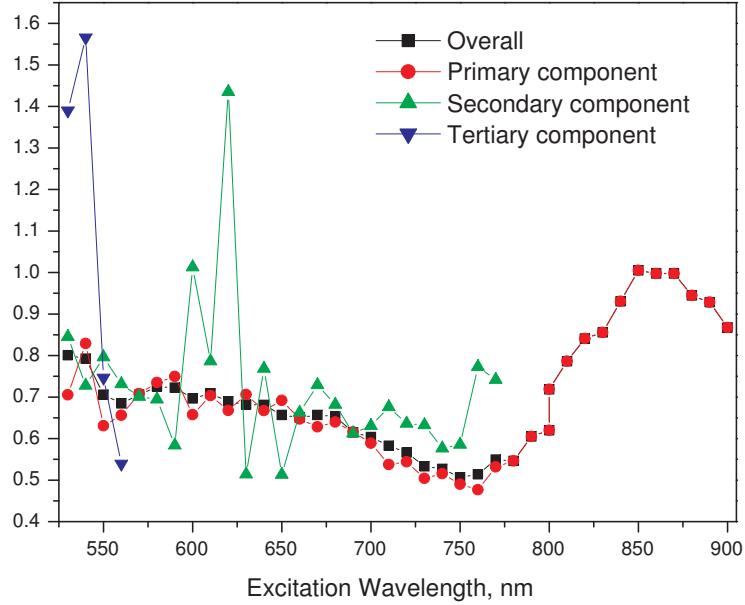


Figure 2.19: The values of the parameter Ω following 2PA for the two individual fluorescing species in the range 530-730 nm. Error bars on scale of point to point fluctuations of data points.

intensity between linearly and circularly polarised measurements

$$R_L = A\tau_1 - B\tau_2, \quad R_C = kA'\tau_1 + kB'\tau_2 \quad (2.9.2)$$

The constant k can then be adjusted such that

$$\Omega = \frac{A + B}{k(A' + B')} \quad (2.9.3)$$

The Ω values of the individual fractions can now be found simply as

$$\Omega_1 = \frac{A}{kA'} \quad \Omega_2 = \frac{B}{kB'} \quad (2.9.4)$$

The values of Omega for the two fluorescing species following 2PA are shown in Figure 2.19. It can be seen that apart from excitation wavelengths where α_2 is small, (690-650 nm), Ω_1 and Ω_2 have similar values and show the same wavelength dependence. When α_2 is small the uncertainties associated with determining Ω_2 are substantial. The observation of similar Ω values for both decay components are consistent with a common 2-photon excitation symmetry.

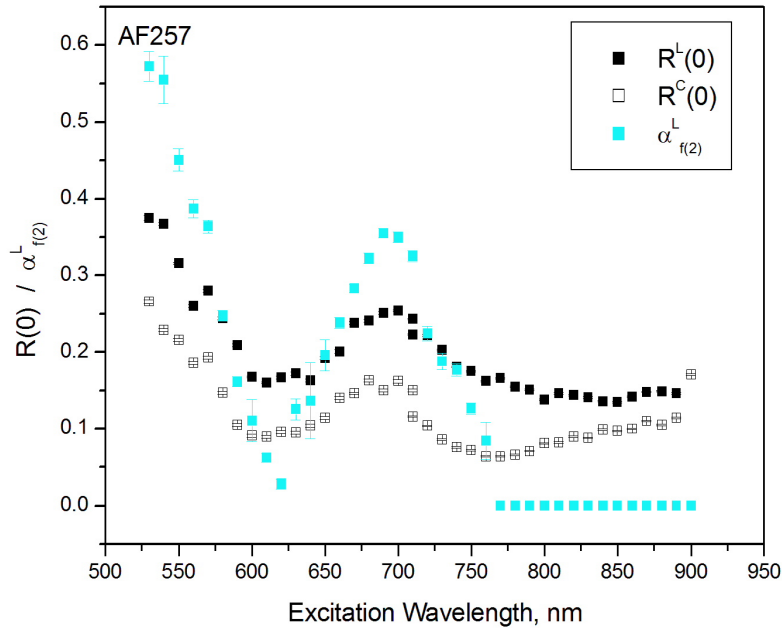


Figure 2.20: Measured initial anisotropy and proportion of second lifetime component following 2PA excitation in the range 530-900 nm.

2.9.4 Fluorescence Anisotropy Measurements

Fluorescence anisotropy decays were recorded for linearly and circularly polarised excitation between 530 and 900 nm using the excitation detection geometry shown in Figure 2.7; results are shown in Figure 2.20 along with the fluorescence amplitude of component 2.

Two photon excited fluorescence anisotropy decays were recorded for excitation wavelengths spanning 710-530 nm; fluorescence anisotropy decay data from 710-900 nm (un-analysed) had been previously obtained by Dr N Nicolau¹. The initial anisotropies for linear and circular polarisations $R_L(0)$ and $R_C(0)$ for this whole data set are shown in Figure 2.20. In the near infra red there is only a single lifetime decay $\alpha_{f(2)}(0) = 0$ and $R_L(0)$ shows a steady increase (850-770 nm) with increasing

¹ This data was collected by Dr N Nicolau during measurement of near infra red two-photon action cross sections for AF257 which formed part of an EPSRC funded collaboration with Dr K McEwan at DSTL.

excitation energy whilst $R_C(0)$ exhibits a more notable decrease (900-770 nm). At excitation wavelengths below 760 nm where a bi-exponential decay is observed, $R_L(0)$ and $R_C(0)$ are both strongly correlated with $\alpha_{f(2)}$. This behaviour indicates that the populations corresponding to the two decays possess different individual anisotropies.

One possibility to consider is that of contamination of the sample. This has previously been suggested as a reason for the increase of initial polarisation at longer excitation wavelengths in similar branched molecules [53]. If a small amount of contaminant were to be present with an emission spectrum peaking around 530 nm this could explain the third component $\tau_{f(3)}$ in the intensity decay occurring in this region. The pronounced rise in $R_L(0)$ and $R_C(0)$ at the shortest two photon excitation wavelengths is coincident with the detection of a third lifetime decay. However, the contribution of this third decay to the total fluorescence signal and the measured anisotropy is small ($\alpha_{f(2)} \approx 0.05$) and the initial anisotropy behaviour is dominated by the relative weighting ($\alpha_{f(1)}$ and $\alpha_{f(2)}$) of the two intense emission anisotropies.

Rotational correlation times were determined from single exponential fits to the anisotropy decays, and these are shown in Figure 2.21. These decay times are consistent with that expected for a molecule of this size. Low χ^2 values demonstrate a good fit to a single exponential throughout the full excitation range 530-900 nm; this implies that the anisotropy decays are dominated by one principle motion, to the extent that it is not possible to pick out any further decay components. A small variation (0.11 ns for linear and 0.17 ns for circular measurements) in this decay lifetime with wavelength can be seen. It appears that anisotropy decay times vary very little with relative proportions of the two components; this implies that the rotational times of the two components are similar if not identical. It is however possible that there might be a very small amount of correlation between rotational decay time and the proportion of the two components. A double exponential decay fit was attempted but offered no improvement in χ^2 value or measured residuals.

More insight into the anisotropy behaviour is produced by further analysis of

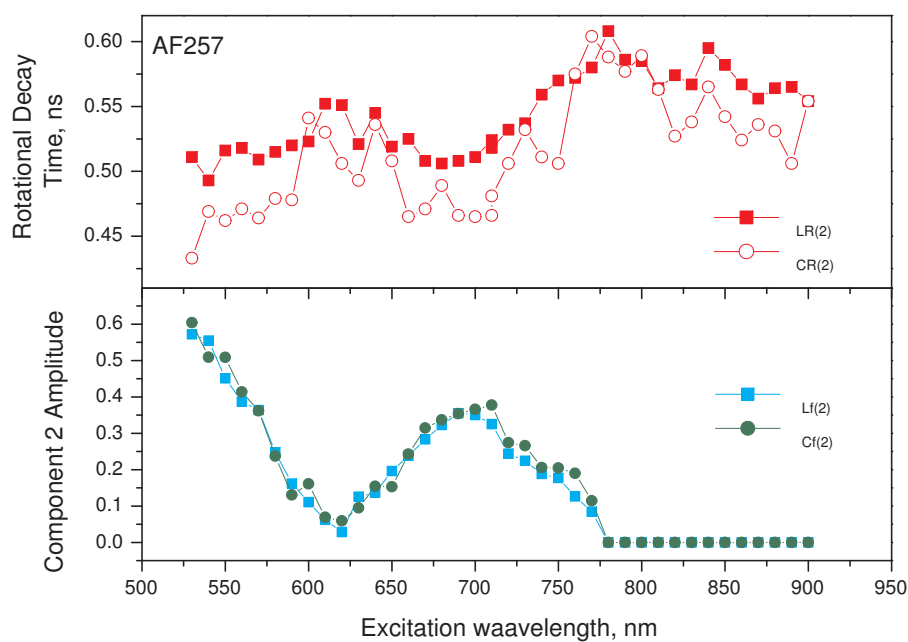


Figure 2.21: Proportion of the second fluorescence lifetime components in addition to anisotropy decay correlation times in AF257 following linearly and circularly polarised 2PA of 530-900 nm. Anisotropy decay times vary very little with relative proportions of the two components; this implies both components have similar rotational times.

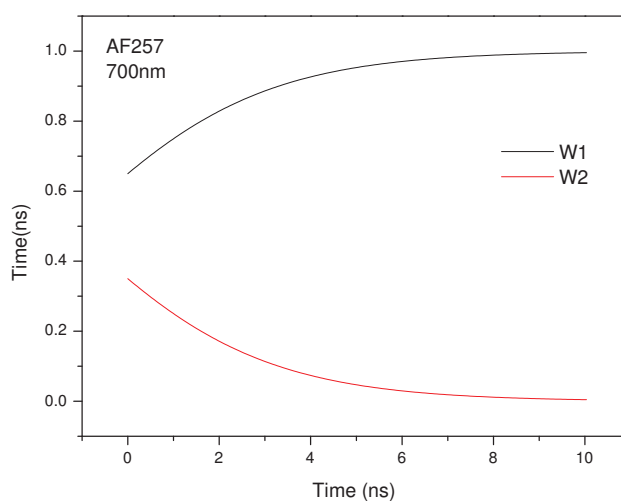


Figure 2.22: Relative weightings of the different fluorescing components involved in calculation of overall anisotropy following 700 nm 2PA.

the fluorescence anisotropy decays. In an inhomogeneous system the fluorescence anisotropy is given by [92]

$$R(t) = \sum_i W_i(t) R_i(t) \quad (2.9.5)$$

where i denotes the population component i with fluorescence anisotropy $R_i(t)$ and a time varying weighting $W_i(t)$. For equivalent fluorescence detection of the decay components $W_i(t)$ is given by

$$W_i(t) = \frac{N_i(t)}{\sum_i N_i(t)} \quad (2.9.6)$$

Combining Equations 2.9.5 and 2.9.6 yields

$$R(t) = \frac{\sum_i N_i(0) \exp[-t/\tau_{f(i)}] R_i(0)}{\sum_i N_i(0) \exp[-t/\tau_{f(i)}]} \quad (2.9.7)$$

where $R_i(0)$ is the initial (intrinsic) fluorescence anisotropy of component i whose subsequent time evolution is governed by the time correlation function $C_i(t)$. At $t=0$ $C_i = 1$ and as t becomes large, C_i tends to zero [93]. Even in a two component system differences between the individual amplitudes and decay times can lead to complex (non-exponential) behaviour. In AF257 this is not observed. $R_L(t)$ and $R_C(t)$ are well described by a single exponential decay time, whose variation with excitation wavelength (and $\alpha_{f(2)}$) is shown in Figure 2.20. When $\alpha_{f(2)} = 0$ the linearly polarised rotational correlation time shows no discernible wavelength variation with values between 550 and 600 ps; comparable rotational diffusion times have been observed for similarly sized branched chromophores in toluene [20]. With increasing $\alpha_{f(2)}$ there is a notable drop to ca. 500 ps at 500 nm; this value is maintained at shorter wavelengths with a rise to ca. 550 ps observed at 630-640 nm when the contribution of $\alpha_{f(2)}$ is small (ca. 0.05). A similar behaviour in τ_R^C is observed, the initial anisotropies obtained following circularly polarised photoselection are lower than in linearly polarised two photon absorption and the anisotropy decays thus have an inherently greater noise. This is reflected in the greater variation of τ_R^C in Figure 2.21 but the general trend in wavelength is the same as that for τ_R^L . A double exponential fit to both sets of anisotropy decays afforded no improvement in χ_R^2 or the measured residuals.

As discussed above the fluorescence anisotropy in a multi-component system can be sensitive to the time dependent weighting of the individual anisotropy components. A comparison between the anisotropy decays and lifetime components for excitation wavelengths of 700 nm (and 880 nm) are shown in Figure 2.22. At 700 nm, $\alpha_{f(2)} = 0.4$ and $\alpha_{f(1)} = 0.6$. At 880 nm $\alpha_{f(1)} = 1$ and $\alpha_{f(2)} = 0$. The variation of the weighting at 700 nm varies considerably over the course of the decay, whilst at 800 nm only the 1.5 ns decay component is present. It is thus reasonable to conclude that the rotational correlation functions $C_1(t)$ and $C_2(t)$ are similar in both emitting populations.

Whilst both states show similar orientational relaxation dynamics their intrinsic initial anisotropies appear to be quite different. Difference in the initial anisotropy of two-photon excited fluorescence can arise from a number of factors: differences in the structure of the two photon transition tensor that describes excitation to the emitting states, the orientation of the emission transition dipole moment in the molecular frame, and any sub-instrument response electronic reorganisation that may follow electronic excitation in branched molecules. These issues will be addressed below.

2.9.5 Transition Tensor Analysis

The initial anisotropy measurements $R_L(0)$ and $R_C(0)$ together with Ω each sample the elements of the transition tensor to a different degree. In the simplest case of a linear molecule with the emission transition dipole moment aligned along the molecular axis, $R_L(0), R_C(0)$ and Ω (independent of emission dipole moment orientation) are given by equations 2.7.15 to 2.7.18. In this approach the three quantities depend on two tensor parameters $S = S_{XX}/S_{YY}$ and $D = S_{XY}/S_{XX}$.

It is thus possible to define S and D from any two measurements of Ω and $R_L(0)$, Ω and $R_C(0)$, and $R_L(0)$ and $R_C(0)$ via the simultaneous solution to the appropriate pairs of equations 2.7.15 to 2.7.18. These values could then be used to assess the value for the third experimental observable parameter (the self-consistency of these results can be used to assess the validity of the model). This is carried out in stage

one of the transition tensor analysis.

Transition Tensor Analysis Stage One

The results of the comparison between observed and calculated values for $R_L(0)$, $R_C(0)$ and Ω as described above are shown in Figures 2.23 to 2.25 where the observed and predicted values of $R_L(0)$ and $R_C(0)$ are shown together with the corresponding values of S and D for the transition tensor and the deviation between the measured and predicted quantities. The mean and standard deviation of the three solutions for S and D calculated in this way are shown in Figure 2.26. In addition the standard deviation of S and D are compared with the root mean square (RMS) errors in calculating $R_L(0)$, $R_C(0)$ and Ω as shown in Figure 2.27. The RMS is calculated as opposed to the mean error such that positive and negative errors do not combine to yield a reduced error, giving a more accurate indication of the overall uncertainty in the model.

From Figures 2.23 to 2.25 it can be seen that the calculated $R_L(0)$ and $R_C(0)$ are consistently higher than those predicted by the model. For excitation wavelengths where a bi-exponential decay is observed the calculated values for both analogues show a similar wavelength variation. However, for the near infra-red excitation which yields a single exponential decay (900 nm) this does not hold, and a decrease in the calculated values of $R_L(0)$ and $R_C(0)$ is observed whilst the measured values remain approximately consistent. The agreement between the measured and calculated values of Ω show the closest agreement; Ω is independent of the molecular frame orientation of the emission transition dipole moment. The results thus far indicate that the planar model with the emission transition dipole moment oriented along the principal (X) axis of the transition tensor is the poorest description of the absorption tensor and emission dipole orientation for near infra red two photon excitation. The strong correlation between emission anisotropy (circular and linear) and the amplitude $\alpha_{f(2)}$ of the shorter (ca. 1 ns) decay component suggests that emission transition dipole orientation effects are likely to be a significant additional factor

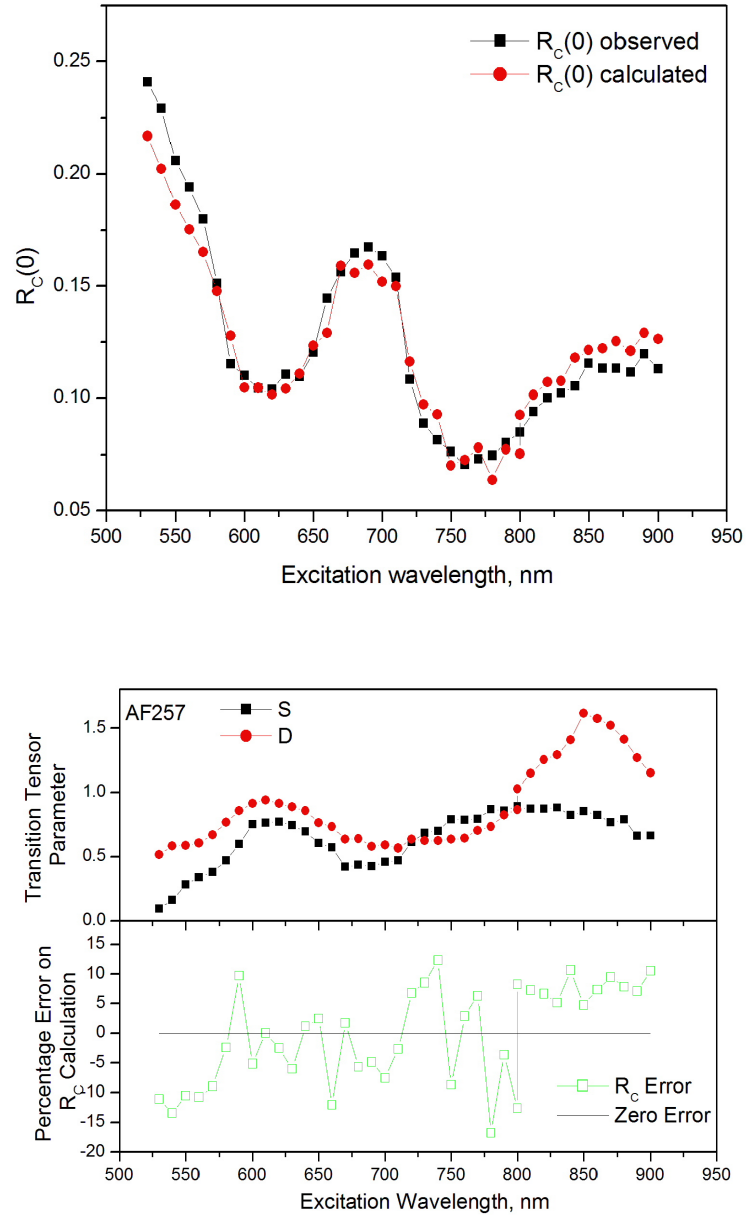


Figure 2.23: a) Wavelength dependence of observed and calculated values following 2PA in AF257 for $R_C(0)$. b) Wavelength dependence of two-photon tensor parameters S and D calculated using parameters Ω and $R_L(0)$. Percentage difference between $R_C(0)$ calculated subsequently using these S and D values and measured $R_C(0)$ plotted beneath; it can be seen that the model error is consistently higher in the single fluorescence lifetime region (770-900 nm). The mean of S in this region is $S = 0.82 \pm 0.08$; a value of $S = 1$ is not within the given error.

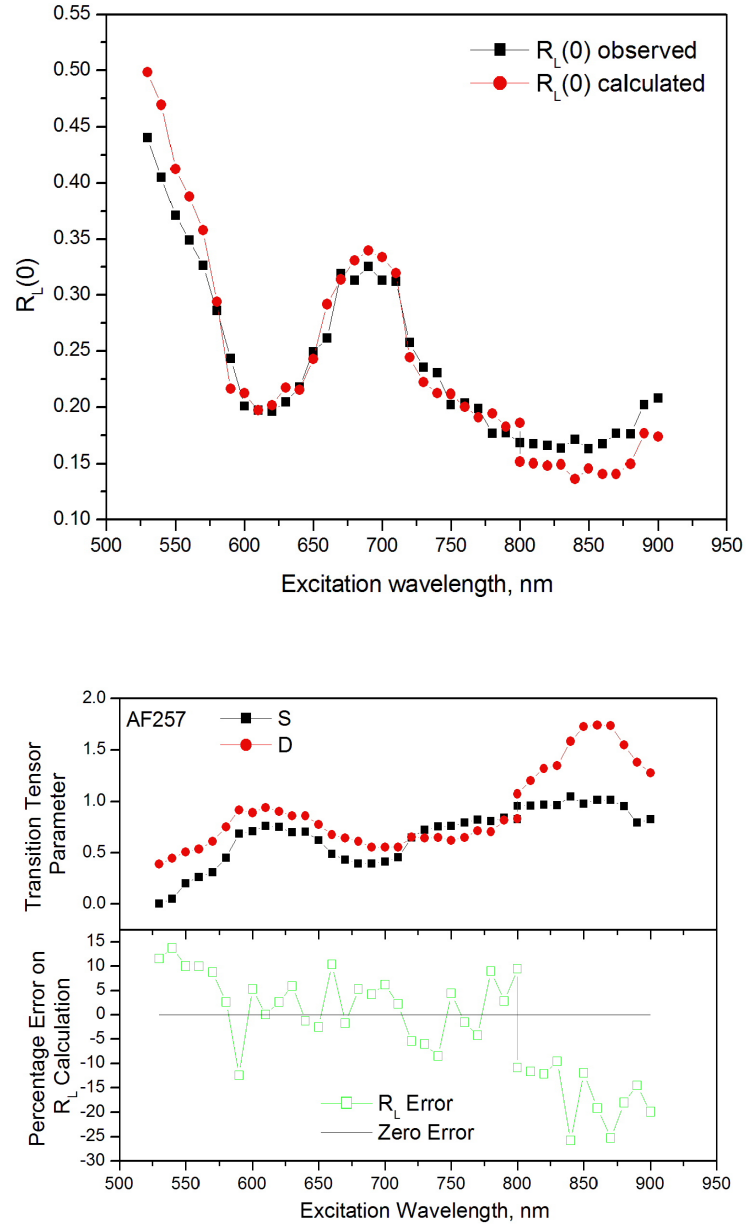


Figure 2.24: a) Wavelength dependence of observed and calculated values following 2PA in AF257 for $R_L(0)$. b) Wavelength dependence of two-photon tensor parameters S and D calculated using parameters Ω and $R_C(0)$. Percentage difference between $R_L(0)$ calculated subsequently using these S and D values and measured $R_L(0)$ plotted beneath; it can be seen that the model error is consistently higher in the single fluorescence lifetime region (770-900 nm). The mean of S in this region is $\langle S \rangle = 0.92 \pm 0.09 \approx 1$.

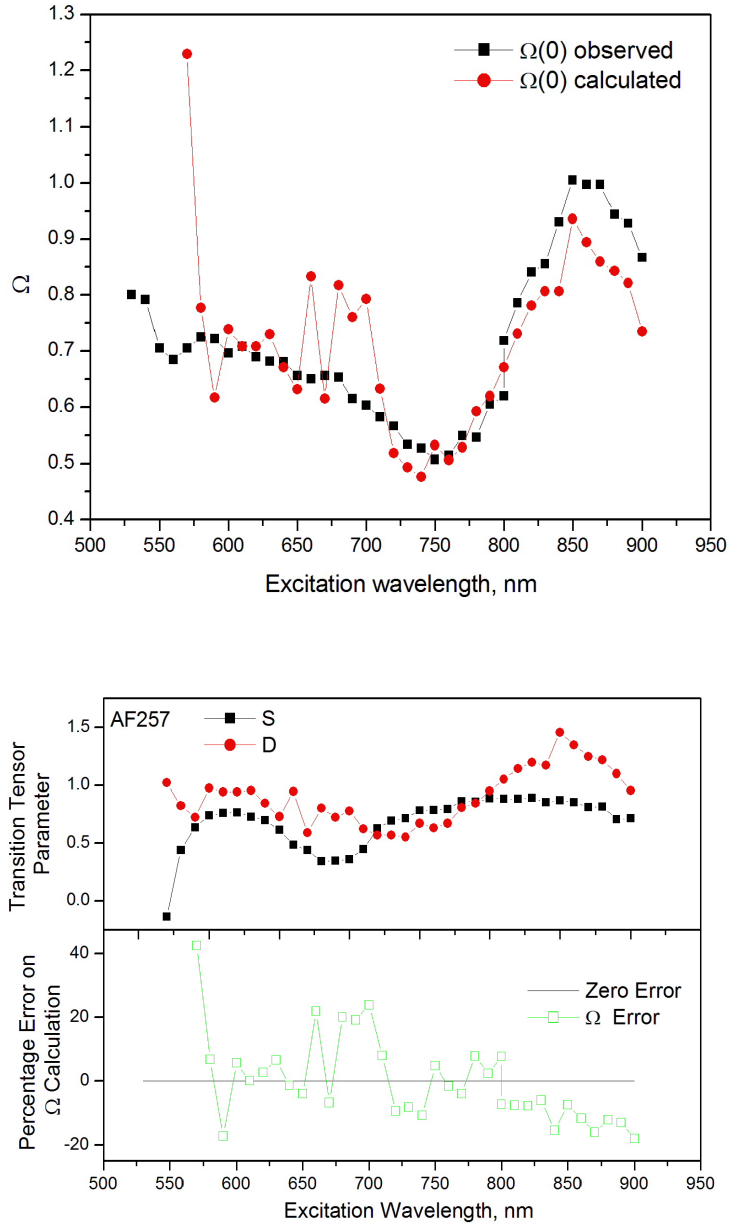


Figure 2.25: a) Wavelength dependence of observed and calculated values following 2PA in AF257 for Ω . b) Wavelength dependence of two-photon tensor parameters S and D calculated using parameters $R_C(0)$ and $R_L(0)$. Percentage difference between Ω calculated subsequently using these S and D values and measured Ω plotted beneath; it can be seen that the model error is consistently higher in the single fluorescence lifetime region (770-900 nm). The mean of S in this region is 0.84 ± 0.06 ; a value of $S = 1$ is not within the given error.

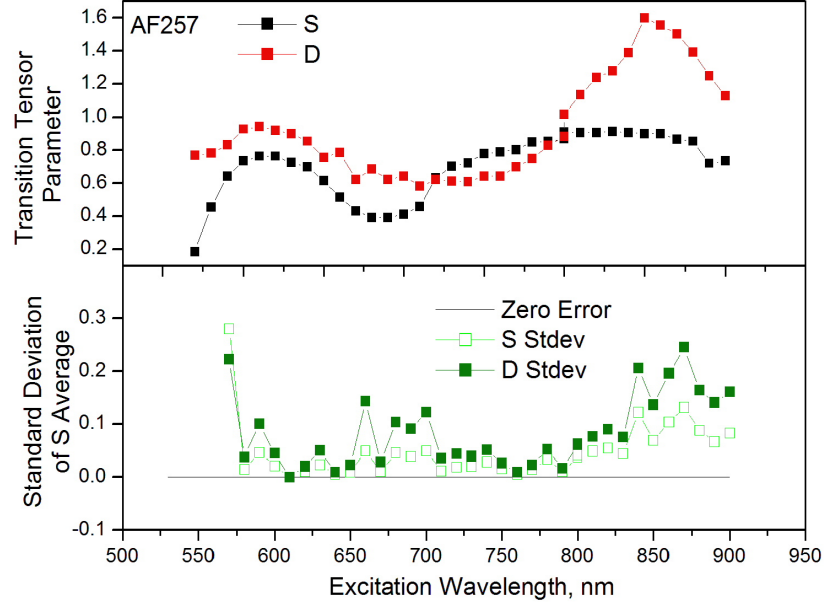


Figure 2.26: Wavelength dependence of the mean and standard deviation of the calculated two-photon tensor parameter D . It can be seen that the standard deviation in both S and D is relatively high in the single fluorescence lifetime region.

in emission from the two main states of AF257. These conclusions are borne out by the standard deviation in the calculated values of S and D , both of which are consistently higher across the near infra red.

In the near infra red the calculated value of S is close to 1. For a planar transition tensor with a transition dipole moment oriented at an angle of ϕ (to X) in the XY plane the two-photon initial anisotropy is given by

$$R_L(0) = \frac{1}{7} \left[\frac{1 + 18D \cos \phi \sin \phi}{2 + D^2} \right] \quad (2.9.8)$$

If the emission becomes averaged over the three branches of the system

$$R_L(0) = \frac{1}{7} \left[1 + \left(\frac{6D}{2 + D^2} \right) \left[\cos \phi \sin \phi + \cos\left(\phi + \frac{2\pi}{3}\right) \sin\left(\phi + \frac{2\pi}{3}\right) + \cos\left(\phi + \frac{4\pi}{3}\right) \sin\left(\phi + \frac{4\pi}{3}\right) \right] \right] \quad (2.9.9)$$

Irrespective of the planar angle ϕ the three angle dependent terms sum to zero giving

$$R_L(0) = \frac{1}{7} \quad (2.9.10)$$

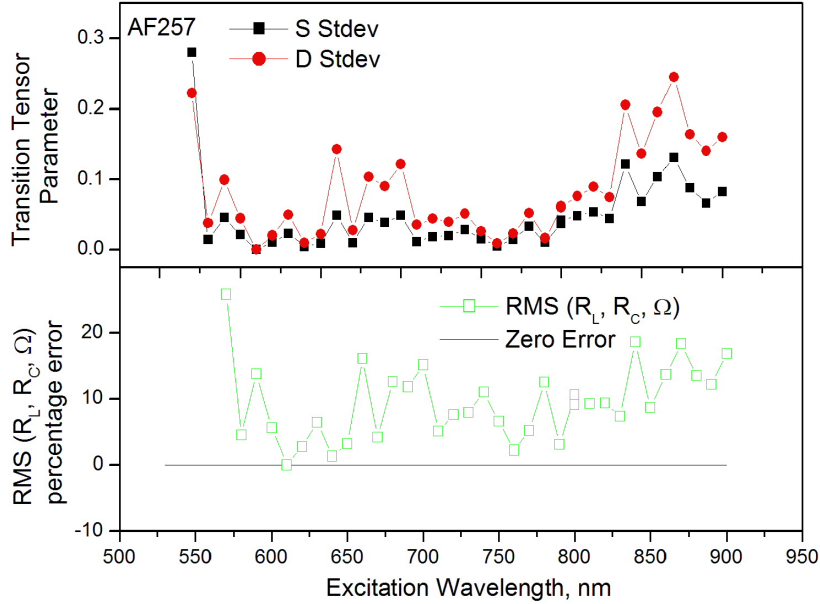


Figure 2.27: Standard deviation of calculation of tensor parameters S and D, in addition to RMS error in subsequent calculations of $R_L(0)$, $R_C(0)$ and Ω . All three values appear consistently higher in the single fluorescence lifetime region.

This is analogous to the ‘relaxed’ anisotropy of 0.1 observed for single photon excitation in branched chromophores [94]. Using this approach ($S = 1$, $R_L(0) = \frac{1}{7}$) Ω is used to calculate D and this value is then used to calculate $R_C(0)$. In this model the circularly polarised anisotropy is given by

$$R_C(0) = \frac{1}{7} \left[\frac{4 - 12D^2 - 12[4D \sin \phi \cos \phi]}{4 + 12D^2} \right] \quad (2.9.11)$$

Averaging the emission over three branches yields

$$R_C(0) = \frac{1}{7} \left[\frac{4 - 12D^2}{9 + 12D^2} \right] \quad (2.9.12)$$

which although independent of $R_L(0)$ retains a dependence on D.

Transition Tensor Analysis Stage Two

The analysis described above utilising the $S=1$ model is now applied to the molecule AF257; the assumption is made that the excitation is spread evenly on the three

branches such that $S=1$ and $R_L(0) = \frac{1}{7}$. Ω is then used to calculate D , and this value of D used to calculate $R_C(0)$. The percentage difference between the calculated and observed $R_C(0)$ is plotted in Figure 2.28, along with the percentage difference between the observed $R_L(0)$ and the assumed value of $\frac{1}{7}$. The proportion of the second lifetime component is plotted beneath. This analysis seems to give an $R_C(0)$ value much closer to the observed value in the single-lifetime region. In addition, there is now an extremely high correlation between the error on the calculated $R_C(0)$ value, and the proportion of the second fluorescence lifetime component, whereas there was no correlation beforehand. The fact that the $S=1$ model fits well in the single-lifetime region but fits less well when the second lifetime component is present implies perhaps that the major component follows the $S=1$ model, but that a different model is needed to describe the minor component.

Transition Tensor Analysis Stage Three

The third stage of analysis is to separate the contributions of each component to the values $R_L(0)$, $R_C(0)$ and Ω in order to apply the $S=1$ model to just component 1.

Contributions to $R_L(0)$ can be split into two components using a similar approach to that for Ω with the introduction of constants A_{L1} and A_{L2} .

$$R_L(0) = \frac{A_{L1}R_{L1}(0) + A_{L2}R_{L2}(0)}{A_{L1} + A_{L2}} \quad (2.9.13)$$

which can be rearranged to find the individual components

$$R_{L2}(0) = \frac{A_{L1}R_L(0) + A_{L2}R_L(0) - A_{L1}R_{L1}(0)}{A_{L2}} \quad (2.9.14)$$

Similar equations can be deduced for $R_C(0)$.

These separate $R_L(0)$, $R_C(0)$ and Ω , values can be used to calculate individual values of S and D for each component. For the primary component the $S=1$ model is used and D is calculated from $\Omega_1(0)$, while for the secondary component no such assumption is made and S and D are calculated using parameters $\Omega_2(0)$ and $R_{L2}(0)$.

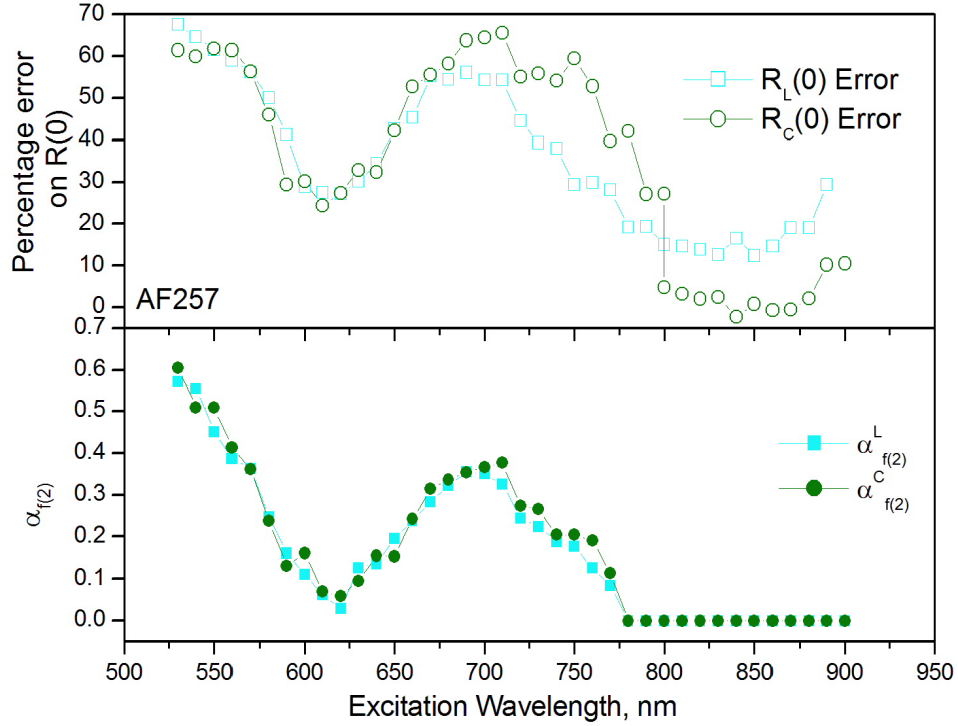


Figure 2.28: Percentage difference between calculated and observed $R_C(0)$ ($R_C(0)$ error), and between observed $R_L(0)$ and $\frac{1}{7}$ ($R_L(0)$ error), following the assumption that $S=1$. The proportion of the second fluorescence lifetime component at these excitation wavelengths is plotted beneath; a strong correlation between this and initial anisotropy can be seen.

The individual S and D values are shown in Figure 2.29² It can be seen that when a value of $S=1$ is assumed for the primary component, the secondary component returns values of $S \approx D \approx 0$, which exactly matches the behaviour expected in a linear molecule. Whilst there are other possible situations that might return such values, it is certainly possible that the secondary component is due to linear-like behaviour (i.e. 2PA and emission localised on one branch) that would occur should the intramolecular redistribution fail. The fact that slightly negative values are returned for the calculated D of the secondary component implies that there may be some slight systematic error, as D values cannot be negative.

² D^2 is depicted rather than D for the secondary component as the values are negative so the square root could not be found.

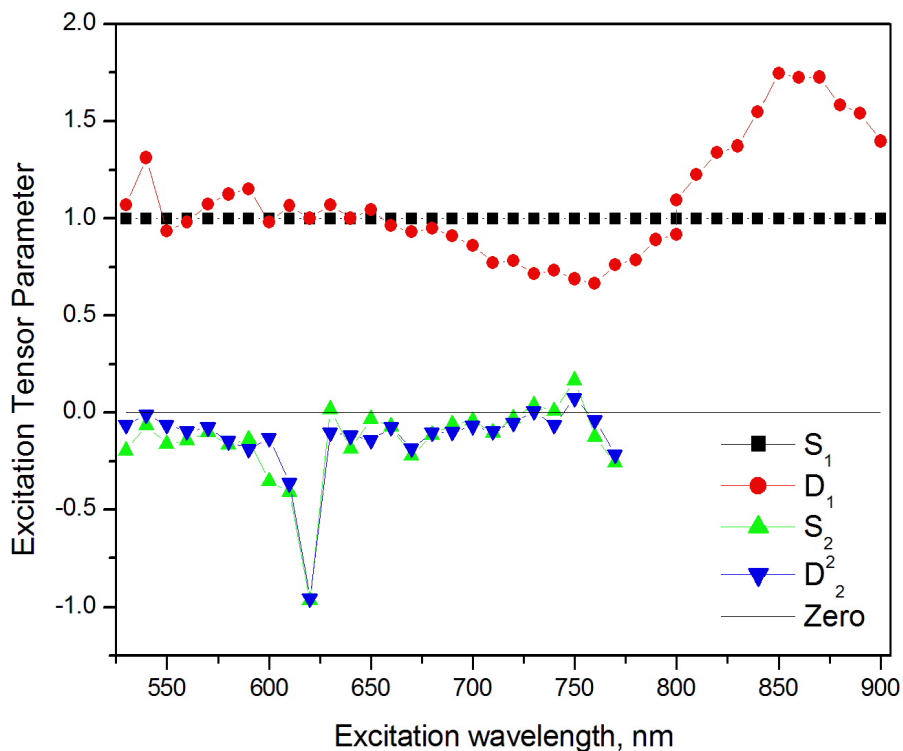


Figure 2.29: The values of the parameters S and D following 2PA for fluorescing component 1 (with model $S=1$), and the parameters S and D^2 for component 2; both following excitation in the wavelength range 530-900 nm. It can be seen that with the $S=1$ model used for the component 1, component 2 returns a value of $S \approx 0$: the behaviour expected from a linear molecule.

All anisotropy components were calculated from the relevant S and D component values (with $S=1$ for the primary component), and are shown in Figure 2.30 (linear) and 2.31 (circular). It can be seen that the ‘overall’ $R_L(0)$ value breaks down into two largely wavelength independent components when true analysis is applied in this way following both linear and circular excitation, though this is more marked in the case of linear excitation.

An alternative calculation of $R_{C2}(0)$ was then found using $R_{C2}(0) = R_C(0) - R_{C1}(0)$. The percentage difference between this and the previous calculated value of $R_{C2}(0)$ from S_2 and D_2 is plotted in Figure 2.32 and can give an indication of the accuracy

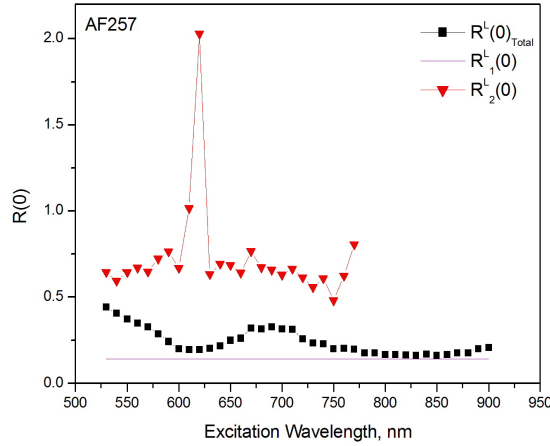


Figure 2.30: Initial anisotropy values in AF257 for the two individual fluorescence lifetime components in addition to the overall initial anisotropy values following linear excitation in the wavelength range 530-900 nm. It can be seen that the wavelength dependence evident in the overall $R_L(0)$ value largely disappears in the second component when the first component is set to $S=1$ (i.e.. $R_L(0) = \frac{1}{7}$.)

of this individual component. The percentage difference between the calculated value of $R_{C2}(0)$ (direct from S_2 and D_2 method) and the linear molecule expected value $R_{C2}(0) = \frac{2}{7}$ is also plotted, along with the percentage difference between the calculated value of $R_{L2}(0)$ and the linear molecule expected value of $R_{L2}(0) = \frac{4}{7}$. The three error plots now show very little variation with wavelength: the correlation of error with the proportion of the second fluorescing component has been broken.

From Figures 2.30 and 2.32 it can also be seen that the values of $R_{L2}(0)$ are calculated as above $R_{L2}(0) = \frac{4}{7}$ which is not possible for linear-molecule-like behaviour. However, the value of $R_{L1}(0)$ would not have to be raised very much in order to bring $R_{L2}(0)$ below the maximum allowed value of $R_{L2}(0) = \frac{4}{7}$. The fact that all three plots in Figure 2.32 show little variation with wavelength implies that there exist two emitting states which are independent of excitation wavelength, and that only the relative proportions of these two emitting components varies with wavelength.

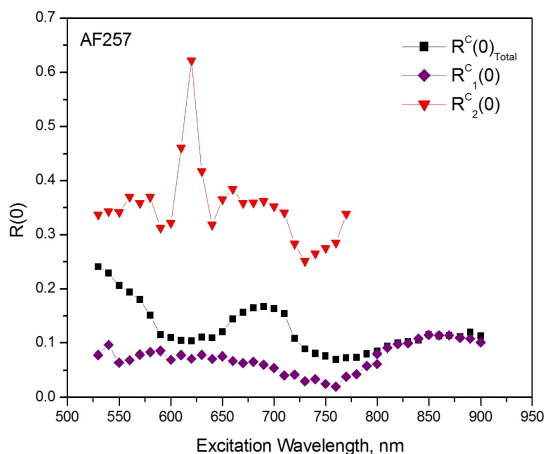


Figure 2.31: Initial anisotropy values in AF257 for the two individual fluorescence lifetime components in addition to the overall initial anisotropy values following circular excitation in the wavelength range 530-900 nm. It can be seen that the wavelength dependence evident in the overall $R_C(0)$ value largely disappears in the second component when the first component is set to $S=1$ (i.e. $R_C(0) = \frac{1}{7}$.)

2.9.6 Discussion

It has been demonstrated that in the trigonal planar branched molecule AF257 there exist up to three fluorescence intensity decay components.

A substantial systematic difference in the behaviour of AF257 has been shown following 2PA in the wavelength region where there exists a single fluorescence lifetime component (780-900 nm) to that of the behaviour in the region of 2-3 fluorescence lifetime components (530-770 nm). This can be seen in the change to accuracy of fit to the four-element absorption transition tensor model (i.e.. reduction of the transition tensor to four elements). The accuracy of fit of this model was determined through use of the model to predict the third parameter after solving the equations for two of the parameters $R_L(0)$, $R_C(0)$ and Ω and comparing the calculated values to observed values for the third parameter. The accuracy of the model can be seen to be different in the two excitation wavelength regions in Figures 2.23 to 2.27. This analysis worked well to predict the behaviour of the branched trigonal

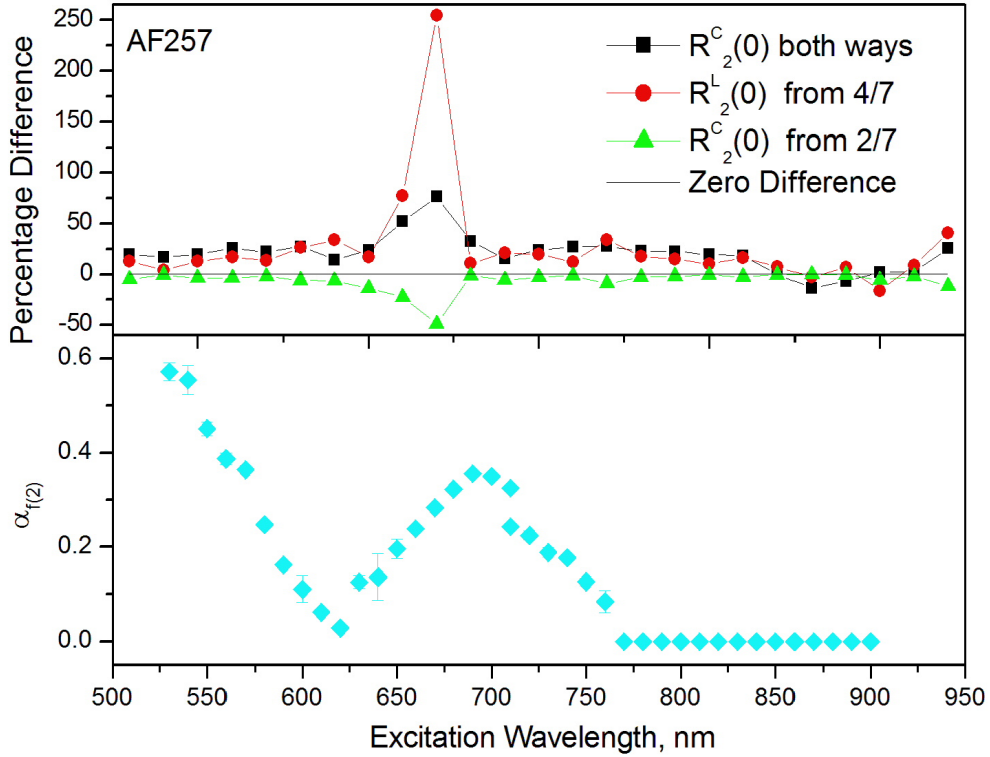


Figure 2.32: The percentage difference of $R_{C2}(0)$ calculated from S_2 and D_2 , and calculated from $R_{C2}(0) = R_C(0) - R_{C1}(0)$ following circularly polarised excitation in the region 530-770 nm. Also shown is the percentage difference of $R_{L2}(0)$ from $\frac{4}{7}$ following linear excitation, and $R_{C2}(0)$ from $\frac{2}{7}$ following circular excitation in the wavelength range 530-770 nm. These values give an idea of the quality of fit of the S=1 model applied to the first component and S=0 model applied to second component. It can be seen that the error of this combined model no longer correlates with the proportion of component 2.

molecule OM77 [64] in experiments completed previously within the group, with all three pairs of parameters predicting a value of the third parameter close to the observed value. It also resulted in a calculated value for S in OM77 of S=1; this reflects an equivalence in the 2PA transition tensor of the X and Y directions in the molecular plane. In OM77 it was therefore implied that a randomisation process occurred during or following excitation before emission took place.

There is a large variation in initial anisotropy parameters $R_L(0)$ and $R_C(0)$ with

wavelength following 2PA of 530-770 nm, while the initial anisotropy values following linearly polarised 2PA of 780-900 nm are relatively constant. A further model of the transition tensor was then applied such that tensor parameter $S=1$, as was the case in OM77. This had the result of reducing the tensor model error substantially in the excitation region 780-900 nm, with the remaining model error correlating extremely closely with the proportion of the second fluorescence lifetime component. This can be seen in Figure 2.28.

It is known that two fluorescing species occur following 2PA in AF257 as two fluorescence lifetimes are observed for excitation region 530-770 nm. An attempt was then made to separate the effects of each species on parameters $R_L(0)$, $R_C(0)$ and Ω . Each of these parameters was split into two components: a primary component present under excitation 530-900 nm with an assumption of equal excitation in both X and Y directions of the molecular plane, and a secondary component present under excitation in the range 530-770 nm with no assumptions made. This removed the wavelength dependence of the initial anisotropy parameters; both primary and secondary components were then independent of wavelength, with only the proportions of the two components showing a wavelength dependence. This model returned values for S_2 and D_2 of close to zero, which reflects the behaviour expected in linear molecules that have a transition dipole moment rather than a transition tensor. The fact that the values of D are in fact slightly negative must mean that there is a systematic error occurring, as it is not possible for tensor parameters S or D to return negative values. Possible systematic errors include a variation in excitation beam properties with wavelength such as beam diameter, position or pulse length, or generation of an imperfect circular polarisation.

It therefore appears that AF257 may consist of a primary component with excitation randomisation behaviour similar to that in OM77, plus a second component with behaviour similar to that of a linear molecule. The fact that the $S=1$ model fits well for the first component indicates zero correlation between absorption and emission, while the $S=0$ value returned for the second component indicates a strong correlation

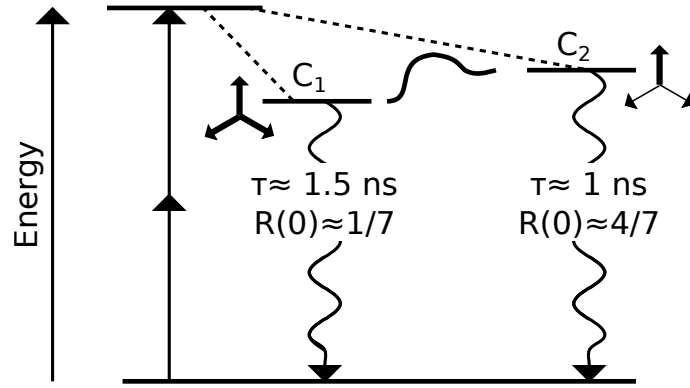


Figure 2.33: The proposed model for the absorption-emission mechanism in AF257 following 2PA. A common absorption mechanism results in two independent emitting states, each with differing fluorescence lifetimes and anisotropy properties. The initial anisotropies measured are consistent with a depolarisation through randomisation of excitation energy among the branches (component 1) and a lack of randomisation process with the excitation energy located on a single branch (component 2). The two emitting states are separated by either an energy gap or an energy boundary (both are depicted in the Figure).

between absorption and emission.

The fact that the values of Ω are very similar for both components (see Figure 2.19) indicates that the absorption process of each component is similar, and that the differentiation occurs following absorption. The two components are likely to have differing quantum yields, but it can be seen in Figure 2.28 that the proportions of each component are very similar following linearly and circularly polarised excitation; the same variations with wavelength (which are substantial) occur with both. This supports the accuracy of the observed Ω values which can only be calculated accurately from $R_L(0)$ and $R_C(0)$ if the quantum yields of the two excitation polarisations are the same. But it also lends credence to the possibility that the absorption process is very similar for both components.

From the results obtained in this chapter thus far, a model is proposed as to the behaviour of AF257 on absorption of two-photon excitation. This is summarised in Figure 2.33. A common absorption mechanism results in two independent emitting states, each with differing anisotropy properties. The fact that the second

component is not observed following excitation to the red of 760 nm suggests that the emitting energy level of this component is either slightly higher than that of component 1 or that there exists an energy boundary between the two emitting levels. However, it is not thought that ‘red edge effects’ sometimes seen in branched molecules as described earlier in the chapter are the reason for the lack of observation of component two as the range over which component 2 is not observed spans a large section of the 2PA spectrum, not just the ‘red edge’; these effects are commonly seen over a shorter portion eg. at most 10-25 nm of the excitation spectrum [55, 56] rather than over 130 nm as is observed here.

The differing proportions of the two components has implications for the measurement of 2PA cross-section. Unless the quantum yield of the two components were identical, the varying proportions with wavelength would be expected to affect the cross-section significantly. It can be seen in Figure 2.34 that there is the possibility of a correlation between a higher proportion of the second component and a lower cross-section.

As can be seen in Figure 2.35 the 1PA correlates with the 2PA when the 1PA is plotted at equivalent energy (double the wavelength). Although the correlation is not perfect, it can be seen that in regions where the 1PA is zero, the 2PA is zero; in regions where 1PA is high the 2PA is high, and in regions where 1PA is low the 2PA is low. This could also provide a reason for the variation in 2PA with wavelength (as opposed to the proportion of the second component being a contributing factor) In previous experiments within the group on other branched chromophores such as OM77 [64], the 2PA cross-section can be seen to dramatically increase as the excitation wavelength approaches the 1PA region, but this behaviour is not seen here in AF257; possibly this is because of the increased proportion of the second lifetime component. If the emitting states are similar (i.e. have similar oscillator strengths) it would be expected that the quantum yield for the second component would be lower due to its shorter fluorescence lifetime; non-radiative decay pathways resemble shortening of the fluorescence lifetime whilst reducing the quantum yield.

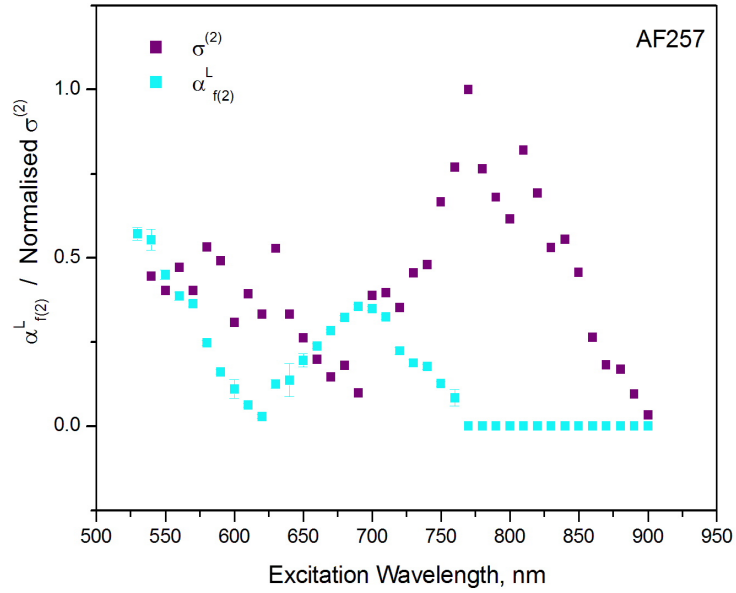


Figure 2.34: 2PA cross-section and proportion of fluorescence lifetime component $\tau_{f(2)}$: all following 2PA. A lack of correlation between the two is shown.

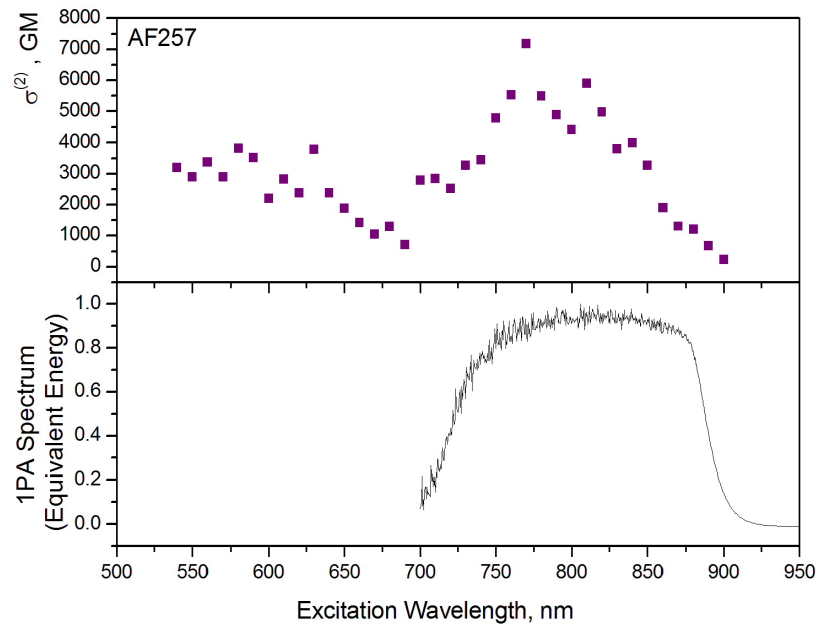


Figure 2.35: Measured normalised 1PA spectrum and 2PA cross-section for AF257. The 1PA spectrum is displayed at equivalent energy to the 2PA i.e.. at double the wavelength. The two spectra appear to correlate loosely.

In light of these suggestions as to the origin of observed behaviour, it is possible to reassess the measured anisotropy decay correlation times which all showed a good fit to a single lifetime following 2PA. A component with C_3 symmetry that undergoes redistribution of excitation in the excited state would present a single rotational correlation time due to out-of-plane rotation, as in-plane rotation would have no effect on the anisotropy decay. However, a component that did not undergo such redistribution would show both in-plane and out-of-plane rotation and thus fit to a double exponential decay with two rotational correlation times. With this in mind, anisotropy decay correlation times are plotted against the proportion of the second fluorescence lifetime component in Figure 2.21. Although there might be a slight difference in the amounts of each rotation following linearly and circularly polarised excitation, the difference induced between $\tau_{LR(2)}$ and $\tau_{CR(2)}$ due to this extra rotational lifetime in the minority component would be small and difficult to resolve. It is possible that there is a small correlation between proportion of component 2 and increased difference in $\tau_{LR(2)}$ and $\tau_{CR(2)}$ values.

If the two emitting species of AF257 share similar energy levels before and after emission, it would be expected that the fluorescence lifetimes of the two species would also be similar. One possibility is that the emission of the two species does occur between similar energy levels, but that one of the species also has a non-radiative decay pathway, causing the fluorescence lifetime to shorten. It is not possible to test this using anisotropy measurements as described in this chapter, but it would be possible to investigate this using the technique of STED. With continuous wave (CW) STED it is possible to distinguish between the radiative and non-radiative decay rates by noting the observed reduction in the fluorescence lifetime as CW STED effectively increases the radiative rate in proportion to the depletion intensity. Differences between the radiative rates of two spectrally indistinguishable states can thus be obtained. Details and applications of this novel technique are given in the next chapter.

2.10 1PA Measurements

Similar measurements were made of AF257 following 1PA to investigate the photophysical behaviour further. With the existence of two emitting states following 2PA it was expected that two states would also be observed following 1PA if similar absorption and emission processes take place. Single-photon excited fluorescence of AF257 was measured following excitation at wavelengths of 470-500 nm. The detection filters used were a LS650 short pass filter, and a LS700 short pass which was used to block any remaining infra-red in the excitation pulse. On increasing the wavelength in the 1PA regime, the first sign of non-linear 2PA occurred at 510 nm, so results for excitation with wavelengths longer than 500 nm were discarded. The fluorescent lifetime of AF257 was measured following single-photon excitation of 360-500 nm as shown in Figure 2.36. The fractional contributions of each fluorescence lifetime component are shown following 1PA in Figure 2.37. It can be seen the the fluorescence lifetime behaviour following 1PA is more complex than that following 2PA; there is a growth in fluorescence intensity between 380 and 430 nm excitation which was not observed following 2PA at the equivalent excitation energies (760-860 nm). 1PA and 2PA must therefore excite different transitions.

In 1PA the anisotropy decays are not so straightforward as those following 2PA - there appear to be a number of decay components that vary in magnitude over the wavelength range 360-500nm. Using the fitting software FluoFit, it was found that following 1PA three lifetimes appeared repeatedly (although the amplitude of one of these lifetimes was negative from excitation wavelengths 380-430 nm and positive for the remaining wavelengths used) such that it was decided to perform a global analysis of each anisotropy decay to three exponential decays for all in the region 360 nm - 500 nm. This gives the three lifetimes for the decay components as 0.549 (+0.012 -0.006) ns, 0.093 (+0.023 -0.019) ns and 2.510 (+0.850 -0.660) ns. A global analysis was considered justified as tests showed that individual fits pick out one, two or three of the same decay lifetimes to within error as those picked out from the global fit - some examples of this are given below. Figure 2.39 plots the

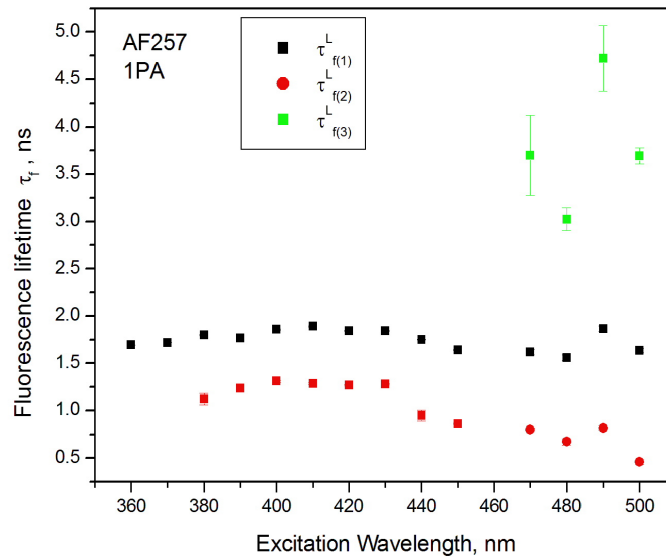


Figure 2.36: Measured fluorescent lifetimes for AF257 following single photon excitation of 360-500 nm. Similar to the results following 2PA regions with one, two and three fluorescence intensity decay components can be seen.

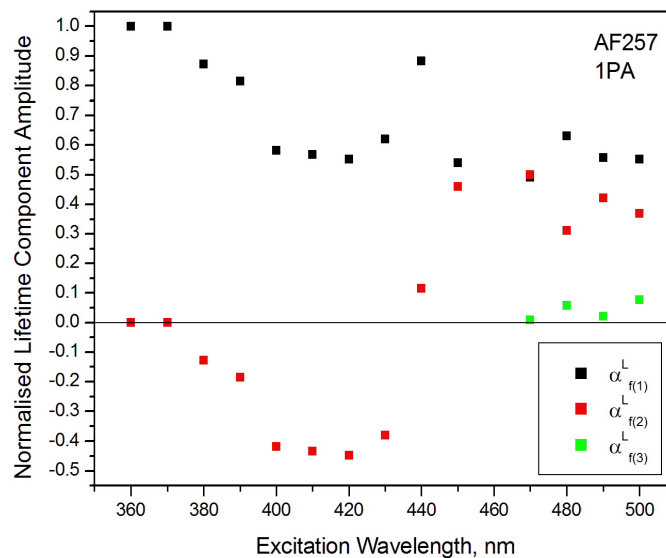


Figure 2.37: Fractional contributions of measured fluorescent lifetimes following for AF257 following single-photon excitation of 360-500 nm. A growth can be seen following 380-430 nm excitation that is not observed following 2PA.

initial anisotropy of these three components: this is the amplitude of each lifetime component (for some of the excitation wavelengths one or more of these decay times have zero amplitudes).

Due to the degree of subjectivity in deciding the number of exponential decays to fit to, some examples of the 1PA anisotropy decays are given in Figure 2.38 to show the fitting method. It can be seen in Figure 2.38(a) that at 360 nm there is a good fit to a single exponential, with no shape to the residual. When fitted individually a decay time of 0.540 (± 0.006) was returned, matching the main global fit time to within errors. For the individual fit the χ^2 value was 1.197, while the global triple exponential fit χ^2 value was very similar at 1.191. The individual double fit (for comparison) gave a χ^2 value of 1.163 - not significantly lower. For these reasons the anisotropy decay at 360 nm was taken to fit to a single exponential decay, or equivalently to a global triple exponential decay with zero values of the amplitude of two of the decay components.

The anisotropy decay at 400 nm is shown as an example of a double exponential decay including a longer additional lifetime. A fit to a single exponential (2.38(b)) can be seen to fit badly with a discernible shape to the residual, and returned a lifetime of 0.618 (± 0.018) ns and χ^2 value of 1.532. A fit to a double exponential (2.38(c)) returns decay times of 0.521 (+0.044 -0.080) ns and 2.96 (+6.72 -2.50) ns with a χ^2 value of 1.148. The χ^2 value is significantly reduced from that of the single fit, and both decay lifetimes are now within given error to those found when fitting to a global triple decay. The global triple decay returned a χ^2 value of 1.169. For these reasons the anisotropy decay at 400 nm was taken to fit to a bi-exponential decay, or equivalently to a global triple exponential decay with a zero value of the amplitude of one of the decay components.

The anisotropy decay at 470 nm is shown to fit badly to a single exponential (2.38(d)) for which a decay time of 0.514 (+0.006 -0.005) ns and a χ^2 value of 2.457 is returned. A fit to a double exponential (2.38(e)) gives the times 0.549 (+0.015 -0.011) ns and 0.093 (+0.043 -0.093) and a much lower χ^2 value of 1.267. A fit to a triple exponential

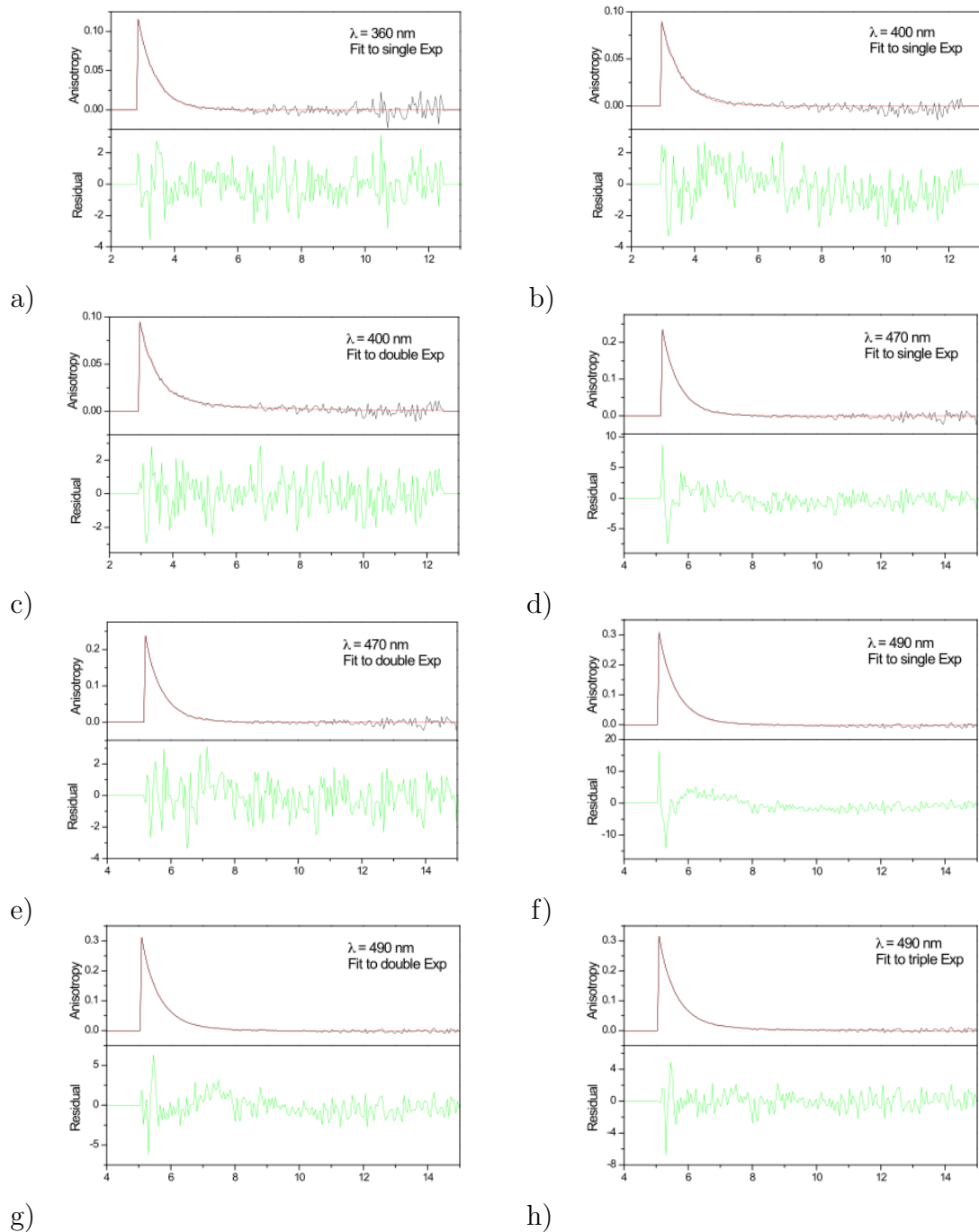


Figure 2.38: Anisotropy decays (black) and best fits (red) as calculated by the program FluoFit for certain excitation wavelengths. The respective fit residuals (green) are shown below these. Examples given are a) An example of a good fit to a single exponential decay, b) An example of a bad fit to a single exponential decay, c) An example of a good fit to a double exponential decay with a slow component in addition to the main component d) An example of a bad fit to a single exponential decay, e) An example of a good fit to a double exponential decay with a fast component in addition to the main component, f) An example of a bad fit to a single exponential decay, g) An example of a bad fit to a double exponential decay, h) An example of a good fit to a triple exponential decay.

gives a marginally lower χ^2 value of 1.259, but since there is already no shape to the residual for a double exponential fit, it cannot be said with certainty that there is a third exponential component. However, when fit to a triple exponential decay the third time returned matches to within error the second time returned for the double exponential fit at an excitation wavelength of 400 nm, although the amplitude of this component is very low. So considered as part of the group 360 - 500 nm the case for a third decay component looks more compelling.

The anisotropy decay at 490 nm is an example of those decays which appear to only fit well to a triple exponential decay. A fit to a double returns the decay times 0.192 (+0.095 -0.061) ns and 0.626 (+0.060 -0.027) ns with a χ^2 value of 2.004. The residual shows some definite shape. Fitting the decay to a triple exponential returns the times of 0.53 (+0.033 -0.200) ns, 0.076 (+0.010 -0.031) ns and 1.77 (+2.000 -0.800) ns with a χ^2 value of 1.476. This has fit to the main decay component, plus the slow component seen in the 400 nm double exponential fit, plus the fast decay component seen in the 470 nm fit; all to within errors. The large reduction in χ^2 along with the change in the residual give a high degree of certainty that this decay has three components.

In an effort to deduce the possibility of these two components creating an apparent third anisotropy decay component due to conversion of one to the other, the two decays were modelled in Mathematica by Dr R. Marsh. The simple program allowed variation of fluorescent lifetimes, amplitudes and interconversion time of the two components. However, it was found that no combination of possible inputs resulted in a spurious third rotational decay component.

A summary of the initial anisotropy values following 1PA is shown in Figure 2.39.

The initial anisotropy will solely reflect the anisotropy of the decay components that are initially present; by definition the growth in the fluorescence intensity will not contribute to the initial anisotropy values. The next stage of analysis attempts to isolate contributions to the anisotropy from the two main fluorescent components as was performed in the analysis of 2PA excited AF257. Possible correlations between

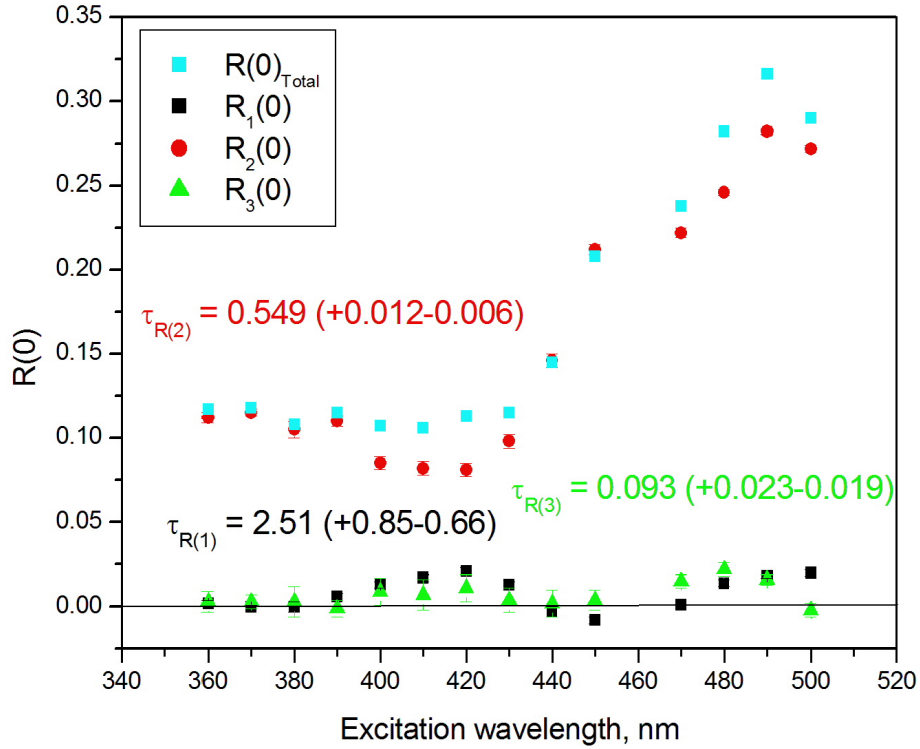


Figure 2.39: Measured results following 1PA for excitation wavelengths 360-450 nm and 470-500 nm. The times shown on the figure are those given by the global fitting process. It can be seen that the anisotropy decay following 1PA is significantly more complicated than that following 2PA.

the initial anisotropy values and the relative magnitudes of the fluorescence decay components were examined. Due to the small regions of the 1PA spectrum that produced a double fluorescence decay an analysis across the absorption spectrum like that carried out following 2PA was not possible, however this analysis was attempted for the anisotropy following excitation at 450 nm. When 0.1 (the theoretical anisotropy following 1PA when the excitation is distributed over the three branches), the resulting anisotropy of the second component is 0.422; slightly above the limit of 0.4 for a linear molecule, reflecting the overall error of the measurement. When the average initial anisotropy of the points at which there is a single anisotropy decay (0.12) is used, the resulting anisotropy for component 2 is 0.399. Although this

analysis was only possible for this point, this does strongly corroborate the evidence found following 2PA that there exist two emitting states with differing anisotropy properties.

2.10.1 Discussion

Fluorescence lifetime and anisotropy studies of AF257 have been carried out following 1PA at wavelengths of 470-500 nm. This data has been added to data previously collected following excitation at 360-450 nm By Dr N. Nicolau within the group and the full dataset has been analysed. The fluorescence intensity decay has been found to feature two decay components for the region 380-500 nm with the lifetimes $\tau_{f(1)} \approx 1.5$ ns and $\tau_{f(2)} \approx 0.5-1.25$ ns, with an additional third component in the region 470-500 nm with a lifetime of $\tau_{f(3)} \approx 3-6$ ns. Measurements of the anisotropy decay have found up to three decay components in the 1PA region with lifetimes $\tau_{a(1)} = 0.549(+0.012, -0.006)$ ns, $\tau_{a(2)} = 0.093(+0.023, -0.019)$ ns and $\tau_{a(3)} = 2.510(+0.850, -0.660)$ ns. The two additional anisotropy decay components in the 1PA region both have maximum amplitudes at 400-430 nm, and 480-490 nm. The region 400-430 nm is of particular interest as this corresponds to two intensity decay components but three anisotropy decay components. The other factor to consider is the rise in initial anisotropy from around 0.1 at shorter excitation wavelengths to around 0.5 for longer wavelengths including those inducing 2PA. This rise begins at around 440 nm.

In the region where a single lifetime is observed following 360 and 370 nm excitation, the behaviour looks similar to that following 2PA in the region where a single fluorescence lifetime is observed (770-900 nm) in that the lifetime is around 1.5 ns a rotational decay time of 0.6 ns is seen, and the anisotropy is consistent with excitation shared between the three branches (as following 2PA the anisotropy is just very slightly higher than this). Thus the emitting state following 1PA at 360-370 nm appears similar to that following 2PA at the longer wavelength 770-900 nm; the shorter wavelength end of the 1PA absorption spectrum results in similar behaviour

to that the longer wavelength end of the 2PA spectrum. The excitation wavelengths resulting in similar behaviour do not correspond in energy.

At excitation wavelengths of 440 nm and longer, where the second fluorescence lifetime component is seen, the behaviour is similar to that following 2PA in the region where two components are seen; the initial anisotropy increases with proportion of component 2 towards a value consistent with a lack of excitation randomisation i.e.. the emission transition dipole moment remains correlated with the absorption transition dipole moment.

In the region where there are three fluorescence lifetime components the initial anisotropy following 1PA increases dramatically, as does the region with 3 fluorescence lifetime components following 2PA, though this region occurs at the longer wavelength end of the 1PA spectrum and the shorter wavelength end of the 2PA spectrum. As following 2PA this increase in $R(0)$ is out of proportion with the increase in lifetime component 2 i.e.. the increase in component 2 is not enough to account for the dramatic rise in $R(0)$.

The fact that similar behaviour is observed following 1PA as 2PA following at least some excitation wavelengths implies that there are two steady emitting states present in AF257 rather than the states resulting from an excited state reaction following 2PA.

Following 1PA it is certainly plausible that there is a common emission process to that following 2PA, but the absorption mechanism including the relaxation path from initial excited state to emitting state is evidently quite different to that following 2PA.

The growth in the fluorescence intensity in the region 380-430 nm has not been addressed during analysis as it is difficult to gain information from such complex behaviour. However, it can be noted that it coincides with a large amplitude of rotational components $\tau_{a(2)}$ and $\tau_{a(3)}$. With a lifetime of $\tau_{f(2)} \approx 1.25$ ns this is too long for solvent relaxation to be a likely cause.

2.11 Conclusions

The many applications of materials with a high 2PA cross-section has driven an search for new fluorescent chromophores optimised for 2PA [7]. Such molecules must be optimised for low-cost mass production and produce significant 2PA at low intensity. Trigonal planar branched molecules such as AF257 are of particular interest due to their intense 2PA coupled with their excitation transfer and depolarisation properties. However, there remain unknown factors in the excitation and fluorescence behaviour of such molecules; these factors could have an important impact on the use of these chromophores in some or all instances. It is for this reason that the systematic study of absorption, emission and anisotropy, and in particular the combined interpretation of these detailed in this chapter may be of significant interest.

The behaviour of the trigonal planar molecule AF257 upon excitation has been found to be extremely complicated, but with precise measurement and careful analysis it has been possible to deduce some properties inherent to the molecule.

Following 2PA in the excitation wavelength region 530-770 nm it appears that two independent components of AF257 exist as there are two components to the fluorescence lifetime decay. There appears to be a common emission mechanism involving two states with very different degrees of excitation energy delocalisation. This seems to be a consistent picture across the majority of both the 2- and single photon absorption spectra. The second component is not present following excitation of 770-900 nm, which implies that this emitting energy level is higher than component 1 or that there is a boundary between the states such that component 2 is not made with lower energy excitation. Separation of anisotropy measurement results through analysis has shown that for component 1 the model of redistribution of excitation in the excited state fits well, as emission appears uncorrelated with absorption. This is demonstrated by a lack of correlation between Ω and initial anisotropy values. However, component 2 appears to follow a model similar to that of a linear molecule with emission correlated with absorption. By splitting the anisotropy properties of

the two components in this way, anisotropy behaviour that was independent of the excitation wavelength was obtained for both components. Absorption characteristics following 2PA of the two components appear similar, as demonstrated by the very similar Ω values shown by each component. The results are therefore consistent with the possibility that a single AF257 species exists prior to excitation, but that following excitation there are two resultant emitting states. This would imply that the differentiation occurs between absorption and emission processes. No similar findings have been published previously for branched trigonal planar molecules.

As well as further characterising the molecule AF257 and the examination of the behaviour of trigonal planar branched molecules in general, the implications of these results apply to other areas of scientific research.

The excitation spectra for 2PA optimised molecules is often measured, and then the absorption cross-section inferred from it. This normally assumes the quantum yield to be independent of excitation wavelength. As stated above, different populations of the two excited states would in general result in a different overall quantum yield, significantly distorting the obtained 2PA spectrum leading to misinterpretation of the observed behaviour. This may be the case here where a strong resonance close to the 1PA is not observed in AF257 that was present in all other 2PA optimised molecules tested within the group [20, 30].

The distribution of emission dipoles is critically important in energy transfer mechanisms. Two populations with different dipole alignments in general will give different transfer rates to a single species with the same average alignment, leading to a misinterpretation of the observed transfer rate. Fluorescence resonance energy transfer has become a popular tool in the life sciences in recent years. A more detailed understanding of the nature of the excited states involved may therefore be required. Some evidence of this has been found by other members of the group in Green Fluorescent Protein, GFP [92]. Investigations into the observed dual fluorescence decay behaviour and the possibility of two different emitting states of this biologically important chromophore are presented in the next chapter.

References

- [1] W. Demtroder and F. K. Tittel, "Laser spectroscopy: basic concepts and instrumentation," *Optical Engineering*, vol. 35, no. 11, pp. 3361–3362, 1996.
- [2] M. Göppert-Mayer, "Über elementarakte mit zwei quantensprüngen," *Annalen der Physik*, vol. 401, no. 3, pp. 273–294, 1931.
- [3] W. Kaiser and C. Garrett, "Two-photon excitation in calcium: Eu^{2+} ," *Physical Review Letters*, vol. 7, no. 6, pp. 229–231, 1961.
- [4] P. F. Moulton, "Spectroscopic and laser characteristics of titanium: Al₂O₃," *J. Opt. Soc. Am. B*, vol. 3, no. 1, p. 125, 1986.
- [5] C. Xu and W. Webb, "Multiphoton excitation of molecular fluorophores and nonlinear laser microscopy," *Topics in Fluorescence Spectroscopy*, pp. 471–540, 2002.
- [6] H. Mahr, H. Rabin, and C. Tang, "Quantum electronics, vol.," *IAcademic, New York*, p. 285, 1975.
- [7] F. Terenziani, C. Katan, E. Badaeva, S. Tretiak, and M. Blanchard-Desce, "Enhanced Two-Photon Absorption of Organic Chromophores: Theoretical and Experimental Assessments," *Advanced Materials*, vol. 20, no. 24, pp. 4641–4678, 2008.
- [8] G. S. He, G. C. Xu, P. N. Prasad, B. A. Reinhardt, J. C. Bhatt, and A. G. Dillard, "Two-photon absorption and optical-limiting properties of novel organic compounds," *Optics letters*, vol. 20, no. 5, pp. 435–437, 1995.
- [9] J. Ehrlich, X. Wu, I. Lee, Z.-Y. Hu, H. Röckel, S. Marder, and J. Perry, "Two-photon absorption and broadband optical limiting with bis-donor stilbenes," *Optics letters*, vol. 22, no. 24, pp. 1843–1845, 1997.
- [10] K. König, "Multiphoton microscopy in life sciences," *Journal of Microscopy*, vol. 200, no. 2, pp. 83–104, 2001.
- [11] W. R. Zipfel, R. M. Williams, R. Christie, A. Y. Nikitin, B. T. Hyman, and W. W. Webb, "Live tissue intrinsic emission microscopy using multiphoton-excited native fluorescence and second harmonic generation," *Proceedings of the National Academy of Sciences*, vol. 100, no. 12, pp. 7075–7080, 2003.
- [12] D. A. Parthenopoulos, P. M. Rentzepis, *et al.*, "Three-dimensional optical storage memory.," *Science (New York, NY)*, vol. 245, no. 4920, p. 843, 1989.

- [13] C. Bauer, B. Schnabel, E.-B. Kley, U. Scherf, H. Giessen, and R. F. Mahrt, "Two-photon pumped lasing from a two-dimensional photonic bandgap structure with polymeric gain material," *Advanced Materials*, vol. 14, no. 9, pp. 673–676, 2002.
- [14] P. N. Prasad, J. D. Bhawalker, P. C. Cheng, and S. J. Pan, "Two-photon upconverting dyes and applications," June 11 2002. US Patent 6,402,037.
- [15] F. Terenziani, C. Katan, E. Badaeva, S. Tretiak, and M. Blanchard-Desce, *Enhanced Two-Photon Absorption of Organic Chromophores: Theoretical and Experimental Assessments*, vol. 20. Dec. 2008.
- [16] C. Ricard, J. Coles, R. Serduc, B. van der Sanden, P. Verant, J.-C. Vial, and C. Ricard, "Two-photon imaging," *Encyclopedia of Neuroscience*, 2008.
- [17] C. Xu, W. Zipfel, J. B. Shear, R. M. Williams, and W. W. Webb, "Multiphoton fluorescence excitation: new spectral windows for biological nonlinear microscopy.," *Proceedings of the National Academy of Sciences of the United States of America*, vol. 93, pp. 10763–8, Oct. 1996.
- [18] F. A. Duck, *Physical properties of tissue: a comprehensive reference book*. Academic Pr, 1990.
- [19] W. Denk, J. H. Strickler, W. W. Webb, *et al.*, "Two-photon laser scanning fluorescence microscopy.," *Science (New York, NY)*, vol. 248, no. 4951, p. 73, 1990.
- [20] N. Nicolaou, *Single and two-Photon fluorescence studies of linear and non-linear optical chromophores*. PhD thesis, UCL, 2007.
- [21] S. W. Pauls, J. F. Hedstrom, and C. K. Johnson, "Rotational relaxation of perylene in n-alcohols and n-alkanes studied by two-photon-induced anisotropy decay," pp. 205–222, 1998.
- [22] D. A. Armoogum, R. J. Marsh, N. Nicolaou, O. Mongin, M. Blanchard-Desce, and A. J. Bain, "Stimulated emission depletion and fluorescence correlation spectroscopy of a branched quadrupolar chromophore," in *Proceedings of SPIE*, vol. 7030, pp. 70300S–70300S–10, SPIE, Aug. 2008.
- [23] C. Xu and W. W. Webb, "Measurement of two-photon excitation cross sections of molecular fluorophores with data from 690 to 1050 nm," *JOSA B*, vol. 13, no. 3, pp. 481–491, 1996.
- [24] G. He, L. Tan, Q. Zheng, and P. Prasad, "Multiphoton absorbing materials: molecular designs, characterizations, and applications," *ChemInform*, vol. 39, no. 24, pp. no–no, 2008.

- [25] C. Le Droumaguet, O. Mongin, M. Werts, and M. Blanchard-Desce, "Towards [U+FFFF] smart [U+FFFF] multiphoton fluorophores: strongly solvatochromic probes for two-photon sensing of micropolarity," *Chemical communications*, no. 22, pp. 2802–2804, 2005.
- [26] B. Strehmel, A. Sarker, and H. Detert, "The influence of σ and π acceptors on two-photon absorption and solvatochromism of dipolar and quadrupolar unsaturated organic compounds," *ChemPhysChem*, vol. 4, no. 3, pp. 249–259, 2003.
- [27] M. P. Joshi, J. Swiatkiewicz, F. Xu, P. N. Prasad, B. Reinhardt, and R. Kannan, "Energy transfer coupling of two-photon absorption and reverse saturable absorption for enhanced optical power limiting," *Optics letters*, vol. 23, no. 22, pp. 1742–1744, 1998.
- [28] S.-J. Chung, K.-S. Kim, T.-C. Lin, G. S. He, J. Swiatkiewicz, and P. N. Prasad, "Cooperative enhancement of two-photon absorption in multi-branched structures," *The Journal of Physical Chemistry B*, vol. 103, no. 49, pp. 10741–10745, 1999.
- [29] L. Porrès, O. Mongin, C. Katan, M. Charlot, T. Pons, J. Mertz, and M. Blanchard-Desce, "Enhanced two-photon absorption with novel octupolar propeller-shaped fluorophores derived from triphenylamine," *Organic letters*, vol. 6, no. 1, pp. 47–50, 2004.
- [30] O. Mongin, J. Brunel, L. Porrès, and M. Blanchard-Desce, "Synthesis and two-photon absorption of triphenylbenzene-cored dendritic chromophores," *Tetrahedron letters*, vol. 44, no. 14, pp. 2813–2816, 2003.
- [31] M. Rumi, J. E. Ehrlich, A. A. Heikal, J. W. Perry, S. Barlow, Z. Hu, D. Mccord-maughon, T. C. Parker, S. Thayumanavan, S. R. Marder, D. Beljonne, and J.-l. Bre, "Structure-Property Relationships for Two-Photon Absorbing Chromophores : Bis-Donor Diphenylpolyene and Bis (styryl) benzene Derivatives," no. 8, pp. 9500–9510, 2000.
- [32] Y. Jiang, Y. Wang, B. Wang, J. Yang, N. He, S. Qian, and J. Hua, "Synthesis, two-photon absorption and optical limiting properties of multi-branched styryl derivatives based on 1,3,5-triazine.," *Chemistry, an Asian journal*, vol. 6, pp. 157–65, Jan. 2011.
- [33] M. Drobizhev, A. Karotki, A. Rebane, and C. W. Spangler, "Dendrimer molecules with record large two-photon absorption cross section," *Optics Letters*, vol. 26, no. 14, pp. 1081–1083, 2001.
- [34] A. Abbotto, L. Beverina, R. Bozio, A. Facchetti, C. Ferrante, G. A. Pagani, D. Pedron, and R. Signorini, "Novel heteroaromatic-based multi-branched dyes with enhanced two-photon absorption activity," *Chemical Communications*, no. 17, pp. 2144–2145, 2003.

- [35] A. Adronov, J. M. Frechet, G. S. He, K.-S. Kim, S.-J. Chung, J. Swiatkiewicz, and P. N. Prasad, "Novel two-photon absorbing dendritic structures," *Chemistry of materials*, vol. 12, no. 10, pp. 2838–2841, 2000.
- [36] S.-J. Chung, T.-C. Lin, K.-S. Kim, G. He, J. Swiatkiewicz, P. Prasad, G. Baker, and F. Bright, "Two-photon absorption and excited-state energy-transfer properties of a new multibranched molecule," *Chemistry of materials*, vol. 13, no. 11, pp. 4071–4076, 2001.
- [37] T. Goodson III, "Optical excitations in organic dendrimers investigated by time-resolved and nonlinear optical spectroscopy," *Accounts of chemical research*, vol. 38, no. 2, pp. 99–107, 2005.
- [38] C. Katan, F. Terenziani, C. Le, O. Mongin, M. H. V. Werts, S. Tretiak, M. Blanchard-desce, E. Organiques, U. D. Rennes, and I. De, "Branching of dipolar chromophores : effects on linear and nonlinear optical properties," pp. 34–36, 2005.
- [39] Y. Jiang, Y. Wang, J. Hua, J. Tang, B. Li, S. Qian, and H. Tian, "Multibranched triarylamine end-capped triazines with aggregation-induced emission and large two-photon absorption cross-sections.," *Chemical communications (Cambridge, England)*, vol. 46, pp. 4689–91, July 2010.
- [40] R. Kannan, G. S. He, T.-c. Lin, P. N. Prasad, R. A. Vaia, and L.-s. Tan, "Toward Highly Active Two-Photon Absorbing Liquids . Synthesis and Characterization of 1 , 3 , 5-Triazine-Based Octupolar Molecules," vol. 502, no. c, pp. 185–194, 2004.
- [41] B. Li, R. Tong, R. Zhu, F. Meng, H. Tian, and S. Qian, "The ultrafast dynamics and nonlinear optical properties of tribranched styryl derivatives based on 1,3,5-triazine.," *The journal of physical chemistry. B*, vol. 109, pp. 10705–10, June 2005.
- [42] S. Ren, D. Zeng, H. Zhong, Y. Wang, S. Qian, and Q. Fang, "Convergent Synthesis and Multifunctional Properties," pp. 10374–10383, 2010.
- [43] Y.-Z. Cui, Q. Fang, G. Xue, G.-B. Xu, L. Yin, and W.-T. Yu, "Cooperative Enhancement of Two-photon Absorption of Multibranched Compounds with Vinylenes Attaching to the s-Triazine Core," *Chemistry Letters*, vol. 34, no. 5, pp. 644–645, 2005.
- [44] L. Zou, Z. Liu, X. Yan, Y. Liu, Y. Fu, J. Liu, Z. Huang, X. Chen, and J. Qin, "Star-Shaped D- π -A Molecules Containing a 2,4,6-Tri(thiophen-2-yl)-1,3,5-triazine Unit: Synthesis and Two-Photon Absorption Properties," *European Journal of Organic Chemistry*, vol. 2009, pp. 5587–5593, Nov. 2009.

- [45] N. Davis.
- [46] W. Verbouwe, M. Van der Auweraer, F. De Schryver, J. Piet, and J. Warman, "Excited State Localization or Delocalization in C₃-symmetric Amino-substituted Triphenylbenzene Derivatives," *J. Am. Chem. Soc.*, vol. 120, no. 6, pp. 1319–1324, 1998.
- [47] O. P. Varnavski, J. C. Ostrowski, L. Sukhomlinova, R. J. Twieg, G. C. Bazan, and T. Goodson III, "Coherent effects in energy transport in model dendritic structures investigated by ultrafast fluorescence anisotropy spectroscopy," *Journal of the American Chemical Society*, vol. 124, no. 8, pp. 1736–1743, 2002.
- [48] S. A. Lahankar, R. West, O. Varnavski, X. Xie, T. Goodson III, L. Sukhomlinova, and R. Twieg, "Electronic interactions in a branched chromophore investigated by nonlinear optical and time-resolved spectroscopy," *The Journal of chemical physics*, vol. 120, p. 337, 2004.
- [49] I. Franco and S. Tretiak, "Electron-vibrational dynamics of photoexcited polyfluorenes," *Journal of the American Chemical Society*, vol. 126, no. 38, pp. 12130–12140, 2004.
- [50] S. Tretiak, A. Saxena, R. Martin, and A. Bishop, "Conformational dynamics of photoexcited conjugated molecules," *Physical review letters*, vol. 89, no. 9, p. 97402, 2002.
- [51] R. Stahl, C. Lambert, C. Kaiser, R. Wortmann, and R. Jakober, "Electrochemistry and photophysics of donor-substituted triarylboranes: symmetry breaking in ground and excited state.," *Chemistry (Weinheim an der Bergstrasse, Germany)*, vol. 12, pp. 2358–70, Mar. 2006.
- [52] G. Weber, "Resolution of heterogeneous fluorescence from proteins and aromatic amino acids by phase-sensitive detection of fluorescence," *Biochem J*, vol. 51, pp. 145–167, 1952.
- [53] B. Valeur, R. D. Hall, and G. Weber, "Polarization of the fluorescence of Triphenylene: A planar molecule with three-fold symmetry," *Chemical Physics Letters*, vol. 116, no. 2, pp. 2–5, 1985.
- [54] D. Beljonne, W. Wenseleers, E. Zojer, Z. Shuai, H. Vogel, S. J. Pond, J. W. Perry, S. R. Marder, and J.-L. Bredas, "Role of dimensionality on the two-photon absorption response of conjugated molecules: the case of octupolar compounds," *Advanced Functional Materials*, vol. 12, no. 9, pp. 631–641, 2002.
- [55] B. Valeur and G. Weber, "A new red-edge effect in aromatic molecules: Anomaly of apparent rotation revealed by fluorescence polarization," *The Journal of Chemical Physics*, vol. 69, no. 6, p. 2393, 1978.

- [56] E. Leroy and H. Lami, "A red-edge effect in the fluorescence polarization of molecules of D_{3h} or D_{6h} symmetry," *Chemical Physics Letters*, vol. 41, no. July, 1976.
- [57] E. Leroy and H. Lami, "A red-edge effect in the fluorescence polarization of molecules of D_{3h} or D_{6h} symmetry," *Chemical Physics Letters*, vol. 41, no. 2, pp. 373–377, 1976.
- [58] R. Stahl, C. Lambert, C. Kaiser, R. Wortmann, and R. Jakober, "Electrochemistry and Photophysics of Donor-Substituted Triarylboranes: Symmetry Breaking in Ground and Excited State," *Chemistry—A European Journal*, vol. 12, no. 8, pp. 2358–2370, 2006.
- [59] C. Sissa, A. Painelli, M. Blanchard-Desce, and F. Terenziani, "Fluorescence anisotropy spectra disclose the role of disorder in optical spectra of branched intramolecular-charge-transfer molecules," *The journal of physical chemistry. B*, vol. 115, pp. 7009–20, June 2011.
- [60] J. C. Slonczewski, "Theory of the dynamical jahn-teller effect," *Physical Review*, vol. 131, no. 4, p. 1596, 1963.
- [61] F. Terenziani, C. Sissa, and A. Painelli, "Symmetry breaking in octupolar chromophores: solvatochromism and electroabsorption," *The journal of physical chemistry. B*, vol. 112, pp. 5079–87, Apr. 2008.
- [62] M. A. Albota, C. Xu, and W. W. Webb, "Two-photon fluorescence excitation cross sections of biomolecular probes from 690 to 960 nm," pp. 1–5, 1998.
- [63] N. S. Makarov, M. Drobizhev, and A. Rebane, "Two-photon absorption standards in the 550-1600 nm excitation wavelength range," *Optics express*, vol. 16, pp. 4029–47, Mar. 2008.
- [64] C. Katan, S. Tretiak, M. H. V. Werts, A. J. Bain, R. J. Marsh, N. Leonczek, N. Nicolaou, E. Badaeva, O. Mongin, and M. Blanchard-Desce, "Two-photon transitions in quadrupolar and branched chromophores: experiment and theory," *The Journal of Physical Chemistry B*, vol. 111, no. 32, pp. 9468–9483, 2007.
- [65] P. N. Butcher and D. Cotter, *The elements of nonlinear optics*, vol. 9. Cambridge University Press, 1991.
- [66] M. Rumi and J. W. Perry, "Two-photon absorption: an overview of measurements and principles," *Advances in Optics and Photonics*, vol. 2, p. 451, Aug. 2010.
- [67] C. Xu and W. W. Webb, "Measurement of two-photon excitation cross sections of molecular fluorophores with data from 690 to 1050 nm," *Journal of the Optical Society of America B*, vol. 13, p. 481, Mar. 1996.

- [68] S. M. Kennedy and F. E. Lytle, "p-Bis (o-methylstyryl) benzene as a Power-Squared Sensor for Two-Photon Absorption Measurements between 537 and 694 nm," pp. 2643–2647, 1988.
- [69] W. Fisher, E. Wachter, F. Lytle, M. Armas, and C. Seaton, "Source-corrected two-photon excited fluorescence measurements between 700 and 880 nm," *Applied spectroscopy*, vol. 52, no. 4, pp. 536–545, 1998.
- [70] DrBio.
- [71] D. M. Brink and G. R. Satchler, *Angular momentum*. Clarendon Press Oxford, 1993.
- [72] A. Bain, P. Chandna, and J. Bryant, "Picosecond polarized fluorescence studies of anisotropic fluid media. i. theory," *The Journal of Chemical Physics*, vol. 112, p. 10418, 2000.
- [73] R. P. Drucker and W. McClain, "Polarized two-photon studies of biphenyl and several derivatives," *The Journal of Chemical Physics*, vol. 61, no. 7, pp. 2609–2615, 1974.
- [74] A. Bain and A. McCaffery, "On the measurement of molecular anisotropies using laser techniques. i. polarized laser fluorescence," *The Journal of chemical physics*, vol. 83, no. 6, p. 2627, 1985.
- [75] W. McClain, "Excited state symmetry assignment through polarized two-photon absorption studies of fluids," *The Journal of Chemical Physics*, vol. 55, p. 2789, 1971.
- [76] C. Wan and C. K. Johnson, "Time-resolved anisotropic two-photon spectroscopy," *Chemical physics*, vol. 179, no. 3, pp. 513–531, 1994.
- [77] P. R. Callis, "On the theory of two-photon induced fluorescence anisotropy with application to indoles," *The Journal of chemical physics*, vol. 99, no. 1, pp. 27–37, 1993.
- [78] M. K. Reed, M. K. Steiner-Shepard, M. S. Armas, and D. K. Negus, "Microjoule-energy ultrafast optical parametric amplifiers," *JOSA B*, vol. 12, no. 11, pp. 2229–2236, 1995.
- [79] G. R. Holtom, "Artifacts and diagnostics in fast fluorescence measurements," in *OE/LASE'90, 14-19 Jan., Los Angeles, CA*, pp. 2–12, International Society for Optics and Photonics, 1990.
- [80] D. Birch and R. Imhof, "The origin of fluorescence from trans-trans diphenylbutadiene," *Chemical Physics Letters*, vol. 88, no. 2, pp. 243–247, 1982.
- [81] H. Leismann, H.-D. Scharf, W. Strassburger, and A. Wollmer, "Determination of subnanosecond fluorescence decays of chlorobenzene, tryptophan and the benzene-triethylamine exciplex using a nanosecond flashlamp," *Journal of Photochemistry*, vol. 21, no. 2, pp. 275–280, 1983.

- [82] M. Bouchy, J. Jezequel, J. Andre, J. Bordet, and M. Bouchy, "Deconvolution and reconvolution of analytical signals," *ENSIC-INPL Editions, France*, 1982.
- [83] W. R. Ware, L. J. Doemeny, and T. L. Nemzek, "Deconvolution of fluorescence and phosphorescence decay curves. least-squares method," *The Journal of Physical Chemistry*, vol. 77, no. 17, pp. 2038–2048, 1973.
- [84] D. J. Birch and R. E. Imhof, "Time-domain fluorescence spectroscopy using time-correlated single-photon counting," in *Topics in fluorescence spectroscopy, Volume 1*, pp. 1–95, Springer, 2002.
- [85] P. E. Greenwood and M. S. Nikulin, *A guide to chi-squared testing*, vol. 280. Wiley-Interscience, 1996.
- [86] P. R. Bevington and D. K. Robinson, *Data reduction and error analysis for the physical sciences*, vol. 2. McGraw-Hill New York, 1969.
- [87] D. O'Connor, *Time-correlated single photon counting*. Academic Press, 1984.
- [88] A. J. Cross and G. R. Fleming, "Analysis of time-resolved fluorescence anisotropy decays," *Biophysical journal*, vol. 46, no. 1, pp. 45–56, 1984.
- [89] A. A. Heikal, S. T. Hess, and W. W. Webb, "Multiphoton molecular spectroscopy and excited-state dynamics of enhanced green fluorescent protein (egfp): acid–base specificity," *Chemical Physics*, vol. 274, no. 1, pp. 37–55, 2001.
- [90] C. W. Ko, Z. Wei, R. J. Marsh, D. a. Armoogum, N. Nicolaou, A. J. Bain, A. Zhou, and L. Ying, "Probing nanosecond motions of plasminogen activator inhibitor-1 by time-resolved fluorescence anisotropy.," *Molecular bioSystems*, vol. 5, pp. 1025–31, Sept. 2009.
- [91] T. S. Blacker, R. J. Marsh, M. R. Duchon, and A. J. Bain, "Activated barrier crossing dynamics in the non-radiative decay of nadh and nadph," *Chemical Physics*, 2013.
- [92] T. A. Masters, R. J. Marsh, D. A. Armoogum, N. Nicolaou, B. Larijani, and A. J. Bain, "Restricted state selection in fluorescent protein fret," *Journal of the American Chemical Society*, 2013.
- [93] B. Valeur *et al.*, *Molecular fluorescence: principles and applications*. Wiley-Vch, 2012.
- [94] Y. Wang, G. S. He, P. N. Prasad, and T. Goodson, "Ultrafast dynamics in multibranch structures with enhanced two-photon absorption," *Journal of the American Chemical Society*, vol. 127, no. 29, pp. 10128–10129, 2005.

Chapter 3

Radiative Decay Dynamics in Fluorescent Proteins Probed by Continuous Wave Stimulated Emission Depletion

3.1 Introduction

In this chapter the effects of continuous wave (CW) stimulated emission depletion (STED) on the time resolved fluorescence of two widely used fluorescent proteins enhanced green fluorescent protein (EGFP) [1] and a red shifted variant mCherry [2] are investigated. The naturally occurring green fluorescent protein (GFP) from the *Aequorea victoria* jellyfish is frequently used as a reporter of protein expression [3]. In modified forms it has been used to make biosensors (e.g. EGFP and mCherry), these have attained widespread usage as naturally fluorescent markers in biophysical and biochemical studies [4]. The development of GFP and its ever expanding family of variants was recognized by the award of the Nobel Prize for Chemistry in 2008 to Martin Chalfie, Osamu Shimomura, and Roger Y. Tsien. The selection of fluorescent protein pairs which exhibit broadly overlapping emission and absorption

spectra have allowed their use in Förster resonance energy transfer (FRET) studies of inter- and intramolecular interactions. FRET involves the non-radiative transfer of electronic energy between a closely spaced pair of donor and acceptor molecules. The rate at which energy is transferred from a population of excited donors and acceptors is dependent on the inverse sixth power of their separation and the relative orientation of their transition dipole moments. Given this sensitive distance dependence, FRET is often referred to as a spectroscopic ruler [5] and has become widely used to detect protein conformation change and intermolecular interactions [6]. FRET is often used in a qualitative rather than quantitative manner i.e. as an indicator of conformational change or association rather than a provider of accurate molecular information [7–9]. An unambiguous indicator of FRET is often taken to be the decrease in the fluorescence lifetime of the donor population [10]; this is easily observable if all the excited donors undergo FRET. However the observation of a sub-100% interacting fraction is not uncommon [11, 12]. A more direct approach to determine the FRET rate is to measure the rise time of the fluorescence arising from acceptor excitation: the so called sensitized acceptor emission [13, 14]. This approach is gaining popularity in fluorescent protein FRET [11–14]. Recent work within the group has used FRET between EGFP and mCherry to discover that the cellular regulation of 3-Phosphoinositide Dependent Protein Kinase 1 (PDK1) occurs via homo-dimerization [15]. Sensitized acceptor emission studies of in-vitro recombinant EGFP-PDK1-mCherry constructs were used to measure the FRET rate and to determine donor-acceptor distances in the PDK1 homo-dimer [15]. A two-photon excited FRET study of the same constructs was employed, as a lower degree of direct acceptor excitation could be achieved and a clearer picture of the underlying photophysics could be obtained [16]. The fluorescence decays of EGFP and mCherry are both bi-exponential [17] and FRET in principle should involve the interaction between two donor and two acceptor populations. This was not observed; ca. 50% of the excited EGFP states played no part in the FRET process and FRET transfer was wholly to the minority decay component of mCherry. It was shown that the high degree of state restriction in FRET could be explained by orientational

differences in the donor-acceptor dipole-dipole angles. The rationale of the FRET studies undertaken in this chapter is twofold. Firstly to see if it were possible to investigate this hypothesis by determining the (relative) stimulated emission rates of the components of the bi-exponential decays in both fluorescent proteins and thus, via the Einstein relations [18, 19] the corresponding relative radiative decay rates. This would indicate whether any differences between the intrinsic FRET rate of the donor states (given an equivalent acceptor interaction) were present and whether the Förster radii of the EGFP-mCherry interaction, based on spectral overlap and average quantum yield measurements [20] would need substantial revision. Secondly, given the increasing use of CW STED in breaking the diffraction limit in fluorescence microscopy (super resolution imaging) [21, 22] it has become apparent that little attention has been given to the fundamental photophysics of this process. A new, low power, super-resolution technique in the group had been developed based on the modification of the time evolution of a fluorescent image by a low power Gaussian CW STED laser and its reconstruction using a linear combination of time slices [23]. To this end an understanding of fundamental CW STED dynamics in time resolved fluorescent probe emission was long overdue. The attraction of using EGFP and mCherry in such studies was that given their large molecular weights (ca. 30 KDa) their rotational correlation times were significantly longer (ca. 18 ns (EGFP) and ca. 30 ns (main rotational component of mCherry) [17]) in Size Exclusion Chromatography (SEC) buffer (see Section 3.5) than their average fluorescence lifetimes (2.7 ns and 1.6 ns respectively [16]) and to a first approximation rotational diffusion during STED could, in principle, be neglected. In pulsed STED, significant population depletion is accompanied by substantial depolarisation of the post pulse emission [24]. In the low power CW STED the equivalent degree of population depletion (lifetime shortening) is less marked. As will be seen, time-resolved non-rotational depolarization effects in fluorescent protein CW STED undertaken in a FLIM microscope are pronounced, indicating that a strong correlation between molecular orientation and probe lifetime cannot be ignored.

3.2 Green Fluorescent Protein (GFP) and Derivatives

The naturally occurring form of the Green Fluorescent Protein, termed wild type GFP (wt-GFP) is composed of 238 amino acids and was originally discovered in samples from the jellyfish *Aequorea victoria* in 1962 by Shimomura and co-workers [25]. Wt-GFP has a major excitation peak at 398 nm and a minor one at 478 nm [26]. The fluorescence emission maximum is at 509 nm, with a high quantum yield of 60% [27]. Other naturally occurring green fluorescent proteins were subsequently discovered such as that from the Sea Pansy *Renilla reniformis* which has a single major excitation peak at 498 nm. Energy transfer from Aequorin (a photoprotein also occurring naturally in the jellyfish *Aequorea victoria*) to wt-GFP producing an emission peaked at 510 nm was demonstrated in 1974 [28]. Wt-GFP has a number of drawbacks which limit its application. These are the lack of a strong absorption feature at common laser outputs (e.g. Argon Ion 488 nm), poor photostability and inconsistent secondary and tertiary structure at biologically relevant temperatures [29].

As a result, there has been significant activity to improve upon wt-GFP by engineering the GFP gene to produce numerous derivatives [30]. The first of these was developed in 1995 and involved a mutation of Serine 65 to threonine (S65T). This resulted in a red shift of the absorption maximum of 488 nm, a 6-fold increase in brightness (the product of the absorption cross section/extinction coefficient and the quantum yield) and increased photostability [31]. A 35-fold increase in brightness compared to wtGFP was obtained with a further mutation (F64L) [29]. This protein was then codon optimized, with the resultant protein termed Enhanced GFP (EGFP) [1]. EGFP is now the standard blue absorbing green emitting fluorescent protein.

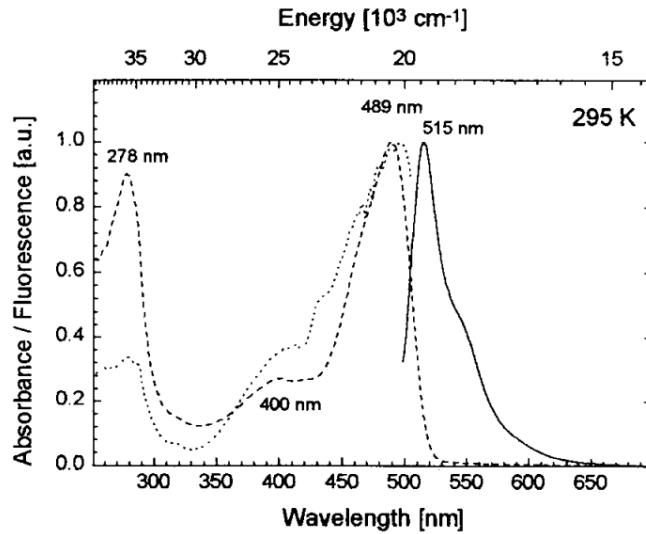


Figure 3.1: Spectra of EGFP at room temperature and with pH = 8. 400 nm excitation used. Dashed line indicates steady state absorption, dotted line fluorescence excitation, and full line the emission spectrum [32].

3.2.1 Photophysics of EGFP

In absorption and time-resolved fluorescence spectroscopy experiments of wt-GFP the data has been interpreted as the existence of two separate inter-convertible states; the high energy protonated form RH (83%) labelled the A state, and the low energy deprotonated form R_{eq}^- (17%) labelled the B state [26] which is achieved via excited state proton transfer (ESPT). The two peaks occurring in the absorption spectrum of wt-GFP at room temperature (298 K) have been attributed to state A (398 nm) and state B (478 nm) [26]. However, in EGFP there is no measurable ESPT [33] and the protonated and de-protonated forms exist in a pH dependent equilibrium [17, 34]. With increase in acidity the strength of the main absorption band at 485 nm decreases, whilst the strength of the minor absorption band at 400 nm increases, with the total emission intensity dependent on pH with an acid dissociation constant $pK_a = 5.8$ [33]. The absorption and emission spectra of EGFP shown in Figure 3.1 were taken at a pH of 8 [32] which is similar to the EGFP samples used in this chapter of pH = 7.4 (PBS) and pH = 8.2 ± 0.5 (SEC). Thus following excitation at 490 nm at room temperature with a pH of 7.4 the vast

majority of EGFP in the excited state will be in the low energy deprotonated B state. To further ensure all observed emission is from the B state a long pass 510 nm filter is used in each EGFP measurement. It can be seen in Figure 3.1 that the absorption band peaks at 489 nm indicating that the the ground state equilibrium distribution comprises mostly the deprotonated B state.

The fluorescence intensity decay of EGFP has been found to be bi-exponential with fluorescence decay times of 2.9-3.1 ns and 1.8-2.4 ns [15–17, 35] for both single and two-photon excited fluorescence. The average fluorescence lifetime in all cases was measured as 2.7-2.8 ns. One published study was found with values outside of these ranges with correlation times of 2.63 and 1.36 and an average of 2.45 [11] (see Table 3.1 in Section 3.6 for further details of studies). Discrepancy between measured lifetimes could be due to environmental effects such as pH [34] and refractive index [36] to which EGFP is sensitive, varying excitation and detection wavelengths, or possibly due to differing signal to noise ratios or the data fitting method used.

3.3 mCherry (Fluorescent Protein)

Most naturally occurring wild-type red to yellow fluorescent proteins are tetrameric and often toxic or disruptive (for example showing strong oligomerisation and slow maturation)[37, 38]. Bevis et al. in 2002 [39] used directed evolution to develop the monomer mRFP1, derived from the *Discosoma sp.* (mushroom coral) fluorescent protein ‘DsRed’. Further work was carried out by Tsien et al. to break the sub-unit interfaces, requiring 33 substitutions in order to do this whilst preserving fluorescence [40]. Improvements to the extinction coefficient, fluorescence quantum yield and photostability using further directed evolution resulted in a number of new variants and colours of fluorescent protein including mCherry [2]. mCherry exhibits an absorption maximum at 587 nm and an emission maximum at 610 nm. Due to its beneficial fluorescence characteristics, since its development mCherry has been widely used for example in Förster resonance energy transfer (FRET) studies [41]

and two-colour fluorescence microscopy (in conjunction with GFP) [42].

3.4 Stimulated Emission Depletion

Stimulated or induced emission is the fundamental process responsible for optical amplification and laser action [43]; the use of stimulated emission as a spectroscopic tool was developed at MIT in the 1980's by Kinsey, Field and co-workers [44]. In stimulated emission pumping (SEP) a narrow bandwidth pulsed laser (PUMP) was used to excite a specific vibration-rotation level in a molecular electronic excited state of a gas phase sample while a second tunable laser pulse (DUMP) was used to stimulate transitions to high lying vibration rotation levels of the ground state. Resonances were detected as 'dips' in the fluorescence signal created by the PUMP as the frequency of the DUMP was tuned across the emission spectrum. The technique afforded access to vibrational and rotational levels that were inaccessible via conventional (single photon) absorption techniques. The use of stimulated emission as a picosecond domain spectroscopic technique (PUMP + time delayed DUMP) was developed by Lakowicz and co-workers and termed light quenching [45]. Stimulated emission depletion (STED) using femtosecond pulses was subsequently used by Hochstrasser to probe ultrafast solvation dynamics [46]. There has been increased interest in the application of STED to attaining what is termed super-resolution in fluorescence microscopy. The planar optical resolution $\Delta_{X,Y}$ of a confocal fluorescence microscope is limited by the optical wavelength and the numerical aperture (NA) of the objective through the Abbé criterion $\Delta_{X,Y} \geq \lambda/2NA$ [47]; this limits the practical resolution limit to ca. 200 nm. The ability to break through this 'barrier' was demonstrated by Hell [48] using pulsed PUMP and DUMP fields but in the spatial rather than temporal domain. The PUMP laser employed a Gaussian spatial profile whilst that of the DUMP was adjusted to produce (when focused) a 'doughnut' intensity distribution. The pulses were spatially overlapped such that an intensity minima in the centre coincided with the Gaussian peak of the PUMP. The DUMP pulse was temporally stretched to minimize saturation effects (see Chap-

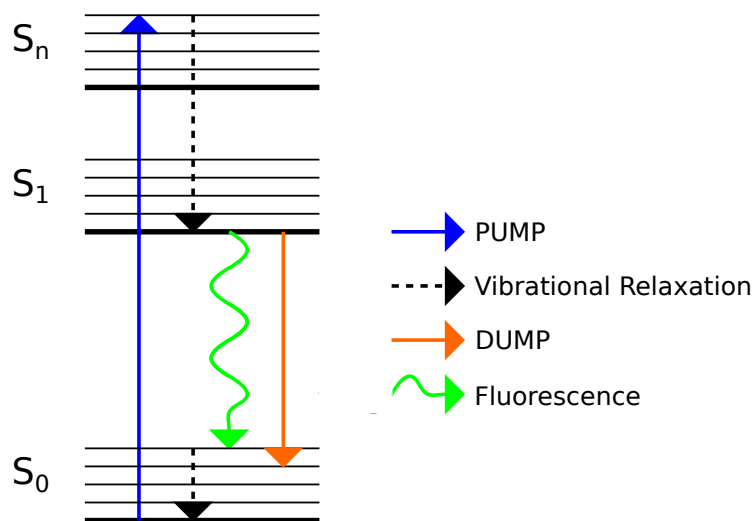


Figure 3.2: Illustration of single-photon STED. Population in the ground vibrational levels of the S_0 electronic ground state is excited through absorption of a PUMP photon to higher vibrational levels in an excited singlet state. Rapid (ps to sub-ps) non-radiative relaxation leads to the population of low vibrational levels of S_1 from where stimulated emission takes place continuously.

ter 4). A DUMP pulse energy was input to ensure depletion by the doughnut was effectively 100%. Localised emission created a fluorescent spot smaller than that allowed by the Abbé limit. The PUMP–DUMP combination was then scanned over the sample yielding a high resolution fluorescent image. In its initial form STED microscopy is an expensive tool requiring ultrashort PUMP and (stretched) DUMP lasers; recent developments in high power low cost CW lasers have stimulated interest in their used for STED microscopy and some systems have been commercialised [21]. The development of CW STED has largely been an optical engineering exercise and a fundamental understanding of CW STED dynamics has to date not been attempted. An attempt to rectify this and to investigate the nature of the bi-exponential fluorescence decays in EGFP and mCherry excited state decay are the principal motivating forces behind this current study. The work in this chapter investigates the influence of a CW DUMP laser on the time dependent fluorescence intensity and anisotropy of EGFP and mCherry. The photophysics of STED are detailed in Figure 3.2.

An excited population is created by a short (picosecond to sub picosecond) laser whose repetition rate gives an inter-pulse separation that allows for full relaxation of the excited state population between successive excitation events. Relaxation to vibrational levels in the electronic ground state occurs via spontaneous emission and stimulated transitions induced by the CW DUMP laser. With fast vibrational relaxation in the ground state, re-pumping of the excited state by the DUMP laser can be neglected at depletion rates comparable to those of fluorescence. The fluorescence decay of the excited state population can be written as,

$$I_i(t) \propto N_{EX}(0) \exp(-k_f t) \int_0^{2\pi} \int_0^{\pi} P_{EX}(\theta, \phi, t) \exp(-k_S(\theta, I_{DUMP})t) P_i^{DET}(\theta, \phi) \sin \theta d\theta d\phi \quad (3.4.1)$$

where $N_{EX}(0)$ is the initial excited state population prepared by the PUMP pulse, I_{DUMP} is the intensity of the depletion beam, k_f is the emission rate of the excited population in the absence of stimulated emission, $P_{EX}(\theta, \phi, t)$ is the orientational distribution function of the excited state population at time t and $P_i^{DET}(\theta, \phi)$ is the detection probability for observation polarisation direction i . Given that the rotational diffusion of fluorescent proteins is slow compared to their fluorescence lifetimes $P_{EX}(\theta, \phi, t)$ can be taken (to a first approximation) as time invariant being proportional to the initial $\cos^2 \theta$ excitation transition probability. The detection probabilities for parallel and perpendicular polarisations are simply

$$P_{\parallel}^{DET}(\theta, \phi) = \cos^2 \theta, \quad P_{\perp}^{DET}(\theta, \phi) = \sin^2 \theta \cos^2 \phi \quad (3.4.2)$$

Inserting into Equation 3.4.1 and integrating over θ and ϕ with the substitution $x = \cos \theta$ gives

$$I_{\parallel}(t) \propto N_{EX}(0) \exp(-k_f t) 2\pi \int_{-1}^1 x^4 \exp(-BI_{DUMP}x^2 t) dx \quad (3.4.3)$$

$$I_{\perp}(t) \propto N_{EX}(0) \exp(-k_f t) \pi \int_{-1}^1 x^2 (1 - x^2) \exp(-BI_{DUMP}x^2 t) dx$$

The fluorescence intensity $I_{\parallel} + 2I_{\perp}$ is thus

$$I_{\parallel} + 2I_{\perp} = CN_{EX}(0) \exp(-k_F t) \int_{-1}^1 x^2 \exp(-BI_{DUMP} x^2 t) dx \quad (3.4.4)$$

Oriental dependence of the fluorescence lifetime in STED has in the most part been generally ignored. As will be seen this cannot be the case even in a system with slow orientational relaxation. Proceeding, however, along ‘conventional’ lines a first approximation would be to treat the stimulated emission rate experienced by the excited population as an orientational average of the θ dependent decay rates. With this approach Equation 3.4.4 becomes

$$I_{\parallel} + 2I_{\perp} = CN_{EX}(0) \exp(-k_F t) \int_{-1}^1 x^2 \exp\left(-\overline{BI_{DUMP}} t\right) dx \quad (3.4.5)$$

Where the averaged stimulated emission depletion rate is given by

$$\overline{BI_{DUMP}} = BI \int_{-1}^1 \frac{3}{2} x^4 dx = BI \frac{3}{5} \quad (3.4.6)$$

This gives a net intensity decay rate that is linearly dependent on the DUMP intensity.

$$I_{\parallel} + 2I_{\perp} = \frac{2}{3} CN_{EX}(0) \exp(-k_F t) \exp\left(-\frac{3BI_{DUMP}}{7} t\right) \quad (3.4.7)$$

In this approximation, as the stimulated emission rate is independent of molecular orientation, the fluorescence anisotropy should remain unchanged from the depolarization experienced by rotational diffusion; in EGFP and mCherry this is slow compared to their fluorescence lifetimes.

3.5 Experimental Set-Up

The experimental set-up for CW STED is based around a confocal fluorescence lifetime imaging microscope (MT200, Picoquant, Germany). This consists of an inverted microscope body (IX71, Olympus, Japan) a piezo scanning stage for the ob-

jective (E710 Piezo Scanner, Physics Instrumente, Germany), a TCSPC system (picoharp 300, PicoQuant) and two PDM single-photon avalanche detectors (SPADs) (Micro Photon Devices, Italy). A schematic of the system layout is shown in Figure 3.3. The excitation source is a 100 ps pulsed, amplified, frequency doubled diode laser operating at 490 nm (PicoTA 490 nm, PicoQuant & Toptica, Germany) The repetition rate of the PicoTA can be internally adjusted between 5 MHz and 80 MHz. Two CW dump sources were used: for EGFP a 594 nm diode laser (Mambo, Cobolt, Sweden) this had a variable output power adjustable up to 100 mW. CW depletion in mCherry was achieved using a 660 nm diode laser (Flamenco, Cobalt). The excitation and dump lasers were combined using a dichroic mirror (560 DCXR, Chroma, US) and coupled into a 3 m long polarisation-maintaining single mode fibre (Schäfter & Kirchhoff, Germany) and input to the MT200. The beams exiting the fibre and are directed into the microscope objective (UplanSApo 60x 1.2 NA, Olympus) via a dichroic mirror (BS5100, Chroma). Around 50 μL of the sample solution is placed on a cover slip using a dropper and this cover slip placed over the microscope objective. The numerical aperture of the objective, 1.2 (with the water immersion) gives rise to a near diffraction limited spot of area $4.5 \times 10^{-10} \text{cm}^2$ as measured by imaging 20 nm fluorospheres (Alexa). In these experiments the objective scanning function of the microscope is not employed; the $4.5 \times 10^{-10} \text{cm}^2$ spot size and short interaction path provided by the confocal optics allows us to achieve significant fluorescence lifetime shortening with moderate on-sample powers (e.g. 5-25 mW). CW stimulated emission depletion would be unfeasible in the cuvette and 90° streak camera imaging system employed in Chapter 4 for pulsed STED as the significantly larger spot size ($1.67 \times 10^{-6} \text{cm}^2$) would necessitate a CW depletion power upwards of 10 W. The fluorescence incident on the objective following passage through the major dichroic is focused through a 30 μm pinhole via a 160 mm focal length tube lens system. The pinhole and tube lens combination is set to reject fluorescence originating outside the focal plane of interest; the tight confocal imaging ensures most fluorescence comes from the Rayleigh range of the focused DUMP beam. A second lens (160 mm focal length) re-collimates the fluorescence

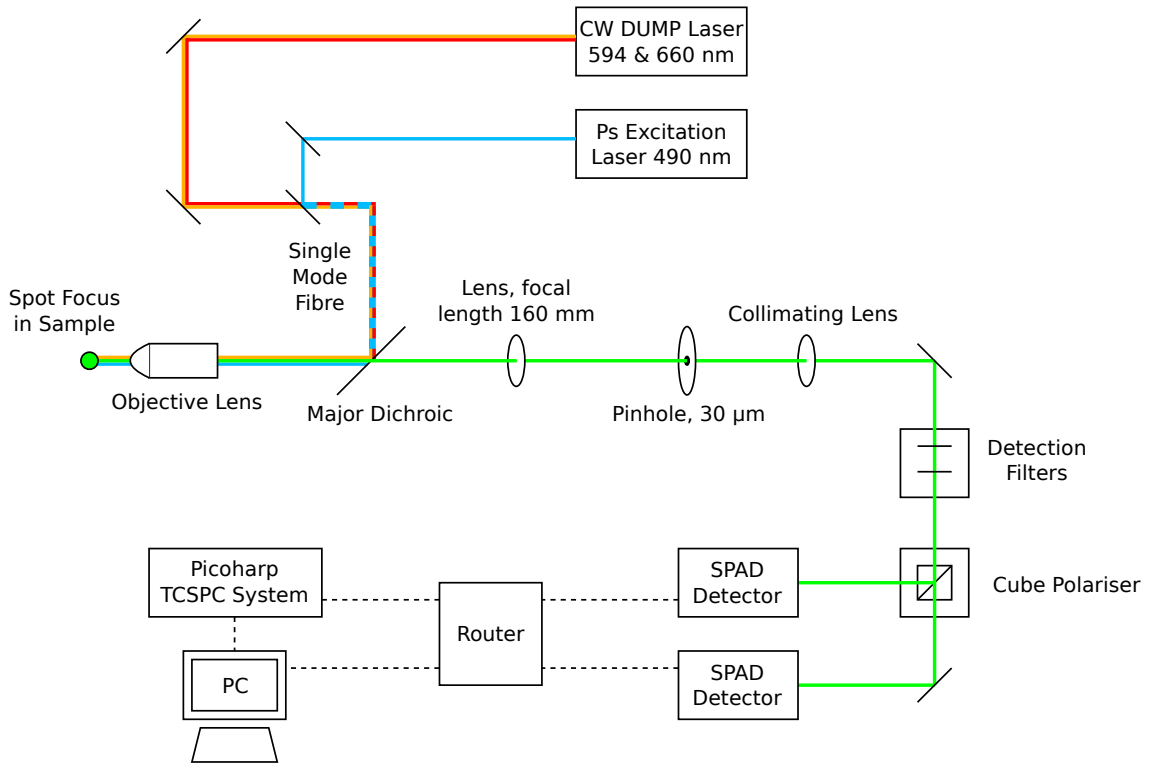


Figure 3.3: MT200 (PicoQuant) system layout used for CW STED experiments of EGFP and mCherry. Excitation beam and DUMP overlap is achieved through use of a 3 m single mode fibre.

which then travels through a set of filters chosen to eliminate laser scatter and isolate the wavelength region of interest, and then to a cube polariser which separates the fluorescence polarised in the parallel and perpendicular directions relative to the input laser polarization. With a slowly rotating diffuser it is not possible to measure the g -factor from the steady state anisotropy; instead estimates can be made using measurements on a fast rotating sample and assuming only minor variation on substitution with the sample of interest. These two fluorescence signals are detected by independent SPAD detectors which feed the signals to a router. The router in turn relays the signal to the TCSPC system (which uses 16 ps bin resolution) and to a computer which controls the process. The start signal for the TCSPC is taken from the laser driver (PDL800B, PicoQuant).

The EGFP and mCherry used were commercial recombinant protein (Biovision

inc., US), and the same batch of each was used for all experiments. A sample of EGFP of concentration 3.50×10^{-5} M and a solution of mCherry of concentration 1.00×10^{-5} M were prepared, both in a solution of phosphate buffered saline (PBS). The PBS was obtained ready-prepared in tablet form (Sigma-Aldrich) and has $\text{pH} = 7.4$. An additional sample of EGFP of concentration 3.06×10^{-6} M and mCherry of concentration 1.00×10^{-6} M in a Size Exclusion Chromatography (SEC) buffer was also prepared. The SEC buffer has $\text{pH} = 8$ and consists of 50 nM Tris(Hydroxymethyl)aminomethane, 150 mM NaCl, 10 nM Benzanidine, 1 mM EDTA and 5% Glycerol.

3.6 Fluorescence Intensity of EGFP following 1PA

Both EGFP and mCherry exhibit bi-exponential fluorescence decays as can be seen with reference to figures 3.4 and 3.5. Single and double exponential fits to the fluorescence intensity decay of EGFP following 1PA is shown in Figure 3.4 along with plots of the weighted residual (See Sections 2.8.3 and 2.8.4 in Chapter 2 for further discussion of fitting procedures). The same is shown for mCherry in Figure 3.5. For both molecules a comparison of the double and single exponential fits and resulting χ_R^2 values demonstrates that to obtain a good fit to the data a double exponential model must be used. The fluorescence lifetimes measured for EGFP and mCherry are in line with previous in-vitro measurements as can be seen in Tables 3.1 and 3.2.

The bi-exponential decay in mCherry is dependent on excitation wavelength as shown in Figure 3.6 though the average lifetime remains approximately constant. The bi-exponential lifetimes in mCherry show a greater separation than in EGFP; the shorter lifetime and quantum yield in mCherry is attributed to twisting of the chromophore [49].

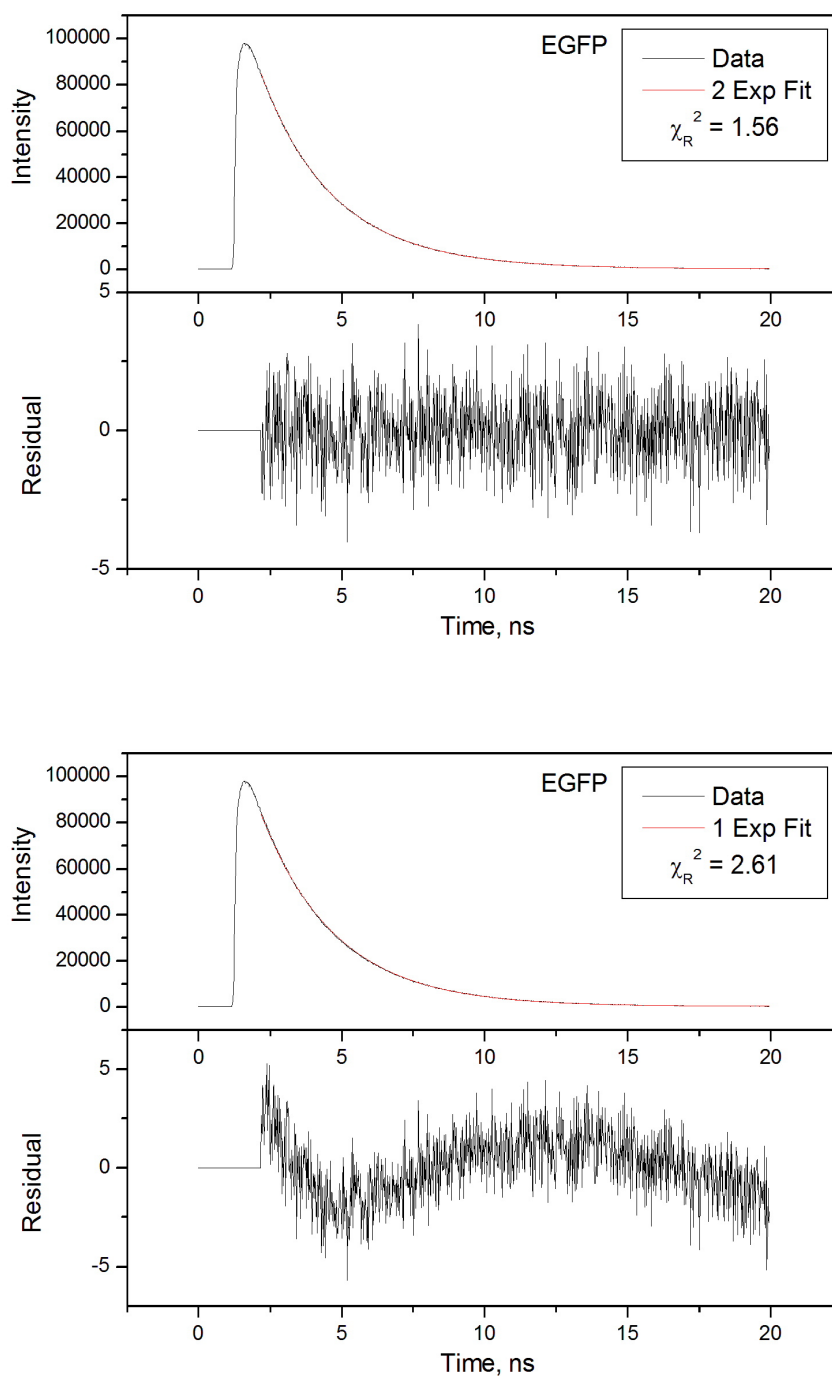


Figure 3.4: Fluorescence intensity decay of EGFP (3.06×10^{-6} M in SEC) following excitation at 490 nm. Top: A double exponential fit to the decay yields lifetimes of 2.79 and 1.71 ns (Amplitudes 0.84 and 0.16 respectively); bottom: A single exponential fit to the decay yields a lifetime of 2.64 ns with higher χ_R^2 and a poorer residual.

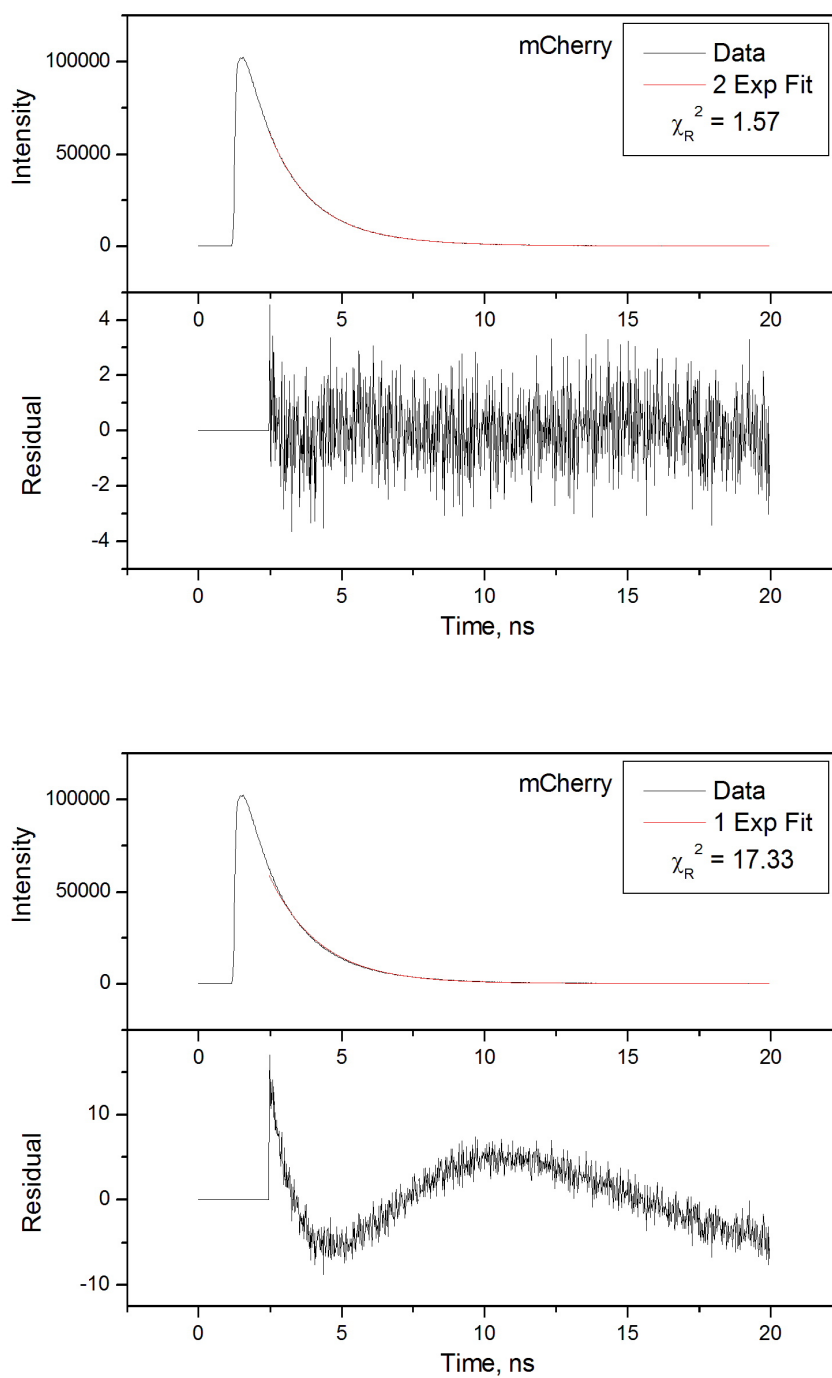


Figure 3.5: Fluorescence intensity decay of mCherry (1.00×10^{-6} M in SEC,) following excitation at 490 nm Top: A double exponential fit to the decay yields lifetimes of 2.57 and 1.38 ns (Amplitudes 0.27 and 0.73 respectively); bottom: A single exponential fit to the decay yields a lifetime of 1.77 ns higher χ_R^2 and a poorer residual.

Parameters	A_1	τ_1 (ns)	A_2	τ_2 (ns)	$\langle\tau\rangle$ (ns)	Reference
(1) EGFP-PDK1 SEC pH=8.0 (2 Photon, NO FRET donor window de- tect	0.503 ± 0.173	3.067 ± 0.11	0.497 ± 0.172	2.43 ± 0.12	2.75	Masters et al. J. AmChem- Soc, 2013 135 7883-90.
(2) EGFP-PDK1 SEC pH=8.0 (1 Photon, NO FRET donor window de- tect	0.622 $+0.253$ -0.153	3.001 $+0.088$ -0.132	0.378 $+0.192$ -0.179	2.304 $+0.271$ -0.178	2.738	Masters et al Sci Signal 2010 2010 3(145):ra78.
(3) EGFP-PDK1 SEC pH=8.0 (2 Photon, ac- ceptor window detect)	1.000	2.738 ± 0.029	NA	NA	2.738	Masters et al. J. AmChem- Soc, 2013 135 7883-90
(4) EGFP SEC (+mCherry) pH=8.0 (1 Photon, donor win- dow NO FRET)	0.653 $+0.258$ -0.079	3.086 $+0.048$ -0.121	0.347 $+0.092$ -0.242	2.426 -0.180 $+0.273$	2.857	Masters et al Sci Signal 2010 2010 3(145):ra78.
(6) EGFP ph 7.2 2- photon 700 nm short pass filter	0.82 ± 0.06	2.88 ± 0.05	0.21 ± 0.01	1.84 ± 0.05	2.68	Hess, Heikal Biophysical J 2003
(7) EGFP PBS buffer 490 nm excite BW detect	0.68	2.93	0.32	1.99	2.62	This work
(8) EGFP PBS buffer 490 nm excite RW detect long pass filter	0.68	2.94	0.32	2.00	2.65	This work
(9) EGFP SEC buffer 490 nm excite BW detect	0.68	2.86	0.32	1.98	2.59	This work

Table 3.1: A comparison between the in vitro fluorescence lifetimes measured for EGFP ((1)-(6)) published data and the present study ((7)-(9)). The results in (7)-(8) were obtained from one set of consecutive data acquisitions in PBS in two different spectral windows to the blue (550 nm short pass filter BW) giving a detection window of 510-530 nm, and red (625 nm /15 nm bandpass filter RW) giving a detection window of 612.5-632.5 nm.

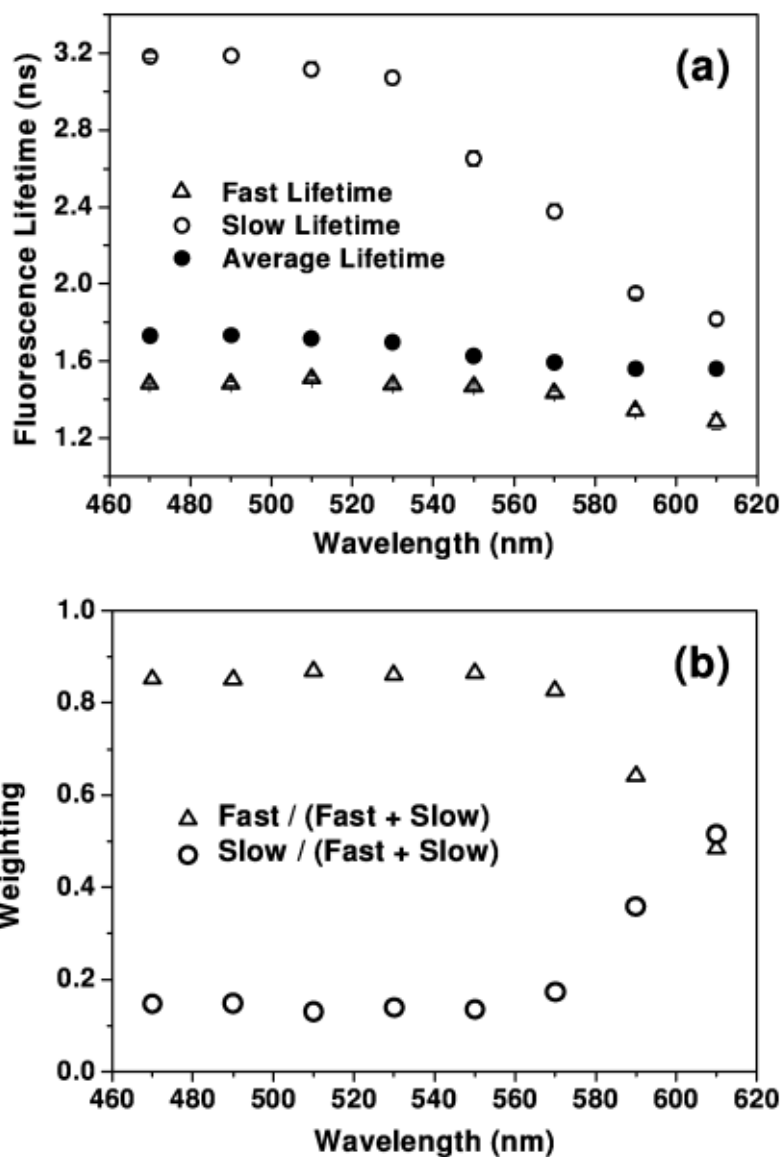


Figure 3.6: Excitation wavelength dependence of the bi-exponential fluorescence decay in mCherry, taken from reference [16].

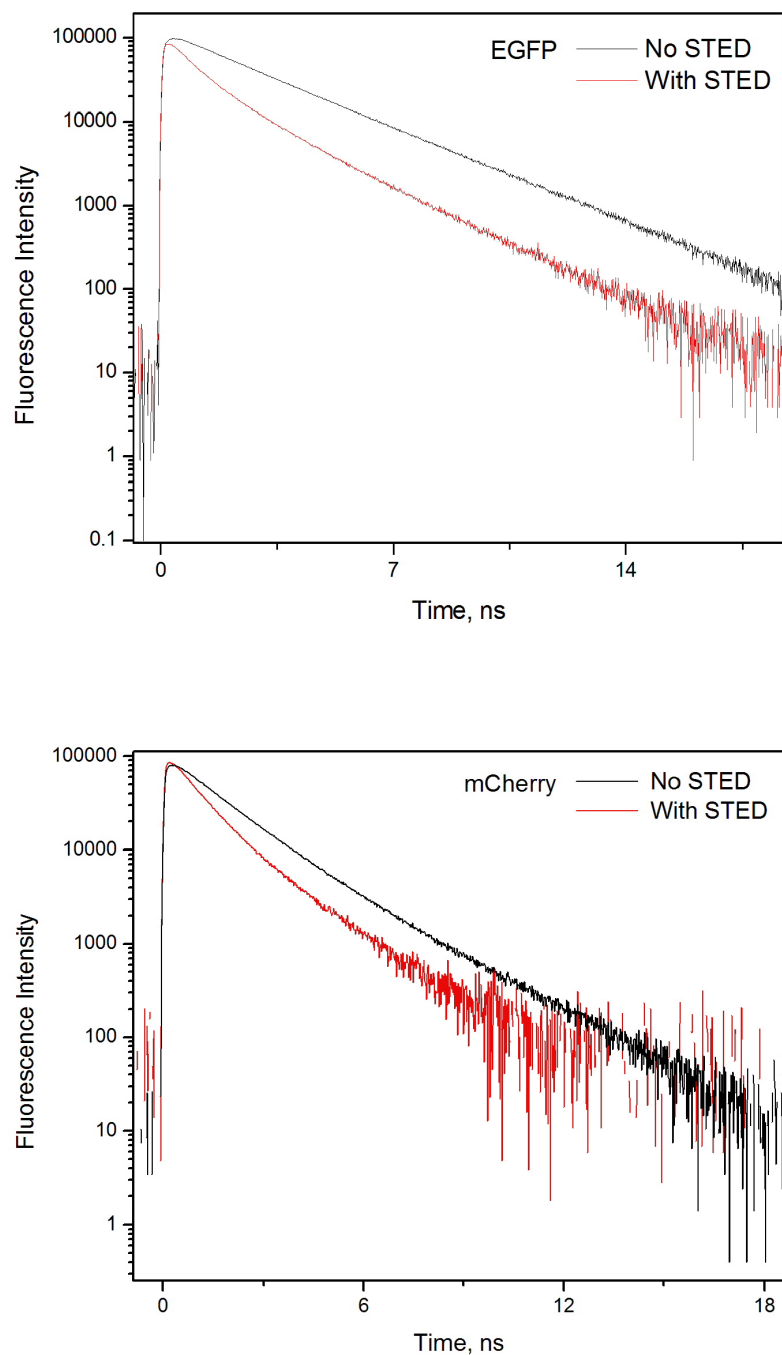


Figure 3.7: Background subtracted fluorescence decays for top: EGFP in SEC; and bottom: mCherry in SEC. Intrinsic Fluorescence Decay (black) and fluorescence decay in the presence of CW depletion (red) of 595 nm (EGFP) and 660 nm (mCherry)

Parameters	A_1	τ_1 (ns)	A_2	τ_2 (ns)	$\langle\tau\rangle$ (ns)	Reference
(1) mCherry 470-619 nm excite	0.16	2.77	0.84	1.47	1.67	Masters et al. 2013 [16]
(2) mCherry-PDK1 630-650 nm detect	0.21	2.50	0.79	1.45	1.68	Masters et al. 2010 [15]
(3) mCherry PBS buffer 490 nm excite 510-630 nm detect	0.36	2.09	0.64	1.30	1.70	This work
(4) mCherry SEC buffer 490 nm excite 510-630 nm detect	0.18	2.59	0.82	1.39	1.61	This work

Table 3.2: A comparison between the in vitro fluorescence lifetimes measured for mCherry ((1)-(2)) published data and the present study ((3)-(4)). Detection in (3)-(4) was made in the observation window between 510 nm long pass and 630 nm short pass filters.

3.7 EGFP and mCherry Fluorescence Intensity Decays in the presence of CW STED

The experiments involving EGFP were undertaken using pulsed 490 nm excitation and CW depletion at 595 nm as described above. A short pass filter (FES 550 Semrock, US) was placed in the optical path before both detectors to block the DUMP, and a long pass filter (HQ 510 Chroma, US) was used to block the PUMP. The experiments involving mCherry also used 490 nm excitation, but used CW depletion at 660 nm. An FES 630 nm filter (Semrock, US) was in this case used before detection to block the DUMP (the HQ 510 filter was again used to block the PUMP).

The CW DUMP intensity was varied between 0 and 23.5 mW for EGFP and 0 and 12.08 mW for mCherry. These powers were measured at the back aperture of the objective; the final on-sample powers are ca. $\frac{1}{3}$ lower than this, but measurement at the back aperture gives a much more repeatable indication of relative power. The powers quoted for the remainder of this chapter are the uncorrected values ie.

measured at the back aperture, except for the quoted cross-section values which have been adjusted such that they are comparable with other published values.

Analysis of the data was performed using the non-linear least squares fitting procedure as described in Chapter 2. Example fluorescence decays are shown for EGFP and mCherry with and without the presence of the depletion beam in Figure 3.7.

The fluorescence lifetimes for EGFP and mCherry in the presence of CW STED are shown in Figure 3.8 and tabulated in Table 3.3 and 3.4. They are both clearly bi-exponential and the two fitted lifetimes in each sample do not show the same power dependence.

From Figure 3.8 it can be seen that the EGFP decay component with the shorter fluorescence lifetime, labelled Q exhibits a more marked shortening with increasing DUMP power as compared to the component with slow fluorescence lifetime, labelled P. A similar behaviour is observed for mCherry. The (weighted) average fluorescence

DUMP Power (mW)	α_P	τ_P (ns)	α_Q	τ_Q (ns)	$\langle\tau\rangle$ (ns)
23.5	0.34	2.21	0.66	0.84	1.31
21.4	0.35	2.22	0.65	0.85	1.33
19.5	0.35	2.24	0.65	0.88	1.35
17.4	0.36	2.26	0.64	0.90	1.39
15.1	0.37	2.26	0.63	0.91	1.42
12.5	0.38	2.30	0.62	0.97	1.48
10.5	0.40	2.34	0.6	1.05	1.56
8.0	0.42	2.39	0.58	1.15	1.67
6.0	0.44	2.47	0.56	1.31	1.82
2.75	0.50	2.57	0.5	1.57	2.07
1.25	0.56	2.66	0.44	1.78	2.27
0	0.68	2.86	0.32	1.98	2.59

Table 3.3: Fitted fluorescence decay parameters for EGFP (3.06×10^{-6} M in SEC buffer) in the presence of the CW DUMP laser.

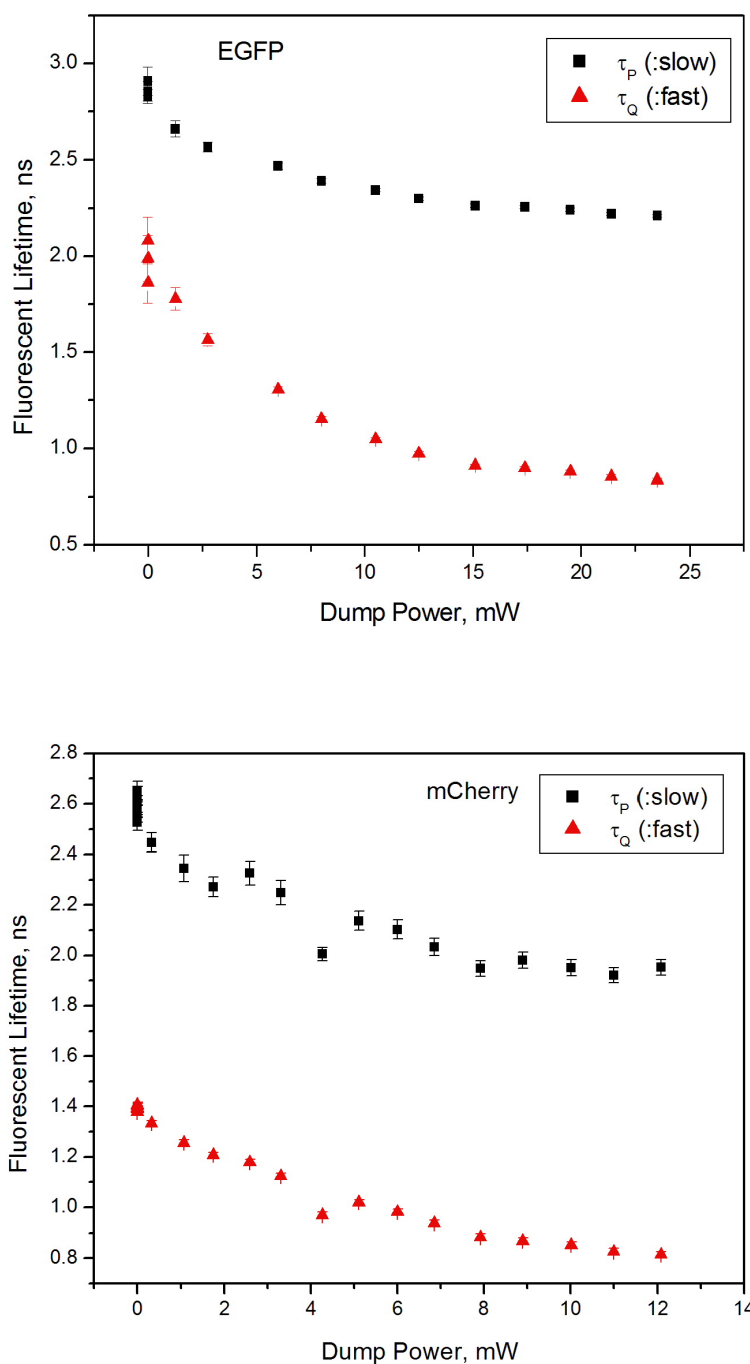


Figure 3.8: Fluorescence lifetimes of the two components of top: EGFP in SEC; and bottom: mCherry in SEC in the presence of CW STED of 595 nm (EGFP) and 660 nm (mCherry). In both EGFP and mCherry these show a greater reduction for the fast lifetime component where a smaller one would be expected if k_S were identical for the two states involved.

DUMP Power (mW)	α_P	τ_P (ns)	α_Q	τ_Q (ns)	$\langle\tau\rangle$ (ns)
12.08	0.22	1.95	0.78	0.81	1.06
11.00	0.23	1.92	0.77	0.83	1.08
10.02	0.23	1.95	0.77	0.85	1.10
8.90	0.22	1.98	0.78	0.87	1.12
7.92	0.24	1.95	0.76	0.88	1.14
6.85	0.21	2.03	0.79	0.94	1.17
6.00	0.20	2.10	0.80	0.94	1.20
5.11	0.19	2.14	0.81	1.02	1.24
4.26	0.19	2.01	0.81	0.97	1.19
3.30	0.16	2.25	0.84	1.12	1.30
2.59	0.17	2.33	0.83	1.12	1.37
1.74	0.20	2.27	0.8	1.21	1.42
1.06	0.18	2.35	0.82	1.26	1.45
0.33	0.19	2.45	0.81	1.33	1.54
0	0.18	2.59	0.82	1.39	1.61

Table 3.4: Fitted fluorescence decay parameters for mCherry ($1 \times 10^{-6} \text{M}$ in SEC buffer) in the presence of the CW DUMP laser.

lifetime in the presence of STED was calculated as

$$\tau_{av} = \tau_P \left(\frac{\alpha_P}{\alpha_P + \alpha_Q} \right) + \tau_Q \left(\frac{\alpha_Q}{\alpha_P + \alpha_Q} \right) \quad (3.7.1)$$

This is shown in Figure 3.9.

A measure of the overall degree of stimulated emission depletion is given by the power dependence of the average fluorescence lifetime (the weighted average of the two component lifetimes). These values are also shown in Tables 3.3 and 3.4 and their variation with DUMP power is shown in Figure 3.9. The lifetime is expected to decrease with increasing DUMP power with the ratio $1/(A+X)$ where X is the DUMP power and A is $1/\tau_f$ i.e. the fluorescence lifetime should tend to zero as the power increases. Re-excitation of the ground state by the DUMP should not

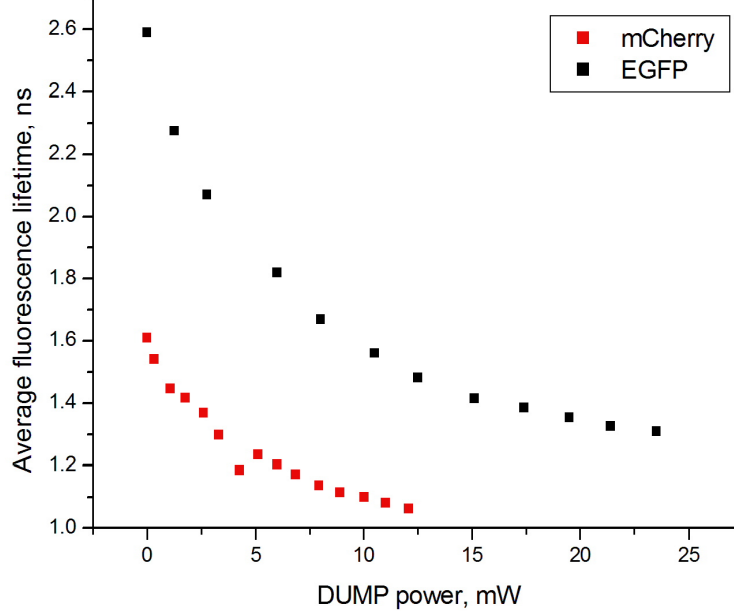


Figure 3.9: (Weighted) average fluorescence lifetimes for EGFP in SEC and mCherry in SEC in the presence of CW STED of 595 nm (EGFP) and 660 nm (mCherry).

be evident unless the fluorescence lifetime is reduced to the point where it becomes comparable with the ground state relaxation time. The STED rates of the two components are calculated using the equations

$$k_Q = \frac{1}{\tau_{f(Q)}} - \frac{1}{\tau_{f(Q)}^0} \quad (3.7.2)$$

$$k_P = \frac{1}{\tau_{f(P)}} - \frac{1}{\tau_{f(P)}^0} \quad (3.7.3)$$

where $\tau_{f(P)}$ and $\tau_{f(Q)}$ are the fluorescence lifetimes of the respective components in the presence of the dump and $\tau_{f(P)}^0$ and $\tau_{f(Q)}^0$ are the intrinsic fluorescence decay lifetimes. These are shown in Figure 3.10 and in both EGFP and mCherry show an initial linear, but different, increase with increasing DUMP power. The Q component shows a greater increase with increasing DUMP in both samples. In both the initial linear rise in k_Q and k_P is over a finite DUMP power range up to ca. 15 mW DUMP power in EGFP and 8 mW in mCherry. Above these powers there is a less marked increase in k_Q whilst k_P is, to within experimental error, power independent. The

average STED rates were calculated using

$$k_{S(av)} = \frac{1}{\overline{\tau_f}} - \frac{1}{\overline{\tau_f^0}} \quad (3.7.4)$$

where $\overline{\tau_f}$ and $\overline{\tau_f^0}$ are the average fluorescence lifetime in the presence of the dump and for the intrinsic fluorescence decay, respectively. These values are shown in Figure 3.11 for the EGFP and mCherry. The two samples show a similar trend with the average STED rate in mCherry increasing with DUMP power to a slightly greater extent up to 12 mW where it is 14% higher than EGFP.

The pre-exponential factors of the fits are shown in Figure 3.12; these show a marked difference in their variation with the DUMP power. The anticipated behaviour for two different emitting states would be varying induced decay rates. The amplitude of each decay would be expected to be proportional to the population of each component that is excited by the PUMP pulse; but to be wholly independent of the DUMP laser as this is not resonant with the PUMP transition. In mCherry the amplitude decay components α_P and α_Q are to within experimental error constant across the entire DUMP range. In EGFP α_P in SEC shows a marked drop with a corresponding rise in α_Q ; at high DUMP powers α_Q is ca. 0.65 (α_P ca. 0.35) in marked contrast to the intrinsic fluorescence decay $\alpha_Q = 0.32$ and $\alpha_P = 0.68$. For fluorescence decays involving two distinct populations the contribution of each to the total fluorescence emission is given by the product of their observed amplitude and lifetime. The DUMP power dependence of these fractions

$$\frac{\alpha_P \times \tau_{f(P)}}{\alpha_P \times \tau_{f(P)} + \alpha_Q \times \tau_{f(Q)}} \quad (3.7.5)$$

and

$$\frac{\alpha_Q \times \tau_{f(Q)}}{\alpha_P \times \tau_{f(P)} + \alpha_Q \times \tau_{f(Q)}} \quad (3.7.6)$$

are shown in Figure 3.13. With differential STED in two populations some variation in these parameters would be expected as the population experiencing a greater STED rate would have a shorter lifetime and its fractional contribution to the total decay would diminish. For mCherry the fractional contribution to total fluorescence emission of component Q (Equation 3.7.6) shows an approximately linear decrease

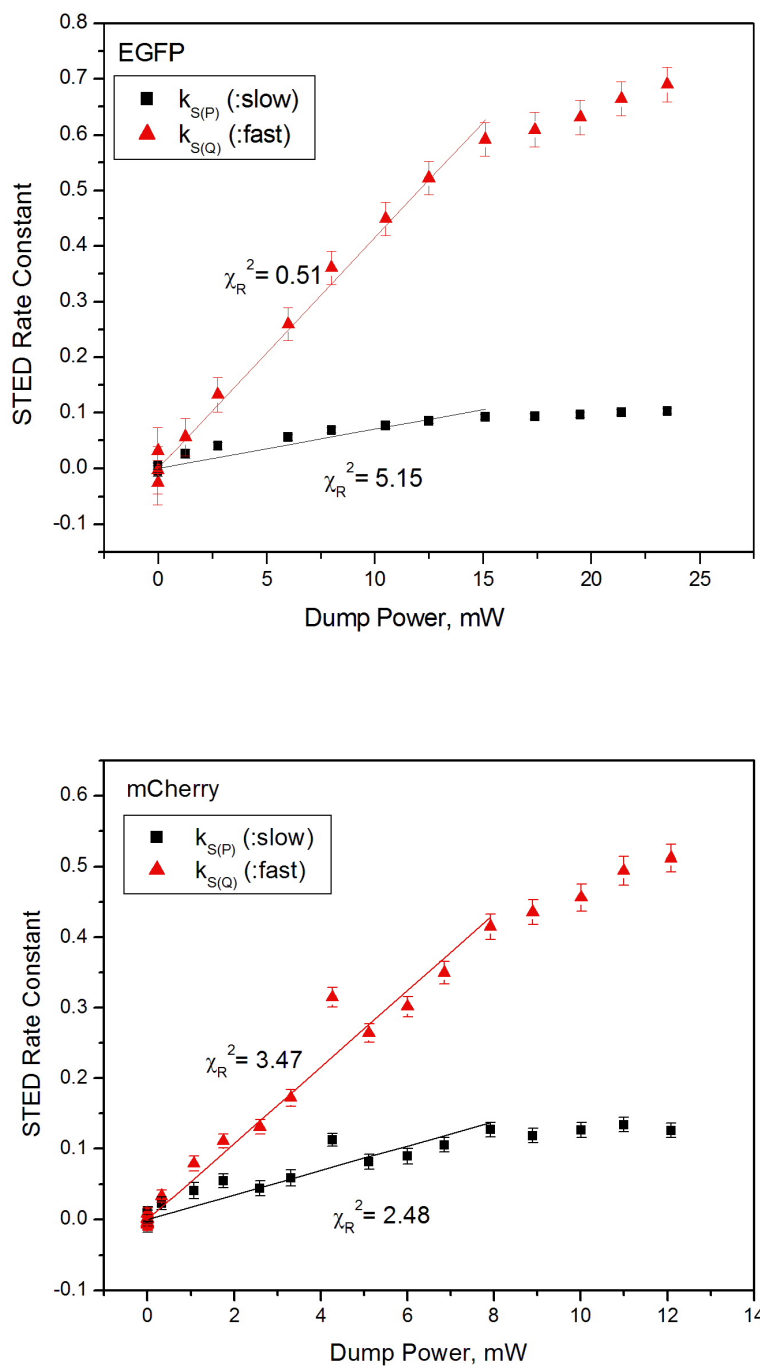


Figure 3.10: STED rates of the two components of top: EGFP in SEC; and bottom: mCherry in SEC. Both show the same behaviour; a linear increase up to ca.15 mW DUMP power in EGFP and 8 mW in mCherry, while above these powers there is little variation in k_P .

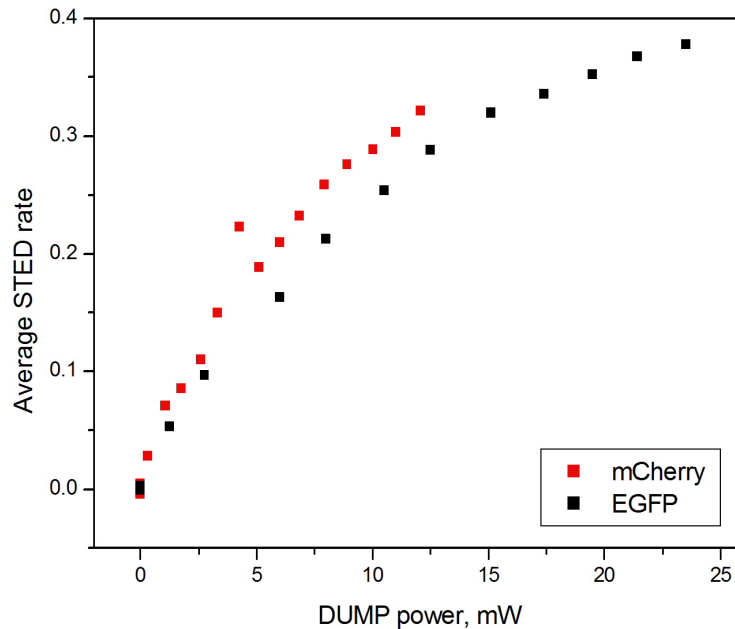


Figure 3.11: Average STED rates of EGFP in SEC (black) and mCherry in SEC (red). For both at lower STED powers the deviation from the expected linear behaviour is not substantial, but as the STED rate increases for both EGFP and mCherry substantial deviation from the expected behaviour is observed. Little difference between the two samples is observed.

across the DUMP power range; at high DUMP powers the fractional contributions of Q and P remain approximately constant at ca. 0.6 and ca. 0.4 respectively. In EGFP this behaviour is not observed; the Q fraction increases rapidly as the DUMP power is increased to ca. 5 mW, this is followed by a slow increase leading at higher DUMP powers (ca. 10-24 mW) to approximately constant values for the Q and P fractions of ca. 0.58 and 0.42 respectively. This is despite the fact that the STED rate for component Q continues to increase with STED power for all measurements taken. This large difference in the STED power dependence of the EGFP and mCherry lifetime amplitudes contrasts starkly with the average STED rate described earlier where only minor differences between EGFP and mCherry were observed.

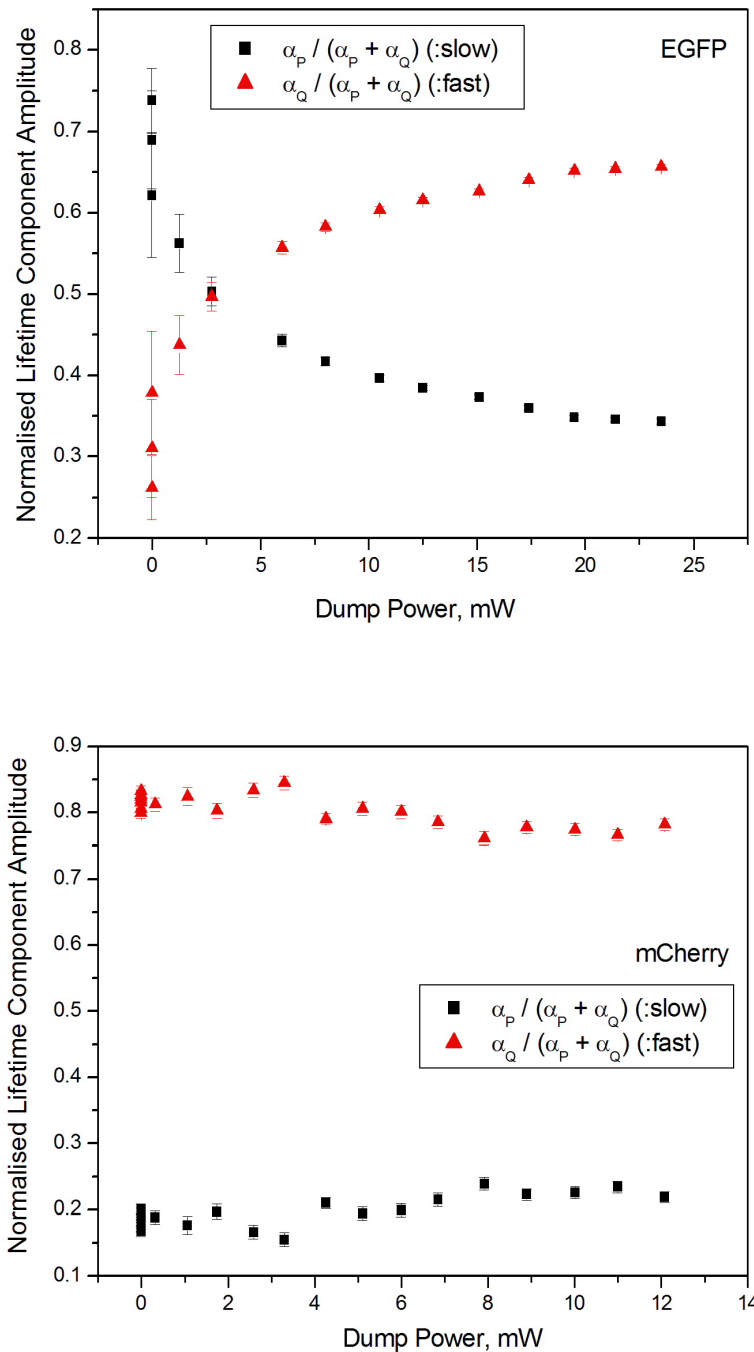


Figure 3.12: Fluorescent lifetime component amplitudes of top: EGFP in SEC; and bottom: mCherry in SEC as a function of STED power.

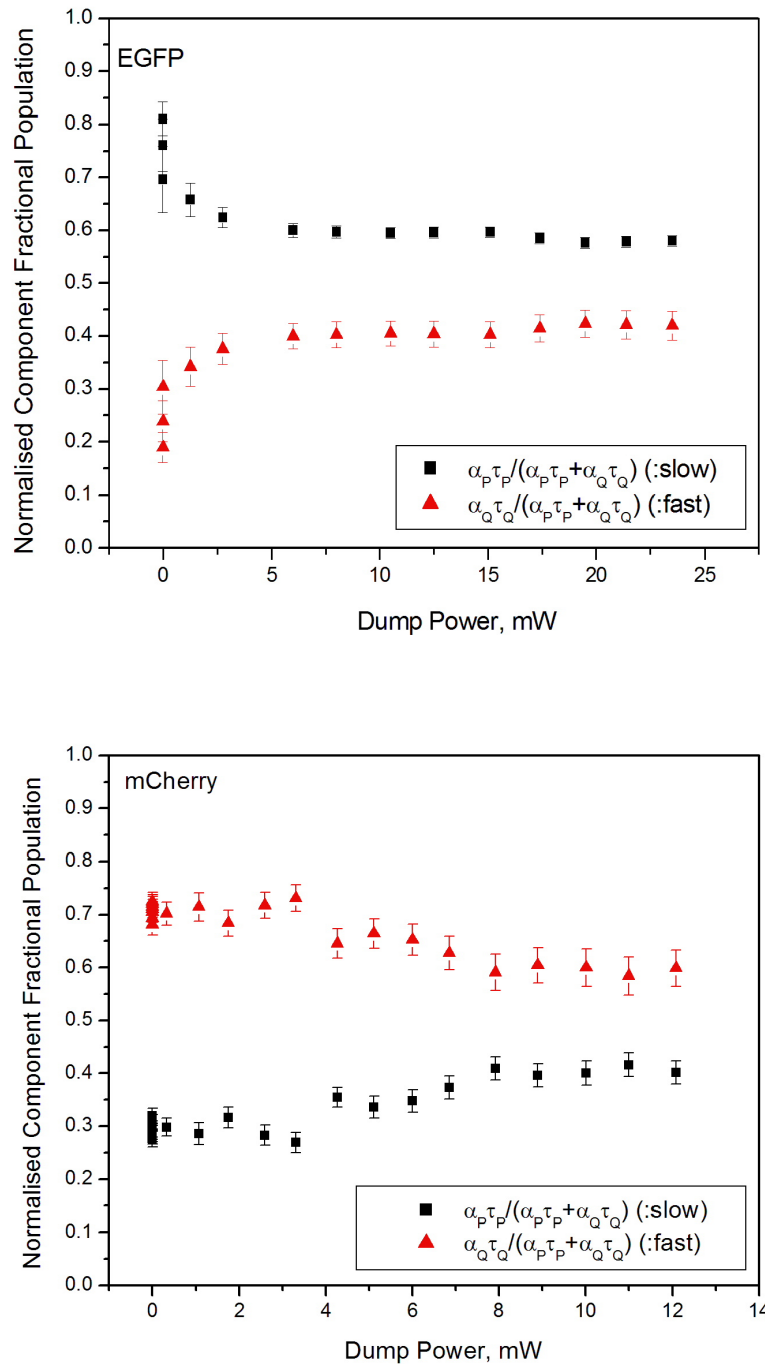


Figure 3.13: Fractional contribution to the fluorescence intensity of the components of top: EGFP in SEC; and bottom: mCherry in SEC. Variation with DUMP power of ca 10% is observed for mCherry. Although in EGFP the observed lifetime continues to decrease with increased STED power the fractional contribution to the fluorescence of component Q levels off at high STED powers.

This apparently anomalous behaviour for EGFP was initially thought to be attributable to its photophysics. If there is a significant difference in emission spectrum of the two components then observation in different spectral windows would give different amplitudes of each component. This is complicated by the need to strongly filter out the DUMP laser wavelength. If only a small spectral difference between the two states exists then this should be maximised at the very red edge of the emission spectrum, where the greatest difference in ratio of amplitudes would be seen. To this end two different approaches were taken.

Firstly, CW depletion experiments were carried out in a PBS buffer and the perturbed fluorescence decays were recorded in spectral windows to the red (617.5-632.5 nm) and blue (510-550 nm) of the DUMP wavelength. The fluorescence lifetimes and amplitudes are shown in Figure 3.14. In both observation windows the same apparently anomalous depletion dynamics were observed.

Secondly, CW depletion experiments also in PBS buffer were carried out at the DUMP wavelength 660 nm and the results compared to previous results (which used a DUMP wavelength of 595 nm) in Figure 3.15. Again, no significant difference between the two datasets was observed, although there is a high degree of noise in the 660 nm DUMP dataset as the degree of STED at this wavelength is low. Additionally, for the 660 nm DUMP dataset a major dichroic that was reflective of both laser wavelengths but allowed transmission of fluorescence was not available so approximately 50% partially reflective beam splitter was used allowing greater CW laser breakthrough, which added a significant background and its associated noise to the measured decays.

In CW STED the DUMP laser would not be expected to affect the relative initial amplitudes of the components, as immediately following the excitation pulse at $t = 0$ no STED has yet taken place. However TCSPC measurements comprise the repeated measurement of excitation and detection coincidences averaged over numerous excitation events (typically ca. 5 million). In the current experiments the DUMP field is present throughout. Were relaxation of the P and Q components to

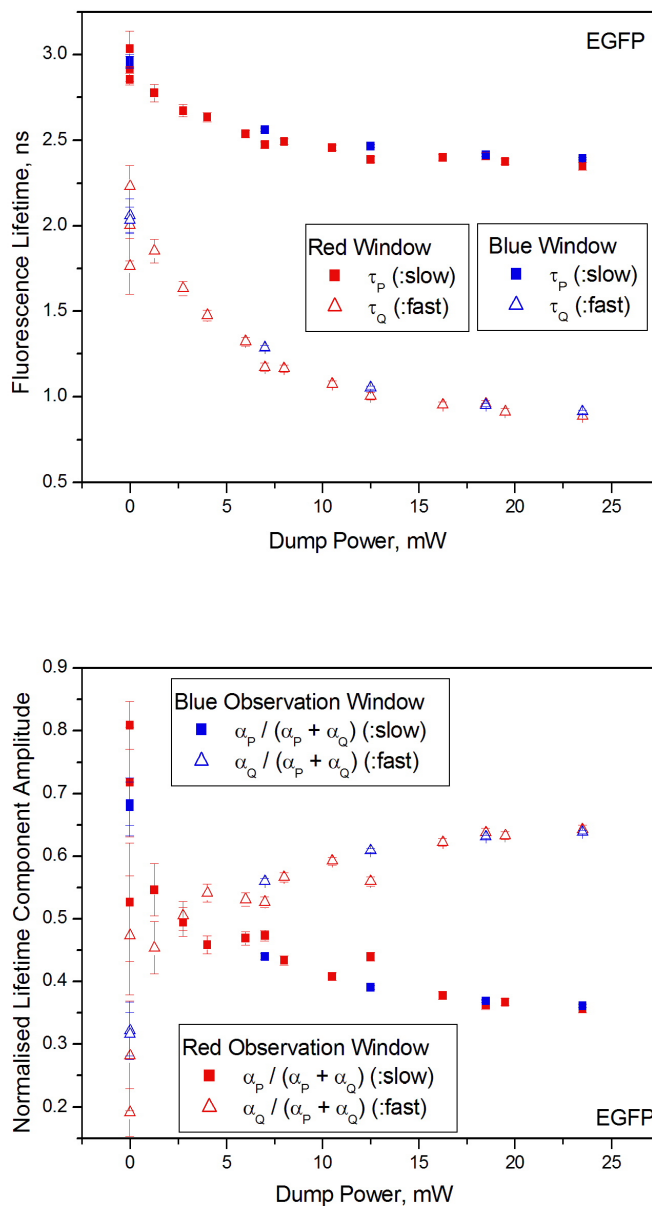


Figure 3.14: Initial fluorescence amplitudes of components of EGFP in PBS following 1PA of 490 nm and CW STED using DUMP of wavelength 595 nm observed at two different emission windows: a blue observation window 510-550 nm, and a red observation window 617.5-632.5 nm. No change in the initial amplitudes was observed between the two windows.

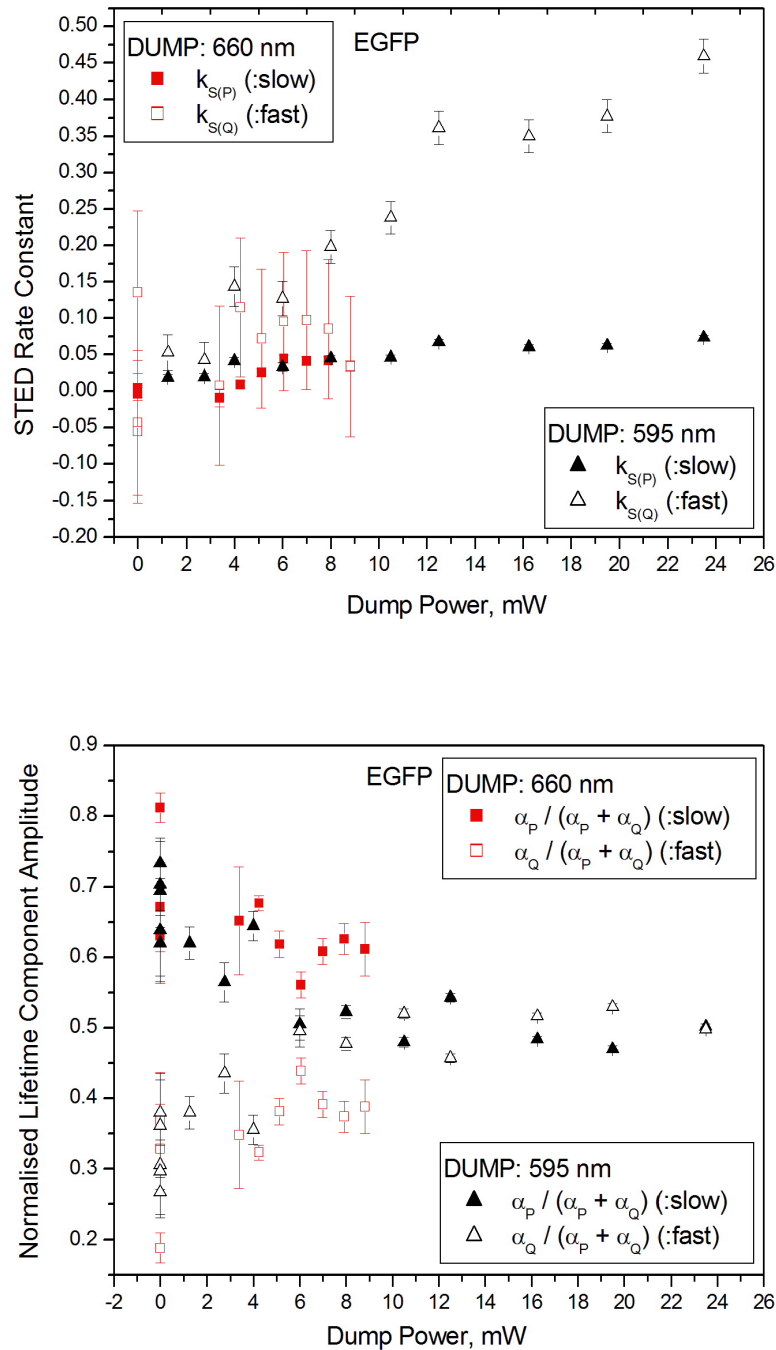


Figure 3.15: Top: STED rates; and bottom: initial amplitudes of the components of EGFP in PBS using DUMP of wavelengths 660 and 595 nm. A similar trend between the two datasets is observed.

the ground state to be influenced by the CW DUMP either by partial photobleaching or by the removal of the excited population to states other than the ground electronic state, the steady state proportions of the P and Q populations might see some power dependent variation. This effect could be observed only if the ground state population did not fully recover between successive PUMP pulses. Also as the DUMP intensity dependent fluorescence lifetime data (above) were collected sequentially with decreasing DUMP power, it is possible that at lower DUMP powers cumulative effects (e.g. an increase in sample concentration due to evaporation or permanent change to the ground state population) might lead to a systematic error. Repeated measurements of the fluorescence decays in the absence of the DUMP were taken across the time course of subsequent experiments with the intermediate power measurements interspersed and no variation in the recorded data was observed.

The probability of re-excitation of molecules involved in the CW depletion cycle depends both on the excitation frequency for each molecule and translational diffusion rates of the fluorescent proteins in the solution. Translational diffusion allows previously excited molecules to diffuse out of the excitation region and new molecules to diffuse in. An estimation of the diffusion time t_D can be made as follows from the diffusion constant D , using a one-dimensional solution to Fick's second law:

$$t_D = \frac{x^2}{2D} \quad (3.7.7)$$

where x is the average net distance travelled. The diffusion constant for EGFP in water is $87 \times 10^{-12} \text{ m}^2\text{s}^{-1}$ [50], giving the diffusion time across the 120 nm radius of the excitation spot focus as 83 μs . With a pulse repetition rate of 20 MHz there will be 50 ns between pulses; a comparison of these two times suggests that a molecule will remain in the excitation region for an average of ca. 1500 laser pulses. As these experiments operate in the limit of weak excitation (see Chapter 1) only a very small proportion of the molecules will be excited. As stated in Chapter 1 the probability of excitation can be estimated from the saturation parameter

$$S_{abs} = \frac{\sigma^{(1)} E}{Ah\nu} \quad (3.7.8)$$

where E is the PUMP pulse energy, A is the focal area of the PUMP ($4.5 \times 10^{-10} \text{cm}^2$), $h\nu$ the PUMP photon energy and $\sigma^{(1)}$ is the absorption cross section of EGFP at the excitation wavelength. These values correspond to $S = 0.01$, an excitation probability of 1% per pulse. It can therefore be estimated that the average number of excitations a single molecule experiences prior to diffusing out of the excitation region varies from 60 to 4 over an 80 MHz to 5 MHz excitation rate. Plots of the variation of the apparent STED rates k_P and k_Q , the pre-exponential factors and fractional contributions of the P and Q components with DUMP power and PUMP repetition rate are shown in Figures 3.16 and 3.17. No discernible PUMP repetition rate could be inferred. Therefore the changes to the ground state population would have to be faster than this, of the order of a single cycle, suggesting that build up of ground state population change is not responsible for the observed behaviour of EGFP. All repetition rates show similar anomalous behaviour.

3.8 Fluorescence Anisotropy induced by STED

It is clear from the experimental results so far that the CW STED dynamics of EGFP do not conform to the simple model proposed. It has so far been assumed that as the fluorescent protein rotational diffusion dynamics are slow, a depletion rate averaged over the initial orientational distribution of EGFP and mCherry transition dipoles would be an accurate model of the stimulated depletion dynamics of the two states involved in both fluorescence decays. One consequence of this approximation is that the fluorescence anisotropy of EGFP and mCherry would be no different from that experienced in the absence of STED. To test this, measurements of the intrinsic and DUMPED fluorescence anisotropy of both fluorescent proteins were performed; the results are shown in Figure 3.18. Measurement of fluorescence anisotropy in an inverted confocal microscope as opposed to the 90° excitation detection geometry employed in Chapter 2 is a more challenging undertaking, as the two SPAD detectors do not have exactly the same response, spectral sensitivity, and degree of after-pulsing [51]. The anisotropy decays in Figure 3.18 have not been corrected for G

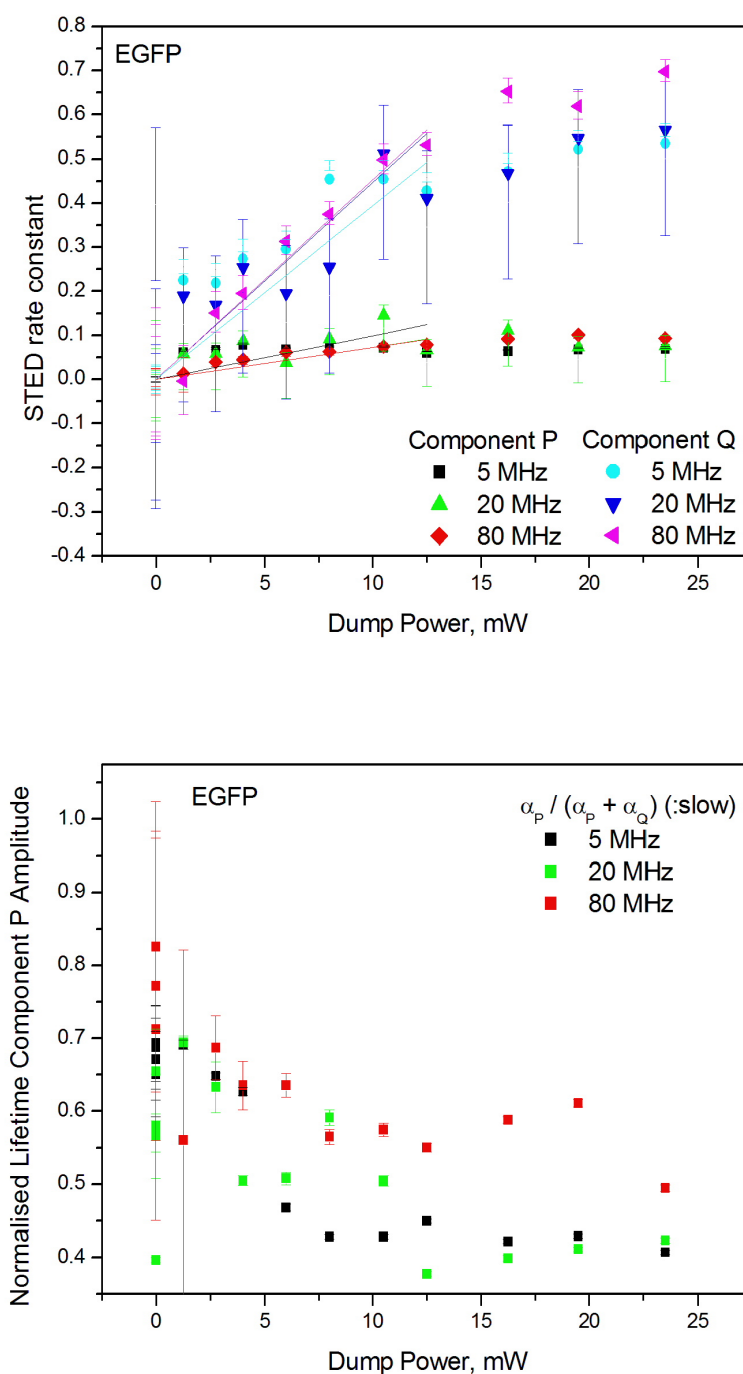


Figure 3.16: Top: STED rates; and bottom: initial amplitudes of the components of EGFP in PBS using PUMP frequencies of 5, 20 and 80 MHz. No discernible correlation of experimental observations with repetition rate was observed. For all repetition rates the same large difference in STED rate constant is observed as in Figure 3.10.

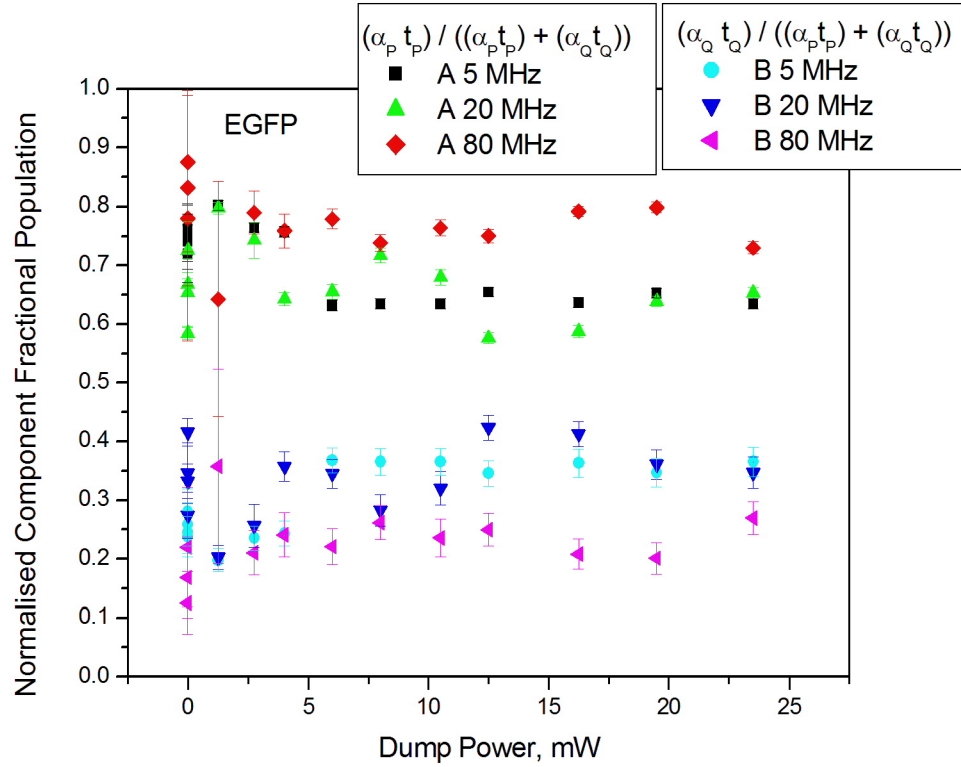


Figure 3.17: Fractional population of the components of EGFP in PBS using PUMP frequencies of 5, 20 and 80 MHz. This shows the same anomalous behaviour as Figure 3.13, as described in the text.

factor effects (see Chapter 2) and there is an appreciable (pre-excitation) background which affects the anisotropy at longer times due to low signal levels. Background consists of dark count of the detector (small) after pulsing (significant) and scattered DUMP light which as it is from a CW source contributes to the detected photon count at all times. In the absence of STED the fluorescence anisotropy of EGFP and mCherry show a slow single exponential decay, however in the presence of STED significant additional depolarization is seen to occur. This is wholly as a result of the orientation dependence of EGFP and mCherry lifetimes. Subtracting the small degree of intrinsic rotational diffusion from each of the decay curves yields a clear picture of the anisotropy change induced by the CW DUMP. These results are shown in Figure 3.19. Both mCherry and EGFP show similar degrees of DUMP induced depolarization. It is clear that at both low and high CW depletion powers, orientation dependent lifetime effects are in play and inclusion of orientational effects

is necessary.

3.9 Orientationally Dependent Lifetimes

In light of the apparent breakdown of the assumption of a single fluorescence decay rate for all molecular orientations as indicated by the fluorescence anisotropy and described in the previous section, incorporation of the angular dependence of the fluorescence lifetime becomes necessary. As described previously the expressions for the fluorescence intensity decay allowing for the orientational dependence of the STED rate (equation 3.4.1 to 3.4.7) contains a term of the form

$$\int_0^{\pi} \cos^2 \theta \exp \left(-(k_S^i \cos^2 \theta)t \right) \sin \theta d\theta d\phi \quad (3.9.1)$$

where the presence of angular terms in the exponent prevents simple analytical solution of the fluorescence intensity decay. The requirement to perform this integration numerically prevents the fitting of the experimental intensity decay measurements using any standard analysis software. The approximate form of the fluorescence intensity decay can be inferred however by the fact that experimental data fits well to a double exponential decay. This is the case for high and low DUMP powers despite the fact that the intrinsic (undumped) decay already contains two exponential components.

Close inspection of Equation 3.9.1 shows that individual molecules should still exhibit a bi-exponential decay but with each lifetime reduced by STED by an amount that is dependent on the orientation, θ . The sum intensity of all such molecules may still appear to be bi-modal with a faster component that represents some weighted average of all the individual faster decay times and a slower decay component that is similarly dependent on all the slower decay component lifetimes.

It is conceivable therefore that the discrepancies between the real intensity decay and the orientationally averaged model described earlier are more quantitative than qualitative. To investigate this quantitative discrepancy, theoretical intensity decays

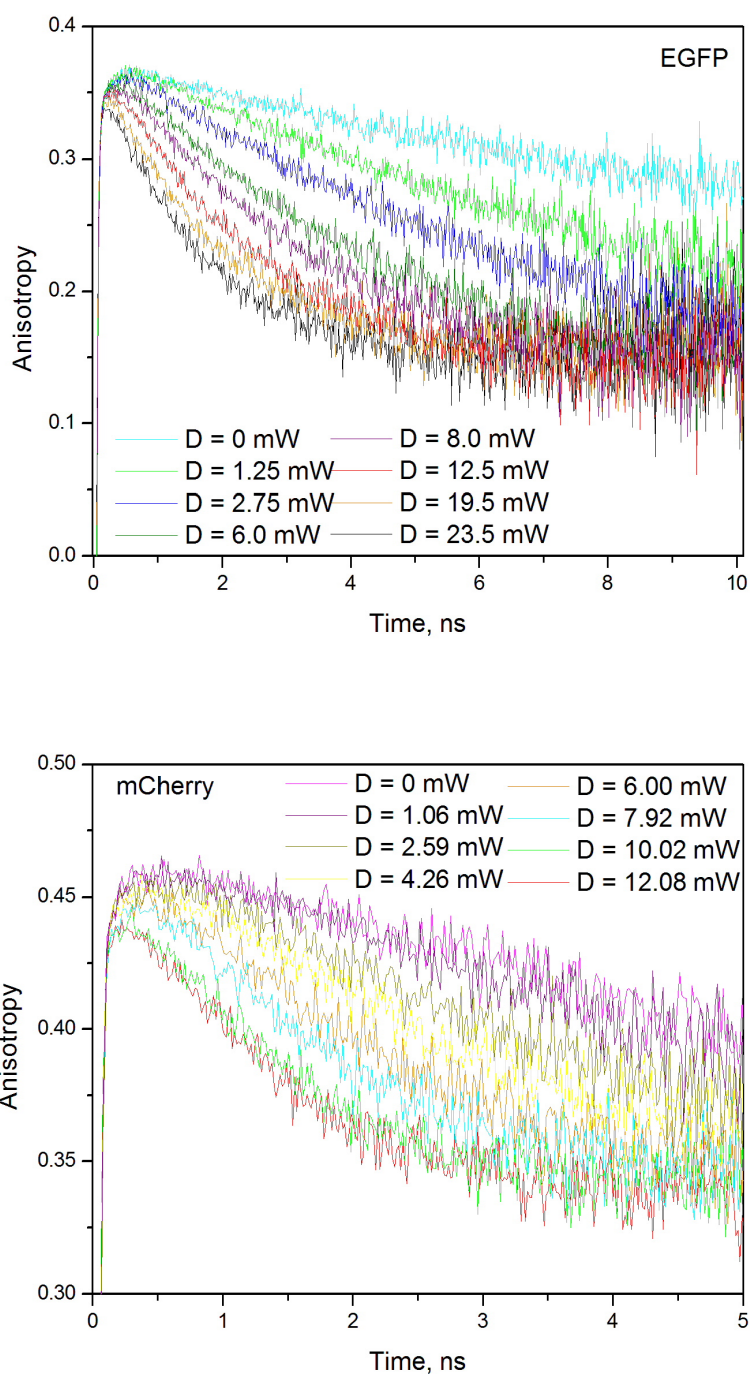


Figure 3.18: Anisotropy decays for top: EGFP; and bottom: mCherry with DUMP powers ranging from 0 to 23 mW (EGFP) and 12 mW (mCherry). STED introduces a rapid decay component into the anisotropy where the decay rate and amplitude increase with increasing DUMP power.

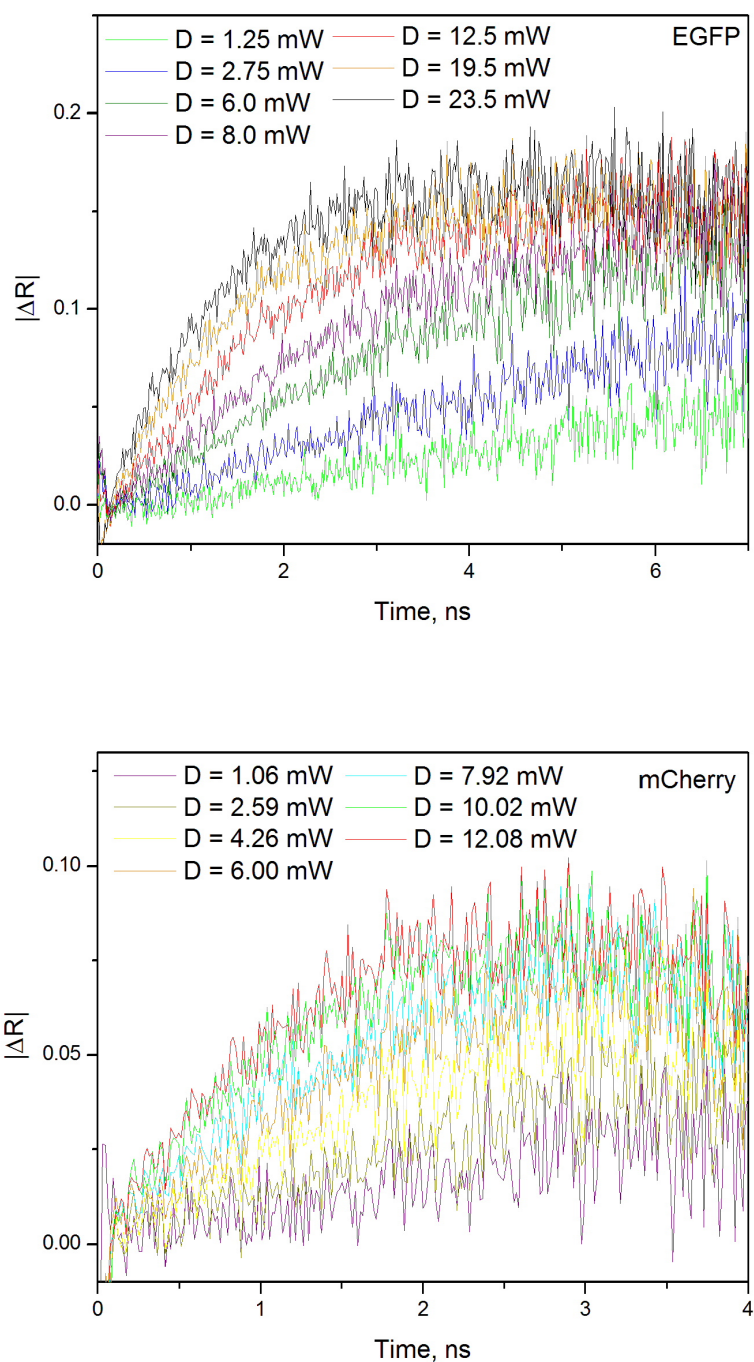


Figure 3.19: CW STED induced anisotropy change for top: EGFP; and bottom: mCherry with DUMP powers ranging from 0 to 23 mW (EGFP) and 12 mW (mCherry). Alternate demonstration of the power dependence of the rapid decay component in anisotropy.

were produced by performing the above integration numerically using a program developed by Dr R J Marsh using Mathematica (unpublished work) for a predetermined set of input parameters i.e.. relative populations, fluorescence lifetimes, and radiative decay rates as described in Section 3.10. The resulting theoretical intensity decays were then fitted to double exponentials in an identical manner to the experimental data. The obtained decay parameters were analysed in an identical manner to the previous analysis and the results obtained compared with the known input parameters.

3.10 Simulated data

Given parallel PUMP and DUMP polarisations, a $\cos^2 \theta$ excitation probability (single photon maximum) and neglecting orientational diffusion the theoretical fluorescence intensity from two excited state populations is given by

$$I_{\parallel} + 2I_{\perp} = \sum_{i=1}^2 N_i(0) \exp(-k_{fi}t) \frac{3}{4\pi} \int_0^{\pi} \cos^2 \theta \exp(-(S'_i \cos^2 \theta)t) \sin \theta d\theta \quad (3.10.1)$$

where $N_i(0)$ is the percentage population of state i, $k_{fi} = 1/\tau_{fi}$ where τ_{fi} is the undumped fluorescence lifetime of state i, and S'_i is the depletion rate of state i and is the CW equivalent of the saturation parameter in pulsed excitation/STED (see Chapter 4). It is related to the STED cross-section σ_S and STED power P_{DUMP} by

$$S' = \frac{\sigma_S P_{DUMP}}{h\nu A} \quad (3.10.2)$$

The input parameters for the populations and fluorescence lifetimes were obtained from an average of all the undumped measurements.

As the earlier analysis indicated the possibility that the STED rates were significantly different for the two states in both EGFP and mCherry, allowances for this possibility were included in the simulations. This was incorporated in making the STED rate for component Q a fixed ratio of that of component P. The numerical integration of Equation 3.10.1 over θ and ϕ is repeated for selected values of S (0.01,

0.1, 0.2, 0.3, 0.5, 0.7, 1.0, 1.2, 1.6 and 2.0 ns⁻¹) and values of t between 0 and 20 ns in steps of 0.05 (simulating a TCSC histogram). The range of these parameters was chosen to reflect those used in the experiments. As this involves repeating the numerical integration 4000 times to reproduce a single STED experiment simulation of the data in this approach is computationally intensive. Analysis was therefore restricted to one dataset each for EGFP and mCherry and only repeated for ratios of $S'_Q : S'_P$ of 1, 2 and 5.

Once the simulated intensity decays were generated for the desired set of input parameters double exponential decay fits were performed on them using the same analysis software and approach as with the experimental data, thus obtaining fluorescence decay rates and amplitudes that can be analysed in an identical manner as previously with the experimental data, where no orientational dependence of the decay rate was assumed. Comparison of the obtained STED rate constants to those input in the simulations then indicate how much discrepancy from the actual rates had been caused by this assumption.

Figure 3.20 shows the new simulated data for $S'_Q : S'_P = 1 : 1$ with (top) low levels of STED ($S'=0.3 \times 10^9 \text{s}^{-1}$) and (bottom) high levels of STED ($S'=2.0 \times 10^{-9} \text{s}^{-1}$) and the respective fits to a double exponential decay. It can be seen that in the case of low STED the simulation is virtually indistinguishable from a double exponential decay, and in the case of high STED is virtually indistinguishable up to ca. 8 ns. Beyond this point the approximation begins to break down, but these distortions may well not be observable over measurement noise as they are principally located in the tail of the decay.

The results obtained were then compared with the previous analysis to see if the observation of substantially different radiative rates for the two emitting species seen there is replicated using this methodology or was just the result of ignoring the angular dependence of the lifetime. As simulated data is a function of the STED rate S' and the experimental data is a function of DUMP power which is proportional to S' the X axis of one set (the simulations) is scaled to reach the best agreement

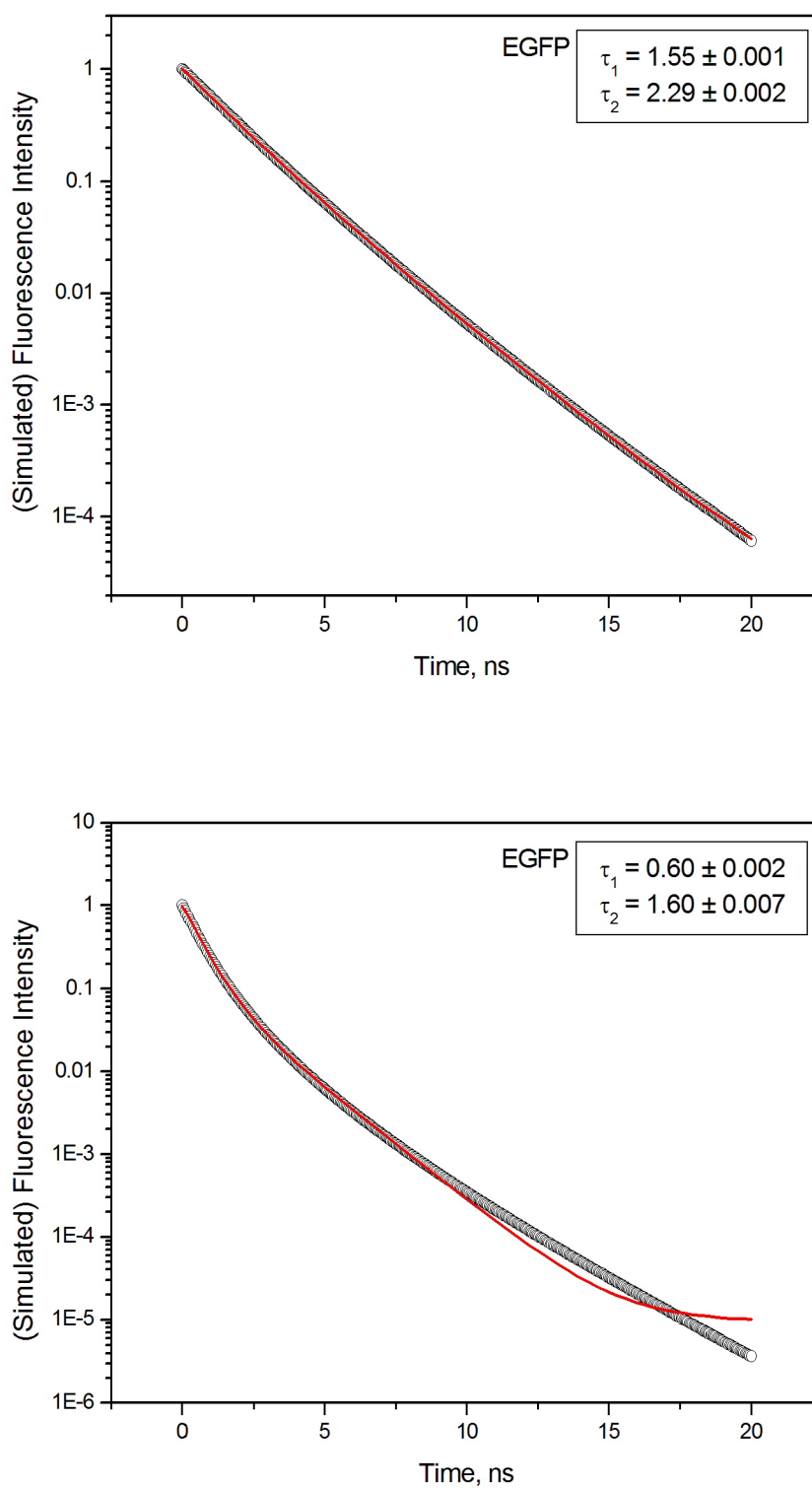


Figure 3.20: Simulated data including orientational averaging effects for EGFP with top: low levels of STED; and bottom: high levels of STED. It can be seen that both cases show a very good fit to a double exponential decay up to ca. 8 ns.

if any between the two sets (in effect adjusting the STED cross-section to reach agreement). The results are shown in Figures 3.21 to 3.25.

It can be seen that the mCherry results fit consistently between the simulations generated for radiative rate ratios of 2 and 5. This remains the case when a common scaling factor between S' and DUMP power is used to fit all of the experimentally measured parameters i.e. the scaling is equal in Figures 3.21 to 3.25. This would suggest that the approach taken of simulating data with the inclusion of the angular dependent lifetime and fitting the obtained results to a double exponential is valid. The fact that all the obtained measured parameters for the mCherry decays consistently suggest that the radiative rate (STED rates) for the two populations vary by a factor of between 2 and 5 (both those dependent on lifetime and decay amplitude). A more precise determination is limited by the noise on experimental data points and therefore simulation of additional ratios was deemed unwarranted. The results suggest that the observation of this difference is a real phenomena and not due to distortions incurred by fitting a double exponential to the non-exponential intensity decay. This leads to a value for the cross-section of mCherry of $8.5 \times 10^{-19} \text{ cm}^2$ for component P, and therefore $1.7 \times 10^{-18} - 4.3 \times 10^{-18} \text{ cm}^2$ for component Q.

Considering just the result for previous analysis with no orientational effects, the lifetime reduction of the two states of mCherry would suggest a difference in the radiative rates of approximately 3 (see Figure 3.10). For this parameter in mCherry the two analytical approaches show broad agreement. The amplitudes for each decay component in mCherry (see Figure 3.12) suggest a slight convergence as the STED power is increased. Given that these amplitudes reflect the weightings of each of the two states immediately after excitation they should be unmodified by the STED process as there has been insufficient time for any depletion to occur. Changes in these weightings therefore might indicate a change in the ground state population of the two species. This might be possible if the differences in the photophysics of the two states meant that STED induced greater loss of population compared with that of the other through a process such as excited state absorption or photobleaching.

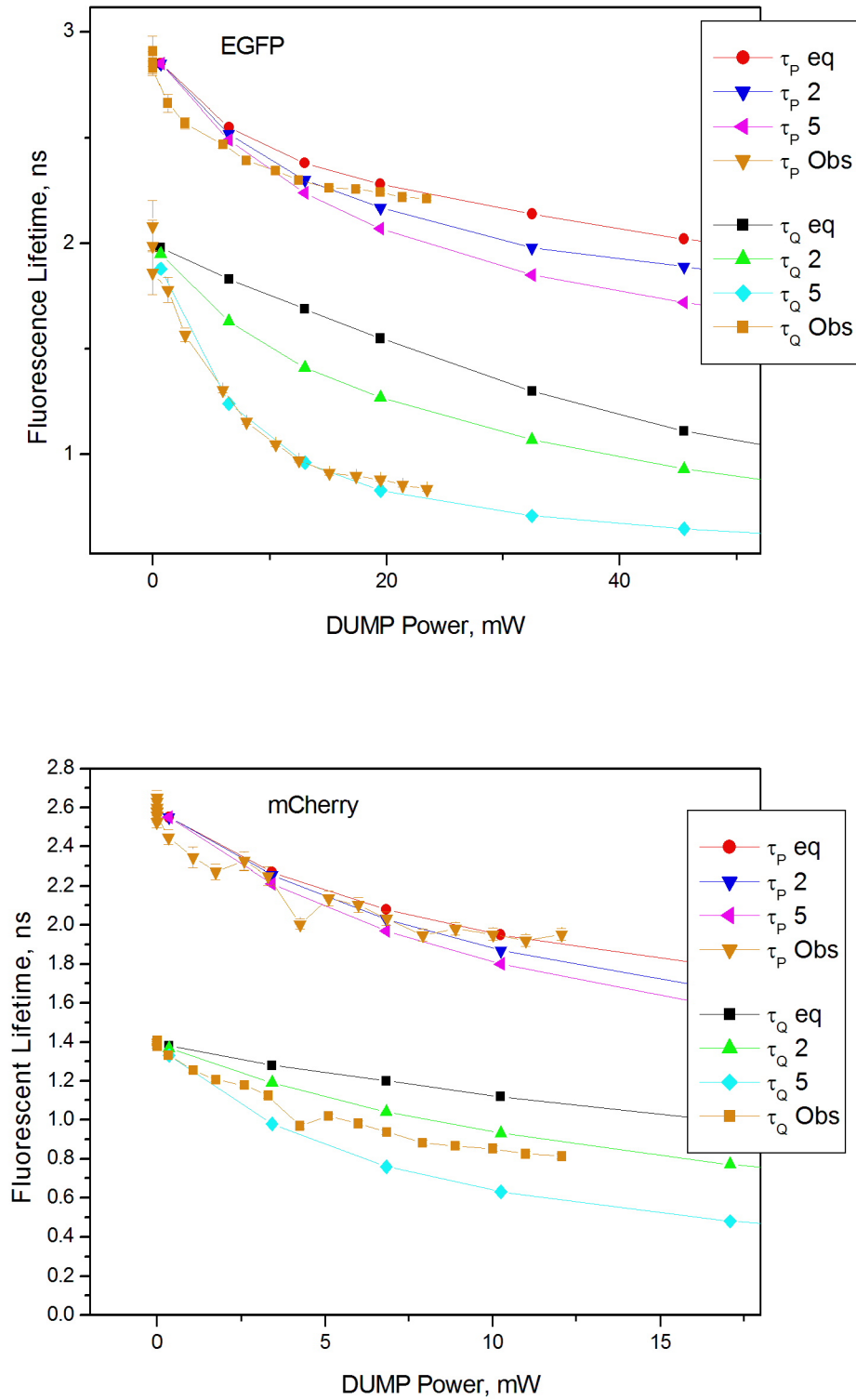


Figure 3.21: Simulated fluorescence lifetime data (for STED rate ratios of 1, 2 and 5) superimposed on observed fluorescence lifetime data (orange) for EGFP (top) and mCherry (bottom). Simulated data has been scaled along the x axis to fit observed data in both cases.

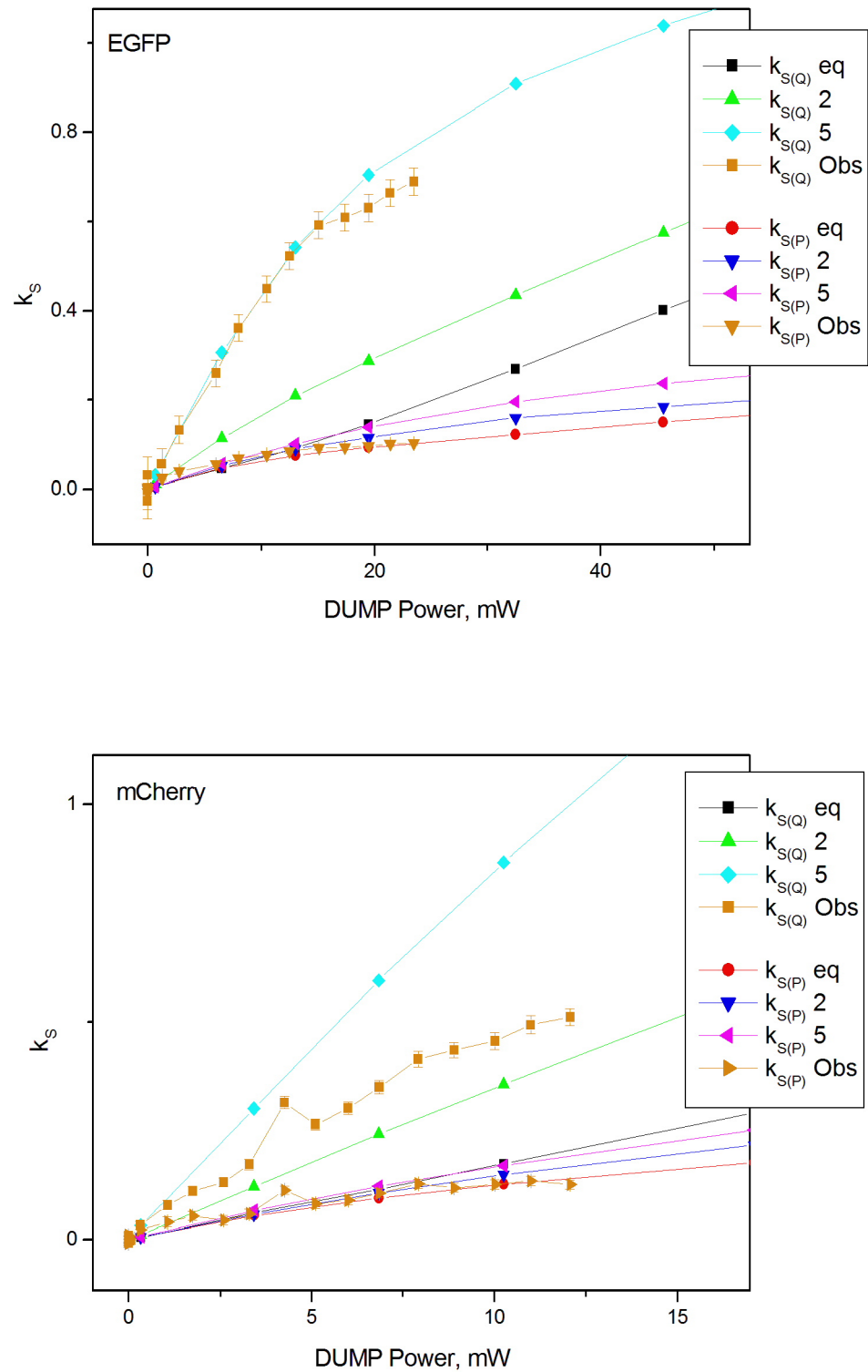


Figure 3.22: Simulated STED rate k_S data (for STED rate ratios of 1, 2 and 5) superimposed on observed fluorescence lifetime data (orange) for EGFP (top) and mCherry (bottom). Simulated data has been scaled along the x axis to fit observed data by the same degree as in Figure 3.21.

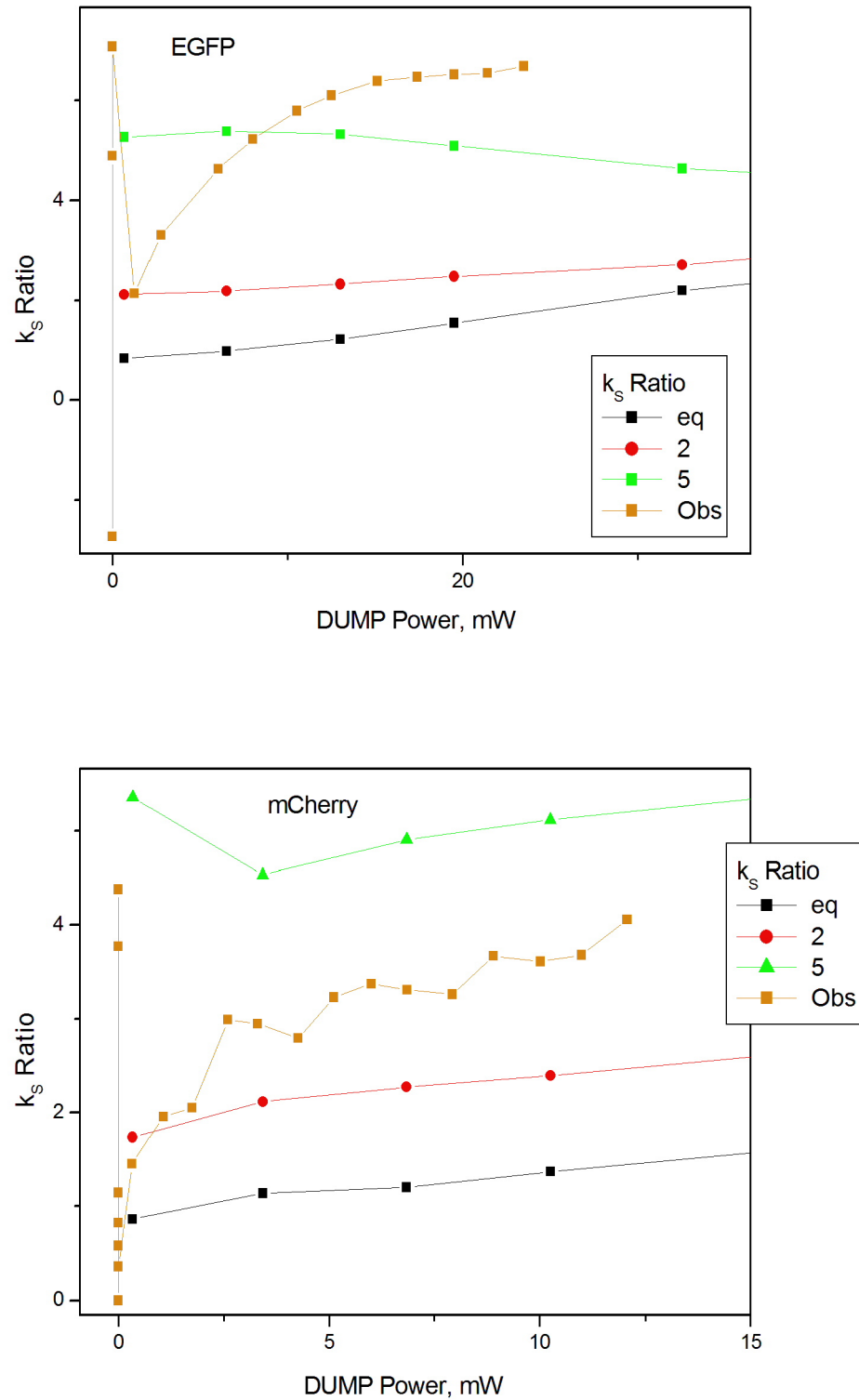


Figure 3.23: Simulated STED rate ratios ($k_{S(Q)} : k_{S(P)}$) data (for STED rate ratios of 1, 2 and 5) superimposed on observed fluorescence lifetime data (orange) for EGFP (top) and mCherry (bottom). Simulated data has been scaled along the x axis to fit observed data by the same degree as in Figure

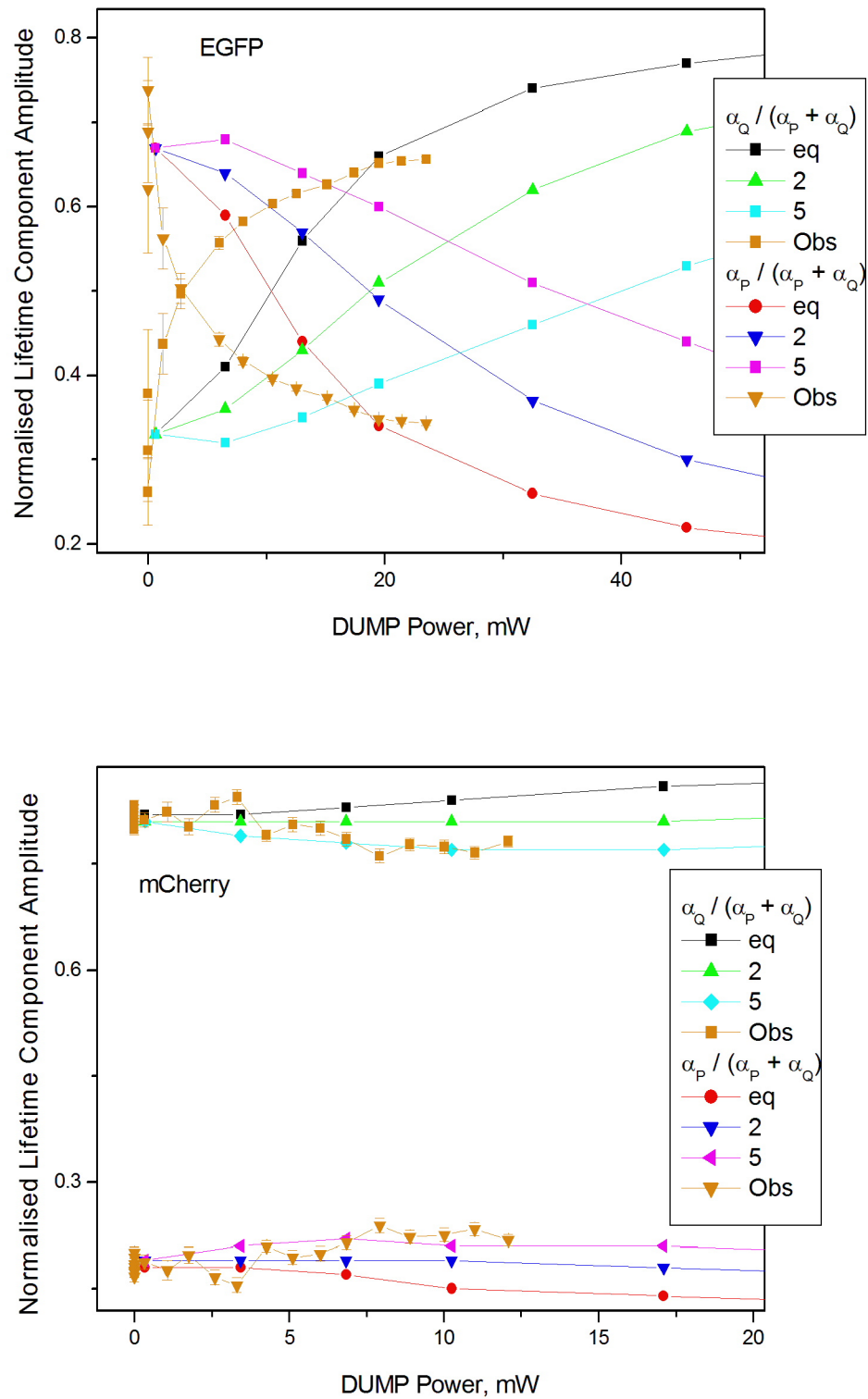


Figure 3.24: Simulated fluorescence amplitude data (for STED rate ratios of 1, 2 and 5) superimposed on observed fluorescence lifetime data (orange) for EGFP (top) and mCherry (bottom). Simulated data has been scaled along the x axis to fit observed data by the same degree as in Figure 3.21.

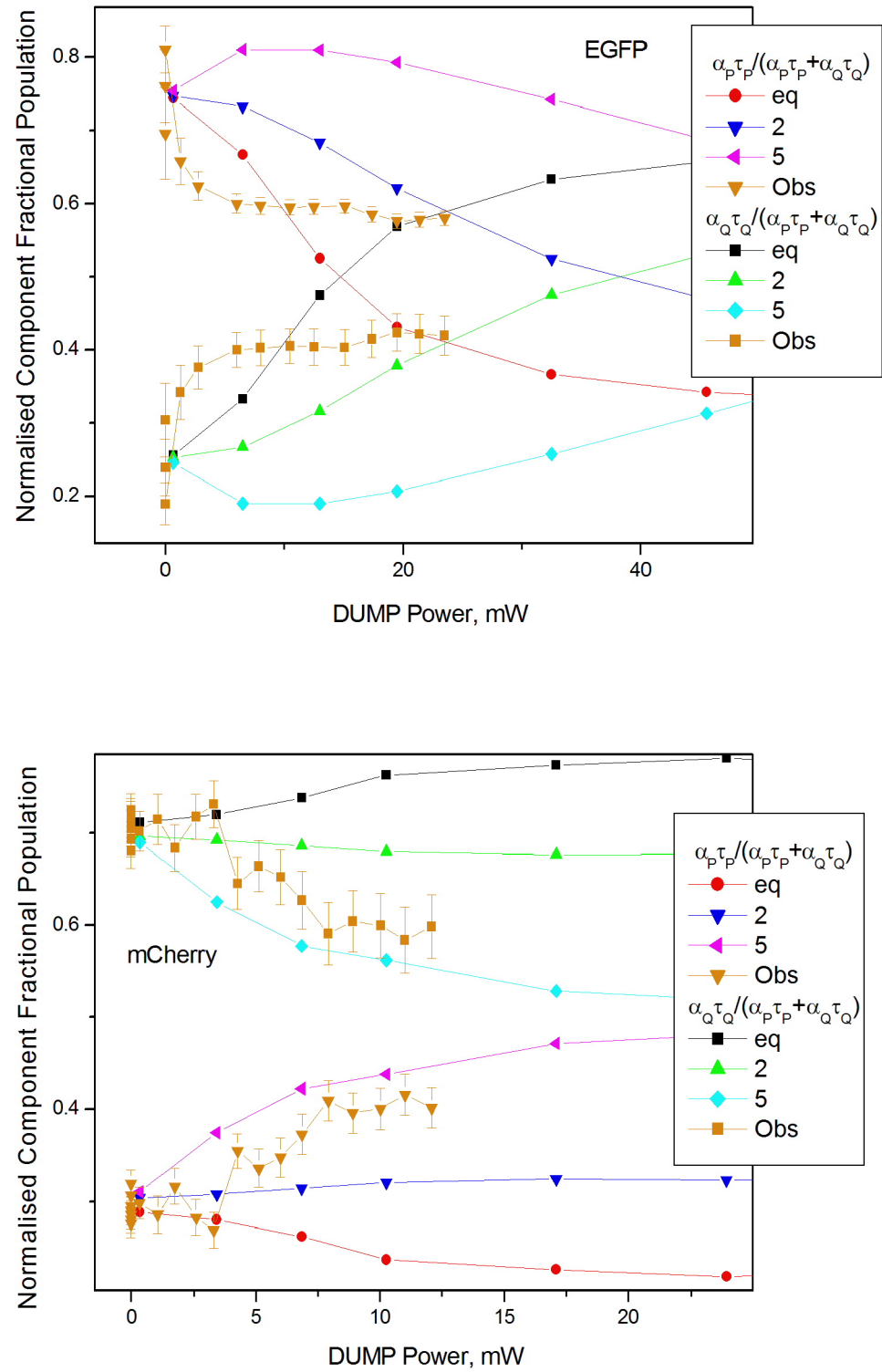


Figure 3.25: Simulated fractional contribution to intensity data (for STED rate ratios of 1, 2 and 5) superimposed on observed fluorescence lifetime data (orange) for EGFP (top) and mCherry (bottom). Simulated data has been scaled along the x axis to fit observed data by the same degree as in Figure 3.21.

It has been shown previously that on average the molecule experiences a number of excitation-depletion cycles before diffusing out of the focal volume, therefore small changes in the ground state population could accumulate. Alternatively this could be an artefact of the fitting process resulting from either the non-exponential nature of the decay which increases with STED power or small errors in the fitting parameters resulting from the finite width of the instrument response function, these becoming more apparent when the decay is faster. However, as the changes in the weightings for the EGFP decay in Figure 3.12 show much greater variation than for mCherry even though the decay rate is, in general, slower; this last possibility is unlikely. Also, the simulations indicate that a good fit to a double exponential decay is expected for low to intermediate powers where these changes are still significant. Inspection of the decay weightings for the simulated data of Figure 3.24 (where there is no instrument response) show that a slight change in the weighting factors is expected for the decay parameters of mCherry and that this variation (at least in part) is a result of fitting a double exponential to the non-exponential intensity decay and is not necessarily indicative of any change in the ground state population.

The case for EGFP is different and somewhat more complex. While it is possible to obtain reasonable agreement with the experimental data for the lifetime and k_S data for the faster decay component (Q) (Figures 3.21 and 3.22) by appropriate choice of scale factor (cross-section) the agreement for the slower decay component P is poorer and no agreement at all, for either decay component, for all other experimental results. While it is possible to improve the fit to the amplitude data (Figures 3.24 and 3.25) by selection of an alternate scaling factor, the agreement is still poor and this results in very poor fitting of the lifetime data. Additionally, whilst the lifetime data suggests a large difference between the radiative rates the amplitude data is more indicative of a smaller or even zero difference between the two rates for each state. However, as the simulations do not even show a good qualitative agreement with the amplitude data it is difficult to draw any conclusions about the relative radiative rates from these particular measurements. Taking the scaling factor used for the lifetime data this would imply a cross-section for EGFP of $4.9 \times 10^{-19} \text{ cm}^2$ for

component P and $2.5 \times 10^{-18} \text{ cm}^2$ for component Q (these cross-section values have been corrected for actual on-sample excitation power). In the case of EGFP therefore it is not possible to explain the observed changes in the weightings of the two emitting states with STED power solely through incorporation of the effects of the angular dependence on the fluorescence lifetime. This indicates the possibility that changes to the populations of the two emitting states are being induced by this STED process. However, if these changes were the result of accumulation over a number of PUMP-DUMP cycles a variation in the effect with the repetition rate of the PUMP laser would be expected, as the amount of time for diffusion to re-establish equilibrium in the ground state changes. As described earlier an investigation into the relative excited state populations of the two species as a function of DUMP power for EGFP in PBS did not show any conclusive variation with repetition rate.

3.11 Conclusions

As a direct consequence of the angular dependence of CW STED in a slowly rotating ($\tau_{ROT} > \tau_F$) or fixed population of molecules the decay rate of each molecular (transition dipole moment) orientation becomes increasingly distinct as the STED power is increased. The separation of lifetime and molecular orientation that is inherent in unperturbed fluorescence experiments (e.g. Equation 1.3.9 in Chapter 1 no longer holds). The fluorescence decay dynamics will, as the STED rate is increased, tend towards that of a highly inhomogeneous system i.e. one with a significant distribution of decay rates. This is certainly the case in both mCherry and EGFP. The maximum average STED decay rates achieved for mCherry and EGFP are ca. 0.3 ns^{-1} and 0.35 ns^{-1} respectively (see Figure 3.9); this is close to 50% of the average fluorescence decay rate in mCherry (0.63 ns^{-1}) and equal to that of EGFP (0.37 ns^{-1}). The fluorescence decays of EGFP and mCherry, both in the absence and presence of CW STED, are well described by bi-exponential decays. Deducing the relationship of these decay parameters to intrinsic molecular properties, e.g. the intrinsic stimulated/radiative rates of the two emitting populations, and the

increasing inhomogeneity induced by CW STED requires detailed simulation. Both the STED lifetime and decay amplitudes of mCherry could be reproduced by a differential radiative (i.e. STED) rate of $k_{S(P)} = xk_{S(Q)}$ where x is between 2 and 5, whilst those for EGFP could not (see Figures 3.21 to 3.25). The intrinsic bi-exponential lifetimes of EGFP (2.86 ns and 1.98 ns) are significantly closer than those of mCherry (2.59 ns and 1.39 ns). In this light the ‘mixing’ of the decay dynamics of the two populations in EGFP by CW STED should be more marked than that in mCherry. The CW STED induced change in anisotropy ΔR was ca. 0.15 for EGFP, but lower for mCherry at ca. 0.07 with equivalent DUMP power.

However, both show similar features - a rapid (few ns) change in anisotropy that levels off, which appears to broadly follow the reduction in lifetime (in that the greater the shortening of the lifetime, the greater the change in anisotropy). It is a consequence of CW STED that it is not possible to physically change the rotational time. Additionally, the timescale of the undumped anisotropy change is too fast for it to be attributable to rotation. These considerations point to the orientationally dependent lifetime being the cause of the observed anisotropy behaviour (the plots in Figure 3.19 show this clearly).

Systems exhibiting bi-exponential decay dynamics with similar lifetimes may become too ‘mixed’ to permit simple analysis and in these circumstances it would be desirable to eliminate the intrinsic orientational de-selection that accompanies STED. For a single beam interaction geometry this is not possible; ‘unpolarised’ STED (i.e. equal polarization intensities in the plane perpendicular to the propagation direction Z) will still lead to angle dependent photo de-selection for molecular orientations out of the XY plane. An angle independent transition probability can only be achieved by a combination of X Y and Z polarised pulses of equal intensity [52]; this might prove difficult to realize in a confocal microscope. However a comparison between unpolarised (e.g. $X+Y$) and polarized (e.g. X) CW STED dynamics may prove helpful in the case of systems such as EGFP. Single and two-photon excitation might also prove useful in this context as the more highly aligned

array of transition dipoles produced by two-photon excitation should lead to a more uniform STED rate for each of the the two decaying populations.

Despite the limitations of modelling orientationally dependent STED dynamics in a population of more than one species described above, substantial differences in the radiative rates (σ_S) were observed for both fluorescence proteins. The consistency between experiment and theory for the case of mCherry suggests a high degree of confidence in this observation although similar behaviour was observed for EGFP the inability to match observations with model predictions means this observation cannot be considered conclusive. However, the existence of two states in fluorescent proteins with substantially different photophysical properties would have significant implications for the use of such chromophores in quantitative fluorescence techniques that have become commonplace in the life sciences such as FRET, FLIM, etc. Radiative rate differences between the two species may lead to stronger interactions for one species compared to the other. Considering only the average behaviour between the two states might lead to misinterpretation of the results.

References

- [1] G. Zhang, V. Gurtu, and S. Kain, "An enhanced green fluorescent protein allows sensitive detection of gene transfer in mammalian cells," *Biochemical and biophysical research communications*, vol. 227, no. 3, pp. 707–711, 1996.
- [2] N. C. Shaner, R. E. Campbell, P. A. Steinbach, B. N. Giepmans, A. E. Palmer, and R. Y. Tsien, "Improved monomeric red, orange and yellow fluorescent proteins derived from *discosoma* sp. red fluorescent protein," *Nature biotechnology*, vol. 22, no. 12, pp. 1567–1572, 2004.
- [3] G. Phillips, "Green fluorescent protein—a bright idea for the study of bacterial protein localization," *FEMS microbiology letters*, vol. 204, no. 1, pp. 9–18, 2001.
- [4] T. Misteli, J. Cáceres, and D. Spector, "The dynamics of a pre-mrna splicing factor in living cells," *Nature*, vol. 387, no. 6632, pp. 523–527, 1997.

-
- [5] L. Stryer, "Fluorescence energy transfer as a spectroscopic ruler," *Annual review of biochemistry*, vol. 47, no. 1, pp. 819–846, 1978.
- [6] P. R. Selvin *et al.*, "The renaissance of fluorescence resonance energy transfer," *Nature structural biology*, vol. 7, no. 9, pp. 730–734, 2000.
- [7] D. Höltter and H. FRET, "Degree of branching in hyperbranched polymers. 2. enhancement of the db: Scope and limitations," *Acta polymerica*, vol. 48, no. 8, pp. 298–309, 1997.
- [8] I. L. Medintz, A. R. Clapp, H. Mattoussi, E. R. Goldman, B. Fisher, and J. M. Mauro, "Self-assembled nanoscale biosensors based on quantum dot fret donors," *Nature materials*, vol. 2, no. 9, pp. 630–638, 2003.
- [9] E. A. Jares-Erijman and T. M. Jovin, "Fret imaging," *Nature biotechnology*, vol. 21, no. 11, pp. 1387–1395, 2003.
- [10] B. Valeur *et al.*, *Molecular fluorescence: principles and applications*. Wiley-Vch, 2012.
- [11] A. Visser, S. Laptенок, N. Visser, A. Van Hoek, D. Birch, J.-C. Brochon, and J. Borst, "Time-resolved fret fluorescence spectroscopy of visible fluorescent protein pairs," *European Biophysics Journal*, vol. 39, no. 2, pp. 241–253, 2010.
- [12] S. P. Laptенок, J. W. Borst, K. M. Mullen, I. H. van Stokkum, A. J. Visser, and H. van Amerongen, "Global analysis of förster resonance energy transfer in live cells measured by fluorescence lifetime imaging microscopy exploiting the rise time of acceptor fluorescence," *Physical Chemistry Chemical Physics*, vol. 12, no. 27, pp. 7593–7602, 2010.
- [13] N. V. Visser, J. W. Borst, M. A. Hink, A. van Hoek, and A. J. Visser, "Direct observation of resonance tryptophan-to-chromophore energy transfer in visible fluorescent proteins," *Biophysical chemistry*, vol. 116, no. 3, pp. 207–212, 2005.
- [14] J. Borst, S. Laptенок, A. Westphal, R. Kühnemuth, H. Hornen, N. Visser, S. Kalinin, J. Aker, A. Van Hoek, C. Seidel, *et al.*, "Structural changes of yellowameleon domains observed by quantitative fret analysis and polarized fluorescence correlation spectroscopy," *Biophysical journal*, vol. 95, no. 11, pp. 5399–5411, 2008.
- [15] T. A. Masters, V. Calleja, D. A. Armoogum, R. J. Marsh, C. J. Applebee, M. Laguerre, A. J. Bain, and B. Larijani, "Regulation of 3-phosphoinositide-dependent protein kinase 1 activity by homodimerization in live cells," *Science Signaling*, vol. 3, no. 145, p. ra78, 2010.

-
- [16] T. A. Masters, R. J. Marsh, D. A. Armoogum, N. Nicolaou, B. Larijani, and A. J. Bain, "Restricted state selection in fluorescent protein fret," *Journal of the American Chemical Society*, 2013.
- [17] T. Masters, *Time-resolved fluorescence studies of Enhanced Green Fluorescent Protein and the molecular dynamics of 3-Phosphoinositide Dependent Protein Kinase 1*. PhD thesis, UCL, 2009.
- [18] A. Einstein, "Strahlungs-emission und absorption nach der quantentheorie," *Deutsche Physikalische Gesellschaft*, vol. 18, pp. 318–323, 1916.
- [19] R. Loudon, *The quantum theory of light*. OUP Oxford, 2000.
- [20] G. H. Patterson, D. W. Piston, and B. G. Barisas, "Förster distances between green fluorescent protein pairs.," *Analytical biochemistry*, vol. 284, no. 2, p. 438, 2000.
- [21] K. I. Willig, B. Harke, R. Medda, and S. W. Hell, "Sted microscopy with continuous wave beams," *Nature methods*, vol. 4, no. 11, pp. 915–918, 2007.
- [22] G. Moneron, R. Medda, B. Hein, A. Giske, V. Westphal, and S. W. Hell, "Fast sted microscopy with continuous wave fiber lasers," *Optics Express*, vol. 18, no. 2, pp. 1302–1309, 2010.
- [23] A. BAIN and R. Marsh, "Improvements relating to fluorescence microscopy," 07 2012.
- [24] R. Marsh, D. Armoogum, and A. Bain, "Stimulated emission depletion of two-photon excited states," *Chemical Physics Letters*, vol. 366, no. 3-4, pp. 398–405, 2002.
- [25] O. Shimomura, F. Johnson, and Y. Saiga, "Extraction, purification and properties of aequorin, a bioluminescent protein from the luminous hydromedusan, aequorea," *Journal of cellular and comparative physiology*, vol. 59, no. 3, pp. 223–239, 1962.
- [26] M. Chattoraj, B. A. King, G. U. Bublitz, and S. G. Boxer, "Ultra-fast excited state dynamics in green fluorescent protein: multiple states and proton transfer," *Proceedings of the National Academy of Sciences*, vol. 93, no. 16, pp. 8362–8367, 1996.
- [27] G. Patterson, R. N. Day, and D. Piston, "Fluorescent protein spectra," *Journal of Cell Science*, vol. 114, no. 5, pp. 837–838, 2001.
- [28] H. Morise, O. Shimomura, F. Johnson, and J. Winant, "Intermolecular energy transfer in the bioluminescent system of aequorea," *Biochemistry*, vol. 13, no. 12, pp. 2656–2662, 1974.
- [29] B. Cormack, R. Valdivia, S. Falkow, *et al.*, "Facs-optimized mutants of the green fluorescent protein (gfp).," *Gene*, vol. 173, no. 1 Spec No, p. 33, 1996.

- [30] N. Shaner, P. Steinbach, and R. Tsien, "A guide to choosing fluorescent proteins," *Nature methods*, vol. 2, no. 12, pp. 905–909, 2005.
- [31] R. Heim, A. Cubitt, and R. Tsien, "Improved green fluorescence," 1995.
- [32] H. Lossau, A. Kummer, R. Heinecke, F. Pöllinger-Dammer, C. Kompa, G. Bieser, T. Jonsson, C. Silva, M. Yang, D. Youvan, *et al.*, "Time-resolved spectroscopy of wild-type and mutant green fluorescent proteins reveals excited state deprotonation consistent with fluorophore-protein interactions," *Chemical physics*, vol. 213, no. 1, pp. 1–16, 1996.
- [33] A. A. Heikal, S. T. Hess, and W. W. Webb, "Multiphoton molecular spectroscopy and excited-state dynamics of enhanced green fluorescent protein (EGFP): acid \pm base specificity," vol. 274, pp. 37–55, 2001.
- [34] U. Haupts, S. Maiti, P. Schwille, and W. W. Webb, "Dynamics of fluorescence fluctuations in green fluorescent protein observed by fluorescence correlation spectroscopy," *Proceedings of the National Academy of Sciences*, vol. 95, no. 23, pp. 13573–13578, 1998.
- [35] S. T. Hess, E. D. Sheets, A. Wagenknecht-Wiesner, and A. A. Heikal, "Quantitative analysis of the fluorescence properties of intrinsically fluorescent proteins in living cells," *Biophysical journal*, vol. 85, no. 4, p. 2566, 2003.
- [36] K. Suhling, D. M. Davis, Z. Petrasek, J. Siegel, and D. Phillips, "Influence of the refractive index on egfp fluorescence lifetimes in mixtures of water and glycerol," in *BiOS 2001 The International Symposium on Biomedical Optics*, pp. 92–101, International Society for Optics and Photonics, 2001.
- [37] M. V. Matz, A. F. Fradkov, Y. A. Labas, A. P. Savitsky, A. G. Zaraisky, M. L. Markelov, and S. A. Lukyanov, "Fluorescent proteins from nonbioluminescent anthozoa species," *Nature biotechnology*, vol. 17, no. 10, pp. 969–973, 1999.
- [38] G. S. Baird, D. A. Zacharias, and R. Y. Tsien, "Biochemistry, mutagenesis, and oligomerization of dsred, a red fluorescent protein from coral," *Proceedings of the National Academy of Sciences*, vol. 97, no. 22, pp. 11984–11989, 2000.
- [39] B. J. Bevis and B. S. Glick, "Rapidly maturing variants of the discosoma red fluorescent protein (dsred)," *Nature biotechnology*, vol. 20, no. 1, pp. 83–87, 2002.
- [40] R. E. Campbell, O. Tour, A. E. Palmer, P. A. Steinbach, G. S. Baird, D. A. Zacharias, and R. Y. Tsien, "A monomeric red fluorescent protein," *Proceedings of the National Academy of Sciences*, vol. 99, no. 12, pp. 7877–7882, 2002.

- [41] L. Albertazzi, D. Arosio, L. Marchetti, F. Ricci, and F. Beltram, "Quantitative fret analysis with the e0gfp-mcherry fluorescent protein pair," *Photochemistry and photobiology*, vol. 85, no. 1, pp. 287–297, 2009.
- [42] F. V. Subach, G. H. Patterson, S. Manley, J. M. Gillette, J. Lippincott-Schwartz, and V. V. Verkhusha, "Photoactivatable mcherry for high-resolution two-color fluorescence microscopy," *Nature methods*, vol. 6, no. 2, pp. 153–159, 2009.
- [43] A. E. Siegman, "Lasers university science books," *Mill Valley, CA*, vol. 37, 1986.
- [44] D. Reisner, R. Field, J. Kinsey, and H. Dai, "Stimulated emission spectroscopy: A complete set of vibrational constants for X A formaldehyde," *The Journal of Chemical Physics*, vol. 80, p. 5968, 1984.
- [45] J. Kuśba, V. Bogdanov, I. Gryczynski, and J. R. Lakowicz, "Theory of light quenching: effects of fluorescence polarization, intensity, and anisotropy decays," *Biophysical journal*, vol. 67, no. 5, pp. 2024–2040, 1994.
- [46] P. Changenet-Barret, C. Choma, E. Gooding, W. DeGrado, and R. Hochstrasser, "Ultrafast dielectric response of proteins from dynamics Stokes shifting of coumarin in calmodulin," *J. Phys. Chem. B*, vol. 104, no. 39, pp. 9322–9329, 2000.
- [47] E. Abbe, "Beiträge zur theorie des mikroskops und der mikroskopischen wahrnehmung," *Archiv für mikroskopische Anatomie*, vol. 9, no. 1, pp. 413–418, 1873.
- [48] S. W. Hell, "Toward fluorescence nanoscopy," *Nature biotechnology*, vol. 21, no. 11, pp. 1347–1355, 2003.
- [49] X. Shu, N. C. Shaner, C. A. Yarbrough, R. Y. Tsien, and S. J. Remington, "Novel chromophores and buried charges control color in mfruits," *Biochemistry*, vol. 45, no. 32, pp. 9639–9647, 2006.
- [50] R. Swaminathan, C. P. Hoang, and A. Verkman, "Photobleaching recovery and anisotropy decay of green fluorescent protein gfp-s65t in solution and cells: cytoplasmic viscosity probed by green fluorescent protein translational and rotational diffusion.," *Biophysical journal*, vol. 72, no. 4, p. 1900, 1997.
- [51] W. Becker, *Advanced time-correlated single photon counting techniques (Series in chemical physics, Vol. 81)*. Springer-Verlag, 2005.
- [52] A. Bain, P. Chandna, and J. Bryant, "Picosecond polarized fluorescence studies of anisotropic fluid media. i. theory," *The Journal of Chemical Physics*, vol. 112, p. 10418, 2000.

Chapter 4

Pulsed Stimulated Emission Depletion Dynamics

4.1 Introduction

Pulsed STED refers to a system where the fluorescence depletion is caused by a short (ps) intense laser pulse instead of continuous illumination. Pulsed STED represents a different regime for the rate of STED compared with the other photophysical processes taking place than is the case for CW depletion as discussed in Chapter 3. Whereas in CW STED the depletion rate is comparable to the fluorescence lifetime, pulsed STED is sufficiently rapid that fluorescence during the DUMP process is negligible. A consequence of this rapid STED rate is however that the finite time taken for the depleted population to relax from the upper vibrational levels of the ground state enables re-pumping of the population back to the excited state whereas in CW depletion experiments of Chapter 3 the intrinsic fluorescence and induced decay rates are comparable (ca. 10^8 s^{-1}) but significantly slower than that of ground state vibrational relaxation (ca. 10^{13} s^{-1}). As a consequence the population of lower STED levels are effectively zero at all times and no repumping of the excited state takes place. In the CW depletion work of Chapter 3 it was found that orientational photo-deselection even at moderate depletion rates was consid-

erably more pronounced than those of rotational diffusion. In pulsed STED work the timescale of the depletion process (ca. 4-42 ps) is significantly shorter than the intrinsic rotational diffusion time τ_{20} (see Section 1.4). Rotational effects during the STED process are now considered.

In this chapter detailed fluorescence intensity and anisotropy measurements are combined with new theoretical modelling in an attempt to attain a better understanding of the physical processes controlling the stimulated emission depletion (STED) mechanism and to determine the conditions by which the efficiency of STED might be most profitably enhanced. Within the group, pulsed STED experiments had initially involved DUMP pulse widths of between 250 fs and 2.5ps which were obtained by stretching the tunable output of a 250 kHz optical parametric amplifier (OPA) in a water cell and performed on standard fluorophores [1, 2]. With 250 kHz PUMP and DUMP pulses and PUMP-DUMP delays greater than the ps time scale taken to populate the lower vibrational (emitting) levels of the fluorophore's excited state, the STED process can be described in terms of induced transitions in a two level system with rapid (sub-picosecond) vibrational relaxation of the target level(s) in the electronic ground state [1]. The efficiency of STED (the percentage of population removal for a specific DUMP pulse energy) is limited by the degree of re-pumping of the excited state arising from incomplete population relaxation in the lower levels during the duration of the DUMP pulse. For a given pulse duration with increasing DUMP energy, the degree of excited state depletion will tend towards a limiting value below 100% [3]. This process is termed saturation and in principle should be mitigated by an increase in the DUMP pulse width allowing minimization of the ground state population and therefore subsequent excited state repopulation. Initial work within the group on STED in two-photon excited fluorescein [1] indicated that the two-level approximation (with relaxation losses of the lower level) was an adequate description of the STED process. As the DUMP pulse width was significantly shorter than the rotational diffusion time of the fluorophore (e.g. 250 fs-2.5 ps vs 2.7 ns in the case of fluorescein in ethylene glycol) rotational relaxation during the dump process was taken to be negligible. The remaining (post DUMP) fluorescence

showed significant depolarization due to preferential depletion of molecular transition dipole moments oriented at angles close to that of the DUMP polarization. The degree of population removal F_D and the change in the fluorescence anisotropy ΔR were measured as a function of DUMP energy (ca. 0-50 nJ) and pulse width τ_P (typically 710 fs – 2.5 ps). Analysis of the F_D and ΔR vs DUMP energy data was undertaken in the two-level approximation assuming a constant DUMP flux over the pulse duration (rectangular pulse). A Mathematica program (written by Dr R. Marsh) was used to solve the two-level rate equations for the ground and excited state populations. These were then numerically integrated to perform the orientational analysis necessary to calculate the predicted F_D and ΔR values as a function of the STED saturation parameter S for ratios of τ_P to τ_R , the ground state relaxation time. The saturation parameter S is proportional to the DUMP pulse energy E_D through,

$$S = \frac{\sigma_S}{h\nu A} E_D \quad (4.1.1)$$

where σ_S is the STED cross section (cm^2), A is the focussed area of the DUMP pulse (cm^2) and $h\nu$ is the DUMP photon energy. A series of F_D and ΔR vs S plots were produced for different τ_P/τ_R values. These were then scaled (by variation of the ratio $\sigma_S/Ah\nu$) to match the experimental F_D and ΔR saturation data. The plots showing the best agreement yielding τ_R (via τ_P) and σ_S (A and $h\nu$ known).

This analysis was consistent with the experimental data, however an apparent increase was found by Marsh et al. in both σ_S and τ_R with increasing values of DUMP pulse width. The degree of increase in τ_R with DUMP pulse that was found is reproduced in Table 4.1 [4]. This increase in τ_R with DUMP width is an observation that has been found repeatedly [2, 4, 5]. The pulse stretching mechanism used [4] was based on group velocity dispersion in a multiple pass water cell. This process produced a positive frequency sweep (up chirp) [6] across the DUMP pulse and it was suggested that this might lead to increased re-pumping of the excited state as the relaxing (cooling) ground state population would remain in resonance with the excited state for a timescale longer than the intrinsic vibrational relaxation dynamics.

$\tau_P \times 10^{-12}(s)$	$\tau_R \times 10^{-15}(s)$
0.71	592
1.45	725
2.50	833

Table 4.1: Variation in the ground state relaxation time τ_R for Fluorescein in Ethylene Glycol for varying DUMP widths τ_P extracted using the 2-level STED model [4].

In addition, in OM77 (branched multipolar chromophore engineered for high 2PA cross-section $\sigma^{(2)}$) lower values of ΔR were observed than anticipated given the high degree of depletion [7]. In this work a substantially longer DUMP pulse (ca. 40 ps) was required to minimise DUMP-induced 2-photon fluorescence arising from the significant visible 2PA cross-section this molecule possesses [8]. For these reasons it was decided to undertake further studies of a well understood fluorophore with non-complex behaviour and with a single exponential decay (unlike EGFP or OM77). DUMP pulsewidth and solvent viscosity were varied to investigate the relation between the accuracy of the model and rotational decay of the sample during the DUMP pulse. Alterations to the model were explored including that of an effective reduction in the rotation of higher order moments, (which are ‘written in’ with saturation of the DUMP transition) during the DUMP pulse.

4.2 Two-Level Model of STED Dynamics

In polarised STED the 2-photon STED mechanism is demonstrated in Figure 4.1. The initial excitation out of low lying vibrational levels in the S_0 ground state occurs by the simultaneous absorption of two (non-resonant) near infra red photons. This processes populates higher vibrational levels of an initial (two-photon allowed) excited electronic state. Fast internal conversion and collisional relaxation with the solvent leads to the rapid (picosecond timescale) population of lower vibrational levels in S_1 . In the absence of external perturbations the population in S_1 decays

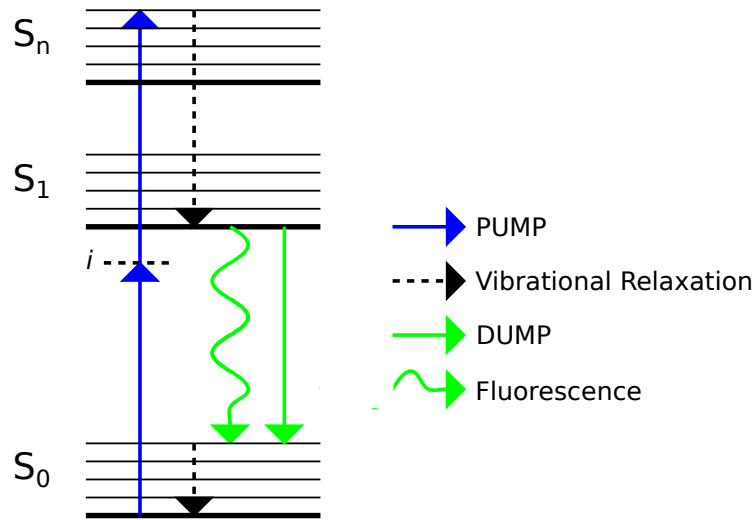


Figure 4.1: Illustration of two-photon STED. Population in the ground vibrational levels of the S_0 electronic ground state is excited through a non-resonant virtual state i to higher vibrational levels in an excited singlet state. Rapid (ps –sub ps) non-radiative relaxation leads to the population of low vibrational levels of S_1 from where stimulated emission takes place on application of the DUMP pulse.

by spontaneous emission to any of the upper vibrational levels of S_0 followed by rapid collisional relaxation. In pulsed STED a visible laser pulse resonant with the $S_1 \rightarrow S_0$ emission is applied at a time delay $\tau_P D$ to induce transitions to upper vibrational levels of S_0 . This results in a sharp reduction in the excited state population shown by a reduction in fluorescence intensity as in the example shown in Figure 4.2), and a change in molecular alignment (fluorescence anisotropy) dependent on the relative polarisation of the two laser pulses as can be seen in Figure 4.3. Given a PUMP-DUMP separation that is longer than the relaxation processes that populate the emitting levels of S_1 and rapid relaxation in S_0 the STED process could be modelled in terms of a two-level system [1, 2, 7, 9]. However, for higher STED rates the relaxation of the vibrational levels of S_0 cannot be assumed to be instantaneous; this is modelled phenomenologically as a decay of the lower level population with characteristic time, τ_R . The rate equations for STED on a timescale that is fast compared to spontaneous emission (nanosecond to sub-nanosecond) and

orientational relaxation (nanosecond) are given by

$$\frac{dN_{EX}(\theta, t)}{dt} = -\frac{I_D(t)\sigma W_D(\theta)}{h\nu} (N_{EX}(\theta, t) - N_{GS}(\theta, t)) \quad (4.2.1)$$

$$\frac{dN_{GS}(\theta, t)}{dt} = -\frac{I_D(t)\sigma W_D(\theta)}{h\nu} (N_{EX}(\theta, t) - N_{GS}(\theta, t)) - \frac{N_{GS}(\theta, t)}{\tau_R} \quad (4.2.2)$$

Where $N_{EX}(\theta, t)$ and $N_{GS}(\theta, t)$ are the ground and excited state populations, $I_D(t)$ is the DUMP pulse intensity, $W_D(\theta)$ is the angular dependence of the DUMP probability and σ is the stimulated emission cross section (cm^2). It is possible to obtain analytic solutions to the rate equations by assuming a rectangular DUMP pulse intensity profile in space and time with width τ_P , which yield the fractional remaining population F_R as a function of $S = E_P\sigma/h\nu A$ for given ratios of τ_P/τ_R . Given that the initial population distribution in the upper ground state vibrational levels is negligible, the excited state population (when using a parallel PUMP-DUMP geometry) evaluated at $t = \tau_P$ is given by [4]

$$N_{EX}(\theta, \tau_P) = \frac{N_{EX}(\theta, 0)}{2d} \left[\exp\left(-\frac{1}{2} \left[\frac{\tau_P}{\tau_R} + 2S \cos^2 \theta + d \right]\right) \right] \left(\frac{\tau_P}{\tau_R} (e^d - 1) + (e^d + 1) \right) \quad (4.2.3)$$

where the parameter d is given by

$$d = \sqrt{(\tau_P/\tau_R)^2 + 4S^2 \cos^4 \theta} \quad (4.2.4)$$

The fractional of the excited state population removed by the pulse can be calculated from,

$$F_D = \frac{\int_0^{2\pi} \int_0^\pi (N_{EX}(\theta, \tau_P) - N_{EX}(\theta, 0)) \sin \theta d\theta d\phi}{\int_0^{2\pi} \int_0^\pi (N_{EX}(\theta, 0)) \sin \theta d\theta d\phi} \quad (4.2.5)$$

where $N_{EX}(\theta, 0)$ is the excited state population immediately prior to STED. The fluorescence anisotropy following the application of the dump pulse is given by [4]

$$R(d) = \sqrt{\frac{4\pi}{5}} \frac{\int_0^{2\pi} \int_0^\pi N_{EX}(\theta, \tau_P) Y_{20}^*(\theta, \phi) \sin \theta d\theta d\phi}{\int_0^{2\pi} \int_0^\pi N_{EX}(\theta, \tau_D) \sin \theta d\theta d\phi} \quad (4.2.6)$$

Calculation of the integrals in Equations 4.2.5 and 4.2.6 was performed and simulation of the experimental data was undertaken using a Mathematica program

(Wolfram, US) [1, 10]. When applied to equation 4.2.5 this yielded numerical solutions for the population removal immediately following STED (i.e. before the onset of significant orientational relaxation), for varying S and specific ratios of DUMP pulse-width to ground state vibrational relaxation time (τ_P/τ_R). A set of numerical solutions for F_D and ΔR with S for different values of τ_P/τ_R is shown in Figure 4.5; this shows that as the DUMP pulse is increased (i.e. τ_P/τ_R rises) re-pumping of S_1 is reduced and higher levels of excited state depletion can be achieved. By matching numerical solutions (as in Figures 4.4 and 4.5) to experimental data, it is possible to obtain values for the stimulated emission cross-section and ground state vibrational relaxation times [1, 2, 7, 10, 11]. The simulations for F_D and ΔR are fit simultaneously and the best global agreement to both is determined by eye, giving the τ_P/τ_R ratio. The changes in F_D predicted in Figure 4.4 with increasing DUMP pulse width are not as marked as those for ΔR . With parallel PUMP and DUMP polarizations the fluorescence anisotropy following STED shows a sharp decrease due to selective de-excitation of transition dipole moments oriented parallel to the excitation polarization. Most STED techniques are purely concerned with maximizing F_D ; however when examining excited state alignment through use of STED anisotropy experiments the accuracy of ΔR predictions by the model become important. It has been previously noted [2, 5] that the fit of the model prediction of ΔR to experimental data does not always match that of the model prediction of F_D to experimental data; both F_D and ΔR experimentally obtained is often significantly less than that predicted. This is further complicated as all simulated values of F_D become very similar at high values of τ_P/τ_R (see Figure 4.4). The mechanisms that affect the anisotropy predicted by the model therefore require further investigation.

4.3 Experimental Set-up

The experimental apparatus for STED in two-photon excited populations is illustrated in Figure 4.6.

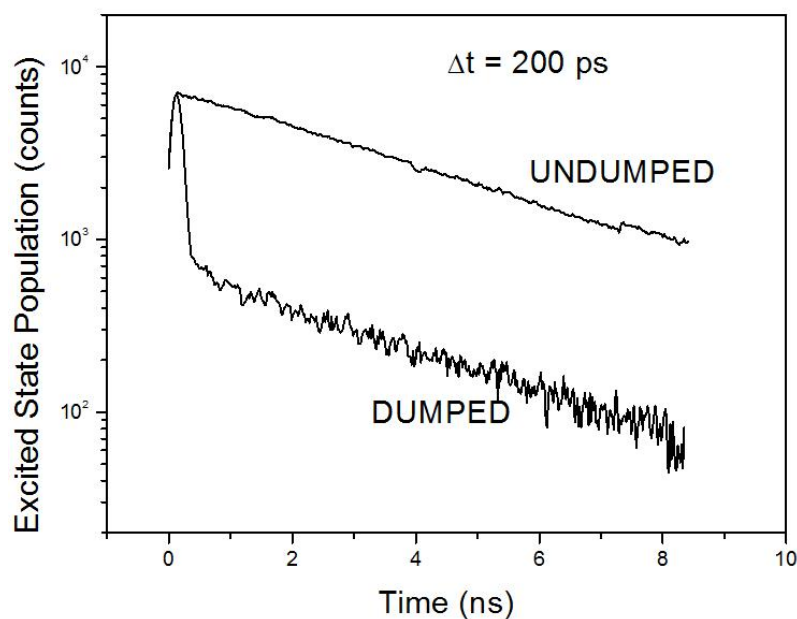


Figure 4.2: Stimulated emission depletion (STED) of Alexa 594 in water following two-photon excitation (800nm, 12 nJ, *ca.* 190 fs). With a 200 ps PUMP-DUMP delay 90% of the excited state population is removed by the DUMP pulse (684 nm, 40 nJ, *ca.* 2 ps)

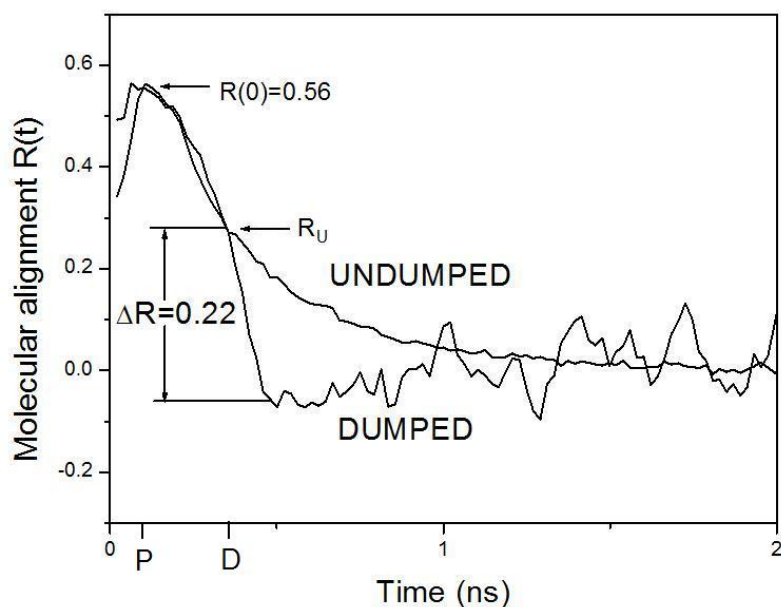


Figure 4.3: STED depolarization in Alexa594 in water (experimental conditions are as in Figure 4.2). Selective removal of molecules oriented parallel to the DUMP polarisation results in an abrupt change in molecular alignment ($\Delta R = 0.22$). Pump and Dump times are labelled as P and D.

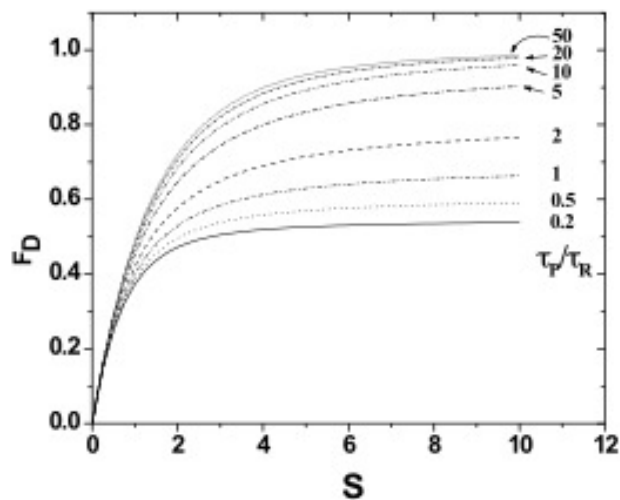


Figure 4.4: Numerical solutions to the coupled rate equations yield a family of saturation curves for population removal by STED for different values of τ_P/τ_R . Here, τ_P/τ_R is varied from 0.2 to 50 and values of S from 0 to 12.

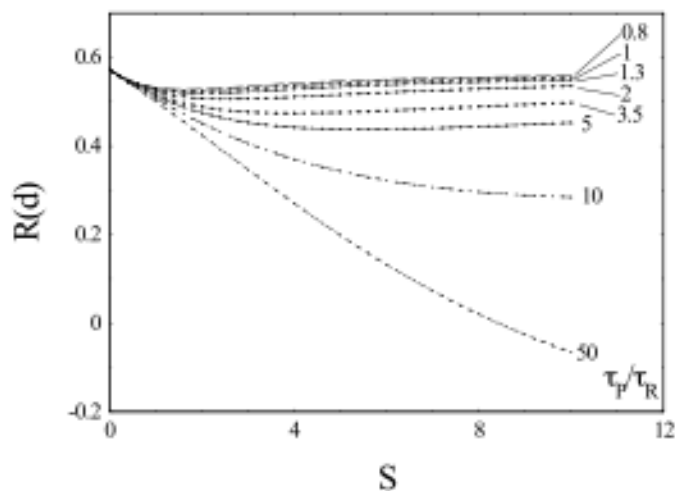


Figure 4.5: Numerical solutions to 4.2.6 predicting the altered excited state anisotropy in a two-photon excited population following STED (immediately before the onset of significant orientational relaxation) with saturation parameter S (varied from 0 to 10), and a pulse width to relaxation time ratio τ_P/τ_R (varied from 0.8 to 50). Significant depolarisation of the excited state requires the dump pulse width to be at least a factor of 5 greater than the relaxation time of the ground state vibrational levels.

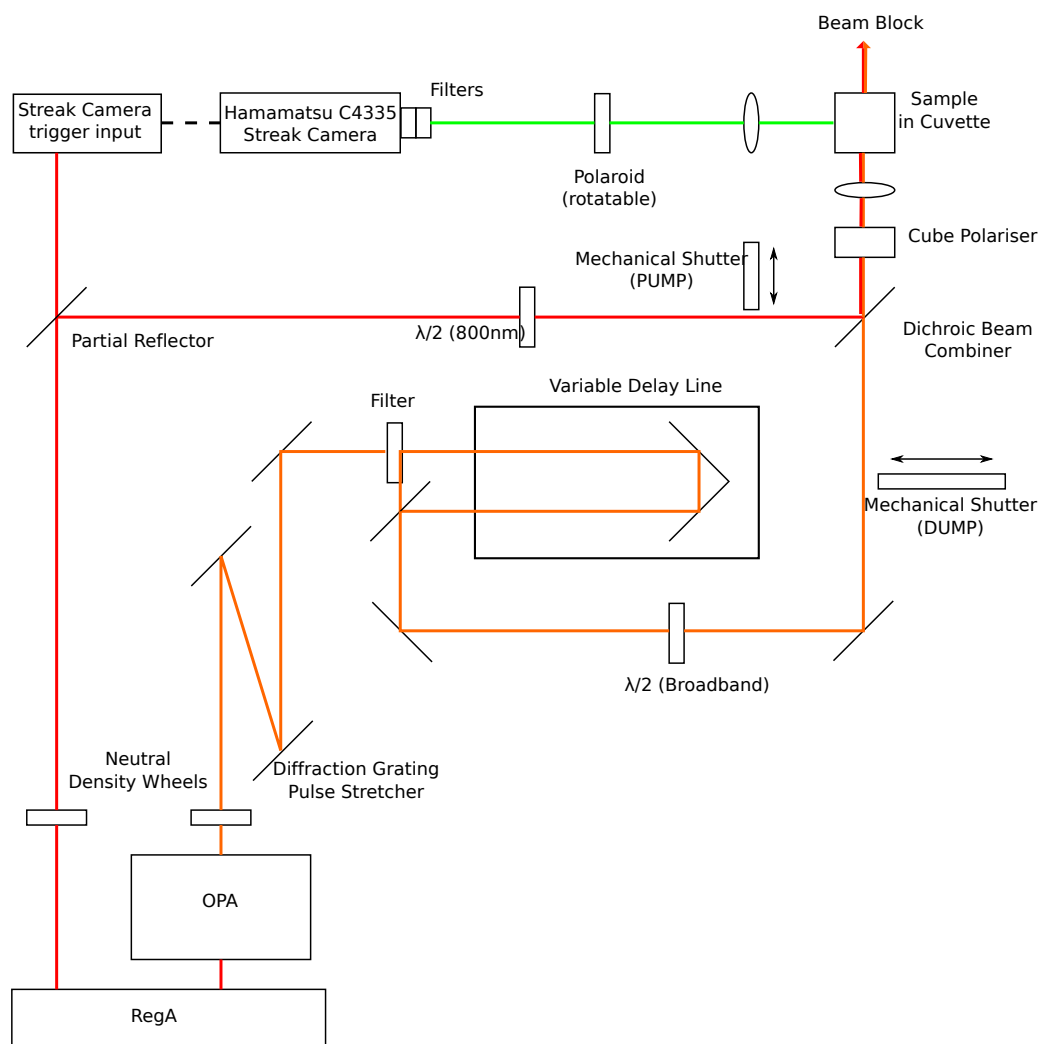


Figure 4.6: Experimental set-up including PUMP and DUMP sources used to carry out STED experiments.

Three samples of Fluorescein were prepared of concentration 1×10^{-4} in Glycerol, Glycerol/water mixtures of 100:0, 80:20 and 60:40 to achieve a range of sample viscosities. As sample viscosity affects the rotational correlation time, this gives a further experimental variable with which to alter the degree of rotation during the DUMP pulse. The samples were contained in a $250 \mu\text{L}$ fluorescence cuvette (Helma) with three optical windows. Two-photon excitation was achieved using the partial output of regeneratively amplified Ti:Sapphire laser (Coherent Mira 900F, Coherent RegA 9000) which provided 800 nm laser pulses with ca. 12 nJ energy and a ca. 190 fs FWHM pulse width at a repetition rate of 250 KHz. The majority of the

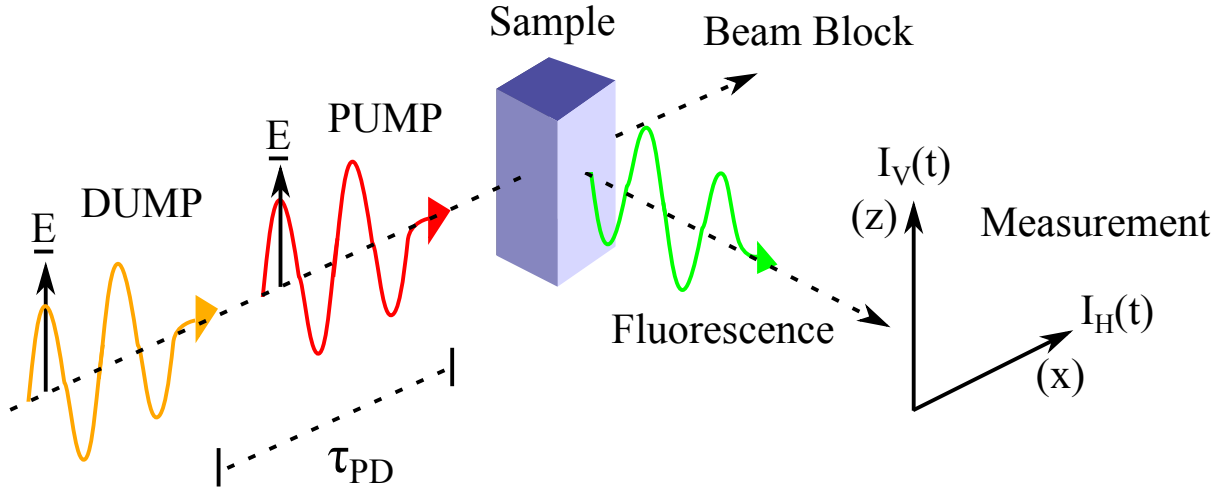


Figure 4.7: Right-angle excitation-detection geometry in combination with parallel PUMP and DUMP polarisations. Fluorescence measurements were taken at 0° (vertical polarisation of measurement) and 90° (horizontal polarisation of measurement).

800 nm output was used to drive an Optical Parametric Amplifier (OPA) (Coherent 9400) which provides a synchronous pulse train with a tunable range of 450-700 nm. A DUMP wavelength of 600 nm was chosen for high STED cross-section, whilst maintaining a low cross-section for single-photon absorption. The DUMP pulse was stretched using a pair of diffraction gratings (3200 lines per inch, Thorlabs, US) to ca. 3.8, 11.3 or 42.4 ns by variation of the inter-grating distance. DUMP length was measured using an auto-correlator (Pulse-Select, APE, Germany), and then directed to a variable optical delay line which was used to set the PUMP-DUMP delay time to 600 ps. The PUMP and DUMP beam polarisations were set using broadband half wave-plates (Melles-Griot, US). A mechanical shutter in the path of the DUMP beam allowed the PUMP beam to operate alone when necessary. Both beams were spatially overlapped using a dichroic beam combiner (Semrock, US), and then focussed into the sample using an achromatic doublet lens ($f = 25$ mm), Melles-Griot) through a 2 mm diameter pinhole. Spontaneous fluorescence was focussed into a C4334 streak camera (Hamamatsu, Japan) through a condensing

lens and a short-pass 650 nm filter (Chroma, US) was used to block scattered laser light. The streak camera records the intensity of the fluorescence signal in both time and one spatial dimension aligned with the beam path. The PUMP power was controlled using a combination of the appropriate half-wave plate and the Glan Taylor cube polariser (Melles-Griot) to minimise non-radiative energy loss in the beam waist, whilst maintaining a high signal to noise ratio.

A number of intensity profiles were taken at both 0° ($I_V(t)$) and 90° ($I_H(t)$) to the z -axis in the lab frame (in this case the z -axis is in the direction of both PUMP and DUMP beams) as shown in Figure 4.7. The measurement polarisation direction with respect to the z -axis was controlled using a rotatable sheet polaroid (Melles-Griot) between the sample and detector. Fluorescence measurements were taken at a range of different DUMP energies (from zero to the maximum available, in the region of 30-50 nJ), and in addition for each experiment a measurement of fluorescence intensity in the absence of STED was also made. The region of interest was spatially selected to coincide with the region of maximum depletion; as well as achieving a higher measured F_D this ensured the signal was maintained at a level approximately constant in the z direction. Intensity profiles of the DUMP induced fluorescence were also taken with the PUMP shut off, to be subtracted from the signal during analysis in cases when the intensity was above 1% that of the signal.

To extract values of F_D from the collected intensity data, the dumped intensity graphs were subtracted from the undumped intensity. A minimum of 50 data points from the measurement at times after the DUMP were used to obtain a mean value for F_D . To extract values of ΔR from the anisotropy data, the anisotropy data was fitted before and after the DUMP pulse using the program Origin, and the instantaneous change in anisotropy calculated by hand at the midpoint of the anisotropy change.

4.4 Rotation of Excited State Population During DUMP

The accuracy of the model used to fit pulsed STED data as described above has been found to depend upon certain experimental parameters. This section summarises the effects that some of these experimental parameters have on the fit, namely DUMP pulse length and viscosity of solution. This dependence had not been fully noticed before, but could be seen when re-examining previous data [2, 5] as well as in the data shown in this section. Section 4.5 then investigates the quality of fit of the model further through manipulation of the model parameters and through alteration of the model in order to better understand the physical processes taking place (i.e. that result in the deviation from model behaviour).

4.4.1 Dump Pulse Length

Efficiency of the DUMP process depends on a lack of re-pumping to the excited state. Figure 4.8 shows the fractional population depletion during STED F_D and the resultant change in anisotropy ΔR for fluorescein in glycerol and glycerol/water solutions for three DUMP pulsewidths. The best individual theoretical fits to the F_D and ΔR data are shown, in addition to the best global fit (i.e. best fit to F_D and ΔR with the same τ_P/τ_R value and scaling factor), with corresponding τ_P/τ_R values noted on the plots. Although the model does not directly appear to be less applicable at the longer DUMP widths, on calculation of the values of τ_R based on these fits it can be seen that these τ_R values vary greatly, which is not possible physically.

Based on the best global fit to both F_D and ΔR of τ_P/τ_R the values measured for τ_R are 0.38 ps (3.80 ps DUMP), 1.256 ps (11.3 ps DUMP) and 6.057 ps (42.4 ps DUMP). Only the value with the shortest DUMP pulse (3.8 ps) yields a value of the order of the value expected for τ_R [2, 5]. This demonstrates that the model breaks down completely at the longer DUMP widths used. Using the value calculated from

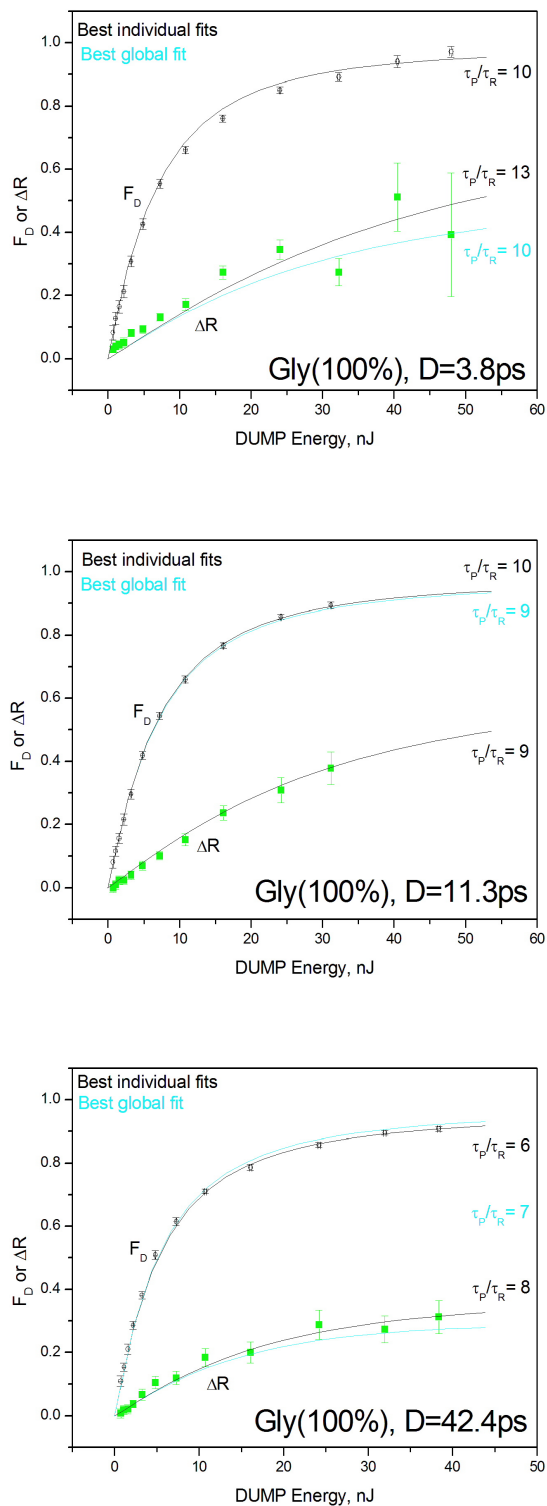


Figure 4.8: 2-photon STED excited state population removal in Fluorescein 1×10^{-4} in Glycerol. Best theoretical fits of model are shown for F_D and ΔR and for the best global fit along with corresponding τ_P/τ_R values. DUMP lengths of top: 3.8 ps; middle: 11.3 ps; and bottom: 42.4 ps were used.

Solvent	$\tau_{ROT}(ns)$
Glycerol	18.7
Glycerol:water 80:20	8.9
Glycerol:water60:40	2.7
Ethylene Glycol	2.8

Table 4.2: Rotational correlations times of Fluorescein in the solvents used.

the 3.8 ps DUMP pulse of $\tau_R = 0.380$ ps an additional τ_P/τ_R fit was added to the same data, as shown in Figure 4.9. It can be seen that this fit differs from the data even further at $\tau_P = 42.4$ ps than at $\tau_P = 11.3$ ps.

4.4.2 Solvent Viscosity

Viscosity alters the rotational diffusion time and so increasing viscosity should reduce and orientational relaxation during the DUMP pulse. Another factor that can be seen to affect the model fit is the viscosity of the solvent; with lower viscosity solvents the model fits the data less well, especially the ΔR data. This is shown for the data with the 3.8 ps pulse width in Figure 4.10. Rotational correlation times of Fluorescein in the various solvents are given in Table 4.2.

The best global fits for the different DUMP pulse widths are shown in Figure 4.11 for all three samples in Glycerol/water mixtures of 100:0, 80:20 and 60:40. For the 100% Glycerol sample, data for all DUMP lengths fits well to simulated curves, although all of these curves have a lower τ_P/τ_R value than expected. For the sample in 80% Glycerol data using the two shorter DUMP pulse lengths fit well to the simulated curves, though again with τ_P/τ_R values too low. However the data when the longest DUMP pulse is used does not fit well to the simulated data. In the case of the 60% Glycerol sample none of the simulations fit the data well, with the long DUMP pulse simulation fitting the data particularly badly.

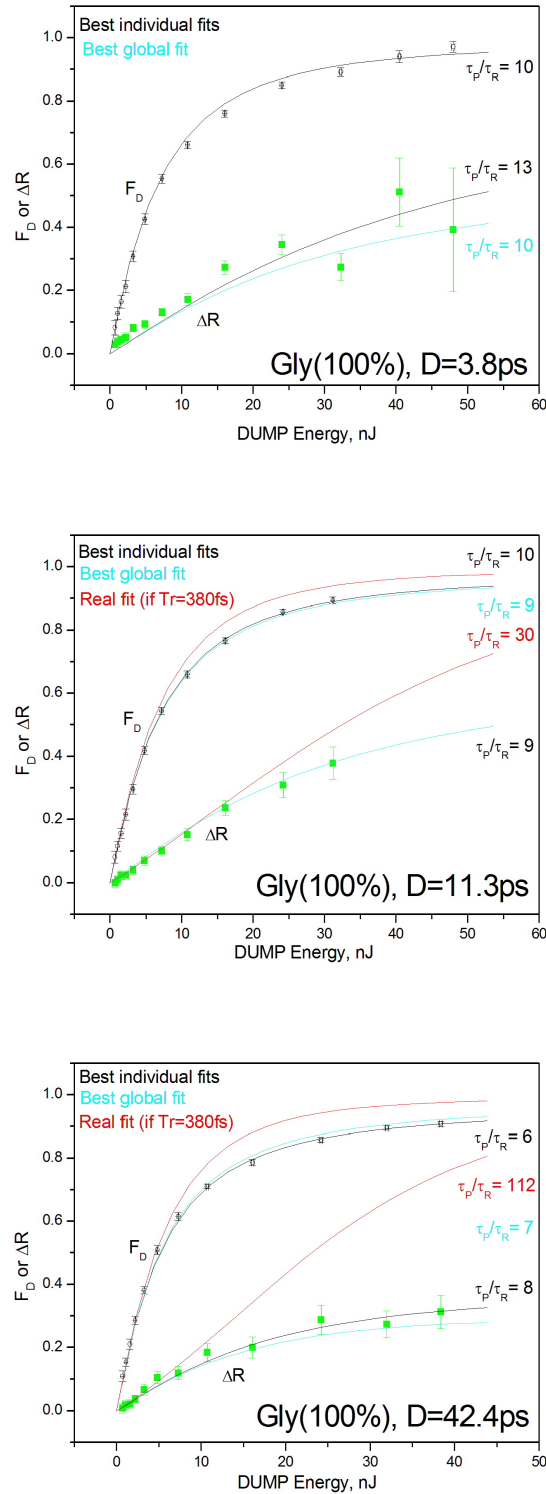


Figure 4.9: 2-photon STED excited state population removal in Fluorescein 1×10^{-4} in Glycerol. DUMP lengths of top: 3.8 ps; middle: 11.3 ps; and bottom: 42.4 ps were used. Best theoretical fits of model are shown for F_D and ΔR and for the best global fit along with corresponding τ_P/τ_R values. For DUMP lengths of 11.3 and 42.4 ps the fit using $\tau_R = 380$ fs is also shown.

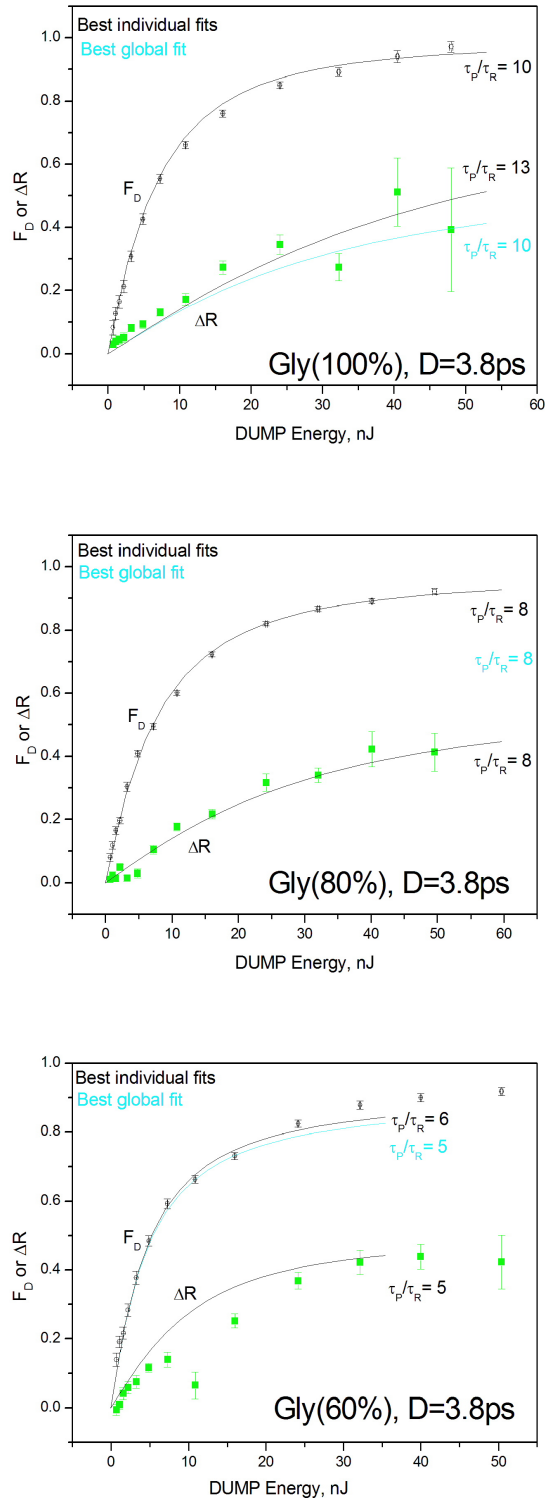


Figure 4.10: 2-photon STED excited state population removal with a 3.8 ps DUMP length in Fluorescein 1×10^{-4} in Glycerol/water mixtures of top: 100:0; middle: 80:20; and bottom: 60:40. Best theoretical fits of model are shown for F_D and ΔR and for the best global fit along with corresponding τ_P/τ_R values.

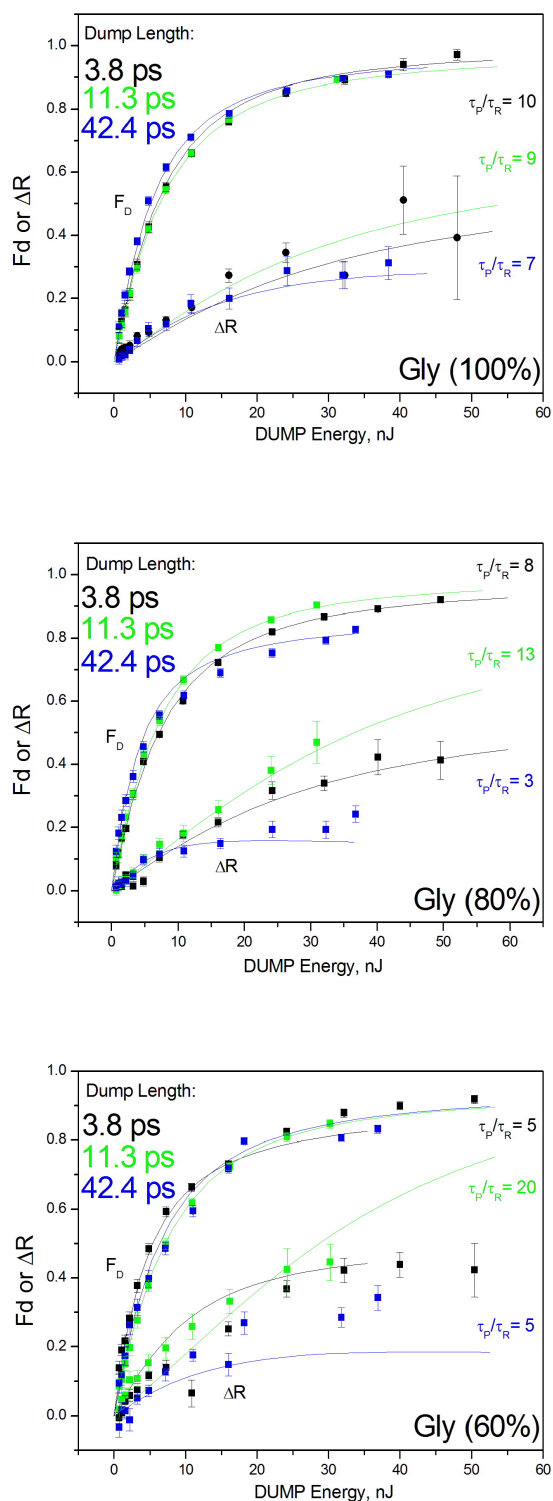


Figure 4.11: The best global fit of simulations to both F_D and ΔR following STED for DUMP pulse widths of 3.8 ps, 11.3 ps, and 42.4 ps shown for a sample of Fluorecein in Glycerol/water mixtures of (top) 100:0, (middle) 80:20 and (bottom) 60:40.

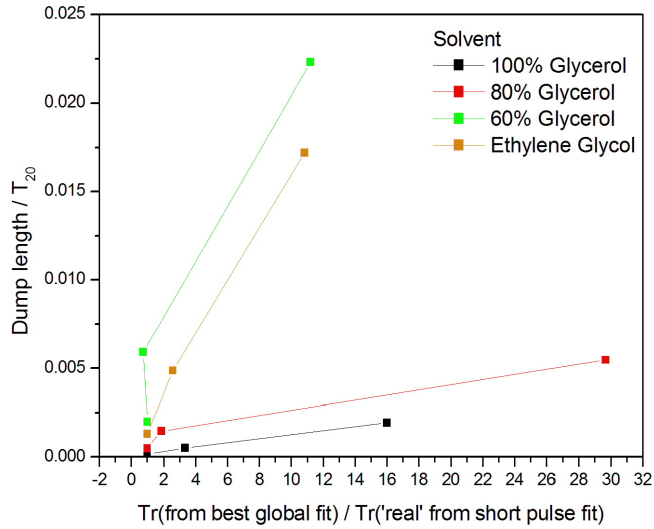


Figure 4.12: Degree of rotation of Fluorescein molecules during DUMP against inaccuracy of theoretical fit. A positive correlation is seen in all cases. With the less viscous solvents the effect of rotation during the DUMP becomes apparent at shorter DUMP pulses.

4.4.3 Discussion

The degree of rotation of the excited molecules during the DUMP pulse is neglected as insignificant in the current model of the STED process and the DUMP is treated as instantaneous. However, when the degree of rotation during the DUMP is increased through use of a longer DUMP pulse or lower solvent viscosity the model becomes a less accurate prediction of the observed data.

The DUMP pulsewidth and viscosity dependence is further demonstrated in Figure 4.12 which plots the inaccuracy of τ_R prediction (τ_R from theoretical fit divided by the τ_R ‘real’: the τ_R determined from the short DUMP pulse data) against degree of rotation during the DUMP pulse (DUMP length τ_P divided by the rotational correlation time τ_{20}). It can be seen that for each sample a positive correlation occurs. This shows that the increasing inability of the model to fit the experimental data strongly correlates with rotation during the DUMP pulse.

Ground state relaxation times τ_R obtained from theoretical fits to data for each of the three DUMP lengths and solvent viscosities are shown in Table 4.3.

τ_P	100% Glycerol	80% Glycerol	60% Glycerol
3.8 ps	380 fs	475 fs	760 fs
11.3 ps	1256 fs	869 f s	565 fs
42.4 ps	6057 fs	14133 fs	8480 fs

Table 4.3: Ground state relaxation time τ_R variation with DUMP pulse length τ_P for Fluorecein solvents of differing viscosity.

The value of τ_P/τ_R is predicted by the model with relative accuracy in the case of short DUMP pulse widths; F_D and ΔR can be fitted simultaneously to the curves generated by the model, implying that the mismatch between experimental and theoretical ΔR values is not due to experimental problems in measuring ΔR . The ratio of F_D and ΔR at low DUMP powers gives information about the molecular alignment in the sample, which does not depend on DUMP power. For the middle DUMP pulse width used (11.3 ps) it can be seen that there is a slightly lower value of F_D and ΔR than is predicted by the model, which gives a value of τ_P/τ_R that is lower than anticipated, in turn giving a higher ground state relaxation time. This effect is most apparent in the case of the long DUMP pulse used (42.4 ps) where the quality of fit is low with any value of τ_P/τ_R .

4.5 Further Investigation of the Model

It has been shown that the standard model of STED dynamics (Section 4.2) does not fully describe the process under all conditions. A summary of the steps taken in calculating F_D and ΔR for a given initial orientational distribution as used so far is given below.

The parameters used are as follows:

$t = \tau_d$: Time at which excitation happens (assumed to be instantaneous)

τ_{PD} : Time between two-photon excitation and application of the DUMP pulse

$t = 0$: Time at which DUMP pulse begins

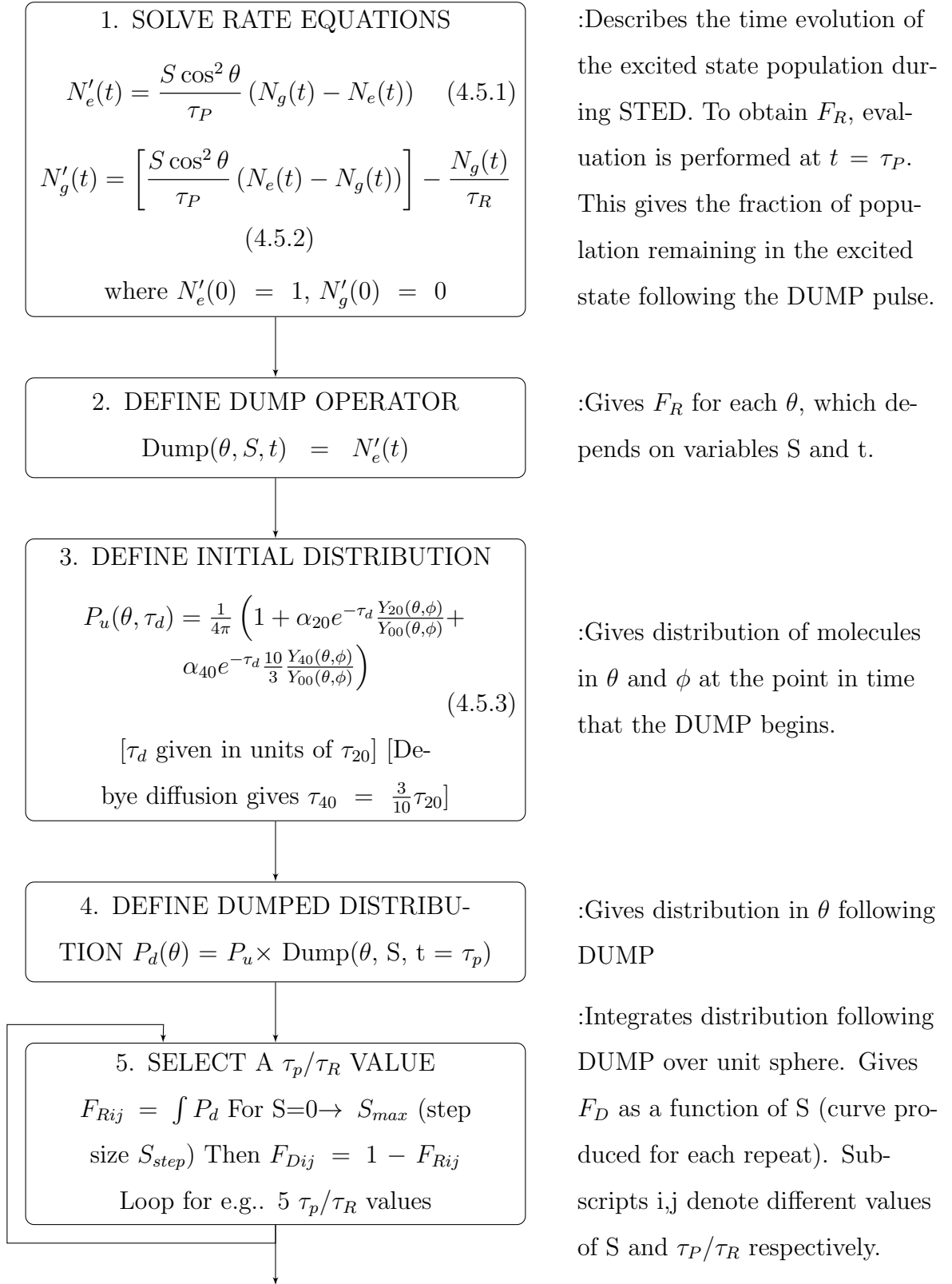
$t = \tau_P$: Time at which DUMP pulse ends

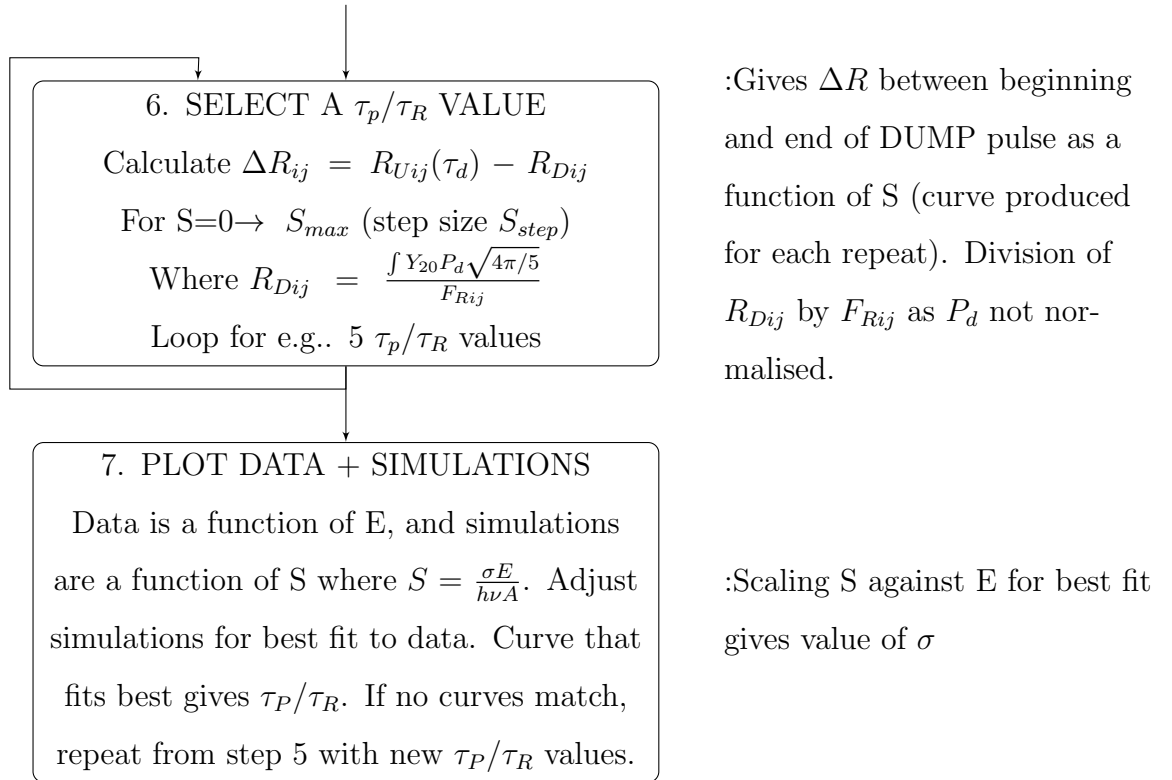
F_R : Fraction of molecules remaining in excited state

F_D : Fraction of molecules that have been depleted ($F_D = 1 - F_R$)

τ_R : Ground state relaxation time

The subscripts g and e are used to denote ground and excited states.





This model assumes a rectangular pulse and negligible rotation during the DUMP pulse; both are approximations to the real behaviour. For larger depletion pulse energies and a short DUMP pulse the rectangular pulse approximation used will have a high rate of STED throughout the pulse, resulting in a higher rate of re-excitation before relaxation in the ground state. However, at the same energy the real DUMP pulse that is approximately Gaussian in shape will have regions of the pulse with high STED rates (in the centre) and regions which experience lower STED rates (in the wings of the pulse). This means that re-excitation may occur less often than predicted for short high energy pulses. This is shown in Figure 4.13 which shows the intensity of the DUMP pulse with respect to position within the pulse. The ground state relaxation rate is equal to $1/\tau_R$. When the DUMP pulse intensity $I \geq \frac{h\nu}{\sigma_S \tau_R}$ then the re-excitation rate becomes comparable to that of relaxation.

With long DUMP pulses the intensity is consistently below this threshold irrespective of the pulse shape and energy, so the rectangular pulse approximation becomes a better description of the pulse, CW STED being the limiting case (although this

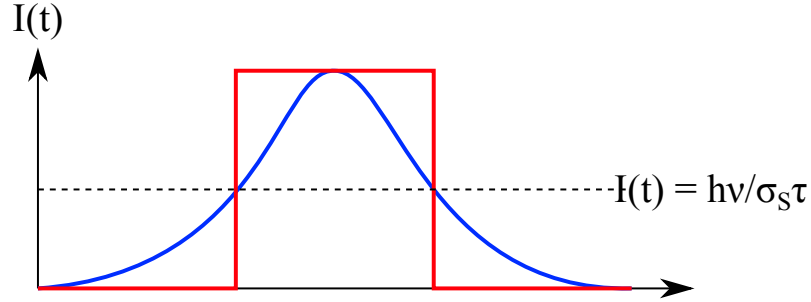


Figure 4.13: DUMP pulse intensity for the Gaussian (actual) pulse (for a short DUMP pulse i.e. saturation occurs in the centre) and the square pulse approximation used in the model. A Gaussian pulse shape (temporal profile) always has regions of minimal saturation.

neglects the increasing effect of the fluorescence rate). The modelling therefore predicts that in order to maximise F_D the DUMP pulse should be stretched to minimise re-excitation through absorption of the DUMP. The fact that the mismatch between simulations and observed data occurs at larger DUMP pulse widths is therefore unexpected, which suggests that other mechanisms are coming into play. For this reason the following adjustments to the model will therefore focus on ways to implicitly include rotation during the DUMP, as it is not possible to evaluate this explicitly. The aim is to modify the model such that it better describes the behaviour observed when long DUMP pulses are used; specifically that the simulated F_D and ΔR are lower (for long DUMP pulses) than currently as this would allow the data to fit to a higher value of τ_P/τ_R for longer DUMP pulses.

Three approaches to this are taken.

Firstly, an artificial increase in the anisotropy prior to the DUMP is applied and the result on prediction accuracy observed, crudely ‘offsetting’ some of the possible depolarisation during STED by increasing the starting alignment. Secondly, the $\cos^2 \theta$ term in Equation 4.5.1 was amended to include a constant which simulates depolarisation of the excited population during the DUMP pulse, enabling STED of molecules at an angle of $\theta \approx 90^\circ$ that may rotate into the hole ‘burnt’ into the distribution around $\theta = 0^\circ$ with strong STED (high F_D). The third approach

examines the impact of higher order moments which are present in the excited state distribution whenever re-pumping of the excited state by the DUMP pulse occurs. The excited state alignment is a product of the ground state distribution and the excitation operator as discussed in Chapter 2. The experiments in this chapter begin in an isotropic ground state and undergo 2PA such that the excited state distribution will contain $K Q = 0 0, 2 0$ and $4 0$ moments. Re-excitation of molecules that were previously excited and have undergone stimulated emission will further increase this effect. The change in magnitude of alignment moments $K Q = 2 0, 4 0, 6 0, 8 0$ and $10 0$ during the STED pulse was calculated in Mathematica using the usual STED model. The results are shown in Figure 4.14 for two different values of τ_P/τ_R . This Figure shows that for a longer DUMP pulse (i.e. greater τ_P/τ_R value) there is a greater magnitude of higher order moments at both low and high DUMP energies; this is further evidence that the presence of higher order moments is responsible for the model breakdown at long DUMP pulses.

Although the ‘writing in of’ higher order moments are accounted for in the STED model used, it does not include depolarisation during the DUMP pulse as discussed previously. Whilst depolarisation of the $\langle\alpha_{20}\rangle$ and $\langle\alpha_{40}\rangle$ moments is small on the timescale of the DUMP width, higher order moments depolarise on an increasingly fast timescale as shown in Section 1.4. Although the magnitude of higher order moments is small as shown by calculation in the simulation in Figure 4.14, it is possible that due to this fast depolarisation of higher order moments the excited state distribution is sufficiently affected during the DUMP pulse. It can be seen that especially at the higher τ_P/τ_R value the amplitudes of the higher order moments are not negligible, with amplitudes up to 10% that of the α_{20} and α_{40} moments. The faster depolarisation of these moments during the DUMP pulse could therefore result in a difference in alignment between the sample and the theoretical model.

The third approach therefore investigates the impact of the rotation of the higher order moments during the DUMP through modification of the STED model to implicitly include the rapid depolarisation of these higher moments by periodically

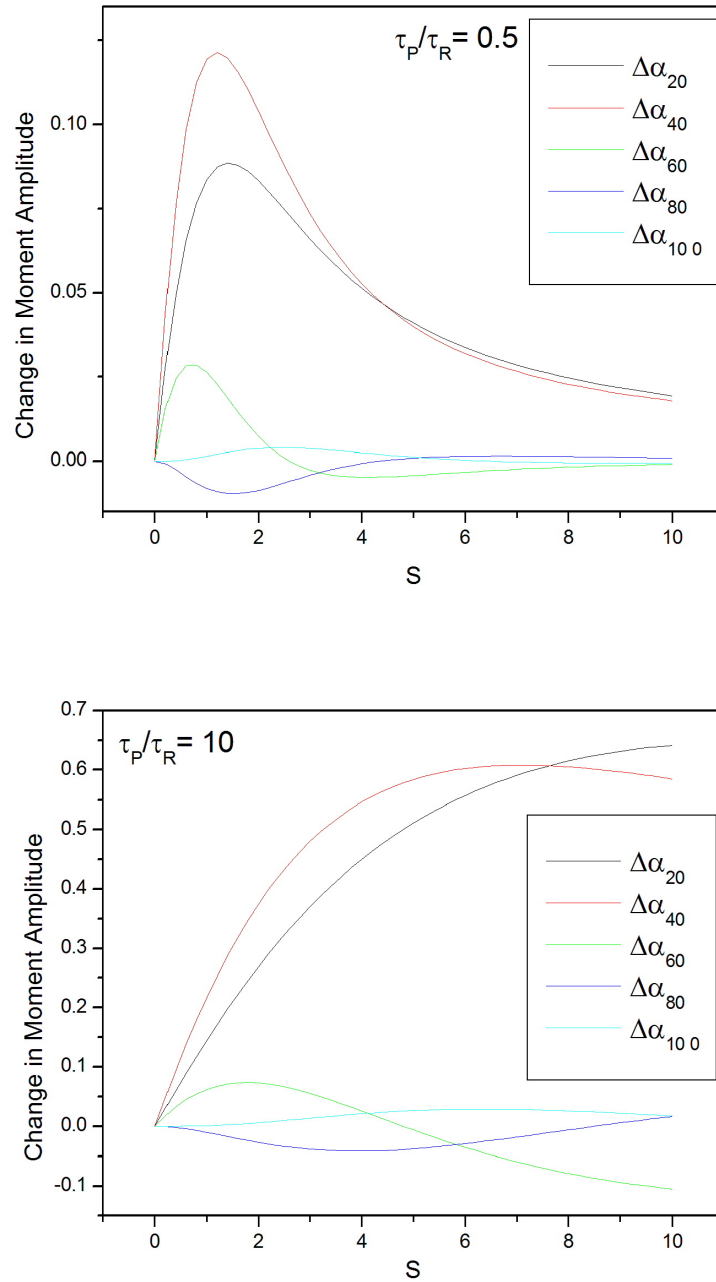


Figure 4.14: Change in excited state distribution alignment moments with time for (top) $\tau_P/\tau_R = 0.5$ and (bottom) $\tau_P/\tau_R = 10$ for a PUMP-DUMP delay of zero and a $\cos^4\theta$ (i.e. 2PA) initial alignment. The change in higher order moments at long times is greater for higher τ_P/τ_R .

resetting them to zero throughout the time course of the DUMP pulse, thereby simulating the effects of rotation during STED.

4.5.1 Alteration of Alignment Moment Amplitudes

The amplitudes of the $\langle\alpha_{20}\rangle$ and $\langle\alpha_{40}\rangle$ moments present in the initial excited state distribution then are determined by the ground state distribution and excitation operator. The values obtained in the limit of weak excitation are $R(0) = 4/7$ (where $\alpha_{20} = \sqrt{5}R(0)$) and $\alpha_{40} = 8/21$ (single element transition tensor, see Chapter 2). However, if the ground state distribution experiences molecular ordering due to the excitation of molecules with an absorption dipole in the direction of the excitation pulse polarisation, the amplitudes α_{20} and α_{40} may change in addition to creation of additional moments.

To investigate this possibility, a range of $R(0)$ and α_{40} value combinations were tested using the model. The resulting simulations are shown in Figure 4.15 for the sample of Fluorescein in 100% Glycerol and the DUMP pulse width of 42.4 ps (this case was used as it has the longest DUMP width and the original simulations showed the worst fit to the data).

The observed value of $R(0)$ can be measured directly as 0.47, which is slightly lower than the theoretical maximum of $4/7$ due to a combination of experimental factors such as the finite instrument response of the streak camera, or due to an angle between absorption and emission transition dipole moments. Previous measurements in the group on more sensitive apparatus had indicated that the angle between absorption and emission was negligible. However, if the sample was being pumped too strongly such that the ground state was being depleted different values of the excited state moments than predicted from a $\cos^4\theta$ excitation probability would be produced. It can be seen in Figure 4.15 that decreasing α_{20} from the theoretical maximum to the observed value lowers the predicted F_D resulting in a better fit to the measured data, but increases the predicted ΔR giving a worse fit to the ΔR data. The parameter α_{40} cannot be measured directly but experimentally decreas-

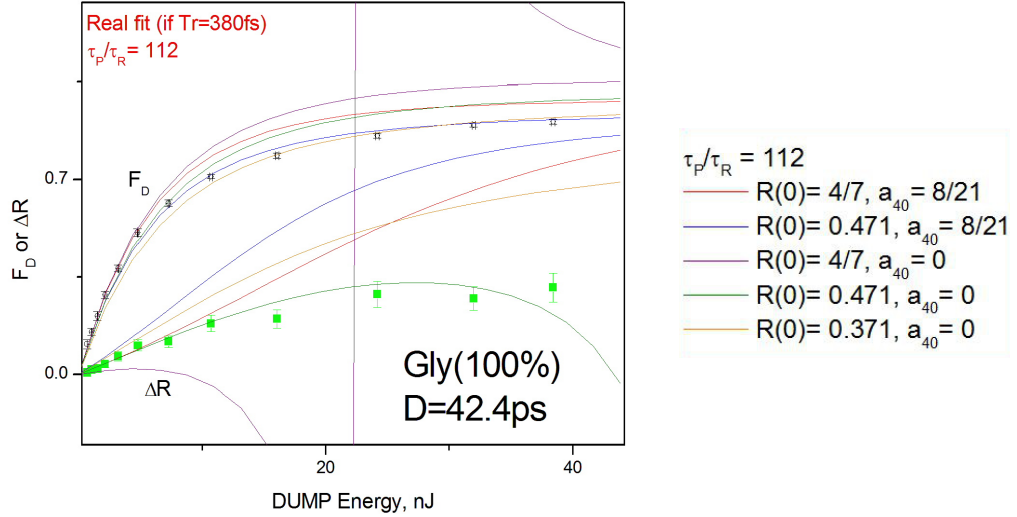


Figure 4.15: Simulations of F_D and ΔR using different combinations of input values of order moment amplitudes a_{20} and a_{40} . The red curve shows the values obtained in the weak excitation regime. The sample used is Fluorescein in 100% Glycerol with a DUMP width of 42.4 ps and a PUMP-DUMP delay of 600 ps.

ing α_{40} increases the predicted F_D resulting in a worse fit to the measured data, but lowers ΔR giving a better fit to the ΔR data. Combining the two effects offsets the decreases in accuracy to some extent, with the simulation using decreased values of both α_{20} and α_{40} (the curve in green) giving a better fit to the data. Lowering the value of α_{20} still further gives a better fit to the F_D data but a worse overall fit.

If there is significant rotation during STED then it might be expected that a higher initial alignment would ‘offset’ a certain amount of intrinsic rotation, giving a qualitatively better fit, although the magnitude of this change is not expected to be high as these moments don’t significantly relax over the timescale of the DUMP pulse.

However, $R(0)$ values above 0.4 must contain some amplitude of α_{40} to form a ‘real’ distribution. The two simulations that curve downwards with $\alpha_{40} = 0$ are therefore not physical.

This model approach therefore does not better explain the Physical effects taking place even though it does improve the results. In addition, the amplitudes of initial

moments will not be affected by the length of the DUMP pulse (i.e. will be the same for both short and long DUMP pulses) so this would not explain why the model fits for short DUMP pulses (where there is a greater sensitivity to initial alignment) but not for long ones. When there is strong saturation in the direction of the absorption transition dipole moment of the molecule, $\cos^2 \theta$ exerts a greater influence on the probability of excited state re-pumping.

4.5.2 Addition of a Constant to the Excited State Distribution

An alternative way to alter the excited state distribution prior to the DUMP pulse in the simulations is through the addition of a constant to the $\cos^2 \theta$ term in Equation 4.5.1. This is to simulate rotation during the DUMP pulse by allowing molecules oriented close to $\theta = 90^\circ$ a greater STED rate than given by $\cos^2 \theta$. As the degree of STED increases, a ‘hole’ is ‘burnt’ into the distribution for small values of θ . The larger this hole, the more net rotational diffusion from θ close to 90° to smaller θ might be expected, increasing the likelihood of these molecules being depleted. This would have the effect of reducing the H polarised fluorescence significantly more, leading to higher R_D and therefore lower ΔR .

giving a revised version of Equation 4.5.1 as

$$N'_e(t) = \frac{S \cos^2 \theta + a}{(1 + 3a)\tau_P} (N_g(t) - N_e(t)) \quad (4.5.4)$$

where a normalisation constant of $1 + 3a$ has been included so that the value of S is still comparable with the original model. This revised model is otherwise identical to the model detailed in Section 4.5. The results of this addition to the model are shown in Figure 4.16, where various simulations resulting from different values of the constant, a , are shown for each dataset. The datasets used are those resulting from STED in Fluorescein in a solvent of 100% Glycerol for three differing DUMP pulse widths.

It can be seen that addition of a constant results in a large change to the simulated

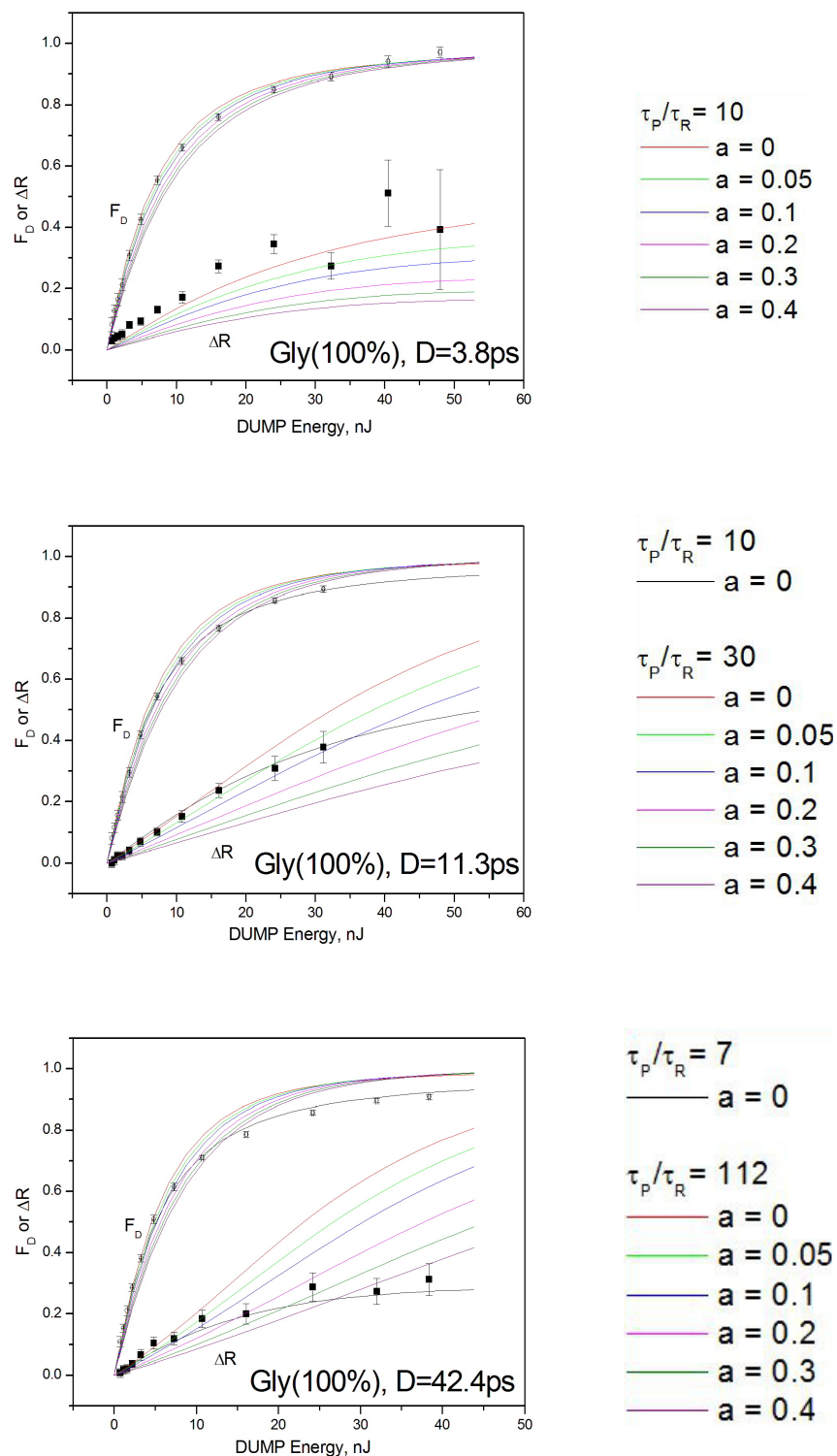


Figure 4.16: Simulations resulting from addition of a constant to the DUMP operator as in Equation 4.5.4 overlaid on observed STED data for Fluorescein in Glycerol (100%) with DUMP pulse widths of top: 3.8 ps; middle: 11.3 ps and bottom: 42.4 ps; for various values of the constant a .

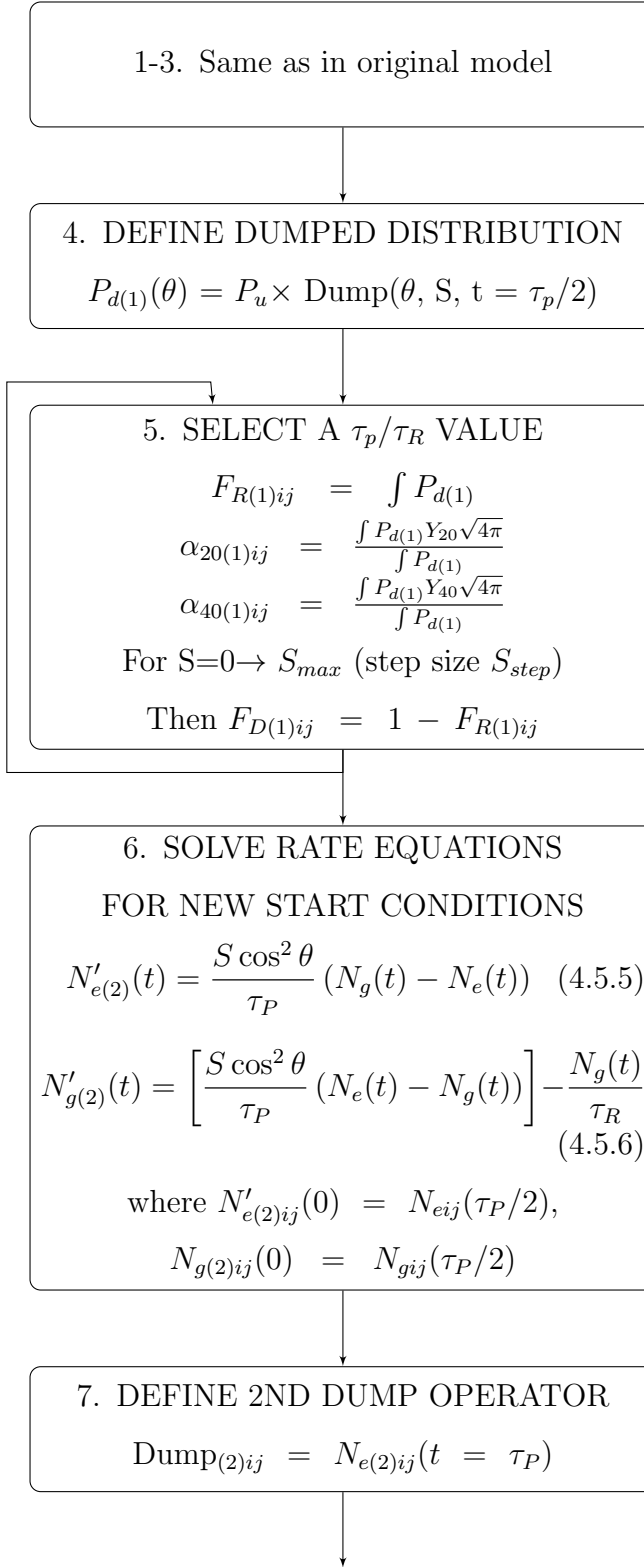
ΔR value, but a small change to the F_D value. In the case of the 3.8 ps DUMP pulse width the simulation with addition of the constant actually results in a worse fit to the data, but a small constant of 0.05-0.1 in the case of the 11.3 ps DUMP pulse width results in a better fit to the data. In the case of the 42.4 ps DUMP pulse width although the addition of a constant reduces the simulated ΔR value, the shapes of the curves do not correspond to the observed data. The addition of a constant in this way is not effective at reducing the predicted value of F_D at high S/Energy , which would leave the data fitting to a higher value of τ_P/τ_R at long DUMP widths. The amplitude of the constant needed to reduce ΔR enough is very high; too high to be the effect of the small amount of rotation expected during the pulse. This shows that rotation cannot be treated this simplistically.

4.5.3 Model in which Amplitude of Higher Order Moments is Reset to Zero Part-way Through the DUMP Pulse

As mentioned earlier, the rate at which the moments of the excited state order diffuse is related to the rank K : $\tau_{KQ} = k(k+1)D$. It can be expected therefore that only moments of high order will relax noticeably on the timescale of the DUMP pulse. For example, for a τ_P of 1% of τ_{20} the $K = 24$ moment has a decay time equal to the DUMP pulse length. As shown in Figure 4.14 (and the supporting text) higher moments are created when saturation of the DUMP transition is strong. Also, considering that the true pulse shape is much longer than the rectangular pulse assumed in the model (Figure 4.13) and that the regions outside the rectangular pulse are more significant at high depletion rates, the time ‘available’ for relaxation of higher moments may be significantly greater than anticipated.

Although it is not possible to explicitly model relaxation of just the higher order moments, it is feasible to break the STED pulse into sections and modify the resulting alignment before continuing with the next section of the DUMP pulse. Resetting the amplitude of all but the $K Q = 2 0$ and $4 0$ moments to zero part way through the DUMP pulse will have the effect of simulating the effect of rotation of these

moments during the DUMP pulse. The decision to reset moments from 6 0 upwards was arbitrary. In this second model it is necessary to perform the evaluation of the second half of the DUMP beam with all sets of starting conditions given by evaluation of the first half of the DUMP beam i.e. each value of S and τ_P used, greatly increasing the calculation complexity. This was possible using the software Mathematica as it allows the input of matrices (complex functions) as initial conditions for calculations.

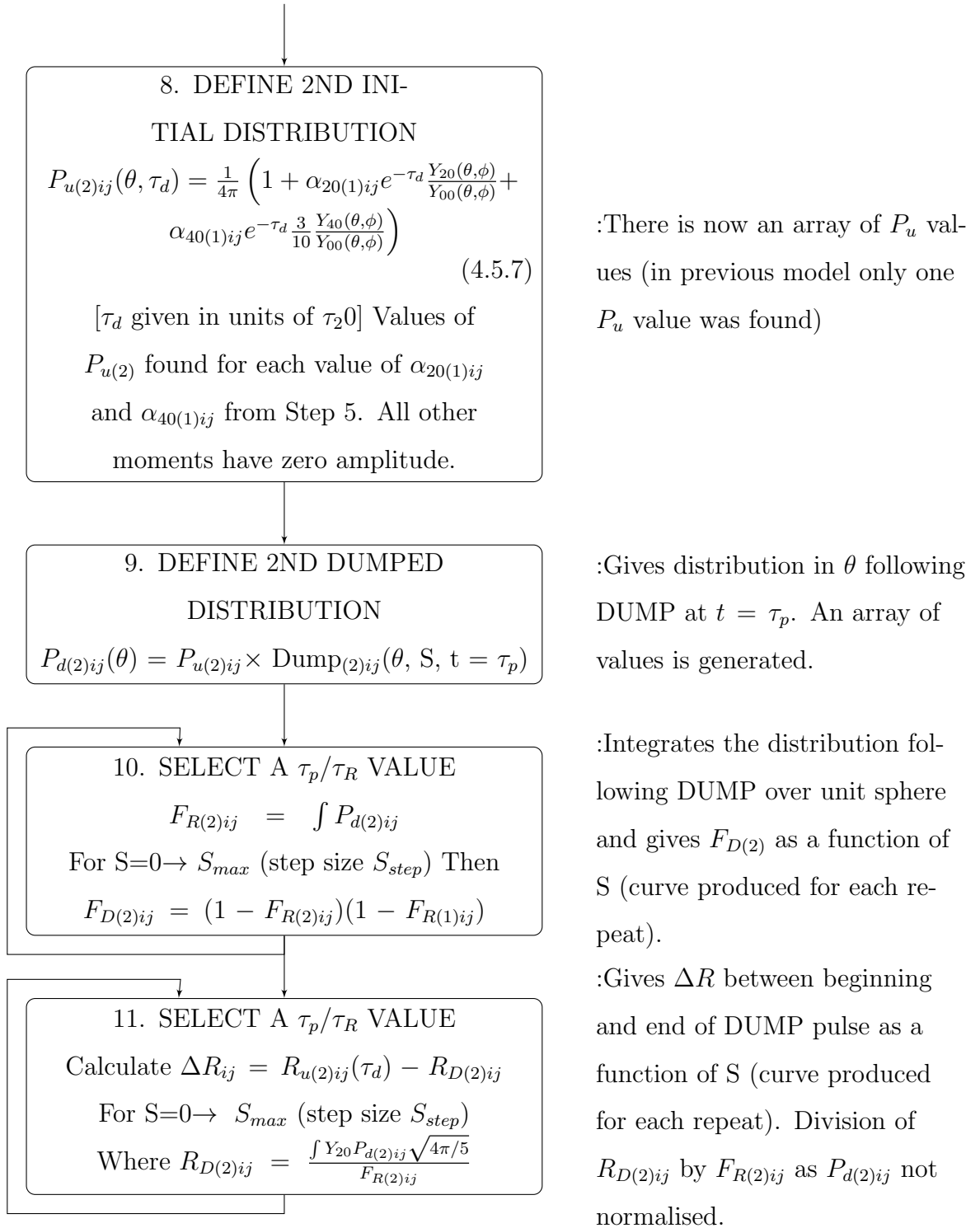


:Gives distribution in θ following DUMP but this time evaluated at $\tau_p/2$.

:As in previous model gives $F_{D(1)}$ as a function of S (curve produced for each repeat) but in this case is evaluated at $\tau_p/2$. In addition, values for $\alpha_{20(1)}$ and $\alpha_{40(1)}$ are found at this time for each value of S .

:Solutions from Step 1 evaluated at $\tau_p/2$ used as start conditions.

:Gives a value of $F_{R(2)ij}$ for all values of S and τ_p/τ_R used in Step 5.



A third model was also developed in which the higher order moments were reset four times during the DUMP pulse, which follows the same process as the model detailed above. The results for the both the model including one reset of higher

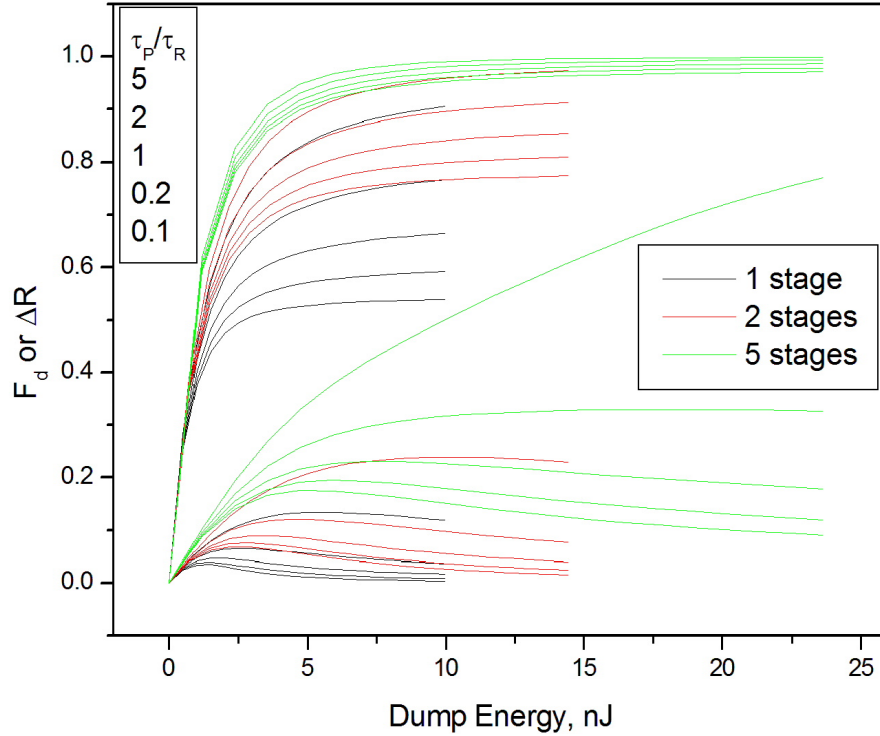


Figure 4.17: Simulations arising from the developed model showing the effect of resetting the amplitude of higher order moments to zero during the DUMP pulse once (red curves), and four times (green curves) for five different τ_P/τ_R values. The original model results are also shown (black curves) for comparison. It can be seen that this resetting results in an increase in both F_D and ΔR which exacerbates the discrepancies between the observed and predicted F_D and ΔR behaviour rather than resulting in improvement.

order moments and the model including four resets are shown in Figure 4.17.

It can be seen in Figure 4.17 that resetting the higher order moments (simulating faster rotation) results in a significant increase in both F_D and ΔR . This does indeed exacerbate the problem in fitting, indicating that rotation of higher order moments during the DUMP pulse could be the cause of an increased F_D and ΔR and therefore the less accurate fit of the model when longer DUMP pulse lengths are used.

4.6 Conclusions

The previous suspicion that there was a DUMP pulse length dependence of the performance of the existing model has been proven. Short pulses (in general a few ps but there is a dependence on the rotational time) give a good fit to experimental data and realistic values of the relaxation rate of the upper vibrational levels can be obtained. As the pulse length is increased, agreement between experiment and theory is still reasonable for most systems, but substantial variation in the obtained value of the relaxation times are observed. For the longest pulses (10's of ps) much greater breakdown of the model is observed. Simulations fit poorly with experimental observation and the obtained values of the ground state relaxation time are an order of magnitude higher than with short DUMP pulses; this is physically unrealistic.

The degree to which the model breaks down and the DUMP pulse length at which it does was seen to have a noticeable dependence on the solvent viscosity. With more viscous solvents the model performs better, particularly in the long pulse regime. This has been observed in other systems for GFP; Masters observed good agreement for relatively long pulses [5] but also observed the increase in obtained relaxation time as the pulse length was increased. Armoogum also observed significant variation of relaxation time with pulse lengths for a number of fluorescent dyes [2], although the pulse lengths used in this experiment were not long enough to observe complete breakdown of the model.

This dependence on pulse length and solvent viscosity of accuracy of the model suggests that a possible reason for this breakdown may be due to relaxation of the orientational distribution during the timescale of the STED pulse. This was not accounted for in the existing model as the timescale was considered insufficient for any significant relaxation of the excited state moments (α_{20} and α_{40}) that are present before the STED pulse. Moments of much higher order are created however when the degree of saturation of the STED transition is high and it is possible for these moments to relax significantly when the DUMP pulse is long and/or the solvent

viscosity is low. To investigate this possibility a number of modifications to the existing model were performed, as explicit inclusion of rotational diffusion is not possible, with the aim of improving the qualitative agreement with experimental observation in this long pulse regime.

The initial alignment was modified in an ad-hoc sense to account for the possibility that initial alignment was different to that anticipated in the model, due to experimental factors, transition tensor shape, or non-Debye diffusion. Although this was successful in improving the qualitative fit, it required large and unphysical values of the initial moments to do so. This cannot therefore be considered an explanation to the problem.

Curves were generated with the inclusion of a constant to the $\cos^2\theta$ term in the DUMP angular dependence to simulate the effect of molecules orientated close to perpendicular to the DUMP polarisation diffusing towards the DUMP polarisation direction substantially increasing their interaction with the field. Whilst this did have the effect of qualitatively reducing the change in alignment ΔR to the levels experimentally observed, the quantitative comparison was poor and the magnitude of the constant term was substantial and not thought to be physically realistic given the relatively small change in alignment possible during the DUMP timescale.

An attempt was made to modify the model to incorporate the much faster relaxation of higher order moments by periodically resetting their magnitudes to zero during the STED pulse. Although this had qualitatively the opposite effect on the F_D and ΔR magnitude to that required to bring them into agreement with observation, the substantially different results of this simulation compared to the existing model for all pulse lengths when the STED rate is high highlights the importance of the contribution of higher order moments; this is the case even though the higher order moment magnitudes are relatively small compared with the initial excited state alignment. This suggests that although it cannot be modelled in this way the relatively small amount of orientational diffusion that happens during the STED pulse may be sufficient to significantly alter the observed effect of the STED pulse

on the excited state alignment. Alternative methods of modelling this reorientation may therefore be more successful, such as perhaps a full numerical solution of the diffusion equation in the presence of STED (although this would be computationally very intensive).

Although the relations with solvent viscosity and pulse length along with the consistency of the effect between chromophore-solvent systems is suggestive of rotational diffusion as being the reason for the breakdown of the model, the possibility of other photophysical effects should not be excluded. Excited state absorption transition linewidths and solvent relaxation for example have not been considered. Such effects might be expected however to be specific to individual chromophores whereas the observed pulse length behaviour described here has been observed so far to be quite general from system to system. More detailed modelling of orientational diffusion during STED may be necessary therefore before it can be dismissed as the cause of the observed anomalous behaviour of STED for long pulses.

In previous applications of STED it has normally been considered advantageous to stretch the pulse as much as possible to maximise its efficiency; little work has been performed in quantifying the optimum conditions for maximising F_D . It is observed in this work that the gain in STED efficiency for longer pulses is minimal to zero, particularly for non-viscous solvents. It may therefore be advantageous to quantify the optimum DUMP length for specific STED applications.

References

- [1] R. J. Marsh, D. A. Armoogum, and A. J. Bain, "Stimulated emission depletion of two-photon excited states," *Chemical Physics Letters*, vol. 366, no. 3-4, pp. 398–405, 2002.
- [2] D. Armoogum, *Time Resolved Excited State Photo-Engineering*. PhD thesis, UCL, 2004.
- [3] J. R. Lakowicz and B. R. Masters, "Principles of fluorescence spectroscopy," *Journal of Biomedical Optics*, vol. 13, p. 29901, 2008.

-
- [4] R. Marsh, D. Armoogum, and A. Bain, “Stimulated emission depletion of two-photon excited states,” *Chemical Physics Letters*, vol. 366, no. 3-4, pp. 398–405, 2002.
- [5] T. Masters, *Time-resolved fluorescence studies of Enhanced Green Fluorescent Protein and the molecular dynamics of 3-Phosphoinositide Dependent Protein Kinase 1*. PhD thesis, UCL, 2009.
- [6] G. P. Agrawal, *Nonlinear fiber optics*. Springer, 2000.
- [7] N. Nicolau, *Single and two-Photon fluorescence studies of linear and non-linear optical chromophores*. PhD thesis, UCL, 2007.
- [8] D. A. Armoogum, R. J. Marsh, N. Nicolaou, O. Mongin, M. Blanchard-Desce, and A. J. Bain, “Stimulated emission depletion and fluorescence correlation spectroscopy of a branched quadrupolar chromophore,” in *Proceedings of SPIE*, vol. 7030, pp. 70300S–70300S–10, SPIE, Aug. 2008.
- [9] R. J. Marsh, “Control of Single Molecule Fluorescence Dynamics by Stimulated Emission Depletion .,” in *Proceedings of SPIE*, vol. 5222, pp. 78–86, 2003.
- [10] A. J. Bain, R. J. Marsh, D. A. Armoogum, O. Mongin, L. Porrès, and M. Blanchard-Desce, “Time-resolved stimulated emission depletion in two-photon excited states.,” *Biochemical Society Transactions*, vol. 31, no. Pt 5, pp. 1047–1051, 2003.
- [11] R. J. Marsh, M. A. Osborne, and A. J. Bain, “Control of single-molecule fluorescence dynamics by stimulated emission depletion,” in *Optical Science and Technology, SPIE’s 48th Annual Meeting*, pp. 78–86, International Society for Optics and Photonics, 2003.

Summary

The work detailed in this thesis has important implications for a number of areas of scientific research.

In Chapter 2 it was shown that in AF257, an example of a branched trigonal planar molecule optimised for 2PA, there exist two separate fluorescing components. Using a combination of fluorescence intensity and fluorescence anisotropy measurements it was shown that these two components exhibit differing characteristics and behavior such as differing degrees of excitation energy delocalisation and differing emitting energy levels. This could have implications for the measurement of the 2PA quantum yield (as they have quite different lifetimes) of such molecules, which has previously been assumed to be wavelength independent. Differentiation between the two components seemed to happen in the excited state, with a common absorption mechanism taking place.

This information will help with electronic structure calculations both in the design of new models of such 2PA molecules, and in the testing of existing ones. Whether or not the emission dipole is oriented parallel to the absorption dipole provides a much more sensitive test of proposed theoretical models of the electronic states of these molecules than trying to make quantitative comparisons of the absorption cross section. In relation to chapters 3 and 4, the knowledge of the relative orientation of the absorption and emission dipole moments can be used for optimising STED, as the two different components may each be better used in different STED experiments. This greater understanding of the molecules may then be useful in the practical application of STED in the future. For example, in the case of excitation

distributed over the three molecular branches, the problems described in Chapter 3 in the implementation of CW STED would be greatly reduced because there would not be so much of a 'hole' generated in the distribution. It could also affect measurements of energy transfer e.g. FRET as the mechanism of transfer would be different for the two components, which could lead to misinterpretation of results.

Further investigation of the case of two fluorescing components was carried out in Chapter 3, in which the CW depletion dynamics of fluorescent proteins were investigated. Here, it was first demonstrated that the two fluorescent proteins investigated, EGFP and mCherry, both consist of a two component fluorescence decay. It was then shown that there are significant differences in the depletion characteristics of each component in both cases; more so in the case of EGFP.

This has important implications for the use of FRET, as what is being measured in this case is the net effect of several FRET pair combinations rather than just one. For example, if major and minor components occur in both donor and acceptor and minor-minor FRET is strong but major-major is weak, a low overall FRET strength will be measured even though the majority of the FRET occurs via a strong interaction.

Previously it has been assumed that differences in FRET rate between different pair combinations arise due to differences in directions of relative emission/absorption dipole moments or differences in inter-molecular distances i.e. that the radiative rates were the same for the different components with only differences in the non-radiative rates occurring. However it has been shown here using CW STED that differences in the radiative rates exist for the components of both of these molecules; finding the individual component radiative rates in this way had not previously been attempted. This means that all previous inferences about intermolecular distance/dipole orientation made using these molecules for FRET could be incorrect.

In the case of CW STED, if there are two components with differing radiative rates then it would be expected that the overall measured radiative rate would change with time as one component was depleted more than the other. It is therefore

important to know the relative radiative rates of the components.

The other factor investigated in Chapter 3 was the fact that CW STED analysis has until this point used the assumption of a single average STED rate for all molecular orientations. In reality there will be a \cos^2 dependence with molecules oriented in the direction of polarisation of the STED beam being more likely to be depleted, with these molecules displaying a shorter lifetime in the presence of CW STED. This would not be an issue if the average orientation remained constant with time, but as some molecules are preferentially depleted the orientational distribution changes, with a corresponding change in the lifetime measured. This had not been investigated before. The use of anisotropy measurements has shown that orientational effects are significant and should be considered in all future CW STED experiments.

Chapter 4 examines the mechanism of, and fitting model used, in pulsed STED. The quantification of STED is not usually modelled in any detail; it is generally assumed that more power and longer DUMP pulses are optimum for STED efficiency (i.e. the amount of depletion achievable with a low laser power). However, it was found that the amount of depletion achieved did not go up with DUMP pulse length as expected, and that there also appeared to be some correlation between depletion level and the solvent viscosity. This suggests a more complex interplay of the STED conditions with the depletion efficiency than suggested by the previous simple assumption. Efficiency in STED has significant industrial relevancy with respect to super-resolution microscopy, not only in terms of the available intensity from low cost, low maintenance, laser diodes, but more importantly in maintaining a STED intensity and heat input that is not detrimental to sensitive live biological samples. Better understanding therefore of the detailed quantification of STED dynamics with the aim of finding the optimum conditions and dye behaviour would be desirable.

The results imply that the rotational motion of the dye molecules is an important contributor to the STED dynamics. Simple attempts to approximate the effects of non-Debye diffusion of the molecular orientations, although not successful in explain-

ing the observation, do demonstrate the significance of rotation during the DUMP pulse. If a more realistic model of the effects of reorientation were successfully developed, STED may provide a useful tool in investigating non-Debye diffusion in dye-host systems.

In each of the cases investigated in this thesis it was found that looking at the fluorescence lifetime alone did not give the whole picture; it was only by looking at the lifetime and anisotropy data together that many relevant details were shown. This was the case in the possible excited state geometries of Chapter 2, in the more precise quantification of CW STED in chapter 3, and for the possible complex re-orientational behaviour in Chapter 4. Additionally, the combined use of time-resolved fluorescence and stimulated emission depletion in this work has demonstrated that there is still much to understand about the detailed behaviour of excited chromophores in solution.